MAGAZINE OF CIVIL ENGINEERING

Magazine of Civil Engineering

Online peer-reviewed open-access scientific journal in the field of Civil and Construction Engineering

Founder and Publisher: Peter the Great St. Petersburg Polytechnic University

This journal is registered by the Federal Service for Supervision of Communications, Information Technology, and Mass Media (ROSKOMNADZOR) in 2020. Certificate El No. FS77-77906 issued February 19, 2020.

Periodicity: 8 issues per year

Publication in the journal is open and free for all authors and readers.

Indexing: Scopus, Web of Sceince (ESCI, RSCI), DOAJ, Compendex, Google Academia, Index Copernicus, ProQuest, Ulrich's Serials Analysis System, CNKI

Corresponding address: 29 Polytechnicheskaya st., Saint Petersburg, 195251, Russia

Chief science editor:
D.Sc., Galina L. Kozinetc

Deputy chief science editors:
D.Sc., Sergey V. Korniyenko

Executive editor: Ekaterina A. Linnik

Translator, editor: Irina Ye. Lebedeva

Proofreader: Philipp Chrysanthes S. Bastian

DT publishing specialist:
Anastasiya A. Kononova

Contacts:
E-mail: mce@spbstu.ru
Web: http://www.engstroy.spbstu.ru

Date of issue: 12.08.2024

Contents

Contents

Deformation of box-sectional structures during torsion with bending

N.I. Karpenko[1], S.N. Karpenko[1], Vl.I. Kolchunov[2] (iD) **, V.I. Kolchunov[2]** ✉

[1] *Research Institute of Building Physics (NIISF RAACS), Moscow, Russian Federation*

[2] *Moscow State University of Civil Engineering (National Research University), Moscow, Russian Federation*

✉ *asiorel@mail.ru*

Abstract. The article is devoted to the problem of complex stress state of reinforced concrete under the action of torsion with bending, taking into account axial and transverse forces. The existing calculation models remain imperfect, despite a significant number of publications in the world on this problem. They are fragmentary and sometimes contradictory and consider individual special cases of stress. The proposed version of the deformation model is based on physical relations for reinforced concrete, static equations and conditions for compatibility of deformations in the design section at the stage after the crack formation. The calculation model takes into account all the components of external forces in the rod element, the spatial nature of cracks, various cases of the location of the compressed concrete zone or its absence, depending on the ratio of the acting forces in the design structure. The obtained analytical dependences allow one to determine interconnected design parameters, such as stresses in the concrete of the compressed zone, the height of the compressed concrete, stresses in axial and transverse rods, deformations in concrete and reinforcement, curvature and twisting angle of a reinforced concrete element, while simultaneously applying a twisting and bending moments, axial and transverse forces to the element. The deformation model obtained in the article can be used in the design of a wide class of reinforced concrete structures under the action of torsion with bending taking into account axial and transverse forces in the calculated element.

1. Introduction

Reinforced concrete structures of civil and industrial buildings and structures are considered as an object of study undergoing a complex stress state – torsion with bending, taking into account axial and transverse forces.

Calculation of such structures remains one of the byways of the theory of reinforced concrete. It is suffice to note that up until now, in foreign and Russian guidelines on the design of reinforced concrete structures and in scientific publications of the last decade, for example, [1–7] and others, conditional design models are used, including even truss analogy models [8–11]. Experimental studies of such structures were few and they were also fragmentary in the study of individual cases and types of the deformed state, cracking and destruction of complexly stressed structures, for example, with the overrepresentation of bending [5, 12, 13], with the overrepresentation of torsion without regard to transverse forces, torsion with bending in the horizontal plane [14], studies of structures reinforced with an external cage [15, 16] and

models of transverse and torsional stability [17], and others. So far, there are no general analytical methods for modeling complexly stressed reinforced concrete structures under the considered stress state, despite the fact that attempts to create them have been made repeatedly. One of the most general calculation models of deformation of reinforced concrete with cracks in a complex stress state is based on the section method and is being developed in Russia. It includes the deformation model of N.I. Karpenko [18] and a block deformation model with a spatial calculated section with a wide range of design parameters taken into account [19]. These models are increasingly receiving experimental substantiation at various ratios, different shapes and structures of sections and for different classes of concrete [20–22].

Numerical methods are used to solve the class of problems under consideration, in particular, the finite element method implemented in software systems [23–25]. An analysis of their application shows [26] that they not only do not allow a qualitative analysis of the studied physical parameters during the deformation of reinforced concrete with cracks but also relatively approximately describe the results of experimental studies of reinforced concrete structures under the considered stress state and, especially, the parameters of the limit states of the second group, for example, crack opening width in structures made of high-strength reinforced concrete and fiber-reinforced concrete [16].

In all known analytical models, including those proposed by the authors [18, 27], cases of a complex stress state are considered, when in a spatial section, not a through crack is formed but a crack that is interrupted in the compressed zone of concrete. In this regard, the article under consideration presents the features of constructing a design model for box-sectional elements under the combined action of bending and torque moments, normal and tangential forces for areas of a reinforced concrete element with through cracks. This case is realized when the element is dominated by bending with torsion and the normal longitudinal tensile force.

The relevance of such a study is determined by the increasingly complex types of impacts on reinforced concrete structures and the need to take them into account when designing buildings and structures to improve their safety.

The aim of the study was to determine the stress-strain state of reinforced concrete box-sectional structures during torsion with bending under the action of transverse and tensile longitudinal forces in the design section.

The tasks of the study were as follows:

- construction of a design scheme for reinforced concrete structures of rectangular box-shaped and solid sections with spatial cracks;
- determination of forces in longitudinal and transverse reinforcement;
- determination of deformations in the lower and upper zones as well as the side walls of the cross-sectional box of the element.

2. Methods

2.1. Scheme of the Reinforcement of a Cross-Sectional Box Element

The cross-sectional box of the reinforced element of size $h \times b$ is reinforced with four longitudinal reinforcement rods. Two rods (1, 2) with area $F_{S(1)}$ and $F_{S(2)}$ are located in the lower tension zone and two rods (3, 4) with area $F'_{S(3)}$ and $F'_{S(4)}$ – in the upper tension zone. We assume that $F'_{S(3)} = F'_{S(4)} = F'_S$, h_1, b_1 is the distance between the rods.

Longitudinal reinforcement is bordered by closed clamps with area F_{SW0} and the pitch U_{SW0}; h_2 and b_2 are the dimensions of the clamps. The clamps are transferred to the level of the longitudinal reinforcement with a reduced pitch U_{SW} as in the more general model, where

$$U_{SW} = U_{SW0} \frac{(b_1 + h_1)}{(b_2 + h_2)}. \tag{1}$$

The running area of the clamps will be:

$$f_{SW} = \frac{F_{SW0}}{U_{SW}} = F_{SW0}\frac{(b_2 + h_2)}{(b_1 + h_1)U_{SW0}}. \tag{2}$$

2.2. The Tangential Force Flows

The design diagram of the cross-sectional box of the element with through cracks is shown in Fig. 1. This diagram is realized when the torques (T) and normal tensile force (N) are predominant. The action of tangential forces is reduced to the flow of tangential forces along the contour 1–2–3–4 (Fig. 2a).
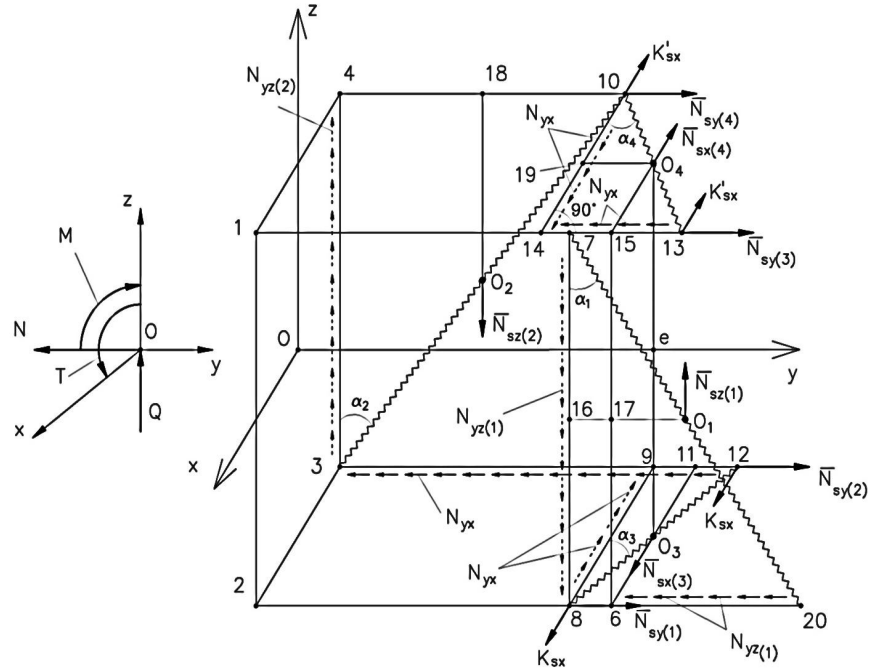
Figure 1. Design diagram of the cross-sectional box with through cracks.
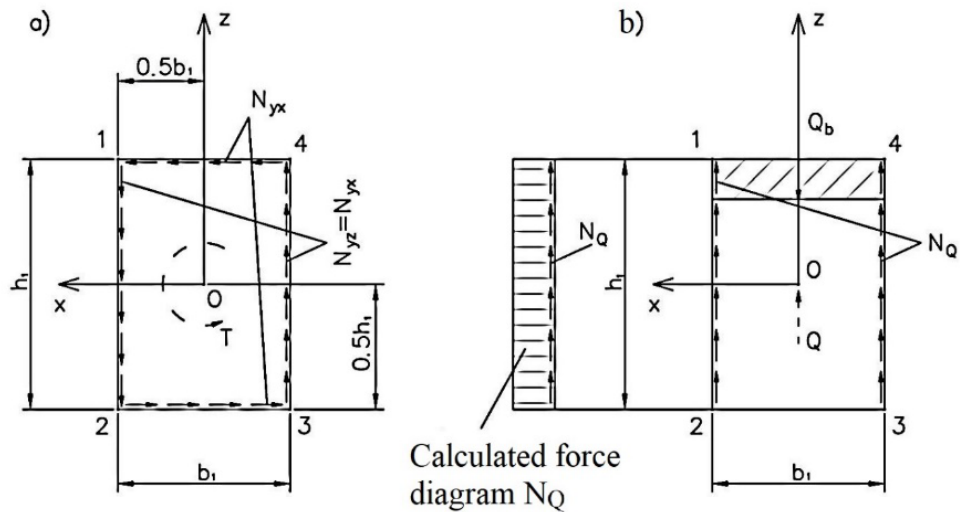
Figure 2. a) – scheme of tangential force flows N_{yx}, N_{zy} from the action of the torque T along the design contours 1–2–3–4; b) – flow diagrams of tangential forces from N_Q from the action of the tangential force along the design contours 1–2–3–4.

$$N_{yx} = N_{yz} = \frac{T}{2h_1 b_1}. \tag{3}$$

The action of tangential forces is reduced to flows

$$N_Q = \frac{Q}{2h_1}. \tag{4}$$

The total flow on line 1–2 will be

$$N_{yz(1)} = \frac{T}{2h_1 b_1} - \frac{Q}{2h_1}. \tag{5}$$

The total flow on line 3–4 will be

$$N_{yz(2)} = \frac{T}{2h_1 b_1} + \frac{Q}{2h_1}. \tag{6}$$

The flows of tangential forces along lines 2–3 and 1–4 will be equal to the values of N_{yx}, determined by dependence (3).

2.3. Determination of Forces and Stresses in Transverse Reinforcement Rods

Inclined lines 7–20 and 3–10 pass along inclined cracks located in the vertical walls of the cross-sectional box of the element, $\overline{N}_{sz(1)}$ and $\overline{N}_{sz(2)}$ are the total forces taken by the vertical rods of the clamps in these walls.

The angles of inclination of cracks in vertical walls approach 45°. In this case, the effect of dowel forces is reduced. In this regard, the vertical thrust forces in the longitudinal reinforcement are neglected. As a result, considering the conditions for the balance of forces in elements 3–4–10 and 8–7–20 from the action of torques, we find that the forces $\overline{N}_{sz(1)}$ and $\overline{N}_{sz(2)}$, perceived, respectively, in inclined cracks 7–20 and 3–10, will be:

$$\begin{aligned}
\overline{N}_{sz(1)} &= N_{yz(1)} l_{7-8} = N_{yz(1)} h_1; \\
\overline{N}_{sz(2)} &= N_{yz(2)} l_{3-4} = N_{yz(2)} h_1.
\end{aligned} \tag{7}$$

The forces $\overline{N}_{sz(1)}$ and $\overline{N}_{sz(2)}$ are expressed through the stresses $\sigma_{sz(1)}$ and $\sigma_{sz(2)}$ in the vertical rods of the clamps located along lines 7–8 and 4–3 in sections 8–20 and 4–10, respectively,

$$\begin{aligned}
\overline{N}_{sz(1)} &= N_{yz(1)} l_{7-8} = \sigma_{sz(1)} h_1 \operatorname{tg}\alpha_1 f_{SW}; \\
\overline{N}_{sz(2)} &= N_{yz(2)} l_{3-4} = \sigma_{sz(2)} h_1 \operatorname{tg}\alpha_2 f_{SW},
\end{aligned} \tag{8}$$

where:

$$\begin{aligned}
\sigma_{sz(1)} &= \frac{N_{yz(1)}}{\operatorname{tg}\alpha_1 f_{SW}} = \left(\frac{T}{2h_1 b_1} - \frac{Q}{2h_1} \right) \frac{1}{f_{SW} \operatorname{tg}\alpha_1}; \\
\sigma_{sz(2)} &= \frac{N_{yz(2)}}{\operatorname{tg}\alpha_2 f_{SW}} = \left(\frac{T}{2h_1 b_1} - \frac{Q}{2h_1} \right) \frac{1}{f_{SW} \operatorname{tg}\alpha_2}.
\end{aligned} \tag{9}$$

Now we will have to determine the stresses in the rods located in the lower and upper walls of the box-section of the element. The inclined lines 8–12 and 10–13 (Fig. 1) pass along the cracks that intersect the lower and upper walls of the cross-sectional box of the element, where $\overline{N}_{SX(3)}$ and $\overline{N}_{SX(4)}$ are the total forces, perceived by the clamps, respectively, in cracks 8–12 and 10–13. According to the design scheme (Fig. 1), these efforts will be equal:

$$\begin{aligned}
\overline{N}_{SX(3)} &= N_{yx} l_{8-9} - 2k_{SX} = N_{yx} b_1 - 2k_{SX}; \\
\overline{N}_{SX(4)} &= N_{yx} l_{10-14} - 2k'_{SX} = N_{yx} b_1 - 2k'_{SX}.
\end{aligned} \tag{10}$$

Following [18], the influence of the dowel conditions k_{SX} and k'_{SX} can be taken into account using the coefficients λ_x and λ'_x. In this case, dependencies (10) are transformed into the form:

$$\overline{N}_{SX(3)} = N_{yx}b_1 - 2k_{SX} = N_{yx}b_1\lambda_x;$$
$$\overline{N}_{SX(4)} = N_{yx}b_1 - 2k'_{SX} = N_{yx}b_1\lambda'_x, \tag{11}$$

where

$$\lambda_x = \frac{15f_{SW}}{15f_{SW} + f_{Sy}\mathrm{ctg}^2\alpha_3};$$
$$\lambda'_x = \frac{15f_{SW}}{15f_{SW} + f'_{Sy}\mathrm{ctg}^2\alpha_4}, \tag{12}$$

at

$$f_{SY} = \frac{F_{sy(1)} + F_{sy(2)}}{b_1};$$
$$f'_{SY} = \frac{F'_{sy(1)} + F'_{sy(2)}}{b_1}. \tag{13}$$

The forces $\overline{N}_{SX(3)}$ and $\overline{N}_{SX(4)}$ are expressed through the stresses σ_{sx} and σ'_{sx}, respectively, in the lower and upper rods of the clamps.

$$\overline{N}_{SX(3)} = N_{yx}b_1\lambda_x = \sigma_{sx}f_{sw}l_{9-12} = \sigma_{sx}f_{sw}b_1\mathrm{tg}\alpha_3;$$
$$\overline{N}_{SX(4)} = N_{yx}b_1\lambda'_x = \sigma'_{sx}f_{sw}l_{14-13} = \sigma'_{sx}f_{sw}b_1\mathrm{tg}\alpha_4. \tag{14}$$

Where, taking into account the values of N_{yx}, determined by the formula (3):

$$\sigma_{sx} = \frac{N_{yx}\lambda_x}{f_{sw}\mathrm{tg}\alpha_3} = \frac{T\lambda_x}{2(b_1 + h_1)f_{sw}\mathrm{tg}\alpha_3};$$
$$\sigma'_{sx} = \frac{N_{yx}\lambda'_x}{f_{sw}\mathrm{tg}\alpha_4} = \frac{T\lambda'_x}{2(b_1 + h_1)f_{sw}\mathrm{tg}\alpha_4}. \tag{15}$$

From (11) the values also follow:

$$k_{SX} = \frac{N_{yx}b_1(1-\lambda_x)}{2} = \frac{T}{2h_1}(1-\lambda_x);$$
$$k'_{SX} = \frac{N_{yx}b_1(1-\lambda'_x)}{2} = \frac{T}{2h_1}(1-\lambda'_x). \tag{16}$$

2.4. Determination of Normal Stresses in Longitudinal Reinforcement Rods

In the design scheme shown in Fig. 1, we select the plane $6-15-O_4-O_3$, parallel to the plane ZOY, respectively, the normal plane XOZ and its two lines $15-O_4$ and $6-O_3$, located on the upper and lower surfaces of the box section.

The sum of the moments of all forces acting parallel to the plane ZOY relative to the upper line $15-O_4$ will be equal to:

$$\bar{N}_{SY(1)}h_1 + \bar{N}_{SY(2)}h_1 - N_{YZ(1)}h_1 l_{8-20} + \bar{N}_{SZ(1)}l_{17-O_1} +$$
$$+ \bar{N}_{SZ(2)}\left(l_{18-10} + l_{14-15}\right) - N_{YX(1)}l_{3-12}h_1 - \tag{17}$$
$$-\left(M + 0.5Nh_1 + Ql_{0-e}\right) = 0$$

or, taking into account dependence (7), and

$$l_{17-O_1} = \left(0.5h_1 \text{tg}\alpha_1 - 0.5b_1 \text{tg}\alpha_3\right);$$
$$l_{18-10} = 0.5h_1 \text{tg}\alpha_2;$$
$$l_{14-15} = 0.5b_1 \text{tg}\alpha_4;$$
$$l_{3-12} = 0.5h_1 \text{tg}\alpha_2 + 0.5b_1 \text{tg}\alpha_4 + 0.5b_1 \text{tg}\alpha_3;$$
$$l_{0-e} = h_1 \text{tg}\alpha_2 + 0.5b_1 \text{tg}\alpha_4;$$
$$l_{8-20} = h_1 \text{tg}\alpha_1;$$
$$M + Ql_{0-e} = M_e, \tag{18}$$

where M_e is the moment applied at point e of the plane $6-15-O_4-O_3$, we find:

$$\left(\bar{N}_{SY(1)} + \bar{N}_{SY(2)}\right) = \frac{M_e + 0.5Nh_1}{h_1} + N_{YZ(1)}h_1 \text{tg}\alpha_1 - 0.5N_{YZ(1)}\left(h_1 \text{tg}\alpha_1 - b_1 \text{tg}\alpha_3\right) +$$
$$+ 0.5N_{YZ(2)}\left(h_1 \text{tg}\alpha_2 + b_1 \text{tg}\alpha_4\right) + 0.5N_{YX(1)}\left(h_1 \text{tg}\alpha_2 + 0.5b_1 \text{tg}\alpha_4 + 0.5b_1 \text{tg}\alpha_3\right), \tag{19}$$

or

$$\bar{N}_{SY(1)} + \bar{N}_{SY(2)} = \frac{M_e + 0.5Nh_1}{h_1} + 0.5N_{YZ(1)}\left(h_1 \text{tg}\alpha_1 + b_1 \text{tg}\alpha_3\right) -$$
$$- 0.5N_{YZ(2)}\left(h_1 \text{tg}\alpha_2 + b_1 \text{tg}\alpha_4\right) + N_{YX(1)}\left(h_1 \text{tg}\alpha_2 + 0.5b_1 \text{tg}\alpha_4 + 0.5b_1 \text{tg}\alpha_3\right). \tag{20}$$

In the case of pure torsion,

$$\left(\bar{N}_{SY(1)} + \bar{N}_{SY(2)}\right) =$$
$$= N_{YX(1)}\left(0.5h_1 + 0.5b_1 - 0.5b_1 - 0.5h_1 + h_1 + 0.5b_1 + 0.5b_1\right) = 0, \tag{21}$$

or

$$\bar{N}_{SY(1)} + \bar{N}_{SY(2)} = \left(h_1 + b_1\right)N_{YX}. \tag{22}$$

To determine the relationship between the forces $\bar{N}_{SY(1)}$ and $\bar{N}_{SY(2)}$, we use the condition that the sum of the torques of all forces in the reinforcement and concrete of the design element is equal to zero relative to the $O_4 - O_3$ axis. In this case, we assume that some influence of the difference in efforts $\bar{N}_{SY(3)}$ and $\bar{N}_{SY(4)}$ can be neglected, assuming that

$$\bar{N}_{SY(3)} \approx \bar{N}_{SY(4)}. \tag{23}$$

In this case, the sum of the moments of all forces applied in the sections of the design scheme (Fig. 1) relative to the vertical line $O_4 - O_3$ is equal to zero and can be represented as:

$$\overline{N}_{SY(1)} l_{6-O_3} - \overline{N}_{SY(2)} l_{11-O_3} + \overline{N}_{SY(3)} l_{15-O_4} - \overline{N}_{SY(4)} l_{19-10} + N_{YX} l_{3-12} l_{11-O_3} -$$
$$- N_{YX} l_{7-13} l_{15-O_4} - N_{YZ(1)} l_{8-20} l_{6-O_3} + k_x l_{8-6} - k_x l_{11-12} = 0,$$

where:

$$l_{6-O_3} = l_{11-O_3} + l_{15-O_4} - l_{19-10} = \frac{b_1}{2};$$
$$l_{3-12} = h_1 \mathrm{tg}\alpha_2 + 0.5\left(b_1 \mathrm{tg}\alpha_4 + b_1 \mathrm{tg}\alpha_3\right);$$
$$l_{7-13} = 0.5\left(b_1 \mathrm{tg}\alpha_4 + b_1 \mathrm{tg}\alpha_3\right);$$
$$l_{8-20} = h_1 \mathrm{tg}\alpha_1;$$
$$l_{8-6} = l_{11-12} = 0.5 b_1 \mathrm{tg}\alpha_3.$$

As a result, the sum of the moments relative to the $O_4 - O_3$ line is converted to the form:

$$\left(\overline{N}_{SY(1)} - \overline{N}_{SY(2)} + \overline{N}_{SY(3)} - \overline{N}_{SY(4)}\right) 0.5 b_1 +$$
$$+ N_{YX}\left(h_1 \mathrm{tg}\alpha_2 + 0.5 b_1 \mathrm{tg}\alpha_4 + 0.5 b_1 \mathrm{tg}\alpha_3 - 0.5 b_1 \mathrm{tg}\alpha_4 - 0.5 b_1 \mathrm{tg}\alpha_3\right) 0.5 b_1 - \qquad (24)$$
$$- N_{YZ(1)} h_1 \mathrm{tg}\alpha_1 0.5 b_1 + k_x\left(0.5 b_1 \mathrm{tg}\alpha_3 - 0.5 b_1 \mathrm{tg}\alpha_3\right) + k'_{sx}\left(0.5 b_1 \mathrm{tg}\alpha_4 - 0.5 b_1 \mathrm{tg}\alpha_4\right) = 0,$$

where, taking into account condition (23), it follows:

$$\overline{N}_{SY(1)} - \overline{N}_{SY(2)} = N_{YZ(1)} h_1 \mathrm{tg}\,\alpha_1 - N_{YX(1)} h_1 \mathrm{tg}\,\alpha_2$$

or

$$\overline{N}_{SY(1)} = \overline{N}_{SY(2)} + N_{YZ(1)} h_1 \mathrm{tg}\,\alpha_1 - N_{YX(1)} h_1 \mathrm{tg}\,\alpha_2. \qquad (25)$$

Substituting the value $\overline{N}_{SY(1)}$ into (20), we find:

$$\overline{N}_{SY(2)} = \frac{M_e + 0.5 N h_1}{2 h_1} - 0.25 N_{YZ(1)}\left(h_1 \mathrm{tg}\,\alpha_1 - b_1 \mathrm{tg}\,\alpha_3\right) -$$
$$- 0.25 N_{YZ(2)}\left(h_1 \mathrm{tg}\,\alpha_2 + b_1 \mathrm{tg}\,\alpha_4\right) + N_{YX(1)}\left(h_1 \mathrm{tg}\,\alpha_2 + 0.25 b_1 \mathrm{tg}\,\alpha_3 + 0.25 b_1 \mathrm{tg}\,\alpha_4\right),$$

or, taking into account (3), (5) and (6):

$$\overline{N}_{SY(2)} = \frac{M_e + 0.5 N h_1}{2 h_1} - \left(\frac{T}{8 b_1 h_1} - \frac{Q}{8 h_1}\right)\left(h_1 \mathrm{tg}\,\alpha_1 - b_1 \mathrm{tg}\,\alpha_3\right) -$$
$$- \left(\frac{T}{8 b_1 h_1} + \frac{Q}{8 h_1}\right)\left(h_1 \mathrm{tg}\,\alpha_2 + b_1 \mathrm{tg}\,\alpha_4\right) + \frac{T}{2 b_1 h_1}\left(h_1 \mathrm{tg}\,\alpha_2 + 0.25 b_1 \mathrm{tg}\,\alpha_3 + 0.25 b_1 \mathrm{tg}\,\alpha_4\right). \qquad (26)$$

Substitution of $\overline{N}_{SY(2)}$ into (25) leads to the dependence

$$\overline{N}_{SY(1)} = \frac{M_e + 0.5 N h_1}{2 h_1} + N_{YZ(1)}\left(0.75 h_1 \mathrm{tg}\alpha_1 + 0.25 b_1 \mathrm{tg}\alpha_3\right) -$$
$$- 0.25 N_{YZ(2)}\left(h_1 \mathrm{tg}\alpha_2 + b_1 \mathrm{tg}\alpha_4\right) + 0.25 N_{XY}\left(b_1 \mathrm{tg}\alpha_3 + b_1 \mathrm{tg}\alpha_4\right),$$

or, taking into account (3), (5) and (6),

$$\overline{N}_{SY(1)} = \frac{M_e + 0.5Nh_1}{2h_1} - \left(\frac{T}{8b_1h_1} - \frac{Q}{8h_1}\right)\left(3h_1 \text{tg} \propto_1 + b_1 \text{tg} \propto_3\right) -$$

$$- \left(\frac{T}{8b_1h_1} + \frac{Q}{8h_1}\right)\left(h_1 \text{tg} \propto_2 + b_1 \text{tg} \propto_4\right) + \frac{T}{8h_1}\left(\text{tg} \propto_3 + \text{tg} \propto_4\right). \tag{27}$$

Let us proceed to the determination of the forces $\overline{N}_{SY(3)}$ and $\overline{N}_{SY(4)}$ in the longitudinal reinforcement. The sum of the moments of all efforts applied to the right side of the design model relative to the lower line 6–11 will be equal to:

$$\overline{N}_{SY(3)}h_1 + \overline{N}_{SY(4)}h_1 - N_{YX}l_{7-13}h_1 - \overline{N}_{SZ(1)}l_{17-O_1} - \overline{N}_{YZ(2)}\left(0.5h_1 \text{tg} \propto_2 + 0.5b_1 \text{tg} \propto_4\right)$$

$$= -M + 0.5Nh_1 - Ql_{0-e} = -M_e + 0.5Nh_1,$$

or, taking into account the values of $\overline{N}_{SZ(1)}$ and $\overline{N}_{SZ(2)}$, determined by formulas (7), and condition (23), we find:

$$\overline{N}_{SY(3)} = \overline{N}_{SY(4)} = \frac{0.5Nh_1 - M_e}{2h_1} + 0.25N_{YX}\left(b_1 \text{tg}\alpha_4 + b_1 \text{tg}\alpha_3\right) +$$

$$+ 0.25N_{YZ(1)}\left(h_1 \text{tg}\alpha_1 + b_1 \text{tg}\alpha_3\right) + 0.25N_{YZ(2)}\left(h_1 \text{tg}\alpha_2 + b_1 \text{tg}\alpha_4\right),$$

or, taking into account (3), (5) and (6):

$$\overline{N}_{SY(3)} = \overline{N}_{SY(4)} = \frac{0.5Nh_1 - M_e}{2h_1} + \frac{T}{8h_1}\left(\text{tg} \propto_4 + \text{tg} \propto_3\right) +$$

$$+ \left(\frac{T}{8b_1h_1} - \frac{Q}{8h_1}\right)\left(h_1 \text{tg} \propto_1 - b_1 \text{tg} \propto_3\right) + \left(\frac{T}{8b_1h_1} + \frac{Q}{8h_1}\right)\left(h_1 \text{tg} \propto_3 + b_1 \text{tg} \propto_4\right). \tag{28}$$

After determining the forces $\overline{N}_{SZ(1)}, \overline{N}_{SZ(2)}, \overline{N}_{SZ(3)}$ in the reinforcement, we determine the stresses in the reinforcement:

$$\sigma_{sy(1)} = \frac{\overline{N}_{sy(1)}}{F_{s(1)}};$$

$$\sigma_{sy(2)} = \frac{\overline{N}_{sy(2)}}{F_{s(2)}};$$

$$\sigma_{sy(3)} = \frac{\overline{N}_{sy(3)}}{F'_{s(3)}};$$

$$\sigma_{sy(4)} = \frac{\overline{N}_{sy(4)}}{F'_{s(4)}}. \tag{29}$$

2.5. Determination of Deformations
in the Lower and Upper Zones of the Element

Average relative deformations in rods 1 and 2 of the lower longitudinal reinforcement in the sections between cracks are determined by the dependencies:

$$\varepsilon_{SY(1)} = \frac{\sigma_{sy(1)}\Psi_{sy(1)}}{E_S} = \frac{\overline{N}_{sy(1)}\Psi_{sy(1)}}{E_S F_{s(1)}};$$

$$\varepsilon_{SY(2)} = \frac{\sigma_{sy(2)}\Psi_{sy(2)}}{E_S} = \frac{\overline{N}_{sy(2)}\Psi_{sy(2)}}{E_S F_{s(2)}},$$

(30)

where $\Psi_{sy(1)}$, $\Psi_{sy(2)}$ are coefficients that take into account the effect of adhesion of reinforcement to concrete in the sections between cracks (V.I. Murashev's coefficients), $\sigma_{sy(1)}$ and $\sigma_{sy(2)}$ are stresses in rods 1 and 2 in cracks, determined from dependencies (26), (29),

$$\Psi_{sy(1)} = 1 - 0.75\varphi_S \frac{\sigma_{cnc}}{\sigma_{sy(1)}};$$

$$\Psi_{sy(1)} = 1 - 0.75\varphi_S \frac{\sigma_{cnc}}{\sigma_{sy(2)}},$$

(31)

where σ_{cnc} are stresses in the reinforcement at the moment of cracking, which in the first approximation can be determined by the formula:

$$\sigma_{cnc} = \frac{2.5 R_{btser} E_s}{E_b},$$

(32)

φ_S = 1 – with short-term load, φ_S = 0.8 – with prolonged action of the load. The calculation includes the average deformations of the two lower reinforcement rods

$$\varepsilon_{SY} = \frac{\varepsilon_{SY(1)} + \varepsilon_{SY(2)}}{2},$$

or given (30),

$$\varepsilon_{sy} = \frac{1}{2E_S}\left(\frac{\overline{N}_{sy(1)}\varphi_{sy(1)}}{F_{S(1)}} + \frac{\overline{N}_{sy(2)}\varphi_{sy(2)}}{E_{S(2)}}\right).$$

(33)

By analogy with (33), the average deformations of the upper longitudinal reinforcement will be equal to:

$$\varepsilon'_{SY} = \frac{1}{2E_S}\left(\frac{\overline{N}_{sy(3)}\varphi_{sy(3)}}{F_{S(1)}} + \frac{\overline{N}_{sy(4)}\varphi_{sy(4)}}{E_{S(4)}}\right),$$

(34)

where $\varphi_{sy(3)}$, $\varphi_{sy(4)}$ are determined by formula (31), where indices 1 and 2 are replaced by indices 3 and 4.

The average value of the deformations of the clamps in the lower and upper walls of the cross-sectional box of the element by analogy with (30) – (32) and taking into account (15) will be:

$$\varepsilon_{SX} = \frac{\sigma_{sx}\Psi_{sx}}{E_S} = \frac{N_{yx}\lambda_x\varphi_{sx}}{f_{sw}E_S \operatorname{tg}\lambda_3}.$$

(35)

By analogy with (35), the average strains of the clamps in the upper wall of the cross-sectional box of the element will be equal to the upper longitudinal reinforcement will be equal:

$$\varepsilon'_{SX} = \frac{\sigma'_{sx}\Psi'_{sx}}{E_S} = \frac{N_{yx}\lambda'_x\varphi'_{sx}}{f_{sw}E_S \operatorname{tg}\lambda_3}.$$

(36)

Introducing into (33), (36) the values $\overline{N}_{sy(1)}$, $\overline{N}_{sy(2)}$, $\overline{N}_{sy(3)}$, $\overline{N}_{sy(4)}$, N_{yx} from (26) – (28) and (3), we obtain the values ε_{SY}, ε'_{SY}, ε_{SX}, ε'_{SX} as a function of M, N, T, Q.

In the future, stresses σ_{bt} and σ'_{bt} and deformations ε_{bt}, ε'_{bt}, respectively, in the lower and upper walls of the element will also be needed. These deformations will mainly depend on the shear stresses τ_{yx} and τ'_{yx}.

$$
\begin{aligned}
\sigma_{bt} &\approx -2_{yx} \sin \alpha_3 \cos \alpha_3; \\
\sigma'_{bt} &\approx -2'_{yx} \sin \alpha_4 \cos \alpha_4;
\end{aligned}
\tag{37}
$$

$$
\begin{aligned}
\varepsilon_{bt} &= \frac{\sigma_{bt}}{E_n \nu_{nx}} = \frac{-2_{yx} \sin \alpha_3 \cos \alpha_3}{E_n \nu_{nx}}; \\
\varepsilon'_{bt} &= \frac{\sigma'_{bt}}{E'_n \nu'_{nx}} = \frac{-2'_{yx} \sin \alpha_4 \cos \alpha_4}{E'_n \nu'_{nx}},
\end{aligned}
\tag{38}
$$

where E_n, E'_n are modules of deformation of concrete strips

$$
E_n = E'_n = E_b \beta_n \approx 0.8 E_b,
\tag{39}
$$

$\beta_n \approx 0.8$ is coefficient of influence of loosening of concrete strips with cracks and reduction of modulus, ν_{nx} is coefficient taking into account the effect of plastic deformations of concrete strips on the increase in deformations ε_{bt} is determined from the dependence (2), (3). Shear stresses are determined depending on the linear shear forces N_{yx}.

$$
\begin{aligned}
\tau_{yx} &= \frac{N_{yx}}{2a\beta_{xy}}; \\
\sigma_{bt} &= \frac{-2N_{yx} \sin \alpha_3 \cos \alpha_3}{2a\beta_{xy}}; \\
\tau'_{yx} &= \frac{N_{yx}}{2a\beta'_{xy}}; \\
\sigma'_{bt} &= \frac{-2N_{yx} \sin \alpha_4 \cos \alpha_4}{2a\beta'_{xy}},
\end{aligned}
\tag{40}
$$

where a is concrete cover, β_{xy}, β'_{xy} are the coefficients of influence of the remaining concrete layers on the values τ_{yx}, τ'_{xy}, a "–" sign means that the stripes are decreasing. Taking into account (37), (39):

$$
\begin{aligned}
\varepsilon_{bt} &= \frac{-2N_{yx} \sin \alpha_3 \cos \alpha_3}{2\alpha\beta_{xy} E_n \beta_n \nu_{nx}} = -\frac{2N_{yx} \sin \alpha_3 \cos \alpha_3}{2a E_b \tilde{\nu}_{nx}}; \\
\varepsilon'_{bt} &= \frac{-2N_{yx} \sin \alpha_4 \cos \alpha_4}{2\alpha\beta'_{xy} E_n \beta_n \nu'_{nx}} = -\frac{2N_{yx} \sin \alpha_4 \cos \alpha_4}{2a E_b \tilde{\nu}'_{nx}},
\end{aligned}
\tag{41}
$$

where

$$
\begin{aligned}
\tilde{\nu}_{nx} &= \beta_n \nu_{nx} \beta_{xy}; \\
\tilde{\nu}'_{nx} &= \beta_n \nu'_{nx} \beta'_{xy}.
\end{aligned}
\tag{42}
$$

The coefficients ν_{nx} and ν'_{nx} are determined experimentally.

Following [18] and taking into account (33) – (35), the shear angles in the lower and upper horizontal walls of the cross-sectional box of the element will be equal:

$$\gamma_{SY} = \varepsilon_{SX} \text{ctg}\alpha_3 + \varepsilon_{SY}\text{tg}\alpha_3 - \frac{\varepsilon_{bt}}{\sin\alpha_3 \cos\alpha_3} =$$

$$= \frac{N_{yx}\lambda_x\varphi_{sx}}{f_{sw}E_S\text{tg}\lambda_3}\text{ctg}\alpha_3 + \frac{1}{2E_S}\left(\frac{\bar{N}_{sy(1)}\varphi_{sy(1)}}{F_{S(1)}} + \frac{\bar{N}_{sy(2)}\varphi_{sy(2)}}{F_{S(4)}}\right)\text{tg}\alpha_3 + \frac{N_{yx}}{\alpha E_b\tilde{\nu}_{nx}}; \quad (43)$$

$$\gamma'_{SY} = \frac{N_{yx}\lambda'_x\varphi'_{sx}}{f_{sw}E_S\text{tg}\lambda_4}\text{ctg}\alpha_4 + \frac{1}{2E_S}\left(\frac{\bar{N}_{sy(3)}\varphi_{sy(3)}}{F_{S(3)}} + \frac{\bar{N}_{sy(4)}\varphi_{sy(4)}}{F_{S(4)}}\right)\text{tg}\alpha_4 - \frac{N_{yx}}{\alpha E_b\tilde{\nu}'_{nx}}.$$

2.6. Determination of the Deformations of the Side Walls of the Cross-Sectional Box of the Element

There are four types of relative deformations: average relative deformations of longitudinal reinforcement $\varepsilon_{y(1)}$ – in the first vertical wall with 1, 3 longitudinal bars and $\varepsilon_{y(2)}$ – in the second vertical wall with 2, 4 longitudinal reinforcement rods as well as average relative deformations $\varepsilon_{sz(1)}$ and $\varepsilon_{sz(2)}$ of the vertical rods of the clamps of the two walls, respectively.

Average relative deformations of longitudinal reinforcement in two vertical walls will be equal:

$$\varepsilon_{y(1)} = \frac{1}{2}\left(\frac{\sigma_{sy(1)}\psi_{sy(1)}}{E_S} + \frac{\sigma_{sy(3)}\psi_{sy(3)}}{E_S}\right);$$

$$\varepsilon_{y(2)} = \frac{1}{2}\left(\frac{\sigma_{sy(2)}\psi_{sy(2)}}{E_S} + \frac{\sigma_{sy(4)}\psi_{sy(4)}}{E_S}\right),$$

or, taking into account the values (29),

$$\varepsilon_{y(1)} = \frac{1}{2E_S}\left(\frac{\bar{N}_{sy(1)}\psi_{sy(1)}}{F_{S(1)}} + \frac{\bar{N}_{sy(3)}\psi_{sy(3)}}{F_{S(3)}}\right);$$

$$\varepsilon_{y(2)} = \frac{1}{2E_S}\left(\frac{\bar{N}_{sy(2)}\psi_{sy(2)}}{F_{S(2)}} + \frac{\bar{N}_{sy(4)}\psi_{sy(4)}}{F_{S(4)}}\right),$$

(44)

where the values of $\bar{N}_{sy(i)}$, $(i = 1, 2, 3, 4)$ are determined by the dependencies (26) – (28).

The stresses in the vertical rods of the clamps are determined by the dependencies (9). Accordingly, the relative deformations will be:

$$\varepsilon_{sz(1)} = \frac{\sigma_{sz(1)}\psi_{sz(1)}}{E_S} = \frac{N_{yz(1)}\psi_{sz(1)}}{f_{sw}E_S\text{tg}\infty_1};$$

$$\varepsilon_{sz(2)} = \frac{\sigma_{sz(2)}\psi_{sz(2)}}{E_S} = \frac{N_{yz(2)}\psi_{sz(2)}}{f_{sw}E_S\text{tg}\infty_2},$$

(45)

where the coefficients $\psi_{sz(1)}$ and $\psi_{sz(2)}$ are determined by dependence (31), where the index "y" is replaced by Z, the values $N_{yz(1)}$, $N_{yz(2)}$ are determined by the dependencies (5), (6).

By analogy with (37) – (41), the stresses $\sigma_{bt(1)}$ and $\sigma_{bt(2)}$ and the relative deformations $\varepsilon_{bt(1)}$ and $\varepsilon_{bt(2)}$ of concrete strips along the cracks in the vertical walls of the cross-sectional box of the element are determined.

$$\sigma_{bt(1)} = -2\tau_{yx} \sin\alpha_1 \cos\alpha_1 = -\frac{2N_{yx} \sin\alpha_1 \cos\alpha_1}{2\alpha\beta_z};$$

$$\sigma_{bt(2)} = -2\tau_{yx} \sin\alpha_2 \cos\alpha_2 = -\frac{2N_{yx} \sin\alpha_2 \cos\alpha_2}{2\alpha\beta_z};$$

(46)

$$\varepsilon_{bt(1)} = \frac{\sigma_{bt(1)}}{E_n \nu_{n(1)}} = -\frac{N_{yx} \sin\alpha_1 \cos\alpha_1}{\alpha\beta_z E_n \nu_{n(1)}};$$

$$\varepsilon_{bt(2)} = \frac{\sigma_{bt(2)}}{E_n \nu_{n(2)}} = -\frac{N_{yx} \sin\alpha_2 \cos\alpha_2}{\alpha\beta_z E_n \nu_{n(2)}},$$

(47)

where E_n is the modulus of deformation of concrete strips. determined from dependence (39), α and β_z are quantities similar to the quantities α, β_{xy}, f'_{sy} included in dependence (41), $\nu_{n(1)}$, $\nu_{n(2)}$ are coefficients that take into account the effect of plastic deformations of concrete strips on an increase in the total deformations $\varepsilon_{bt(1)}$ and $\varepsilon_{bt(2)}$.

By analogy with (43), the total shear angles in the first and second walls of the element will be equal:

$$\gamma_{yz(1)} = \varepsilon_{sz(1)}\text{ctg}\alpha_1 + \varepsilon_{y(1)}\text{tg}\alpha_1 + \frac{\varepsilon_{bt(1)}}{\sin\alpha_1 \cos\alpha_1};$$

$$\gamma_{yz(2)} = \varepsilon_{sz(2)}\text{ctg}\alpha_2 + \varepsilon_{y(2)}\text{tg}\alpha_2 + \frac{\varepsilon_{bt(2)}}{\sin\alpha_2 \cos\alpha_2},$$

or, taking into account (45), (47):

$$\gamma_{yz(1)} = \frac{N_{yz(1)}\Psi_{sz(1)}}{f_{sw}E_S\text{tg}\infty_1}\text{ctg}\alpha_1 +$$

$$+\frac{\text{tg}\alpha_1}{2E_S}\left(\frac{\overline{N}_{sy(1)}\Psi_{sy(1)}}{F_{S(1)}} + \frac{\overline{N}_{sy(3)}\Psi_{sy(3)}}{F_{S(3)}}\right) + \frac{N_{yx}}{E_n\alpha\beta_z\nu_{n(1)}};$$

$$\gamma_{yz(2)} = \frac{N_{yz(2)}\Psi_{sz(2)}}{f_{sw}E_S\text{tg}\infty_2}\text{ctg}\alpha_2 +$$

$$+\frac{\text{tg}\alpha_2}{2E_S}\left(\frac{\overline{N}_{sy(2)}\Psi_{sy(2)}}{F_{S(2)}} + \frac{\overline{N}_{sy(4)}\Psi_{sy(4)}}{F_{S(4)}}\right) + \frac{N_{yx}}{E_n\alpha\beta_z\nu_{n(2)}}.$$

(48)

The twisting angles, following [18], are determined through the values of the shear angles γ_{xy} and γ'_{xy} of the lower and upper surfaces according to (43) and $\gamma_{xz(1)}$, $\gamma_{xz(2)}$ of the first and second walls box-section of the element according to the constraints (48), after which

$$\varphi = \frac{b_1\left(\gamma_{xy} + \gamma'_{xy}\right) + h_1\left(\gamma_{xz(1)} + \gamma_{xz(2)}\right)}{2b_1 h_1}.$$

(49)

The curvature of the element $\left(1/\rho_y\right)$ and relative deformations $\left(\varepsilon_{0y}\right)$ at the level of the y axis are determined from the dependencies

$$
\frac{1}{\rho_y} = \frac{\varepsilon_{sy} - \varepsilon'_{sy}}{h_1};
$$

$$
\varepsilon_{0y} = \frac{\varepsilon_{sy} + \varepsilon'_{sy}}{2},
$$

(50)

where ε_{sy}, ε'_{sy} are defined according to (33), (34).

Based on dependencies (3), (5), (6), (26) – (28), the twist angle, curvature and relative deformations at the levels of the y axis are expressed depending on M, T, N, Q.

3. Results and Discussion

The calculated dependences for determining the deformations and angles of rotation of the cross-sectional box of the element are constructed in such a way that the wall thickness of the section element is not limited and makes it possible to switch to a solid section. It should only be taken into account that in elements of a solid section, according to the data of experimental studies [20–21], after the formation of cracks, a part of the torque T_2 can be perceived by some solid core of the section that remains after cracking, and a part of the moment T_1 is perceived by the reinforcement in the section with a crack. In this case, for the application of the dependences obtained for the cross-sectional box when calculating the solid section in the formulas, the torque T is replaced by T_1. The values of the moments T_1, T_2 in relative values can be determined from the experimental "torque-angle of twisting" graphs [21]. As a first approximation, you can use the formula proposed in [18]:

$$
T = T_1 + T_2;
$$

$$
T_1 = T\left[1 - 0.3\left(\frac{T_{cr}}{T}\right)^4\right],
$$

(51)

where T_{sr} is the torque at the moment of cracking, T is the current torque $\left(T > T\right)$.

In this case, the question of the expediency of taking into account the effect of the concrete core is determined by the ratio of the torque and bending moments, the presence and value of longitudinal forces in the section under consideration as shown by experimental studies. It is advisable to take this effect into account only in the presence of spiral cracks developing along the entire contour [21]. In the presence of concrete in the compressed zone without cracks, the effect of the concrete core can be neglected, assuming $T_2 = 0$.

4. Conclusions

1. The refined calculation model of the complex resistance of reinforced concrete structures of the cross-sectional box, experiencing the combined action of bending and torque moments, axial and transverse forces in the stage after the formation of spatial cracks, is proposed. This stage allows you to determine analytically the stresses in the concrete in the compressed zone, the height of the compressed concrete, the stresses in the clamps, the deformations in the compressed zone of concrete as well as in the longitudinal and transverse reinforcement rods, the curvature of the element and the angle of its twisting.

2. The given design dependencies take into account all the main external influences for a reinforced concrete rod element of the cross-sectional box: torsional (T) and bending (M) moments, transverse (Q) and axial (N) forces. In this case, the action of the torque and transverse force is reduced to the action of the flow of tangential forces along the rectangular contour of the section.

3. The developed model can be used in the design of a wide class of reinforced concrete structures of buildings and structures made of ordinary and high-strength concrete and fiber-reinforced concrete, experiencing complex stress state – torsion with bending and the action of axial forces.

References

1. Ali, A.H., Mohamed, H.M., Chalioris, C.E., Deifalla, A. Evaluating the shear design equations of FRP-reinforced concrete beams without shear reinforcement. Engineering Structures. 2021. 235. Article no. 112017. DOI: 10.1016/j.engstruct.2021.112017

2. Ban, H., Tan, E.L., Uy, B. Strength of multi-span composite beams subjected to combined flexure and torsion. Journal of Constructional Steel Research. 2015. 113. Pp. 1–12. DOI: 10.1016/j.jcsr.2015.05.023

3. Mostofinejad, D., Talaeitaba, S.B. Nonlinear Modeling of RC Beams Subjected to Torsion using the Smeared Crack Model. Procedia Engineering. 2011. 14. Pp. 1447–1454. DOI: 10.1016/J.PROENG.2011.07.182

4. Kalkan, I., Kartal, S. Torsional rigidities of reinforced concrete beams subjected to elastic lateral torsional buckling. International Journal of Civil and Environmental Engineering. 2017. 11(7). Pp. 969–972.

5. Arzamastsev, S.A., Rodevich, V.V. By the calculation of reinforced concrete elements under bend with torsion. Proceedings of higher educational institutions. Construction. 2015. 9. Pp. 99–109.

6. Gunasekaran, K., Ramasubramani, R., Annadurai, R., Prakash Chandar, S. Study on reinforced lightweight coconut shell concrete beam behavior under torsion. Materials and Design. 2014. 57. Pp. 374–382. DOI: 10.1016/j.matdes.2013.12.058

7. Rahal, K.N. A unified approach to shear and torsion in reinforced concrete. Structural Engineering and Mechanics. 2021. 77(5). Pp. 691–703. DOI: 10.12989/sem.2021.77.5.691

8. Bernardo, L.F.A., Andrade, J.M.A. A unified softened truss model for RC and PC beams under torsion. Journal of Building Engineering. 2020. 32. Article no. 101467. DOI: 10.1016/j.jobe.2020.101467

9. Bernardo, L.F.A., Andrade, J.M.A., Nunes, N.C.G. Generalized softened variable angle truss-model for reinforced concrete beams under torsion. Materials and Structures. 2015. 48(7). Pp. 2169–2193. DOI: 10.1617/s11527-014-0301-z

10. Jafari, F., Akbari, J. Reliability-based design of reinforced concrete beams for simultaneous bending, shear, and torsion loadings. Frattura ed Integrita Strutturale. 2020. 14(51). Pp. 136–150. DOI: 10.3221/IGF-ESIS.51.11

11. Rahal, K. Combined Torsion and Bending in Reinforced and Prestressed Concrete beams Using Simplified Method for Combined Stress-Resultants. ACI Structural Journal. 2007. 104(4). Pp. 402–411.

12. Thomas, A., Hameed, A.S. An Experimental Study on Combined Flexural and Torsional Behaviour of RC Beams. International Research Journal of Engineering and Technology. 2017. 4(5). Pp. 1367–1370. DOI: 10.13140/RG.2.2.19425.51045

13. Behera, G.C., Rao, T.D.G., Rao, C.B.K. Torsional behaviour of reinforced concrete beams with ferrocement U-jacketing – Experimental study. Case Studies in Construction Materials. 2016. 4. Pp. 15–31. DOI: 10.1016/j.cscm.2015.10.003

14. Ajeel, A.E. Torsion plus bending and shear on reinforced concrete beams. Journal of Engineering and Sustainable Development. 2016. 20(4). Pp. 277–878.

15. Al-Bayati, G., Kalfat, R., Al-Mahaidi, R., Hashemi, J. Experimental study on crack propagation of CFRP-strengthened RC beams subjected to torsion. Australian Journal of Structural Engineering. 2018. 19(4). Pp. 279–297. DOI: 10.1080/13287982.2018.1523293

16. Jariwala, V.H., Patel, P.V., Purohit, S.P. Strengthening of RC beams subjected to combined torsion and bending with GFRP composites. Procedia Engineering. 2013. 51. Pp. 282–289. DOI: 10.1016/j.proeng.2013.01.038

17. Lee, J.H., Park, Y.M., Jung, C.Y. et al. Experimental and Measurement Methods for the Small-Scale Model Testing of Lateral and Torsional Stability. International Journal of Concrete Structures and Materials. 2017. 11. Pp. 377–389. DOI: 10.1007/s40069-017-0198-3

18. Karpenko, N.I., Kolchunov, Vl.I., Travush, V.I. Calculation model of a complex stress reinforced concrete element of a boxed section during torsion with bending. Russian journal of building construction and architecture. 2021. 3(51). Pp. 7–26. DOI: 10.36622/VSTU.2021.51.3.001

19. Kolchunov, V.I., Dem'yanov, A.I. The modeling method of discrete cracks in reinforced concrete under the torsion with bending. Magazine of Civil Engineering. 2018. 81(5). Pp. 160–173. DOI: 10.18720/MCE.81.16

20. Demyanov, A.I. Crack formation in high-strength reinforced concrete structures at complex resistance – torsion with bending. Building and Reconstruction. 2019. 5. Pp. 3–10. DOI: 10.33979/2073-7416-2019-85-5-3-10

21. Travush, V.I., Karpenko, N.I., Kolchunov, V.I., et al. Main results of experimental studies of reinforced concrete structures of high-strength concrete B100 round and circular cross sections in torsion with bending. Structural Mechanics of Engineering Constructions and Buildings. 2019. 15(1). Pp. 51–61. DOI: 10.22363/1815-5235-2019-15-1-51-61

22. Kumar, C.A., Mohan, M., Rajesh, D.V.S.P., Kulkarni, P. Behavior of fibre reinforced concrete beam in combined bending and torsion. International Journal of Research in Engineering and Technology. 2015. 4. Pp. 450–455.

23. Jog, C.S., Imrankhan, S.M. A finite element method for the Saint-Venant torsion and bending problems for prismatic beams. Computers & Structures. 2014. 135. Pp. 62–72. DOI: 10.1016/j.compstruc.2014.01.010

24. Nguyen, T.A., Nguyen, Q.H., Somja, H. Nonlinear analysis of RC members subjected to combined bending–shear–torsion stresses: a numerical multi-fiber displacement-based finite element model with warping. Acta Mechanica. 2021. 232(3). Pp. 2635–2658. DOI: 10.1007/s00707-021-02966-x

25. Nguyen, T.A., Nguyen, Q.H., Somja, H. An enhanced finite element model for reinforced concrete members under torsion with consistent material parameters. Finite Elements in Analysis and Design. 2019. 167. Article no. 103323. DOI: 10.1016/j.finel.2019.103323

26. Bulkin, S.A. Torsion with bending of rectangular steel fiber reinforced concrete beam. Building and Reconstruction. 2021. 2. Pp. 3–13.

27. Karpenko, N.I., Kolchunov, Vl.I., Kolchunov, V.I., Travush, V.I., Dem'yanov, A.I. Deformation of reinforced concrete structures during bending with torsion. Stroitel'nye Materialy (Construction Materials Russia). 2021. 6. Pp. 47–56. DOI: 10.31659/0585-430X-2021-792-6-48-56

Information about the authors:

Nickolay Karpenko, *Doctor of Technical Sciences*
E-mail: niisf_lab9@mail.ru

Sergey Karpenko, *Doctor of Technical Sciences*
E-mail: niisf@niisf.ru

Vladimir Kolchunov, *Doctor of Technical Sciences*
ORCID: https://orcid.org/0000-0001-5075-1134
E-mail: vlik52@mail.ru

Vitaly Kolchunov, *Doctor of Technical Sciences*
E-mail: asiorel@mail.ru

Cable roof with stiffening girder and flexible membrane shell

A.V. Chesnokov ✉ iD , *V.V. Mikhailov* iD

Lipetsk State Technical University, Lipetsk, Russian Federation

✉ *andreychess742@gmail.com*

Abstract. The framework of the roof, considered in the research, is a two-chord truss-like structure. The chords are joined by vertical struts. They are made of high-strength steel cables. A flexible polymer membrane is attached to the restraining chord. The opposite supports of the roof are joined by a girder made of ordinary structural steel. The girder mitigates deformations of the truss under non-uniform external loads. It is loosely connected to the vertical struts. The loose connections (so-called design clearances) prevent overstressing the girder by uniform impacts. Computational technique for static analysis of the cable roof is proposed. The main structural parameters are estimated under the condition of the full use of the material properties. The bearer chord reaches the ultimate limit state under the uniformly distributed transverse load, which is taken by the cable truss in full. A non-uniform impact is split between the truss and the girder by the condition of compatibility of deformations. The expressions for the axial stiffnesses of the chords, the design clearance values, and the allowable deformations of the roof are given. The work contributes to the development of hybrid building constructions by providing the initial data for the conceptual design stage. It allows to validate structural models and to verify the results of numerical computer analysis.

Citation: Chesnokov, A.V., Mikhailov, V.V. Cable roof with stiffening girder and flexible membrane shell. Magazine of Civil Engineering. 2024. 17(5). Article no. 12902. DOI: 10.34910/MCE.129.2

1. Introduction

The framework of the roof, considered in the research, is a two-chord cable truss with a girder arranged between the opposite supports. The chords are joined by vertical struts (Fig. 1). The struts are loosely connected to the girder: the truss moves freely by design clearances before the girder begins taking external transverse loads.

The truss is pre-stressed by tensioning the bearer chord '*b*', which is situated below the restraining chord '*r*'. The flexible shell is attached to the restraining chord. It is made of architectural fabrics or a polymer membrane [1].
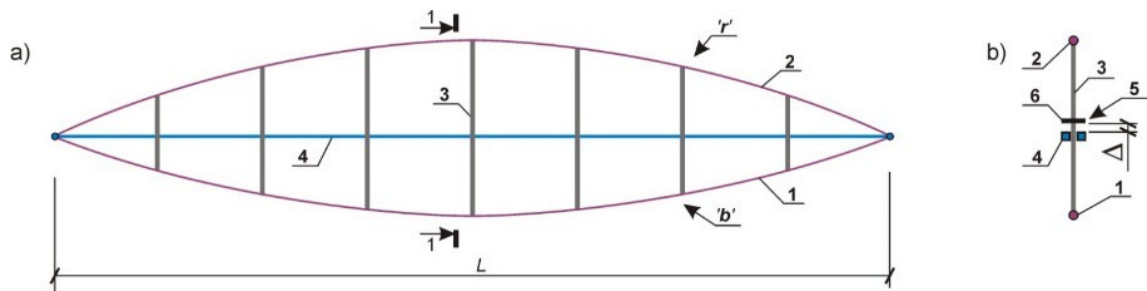
Figure 1. The framework of the roof structure considered in the research:
a – general view, b – view along the line 1-1; 1 – bearer chord 'b'; 2 – restraining chord 'r';
3 – vertical strut; 4 – stiffening girder; 5 – loose connection of the strut and the girder
(design clearance); 6 – retainer.

The roof can be split into separate sections. An ordinary section is encompassed by catenary and backstay cables (Fig. 2). The section, considered in the research, is highlighted in blue in Fig. 2.
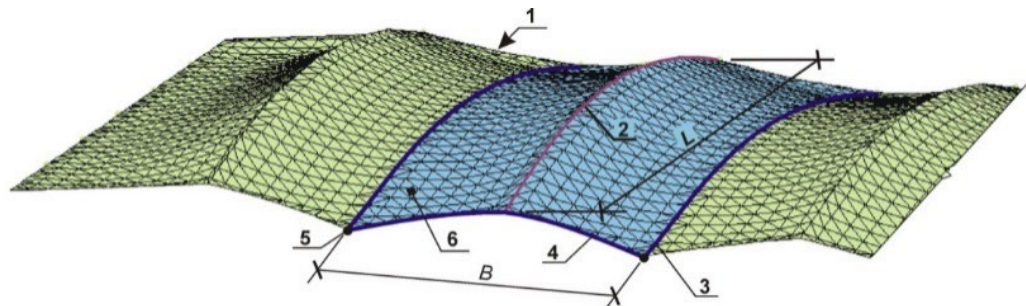

Figure 2. The shell of the roof: 1 – the flexible membrane;
2 – ridge, formed by the restraining chord of the roof's framework; 3 – backstay cable;
4 – catenary cable; 5 – fixed support; 6 – roof's section, considered in the research.

Pre-stressed cable structures with flexible shell belong to hybrid building constructions. They are an efficient solution for sheltering urban spaces, exhibition halls, airports, railway stations, and stadiums, as well as for temporary covering archeological areas, sites of architectural heritage and emergency facilities [2–6].

The key factor, which stimulates the growth of popularity of the hybrid constructions, is the emergence of high-quality steel cables and polymer membranes in the market. Development of multifunctional structural membranes offers great opportunities for self-sensing envelopes of buildings, as well as in the field of energy harvesting and storage [7]. Being far superior to the ordinary building materials, the cables and the membranes are a competitive solution in spite of relatively high cost.

Cable and membrane structures, however, exhibit complex behavior under load. Kinematic displacements, brought about by non-uniform external impacts, can far exceed deflections by uniform loads of higher intensity [8]. Thus, the limit state of serviceability is violated. It prevents the full use of strength properties of structural materials and requires further enhancement of the design solutions.

In order to reduce the deformations, cable structures are combined with rigid threads and stiffening girders. Load-carrying behavior of a suspended roof structure with lattice threads is analyzed in [9]. Arrangement of a stiffening girder between the opposite supports of cable structures is transferred from the bridge engineering [10]. The girder is suspended by the cables, which reduce its material capacity. The cable spacing is investigated by means of static and dynamic analysis of cable-stayed bridges [11].

Horizontal cantilever girders, supported by guy cables, form the bearer framework for the roofs of small capacity stadiums [12]. Such a solution, however, suffers from the uplift wind loads, which can cause slackening of the cables and overstress the cantilever.

The stiffening girders, being embedded into the cable structures, form strutted systems [13]. In addition to the effective mitigation of the deflections, the girders bear the thrust brought about by the flexible chords of the construction thus preventing overstress of the supporting structures.

The strutted systems have found use for radio transmitting towers, providing reduction of cost up to 50 % [14]. The girder, being arranged in the vertical direction, serves as a lightweight mast or a pole for supporting temporary building constructions, such as awnings and tents [15, 16].

Deformability of the strutted systems is decreased by means of multilevel arrangement of the cable chords [13], as well as by transforming the top chord into a secondary cable truss with inclined web ties

[17, 18]. The secondary truss results in reduction of the vertical displacements by 32 % in comparison to a single cable [19].

A common disadvantage of the strutted systems is that the girder, being of high relative stiffness, becomes overstressed by external transverse loads, while high-strength chords of the cable truss remain underused. Mitigation of the stresses in the structural elements is achieved by means of passive adaptation strategy. The passive adaptation means, that the structural compliance is implemented into the structural behavior [20].

Design clearances, which allow the structural elements to move freely a certain distance, can be considered as the means for the passive adaptation. An emergency-proof girder structure is proposed and optimized in [21, 22]. The girder transforms into a truss-like structure in case of failure of the middle support. The transformation is performed using loosely connected structural elements.

The solution [23] allows the girder to bear only its own weight in the transverse direction until the design clearances are exhausted. It contributes to more efficient stress redistribution in the construction, because the flexible chords, made of high-strength steel cables, take the major portion of the external impacts.

Structural analysis of the hybrid building constructions, which include flexible cable and membrane elements, must take into account complex nonlinear behavior under load. Pseudo linear approach, based on replacing of the flexible catenaries with trussed elements, is not appropriate [24]. Numerical methods are commonly used for geometrically nonlinear structural analysis. They allow thorough consideration of the external loads and provide detailed information on the stress and force distribution in the structural members.

A two-step numerical strategy for the static analysis of cable structures is proposed in [25]. The initial stresses in the cables and the reference configuration of the structure is determined by the catenary force density method. The convergence of the numerical analysis is achieved by the iterative Newton–Raphson method.

The mixed algorithm for nonlinear analysis of hybrid structures made of cable and rigid (truss) elements is proposed in [26]. The equilibrium is achieved iteratively by the secant method.

In [27] point based iterative approach is used for geometrically nonlinear analysis of cable trusses and nets. Such an approach, in comparison to similar methods of structural analysis, requires much less computational resources.

The design process of the flexible membranes, which form the shell of the hybrid buildings, is considered in [28]. The equilibrium shape of the flexible membrane strongly depends on the stress distribution in the surface. The influence of the membrane geometry on the structural behavior of the whole construction is investigated in [29]. Form-finding theories and approaches are considered in [30]. Improved "force density" numerical technique for shape determination of hybrid structures is devised in [31]. The problem of multiple shapes and unstable equilibrium positions is considered in [32].

Coupled analysis of the flexible membrane and the supporting structure is considered in [33–35]. Numerical analysis of the arch structure restrained by the membrane is considered in [36]. Integrated approach, which includes optimization steps, is proposed in [28]. The approach allows finding the intermediate stress-free configuration of the membrane, from which it is stretched, into the desired shape with the appropriate stress distribution [37].

The procedure for the numerical simulation of flexible membrane structures is summarized in [38]. The analysis is based on the finite element method, which is implemented using specialized software packages for nonlinear structural simulation.

Numerical methods, however, require the main structural parameters to be given in advance. Thus, analytical technique is needed to determine stiffness properties of the structural elements and the magnitude of the pre-stressing of the cables and the membranes [39]. Simplified approach is also required for validating structural models and for verifying the numerical results.

The analysis of single cables, cable nets and trusses is considered in [8]. The analytical dependence for the length of the cables is proposed. The cubic equation for determination of the thrust is given. The compatibility of deformations of the chords of the cable trusses is used for the static analysis under load.

The engineering approach for simulating suspension bridges with rigid cables and girders is devised in [40]. The analytical expressions for the thrust induced by the cables, as well as for the vertical deflections at the middle and at the quarter points of the span are derived.

The equilibrium equations for a flexible cable, subjected to self-weight and temperature variations, are given in [41]. The equations are written in the differential form. Having been integrated, they are solved

given the boundary conditions for the cable. This approach is used for analyzing single cables and cable nets.

Analysis of girders with reinforcing flexible ties is considered in [14]. The condition of compatibility of deformations is used for obtaining the deflections and the stress-strain state under load.

According to the literature review, the following gaps in the field of the cable and membrane structures may be highlighted:

– cable truss systems, stiffened with girders, and flexible membrane shells are considered separately. Multistructure integration should be investigated, because the united (hybrid) system is expected to be a competitive design solution;

– structural compliance should be used for improving the structural behavior. Thus, the passive adaptation needs to be implemented into the hybrid roofs;

– simplified solution techniques must be developed for the static analysis of the hybrid constructions, as well as for estimating their main structural parameters.

The purpose of the present work is to devise the computational technique for structural analysis of the cable roofs, stiffened with girders and enveloped with flexible membranes.

The tasks to be solved are the following:

1. To include polymer membrane shell into the structural model of the plane cable truss. To propose the numerical technique for estimating the effective stiffness of the membrane in the model.

2. To propose computational technique for static analysis of the cable truss with the girder and the passive adaptation means in the form of design clearances. To take into account both uniform and non-uniform external loads.

3. To provide analytical expressions for calculation of design clearances, pre-tensioning of cable truss and stiffness properties of the chords under the satisfied limit states conditions.

2. Methods

The structural model of the section of the roof highlighted in Fig. 2 is shown in Fig. 3.
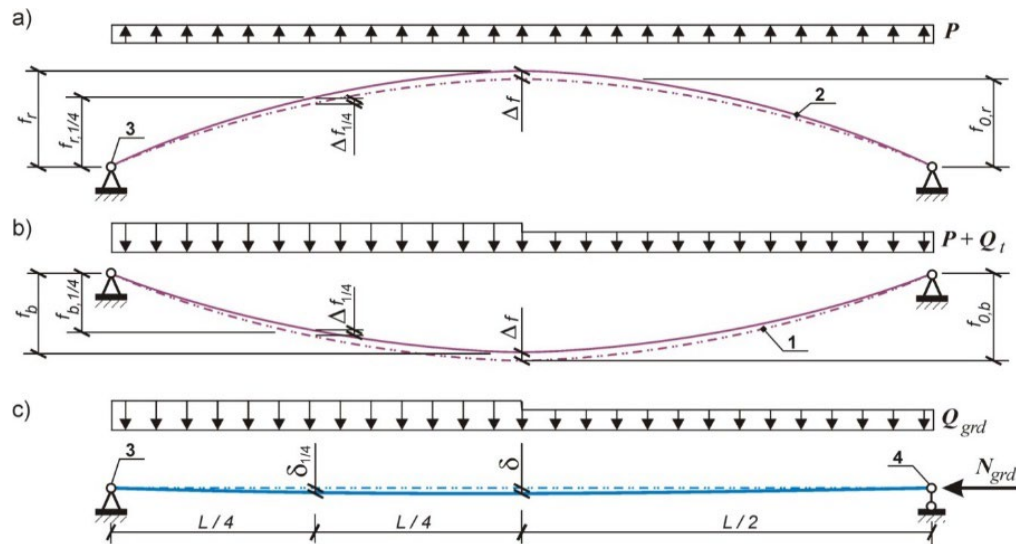
Figure 3. Structural model of the section of the roof: a, b – restraining and bearer chords, respectively, c – the stiffening girder; 1, 2 – initial and deformed positions of the elements, respectively; 3 – fixed support; 4 – support fixed in vertical direction only; P is the link load between the chords; Q_t and Q_{grd} are the external transverse loads on the cable truss and the girder; N_{grd} is the longitudinal load on the girder.

The following assumptions are considered in the present work. No material nonlinearity is present and Hook's law is valid. Longitudinal shortening of the girder under load is negligible, and the roof's span L is stationary. Nodal displacements are allowed only in the vertical direction and the struts between the chords are incompressible. Thus, the rises of the chords f are mutually dependent at the deformed state:

$$f_b = f_{0,b} - \Delta f \qquad (1a)$$

$$f_r = f_{0,r} + \Delta f \tag{1b}$$

$$f_{b,1/4} = 0.75 \cdot f_{0,b} - \Delta f_{1/4} \tag{1c}$$

$$f_{r,1/4} = 0.75 \cdot f_{0,r} + \Delta f_{1/4} \tag{1d}$$

where Δf, $\Delta f_{1/4}$ are the displacements of the roof in the center and in the quarter point of the span, respectively; $f_{0,b}$ and $f_{0,r}$ are the initial rises of the parabolic chords.

Only shallow cables are considered in the present work. Thus, the rises of the chords f_b and f_r, as well as $f_{0,b}$ and $f_{0,r}$, must obey the following condition:

$$\frac{L}{f} \ge \varsigma, \tag{2}$$

where ς is the limiting span-to-rise ratio for the chords, which is taken the following: $\varsigma = 8$.

The bearer chord of the roof structure is a steel cable or a cable bundle with the overall axial stiffness EA_b. The restraining chord is composed of a cable '*cab*' with the stiffness $EA_{r,cab}$ and a membrane shell '*m*'. In the present work, the shell is modeled by means of membrane-simulating element, which behaves under load like an ordinary cable with the stiffness $\overline{EA}_{r,m}$.

Considering the equality of the relative deformations $\left(\varepsilon_r = \varepsilon_{r,cab} = \varepsilon_{r,m} \right)$, the overall stiffness EA_r of the restraining chord is the sum of the stiffness values of its components:

$$EA_r = EA_{r,cab} + \overline{EA}_{r,m}. \tag{3}$$

The axial force N in a chord or its components is obtained by Hook's law:

$$N = EA \cdot \varepsilon, \tag{4}$$

where EA is the axial stiffness; ε is the chord's relative elongation given the rise f:

$$\varepsilon = \frac{L_c}{L_{c0}} - 1, \tag{5}$$

where L_c and L_{c0} are the current and initial chord lengths, respectively:

$$L_c = \Psi_4 \cdot f^4 + \Psi_2 \cdot f^2 + L; \tag{6}$$

$$L_{c0} = L_g - \Delta L_p, \tag{7}$$

where $\Psi_2 = 8/(3 \cdot L)$ and $\Psi_4 = -32/\left(5 \cdot L^3\right)$ are the coefficients for a parabola-shaped curve; L_g is the geometric length of the chord, obtained from (6) given the initial rise f_0; ΔL_p is the tensioning of the chord, which is introduced for pre-stressing the roof structure.

The effective stiffness of the membrane-simulating element $\overline{EA}_{r,m}$ is proposed to be obtained numerically. The membrane is substituted by a mesh of elastic elements. The initial shape of the mesh is obtained by means of the force density method [30, 31]. The membrane is loaded along the ridge with uniformly distributed test load q (Fig. 4). An auxiliary cable with the stiffness $EA_{r,cab}^{aux}$ is used for redistributing the load and transmitting it to the membrane. Finite element method is used for the analysis.
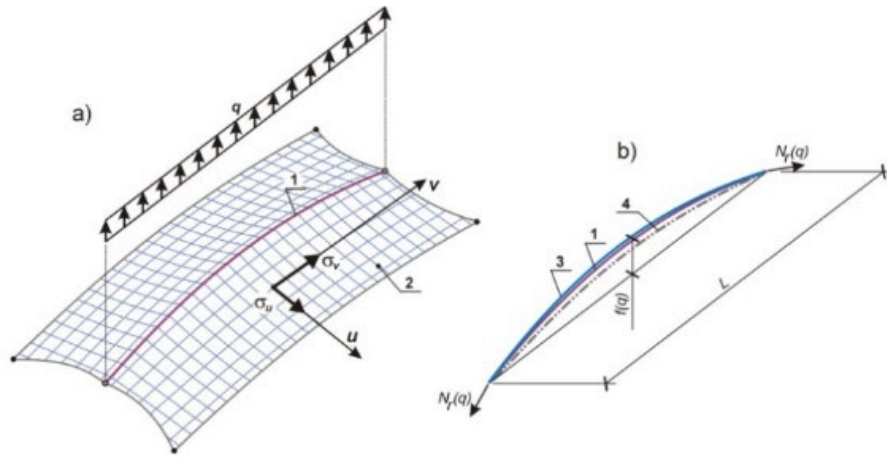
**Figure 4. Determination of the effective stiffness of the membrane-simulating element $\overline{EA}_{r,m}$:
a – the model for the finite element analysis; b – structural model for the stiffness calculation;
1 – the auxiliary cable with the stiffness $EA_{r,cab}^{aux}$; 2 – the membrane; 3 – the membrane-simulating
element; 4 – the initial shape of the ridge of the membrane; σ_u and σ_v are the membrane stresses
in the principal directions u and v.**

The membrane with the auxiliary cable deforms from the initial rise $f_{0,r}$ to the resultant one. The effective stiffness $\overline{EA}_{r,m}$ is calculated by the following expression:

$$\overline{EA}_{r,m} = \frac{N_r(q)}{\varepsilon_r(f(q))} - EA_{r,cab}^{aux}, \tag{8}$$

where $N_r(q) = \dfrac{q \cdot L^2}{8 \cdot f(q)}$ is the overall axial force in the restraining chord; $f(q)$ is the rise of the chord under the load q; $\varepsilon_r(f(q))$ is the relative elongation of the chord (5) given the rise $f(q)$ and the chord tensioning $\Delta L_p = 0$.

The girder equilibrates the horizontal forces, which are induced by the cable truss. Considering, that the membrane effective force is distributed by the catenary cables between the girder and the neighboring fixed supports (Fig. 2), the axial force in the girder N_{grd} is estimated as follows:

$$N_{grd} = N_{b,cab} + N_{r,cab} + \frac{N_{r,m}}{2}, \tag{9}$$

where $N_{b,cab}$ and $N_{r,cab}$ are the forces in the bearer chord and in the cable of the restraining chord, respectively; $N_{r,m}$ is the membrane effective force.

The axial force in the girder, being compressible, is taken positive in the present work. The ultimate limit state condition for the girder may be written as follows:

$$\Theta_{grd} \le \Theta_{\lim,grd}, \tag{10}$$

where $\Theta_{\lim,grd}$ is the allowable stress-strength ratio for the girder; Θ_{grd} is the ratio given the axial force N_{grd} and the maximum absolute value of the bending moment M_{grd}:

$$\Theta_{grd} = \frac{N_{grd}}{\varphi_e \cdot A_{grd} \cdot R_{grd}}, \text{ if } m_{ef} < 20; \tag{11}$$

$$\Theta_{grd} = \frac{M_{grd}}{W_{grd} \cdot R_{grd}}, \text{ otherwise,} \tag{12}$$

where A_{grd} and W_{grd} are the area and the elastic section modulus of the girder's cross section; R_{grd} is the material strength of the girder; φ_e is the buckling coefficient which is obtained by the Design Code (SP 16.13330.2017) given the effective slenderness $\bar{\lambda}$ and the adjusted relative eccentricity m_{ef}.

Bending moment in the girder M_{grd} is induced by transverse and longitudinal impacts:

$$M_{grd} = M_Q + N_{grd} \cdot \delta, \tag{13}$$

where M_Q is the bending moment brought about by the transverse load; δ is the deflection of the girder under load:

$$\delta = \frac{\delta_Q}{1 - N_{grd}/N_{el}}, \tag{14}$$

where δ_Q is the deflection by the transverse load only; N_{el} is the Euler load, $N_{grd} < N_{el}$:

$$N_{el} = \pi^2 \cdot E_{grd} \cdot I_{grd}/L^2. \tag{15}$$

Considering the chords of the cable structure, the limit state conditions may be written as follows:

– the ultimate limit state:

$$\Theta_c \leq \Theta_{\lim,2}; \tag{16}$$

– the serviceability limit state:

$$\omega_{ld} \leq \omega_{\lim}; \tag{17}$$

$$\Theta_{\lim,1} \leq \Theta_c, \tag{18}$$

where ω_{ld} is the deflection caused by the external load; $\omega_{\lim}$ is the allowable deflection; Θ_c is the stress-strength ratio for the chord, while $\Theta_{\lim,1}$, $\Theta_{\lim,2}$ are the allowable boundary values:

$$\Theta_c = \frac{\sigma_c}{R_c} \in \left[\Theta_{\lim,1} \ldots \Theta_{\lim,2} \right], \tag{19}$$

where σ_c is the normal stress in the chord; R_c is the chord's strength.

Having considered Hook's law, the ratio Θ_c can be converted as follows:

$$\Theta_c = \varepsilon/\zeta, \tag{20}$$

where ζ is the maximum relative deformation given the material strength and the stiffness properties.

Considering the cable elements of the chords, the ζ_{cab}-value is obtained as follows:

$$\zeta_{cab} = R_{cab}/E_{cab}, \tag{21}$$

where R_{cab} and E_{cab} are the strength and the modulus of elasticity of the steel cables.

The allowable deformation of the bearer cable can be written as follows:

$$\varepsilon_b \in \left[\varepsilon_{cab,1} \ldots \varepsilon_{cab,2} \right], \tag{22}$$

where

$$\varepsilon_{cab,1} = \Theta_{\lim,1} \cdot \zeta_{cab}; \tag{23a}$$

$$\varepsilon_{cab,2} = \Theta_{\lim,2} \cdot \zeta_{cab}. \tag{23b}$$

Considering the membrane-simulating element of the restraining chord, the ζ_m-value is obtained numerically:

$$\zeta_m = \varepsilon_r \left(f_{m,\lim} \right), \tag{24}$$

where ε_r is the relative elongation (5) given the maximum rise of the restraining chord $f_{m,\lim}$ under the conditions:

$$\sigma_u \le \sigma_{\lim,u}; \tag{25a}$$

$$\sigma_v \le \sigma_{\lim,v}, \tag{25b}$$

where σ_u and σ_v are the membrane stresses in the u and v directions (Fig. 4); $\sigma_{\lim,u}$ and $\sigma_{\lim,v}$ are the allowable membrane stresses in the orthotropic shell:

$$\sigma_{\lim} = \sigma_{break} / K, \tag{26}$$

where σ_{break} is the membrane breaking strength; K is the stress factor [42].

The allowable range for the relative deformations of the restraining chord in a whole:

$$\varepsilon_r \in \left[\varepsilon_{r,1} \ldots \varepsilon_{r,2} \right], \tag{27}$$

where $\varepsilon_{r,1}$ and $\varepsilon_{r,2}$ are the following boundary values:

$$\varepsilon_{r,1} = \max \left(\varepsilon_{cab,1}, \ \varepsilon_{m,1} \right); \tag{28a}$$

$$\varepsilon_{r,2} = \max \left(\varepsilon_{cab,2}, \ \varepsilon_{m,2} \right), \tag{28b}$$

where $\varepsilon_{cab,i}$ are the limiting deformations of the cable element of the restraining chord (23), while $\varepsilon_{m,i}$ are the limiting deformations of the membrane-simulating element:

$$\varepsilon_{m,i} = \Theta_{\lim,i} \cdot \zeta_m, \tag{29}$$

where $i = \{1, 2\}$, and ζ_m is given by (24).

Pre-stressing of the roof and the operational phase are considered separately. At the pre-stressing phase the roof structure cambers by the distance Δf_{pr} thus transforming the chords' rises from f_0 into f_{pr} (1):

$$\Delta f = \Delta f_{pr}; \tag{30a}$$

$$\Delta f_{1/4} = 0.75 \cdot \Delta f_{pr}. \tag{30b}$$

The cambering of the roof is induced by tensioning of the bearer chord. The girder is subjected by its own weight ρ_{grd} in the vertical direction, while the weight of the cable truss and the membrane is considered negligible. The longitudinal force in the girder N_{grd}^{pr} is brought about by the cables.

At the operational phase, the roof deforms downwards under vertical external loads. The full uniform load Q_{tot}, as well as partial uniform load Q_{prt} and the load Q_{hlf} acting on a half of the span of the roof,

are taken into account (Fig. 5). It is assumed, that the full uniform load exceeds the overall sum of the non-uniform impacts:

$$Q_{prt} + Q_{hlf} \leq Q_{tot}. \tag{31}$$
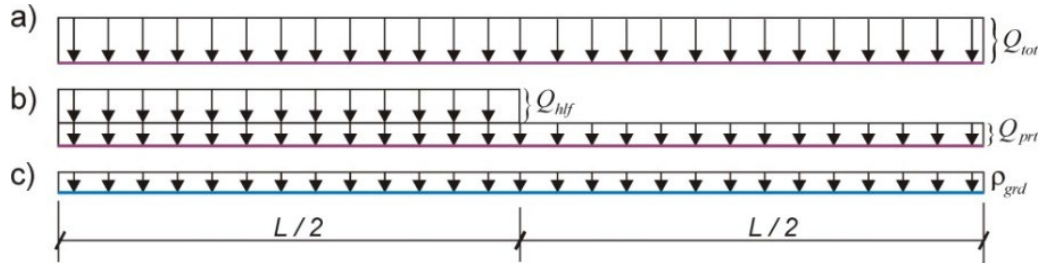
**Figure 5. External loads considered: a – the full uniform load,
b – non-uniform load, c – the girder's own weight.**

Under a uniformly distributed load, the chord's rises transform into f_{ld} (1) by the following overall displacements:

$$\Delta f = \Delta f_{pr} - \omega_{ld}; \tag{32a}$$

$$\Delta f_{1/4} = 0.75 \cdot \left(\Delta f_{pr} - \omega_{ld} \right), \tag{32b}$$

where ω_{ld} is the deflection of the roof at the center of the span.

The deflection of the roof under the full uniform load Q_{tot} is considered equal to the allowable deformation $\omega_{ld} = \omega_{lim}$. It is assumed, that the cable truss takes the full amount of the load Q_{tot}, and the bearer chord reaches the ultimate limit state: $\varepsilon_{ld,b} = \varepsilon_{cab,2}$. The girder is only influenced by its own weight ρ_{grd} and by the longitudinal forces N_{grd}^{ld}.

The non-uniform load considered in the research consists of a uniform part Q_{prt} and a half-span load Q_{hlf} (Fig. 5). The partial uniform load Q_{prt} is completely taken by the cable truss, while the half-span load splits between the truss and the girder into $Q_{hlf,t}$ and $Q_{hlf,grd}$, respectively:

$$Q_{hlf,t} = \xi_{Qh} \cdot Q_{hlf}; \tag{33a}$$

$$Q_{hlf,grd} = \left(1 - \xi_{Qh} \right) \cdot Q_{hlf}, \tag{33b}$$

where $\xi_{Qh} \in \left(0 \ldots 1 \right]$ is the parameter of splitting the load, which is to be determined.

Thus, the left-hand side of the cable truss is influenced by the load Q_L, while the load Q_R acts on the right part of the span (Fig. 6):

$$Q_L = Q_{prt} + Q_{hlf,t}; \tag{34a}$$

$$Q_R = Q_{prt}. \tag{34b}$$

The corresponding loads acting on the girder are the following:

$$Q_{L,grd} = \rho_{grd} + Q_{hlf,grd}; \tag{35a}$$

$$Q_{R,grd} = \rho_{grd}. \tag{35b}$$
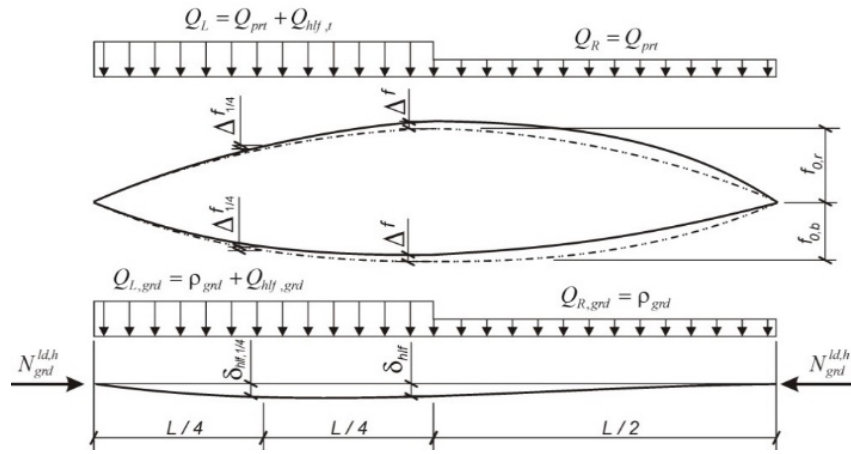
Figure 6. Structural model under the non-uniform load.

The parameter of splitting the load, ξ_{Qh}, is obtained by the condition of compatibility of deformations of the truss and the girder in the quarter of the span. The secant method is used.

The girder deflection $\delta_{1/4}$ is obtained by (14) given the loads $Q_{L,grd}$ and $Q_{R,grd}$. The overall displacements of the cable truss (Δf and $\Delta f_{1/4}$, Fig. 6) under the loads Q_L and Q_R are obtained by minimization of the following discrepancy using the coordinate descent method:

$$\Xi = \left|\vartheta_1\right| + \left|\vartheta_2\right| \to 0, \tag{36}$$

where the functions $\vartheta_1\left(\Delta f, \Delta f_{1/4}\right)$ and $\vartheta_2\left(\Delta f, \Delta f_{1/4}\right)$ are derived from [43]:

$$\vartheta_1 = \frac{f_{0,b} - \Delta f}{q_{Sym} + p_{Eq}} \cdot \frac{\Delta L_{c,b}}{\rho_b} - 1; \tag{37a}$$

$$\vartheta_2 = \frac{q_{Inv} + \eta_r \cdot p_{Eq}}{q_{Sym} + p_{Eq}} \cdot \frac{1}{\eta_b} - 1, \text{ if } \eta_b \neq 0, \text{ and } \vartheta_2 = 1 \text{ otherwise}, \tag{37b}$$

where p_{Eq} is the link load between the chords and η_b, η_r are the coefficients of load non-uniformity, which depend on the displacements Δf and $\Delta f_{1/4}$; $\Delta L_{c,b}$ is the bearer chord elongation given the η_b-value; ρ_b and ρ_r are the ratios, which depend on the chords stiffness properties; q_{Sym} and q_{Inv} are the symmetrical and inverse-symmetrical parts of the external load:

$$q_{Sym} = \frac{Q_L + Q_R}{2}; \tag{38a}$$

$$q_{Inv} = \frac{Q_L - Q_R}{2}. \tag{38b}$$

The value $\eta_b = 0$ means, that the load must be uniform. It contradicts the assumption, that there is non-zero impact Q_{hlf}, thus raising the maximum discrepancy value in (37b).

The coordinate descent method is used for minimizing the discrepancy (36). Having started from the initial guess values $\left(\Delta f, \Delta f_{1/4}\right)_{init} = \left(\Delta f_{pr}/2, 0\right)$ the result is achieved iteratively by variation of the displacements.

3. Results and Discussion

The roof structure, considered in the research, consists of the framework and the flexible membrane shell. The framework is protected by the patent RF no. 2439256, 2010.

3.1. The allowable rise of a parabola-shaped chord

The rise of a parabola-shaped chord at the center of the span f_c is derived given the chord's length L_c:

$$f_c = \frac{L}{2} \cdot \sqrt{\frac{5}{6}} \cdot \sqrt{1 - \sqrt{1 - 3.6 \cdot \left(\frac{L_c}{L} - 1\right)}}. \tag{39}$$

Considering that the radical expressions in (39) must be positive, the length of the chord is confined as follows:

$$L_c \in [1.0 \ldots 1.278] \cdot L. \tag{40a}$$

On the other hand, substituting the boundary values for the chord rises ($f = 0$ and $f = L/\varsigma$ (2)) into (6) yields in the following range:

$$L_c^{\lim} \in \left[1.0 \ldots \left(\frac{-32}{5 \cdot \varsigma^4} + \frac{8}{3 \cdot \varsigma^2} + 1.0\right)\right] \cdot L. \tag{40b}$$

Considering $\varsigma = 8$, one can see, that the range (40b), $L_c^{\lim} \in [1.0 \ldots 1.04] \cdot L$, fully belongs to (40a), thus providing no singularity in (39).

Assuming, that the chord reaches a limit state, the allowable length $L_c^{\lim}$ is the following:

$$L_c^{\lim} = L_{c0} \cdot (\varepsilon_{\lim} + 1), \tag{41}$$

where $\varepsilon_{\lim}$ is a boundary value $\varepsilon_{cab,i}$ or $\varepsilon_{r,i}$ (22 or 27), $i = \{1, 2\}$; L_{c0} is the initial chord's length (7).

Substituting the length $L_c^{\lim}$ into (39) gives the allowable rise of a parabola-shaped chord under the limit states condition specified.

3.2. Deformation of the roof at the pre-stressing phase

Considering the restraining chord, the deformation of the roof during the pre-stressing Δf_{pr} is confined as follows:

$$\Delta f_{pr} \in \left[\Delta f_{pr,\lim 1}, \ \Delta f_{pr,\lim 2}\right], \tag{42}$$

where $\Delta f_{pr,\lim 1}$ and $\Delta f_{pr,\lim 2}$ are the following boundary values:

$$\Delta f_{pr,\lim 1} = f_{\lim_1,r} + \omega_{\lim} - f_{0,r}; \tag{43a}$$

$$\Delta f_{pr,\lim 2} = f_{\lim_2,r} - f_{0,r}, \tag{43b}$$

where $f_{\lim_1,r}$, $f_{\lim_2,r}$ are the lower and upper bounds for the rise of the restraining chord, respectively.

The $f_{\lim_1,r}$-value is calculated by (39) given the allowable length (41) $L_{c,r}^{\lim 1} = L_{c0,r} \cdot (\varepsilon_{r,1} + 1)$, while the $f_{\lim_2,r}$-value is obtained as follows:

$$f_{\lim_2,r} = \min\left(f_{\lim 2,r}^u, \ f_{\lim 2,r}^s\right), \tag{44}$$

where $f_{\lim 2,r}^{s} = L/\varsigma$ is imposed by the condition of the shallow shape of the chord (2), while $f_{\lim 2,r}^{u}$ is obtained by (39) given the length, which is determined by the ultimate limit state condition $L_{c,r}^{\lim 2} = L_{c0,r} \cdot \left(\varepsilon_{r,2}+1\right)$; $L_{c0,r}$ is obtained by (7) for the restraining chord given $\Delta L_{p} = 0$.

In order to keep the range (42) nonsingular the allowable deflection $\omega_{\lim}$ must obey the following condition:

$$\omega_{\lim} \le \omega_{\lim,up} = f_{\lim_2 r} - f_{\lim_1 r}. \tag{45a}$$

The serviceability limit state also confines the $\omega_{\lim}$ -range:

$$\omega_{\lim} \le \Omega_{\lim}, \tag{45b}$$

where $\Omega_{\lim}$ is the given value, which is defined for preventing large structural deformations.

Considering the bearer chord, the serviceability limit state imposes the following condition on its rise:

$$f_{pr,b} \ge f_{\lim 1,b}, \tag{46}$$

where $f_{pr,b}$ is the chord's rise (1a) given the roof deformation at the phase of the pre-stressing (30a); $f_{\lim 1,b}$ is obtained by (39) given the allowable chord's length $L_{c,b}^{\lim 1} = L_{c0,b} \cdot \left(\varepsilon_{cab,1}+1\right)$; $L_{c0,b}$ is the initial length of the bearer chord, derived from the ultimate limit state condition:

$$L_{c0,b} = L_{c,b}^{ld} \cdot \frac{1}{1+\varepsilon_{cab,2}}, \tag{47}$$

where $L_{c,b}^{ld}$ is the length (6) of the bearer cable given the rise $f_{ld,b}$ (1a), which corresponds to the displacement (32a).

Both sides of (46) depend on the deformation of the roof at the phase of the pre-stressing, Δf_{pr}. Thus, it supplements the condition (42) imposed on the Δf_{pr} -range.

3.3. The stiffness of the chords

Considering Hook's law and the uniformity of the load distribution at the pre-stressing phase, the axial stiffness values of the chords EA_b and EA_r may be written as follows:

$$EA_b = P_{pr} \cdot \frac{L^2}{8 \cdot f_{pr,b} \cdot \varepsilon_{pr,b}}; \tag{48a}$$

$$EA_r = P_{pr} \cdot \frac{L^2}{8 \cdot f_{pr,r} \cdot \varepsilon_{pr,r}}, \tag{48b}$$

where the chord rises $f_{pr,b}$, $f_{pr,r}$ and the corresponding relative deformations $\varepsilon_{pr,b}$, $\varepsilon_{pr,r}$ are determined by the roof's cambering Δf_{pr}; P_{pr} is the link load between the chords at the pre-stressing phase.

The boundary value for the link load between the chords is obtained under the condition that the full uniform load Q_{tot} is completely taken by the cable truss:

$$P_{pr,bound} = \frac{Q_{tot}}{\dfrac{f_{ld,b} \cdot \varepsilon_{cab,2}}{f_{pr,b} \cdot \varepsilon_{pr,b}} - \dfrac{f_{ld,r} \cdot \varepsilon_{ld,r}}{f_{pr,r} \cdot \varepsilon_{pr,r}}}, \tag{49}$$

where $\varepsilon_{cab,2}$ is the limiting deformation (23b), which ensures the full use of the strength properties of the bearer chord under the condition of reaching the allowable rise $f_{ld,b}$ under load; $\varepsilon_{pr,b}$, $\varepsilon_{ld,r}$ and $\varepsilon_{pr,r}$ are the relative deformations of the chords given the rises $f_{pr,b}$, $f_{ld,r}$ and $f_{pr,r}$, respectively.

If the link load is less than its boundary value, $P_{pr} < P_{pr,bound}$, then the cable truss takes only a fraction of the uniform load Q_{tot}. The remaining part of Q_{tot} influences the girder and increases its material capacity. If the link load exceeds the boundary value $P_{pr} > P_{pr,bound}$, then the structure deforms less, than it is allowed by the serviceability limit state: $\omega_{ld} < \omega_{lim}$. Both cases are worse from the economic point of view, than the case of $P_{pr} > P_{pr,bound}$, when the deformation is equal to the allowable one and the cable truss, being subjected by uniform loads, induces only horizontal force in the girder.

3.4.　　　The design clearances

The design clearances are used in emergency-proof girders in form of "curved gains" thus using the principle of passive adaptability [21, 22]. They allow transformation of the construction in order to enhance structural performance. The clearances Δ (loose connections, Fig. 1) are introduced into the structural framework of the roof after the pre-stressing phase is completed.

Assuming, that the uniform load Q_{tot} is fully taken by the cable truss, the design clearance at the center of the span may be expressed as follows:

$$\Delta_{1/2} = \omega_{lim} + \delta_{pr} - \delta_{ld}, \tag{50}$$

where δ_{pr} and δ_{ld} are the deformations of the girder (14) at the center of the span under its own weight ρ_{grd} and the horizontal loads N_{grd}^{pr} and N_{grd}^{ld}, respectively.

The expressions for the horizontal loads, which are brought about by the cable chords, may be written according to (4) and (9) as follows:

$$N_{grd}^{pr} = N_{b,cab}^{pr} + N_{r,cab}^{pr} + \frac{N_{r,m}^{pr}}{2}; \tag{51a}$$

$$N_{grd}^{ld} = N_{b,cab}^{ld} + N_{r,cab}^{ld} + \frac{N_{r,m}^{ld}}{2}, \tag{51b}$$

where

$$N_{b,cab}^{pr} = EA_b \cdot \varepsilon_{pr,b}, \ N_{r,cab}^{pr} = EA_{r,cab} \cdot \varepsilon_{pr,r}, \ N_{r,m}^{pr} = \overline{EA}_{r,m} \cdot \varepsilon_{pr,r}; \tag{51c}$$

$$N_{b,cab}^{ld} = EA_b \cdot \varepsilon_{cab,2}, \ N_{r,cab}^{ld} = EA_{r,cab} \cdot \varepsilon_{ld,r}, \ N_{r,m}^{ld} = \overline{EA}_{r,m} \cdot \varepsilon_{ld,r}, \tag{51d}$$

The design clearance at the quarter point of the span may be written in a similar way:

$$\Delta_{1/4} = 0.75 \cdot \omega_{lim} + \delta_{pr,1/4} - \delta_{ld,1/4}, \tag{52}$$

where $\delta_{pr,1/4}$ and $\delta_{ld,1/4}$ are the girder's deformations at the quarter point of the span under the loads ρ_{grd}, N_{grd}^{pr} and N_{grd}^{ld}.

Considering the uniformity of the load Q_{tot}, the design clearance values throughout the span are taken by the parabola-shaped curve.

3.5. Non-uniform load on the roof

The non-uniform load considered in the research is shown in Figs. 5 and 6. In order to split the load Q_{hlf} between the truss and the girder by ξ_{Qh}-parameter (33) the condition of compatibility of deformations at the quarter point of the span may be written as follows:

$$\omega_{h,1/4} = \Delta_{1/4} + \delta_{h,1/4} - \delta_{pr,1/4}, \tag{53}$$

where $\omega_{h,1/4}$ and $\delta_{h,1/4}$ are the deformations of the truss and the girder under the loads (Q_L, Q_R) and $(Q_{L,grd}, Q_{R,grd})$, respectively; $\delta_{pr,1/4}$ is the deformation of the girder under its own weight at the pre-stressing phase.

Substituting (52) into (53) yields in the following equation in one unknown ξ_{Qh}:

$$h(\xi_{Qh}) = 0, \tag{54a}$$

where $h(\xi_{Qh})$ is the following function:

$$h(\xi_{Qh}) = \frac{0.75 \cdot \Delta f_{pr} + \delta_{ld,1/4} - \Delta f_{1/4}}{0.75 \cdot \omega_{\lim} + \delta_{h,1/4}} - 1, \tag{54b}$$

where $\Delta f_{1/4}$ is the overall displacement of the cable truss at the quarter point of the span, which includes the displacement at the pre-stressing phase and the displacement under the non-uniform load (Q_L, Q_R):

$$\Delta f_{1/4} = 0.75 \cdot \Delta f_{pr} - \omega_{h,1/4}. \tag{54c}$$

Only $\Delta f_{1/4}$ and $\delta_{h,1/4}$-values in (54b) depend on ξ_{Qh}, while all the remaining terms may be held constant. The value $\delta_{h,1/4}$ is obtained from (14), while $\Delta f_{1/4}$-value is obtained by the minimization of (36) given the ξ_{Qh}-ratio.

The value of ξ_{Qh}, which closely satisfies (54a), is obtained by means of the iterative secant method. The middle point ξ_M between the left and right bounds (ξ_L and ξ_R) is obtained as follows:

$$\xi_M = \frac{\left|h(\xi_R)\right| \cdot \xi_L + \left|h(\xi_L)\right| \cdot \xi_R}{\left|h(\xi_R)\right| + \left|h(\xi_L)\right|}, \tag{55a}$$

under the condition:

$$h(\xi_R) > 0. \tag{55b}$$

The bounds, used by ξ_L = 0.0 and ξ_R = 1.0, are modified during the iteration process as follows: if $h(\xi_R) \cdot h(\xi_M) > 0$, then $\xi_R = \xi_M$ and $\xi_L = \xi_M$, otherwise. Having reached the acceptable value of the discrepancy $\mu_\varepsilon \left(\left|h(\xi_M)\right| < \mu_\varepsilon\right)$, the iteration process finishes: $\xi_{Qh} = \xi_M$.

If, however, the condition (55b) is not met, the girder does not take transverse load $(\xi_{Qh} = 1.0)$ and the deformations of the cable truss are less than the design clearances.

3.6. Numerical example

3.6.1. General specification

A fragment of the roof structure is considered as an example. The fragment is highlighted in blue in Fig. 2. It consists of the cable truss with the girder and two pieces of the membrane. The membrane is situated symmetrically about the ridge of the truss.

The span of the roof L is 12 m. The initial chords' rises are taken the following: $f_{0,b}$ = 1.5 m and $f_{0,r}$ = 1.0 m. The rise-to-span ratio for the bearer chord $\left(f_{0,b}/L = 1/8 \right)$ belongs to the optimal range $\left[1/10 \ldots 1/6 \right]$ providing efficient force transfer to the supporting structures [44]. The rise-to-span ratio for the restraining chord $\left(f_{0,r}/L = 1/12 \right)$ belongs to the allowable range $\left[1/20 \ldots 1/10 \right]$ in order to reduce the overall height of the roof [33]. The width of the fragment B is 6 m. The following loads are considered: Q_{tot} = 18 kN/m, Q_{prt} = 9.0 kN/m and Q_{hlf} = 9.0 kN/m (Fig. 5). The allowable displacement of the roof under load is $\Omega_{\lim}$ = 0.1 m.

The girder is made of two steel channel bars with the following strength property and the modulus of elasticity: R_{grd} = 2.1·10⁵ kN/m² and E_{grd} = 2.1·10⁸ kN/m². The allowable stress-strength ratio is adopted the following: $\Theta_{\lim,grd}$ = 1.0.

The chords of the truss are made of steel cables with the following material properties: R_{cab} = 7.0·10⁵ kN/m² and E_{cab} = 1.3·10⁸ kN/m². Thus, the maximum relative deformation of the cables is ζ_{cab} = 5.385·10⁻³ (21). The boundary values for the stress-strength ratio of the chords are taken the following: $\Theta_{\lim,1}$ = 0.01 and $\Theta_{\lim,2}$ = 1.0.

The membrane is made of architectural fabrics with the elastic moduli E_u = 600 kN/m and E_v = 400 kN/m in u and v-directions, respectively. The membrane axes are shown in Fig. 4. They coincide with the direction of the main curvatures [44].

Considering the stress factor K = 5.0 [42, 45], the allowable membrane stresses are the following: $\sigma_{\lim,u}$ = 15 kN/m and $\sigma_{\lim,v}$ = 12 kN/m. The membrane pre-tension is taken 1.5 kN/m in u and v-directions that complies with the requirements [42].

3.6.2. Obtaining the effective stiffness and the allowable relative deformation of the membrane-simulating element

The membrane is numerically simulated using the specialized software package for nonlinear structural analysis EASY [46]. The membrane is substituted by a mesh of the size 0.5 m, which belongs to the range $\left[0.1 \ldots 0.6 \right]$ m considered in [47]. An auxiliary cable is used for redistributing the test load q along the membrane ridge (Fig. 4). The membrane is able to slide along the auxiliary, catenary and backstay cables, which are arranged at the perimeter [35]. In order to obtain precise properties of the membrane-simulating element the stiffness of the auxiliary cable must be in the range of the restraining chord stiffness EA_r.

The initial guess for the stiffness of the restraining chord ($EA_{r,guess}$ = 6310 kN) is obtained by (48b) using the $P_{pr,bound}$-value (49), the upper bound for the roof cambering during the pre-stressing $\Delta f_{pr,\lim 2}$ (43b), and the allowable cable deformation $\varepsilon_{cab,2}$ for the restraining chord. Thus, two variants of the auxiliary cable, which do not exceed the $EA_{r,guess}$-value, are taken into account: the cable with the diameter of 6.1 mm ($EA_{r,cab}^{aux,I}$ = 2860 kN) and the cable with the diameter of 8.1 mm ($EA_{r,cab}^{aux,II}$ = 4940 kN) [48].

In both cases the ridge load q (Fig. 4) increases from zero up to the value $q_{\lim}$, which results in

failing one of the conditions (25). The increment of the load q is 3.0 kN/m. The maximum loads are $q_{\lim,I}$ = 24 kN/m and $q_{\lim,II}$ = 30 kN/m for the cases considered. The peak stresses in the membrane in u and v directions, as well as the rise of the auxiliary cables in the middle of the span $f(q)$ given the load q are obtained by the EASY-software. The membrane stresses are shown in Fig. 7.
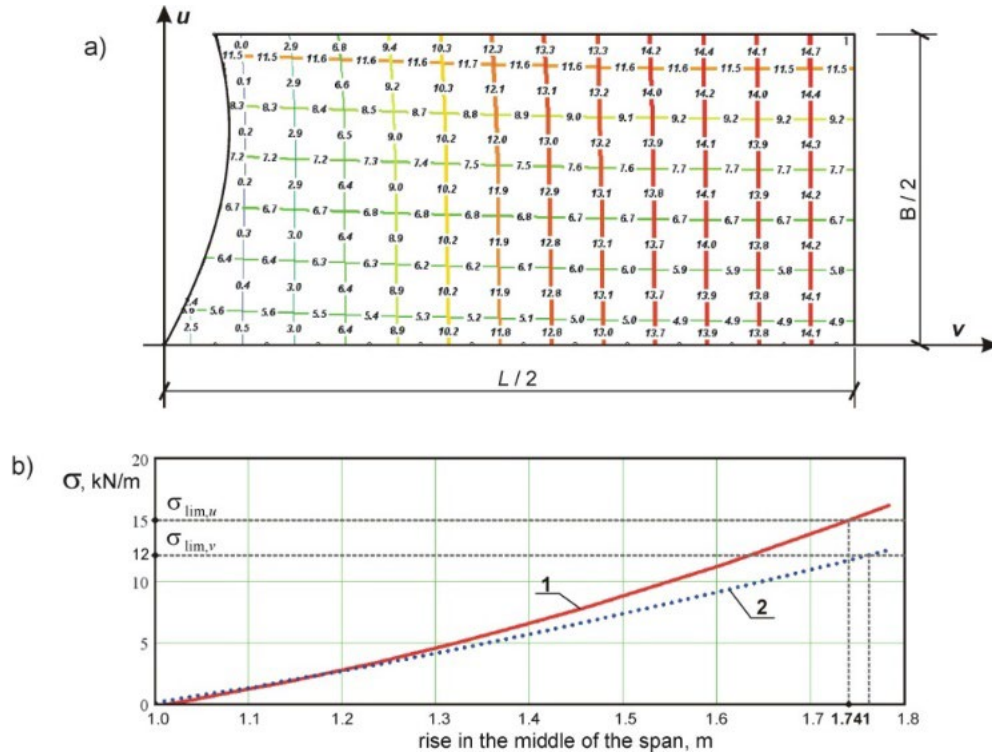

Figure 7. The membrane stresses induced by the increase of the rise in the middle of the ridge:
a – the membrane stress distribution, kN/m; b – the peak membrane stresses;
1 – the membrane stress in the *u*-direction, σ_u; 2 – the membrane stress in the *v*-direction, σ_v.

The figure shows, that the rise $f_{m,\lim}$, which equals 1.741 m, corresponds to the membrane allowable stress $\sigma_{\lim,u}$. The maximum relative deformation of the membrane-simulating element is obtained by (24) given $f_{m,\lim}$: ζ_m = 0.034. Thus, the allowable range for the relative deformations of the restraining chord (27) is the following: $\varepsilon_r \in \left[3.4 \cdot 10^{-4} \dots 5.385 \cdot 10^{-3} \right]$.

The graphs of the effective stiffness values $\overline{EA}_{r,m}$ of the membrane-simulating element (8), obtained for the considered variants of the auxiliary cable, are shown in Fig. 8. In spite of substantial nonlinearity of the graphs in the full range of the allowable membrane rise $f_{m,\lim}$ (Fig. 8a), the graphs tend to straight lines and exhibit the variation less than 2 % in the allowable range of the roof structure in the whole (Fig. 8b). This range is determined by the upper bound of the roof cambering during the pre-stressing (43b): $\Delta f_{pr,\lim 2}$ = 0.143 m. Thus, the averaged effective stiffness value may be applied:
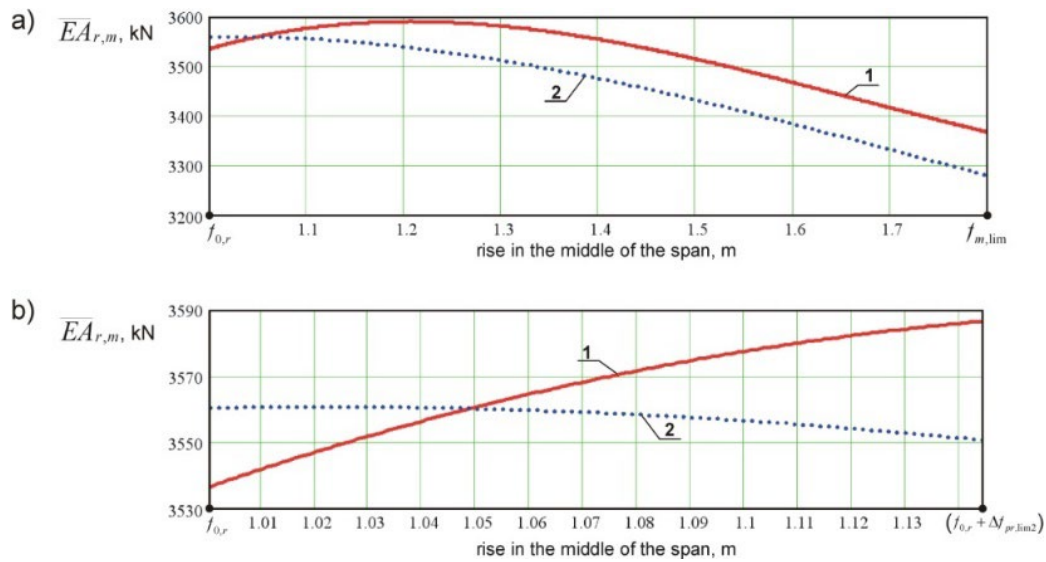
$\overline{EA}_{r,m}$ = 3560 kN.

Figure 8. The graphs of the effective stiffness values $\overline{EA}_{r,m}$ of the membrane-simulating element: a – the full range of the allowable membrane rise, b – the allowable range for the rise of the restraining chord as a composite element; 1, 2 – curves, which correspond to the first and the second variants of the auxiliary cable, respectively.

3.6.3. Estimating the structural parameters of the roof

The range for the roof deformation at the phase of the pre-stressing Δf_{pr} is determined by (42) and (46). The condition (46) is converted as follows:

$$\chi\left(\Delta f_{pr},\ \omega_{\lim}\right) \geq 0, \tag{56a}$$

where χ is the following function:

$$\chi\left(\Delta f_{pr},\ \omega_{\lim}\right) = \left(f_{pr,b}\big/f_{\lim 1,b} - 1\right)\cdot 100\%. \tag{56b}$$

The function χ is shown in Fig. 9 for the following cases of the allowable deflection: $\omega_{\lim} = \{0.08,\ 0.10,\ 0.12,\ 0.133\}$ m. Only those graphs (or their parts), which are situated above the zero-value, ensure the minimum allowed stress in the bearer chord. The green points in the graphs denote the boundary values for the deformation (43a) above which the restraining chord of the roof does not slack under load. The red points denote the upper bound for the deformation (43b) below which the ultimate limit state requirements are fulfilled for the restraining chord.
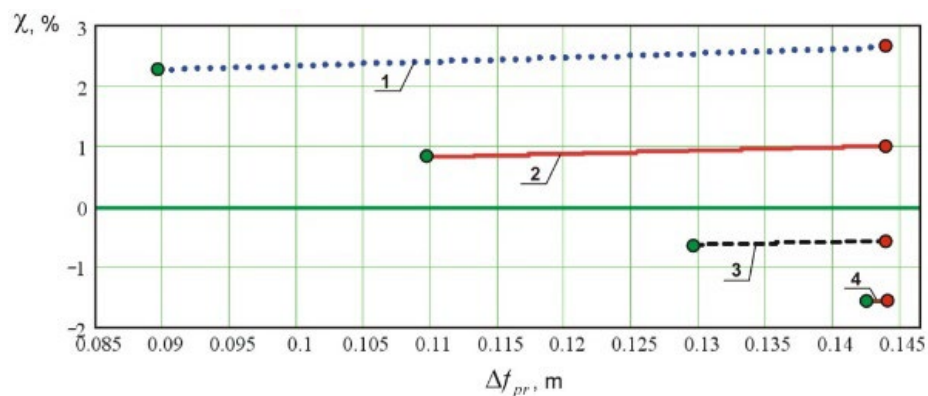

Figure 9. Graphs of χ-function (56b) given the allowable deflections: 1 – ω_{lim}=0.08, 2 – ω_{lim}=0.1, 3 – ω_{lim}=0.12, 4 – ω_{lim}=0.133 m.

The figure shows, that in accordance with growth of the deflection $\omega_{\lim}$, the allowable range for Δf_{pr} decreases. It completely vanishes, when the deflection reaches its upper bound value (45a): $\omega_{\lim,up}$ = 0.134 m.

Considering that the given displacement of the roof meets the condition $\Omega_{\lim} < \omega_{\lim,up}$, it is taken as the allowable deflection: $\omega_{\lim} = \Omega_{\lim}$ = 0.1 m. The corresponding range for the roof cambering is $\Delta f_{pr} \in [0.1096,\ 0.143]$ m. The ratios of the relative deformations of the chords are shown in Fig. 10.
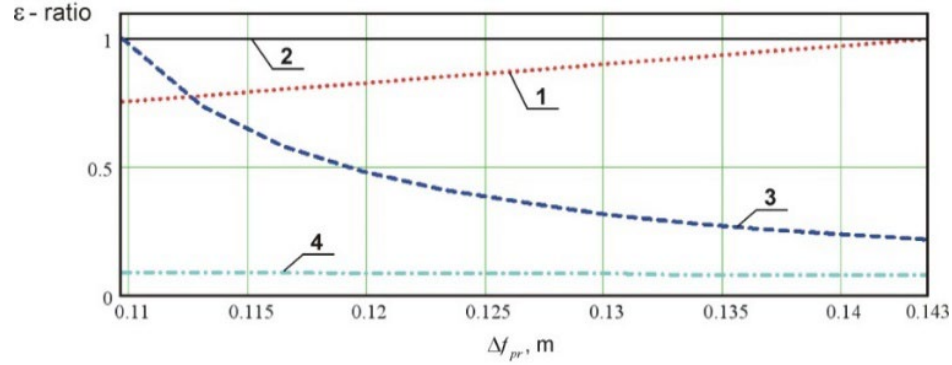

Figure 10. Graphs of ε-ratios: 1 – $\varepsilon_{pr,r} / \varepsilon_{r,2}$; 2 – $\varepsilon_{ld,b} / \varepsilon_{cab,2}$; 3 – $\varepsilon_{r,1} / \varepsilon_{ld,r}$; 4 – $\varepsilon_{cab,1} / \varepsilon_{pr,b}$.

The first two graphs illustrate the ultimate limit state conditions, while graphs 3 and 4 show the serviceability limit state. All the ratios in Fig. 10 are less than or equal to 1.0 meaning that the conditions (22, 27) are met entirely.

Fig. 10 shows that the strength properties of the bearer chord are fully used for all the range of the pre-stressing cambering: $\varepsilon_{ld,b} = \varepsilon_{cab,2}$. The right-hand side bound of the range also provides the full use of the strength properties of the restraining chord $\varepsilon_{pr,r} = \varepsilon_{r,2}$, while at the left-hand side bound the restraining chord keeps the minimum specified tensioning thus remaining workable, $\varepsilon_{ld,r} = \varepsilon_{r,1}$.

The stiffness properties of the chords of the roof are calculated by (48). The restraining chord is a composite element with the overall stiffness equal to the sum of its components [49]. Thus, the stiffness of the restraining cable $EA_{r,cab}$ is obtained from (3) given the stiffness of the membrane-simulating element $\overline{EA_{r,m}}$ and the stiffness of the chord in the whole EA_r. The cross section areas of the cable elements are calculated given the modulus of elasticity E_{cab}.

The graph of the total mass of the cable elements is shown in Fig. 11. The figure shows the trend of the mass increase. The mass growth, however, does not exceed 2.2 %. Cross section areas of the cable chords are shown for the boundary points.

Figure 11. Graph of the total mass of the cable elements, kg
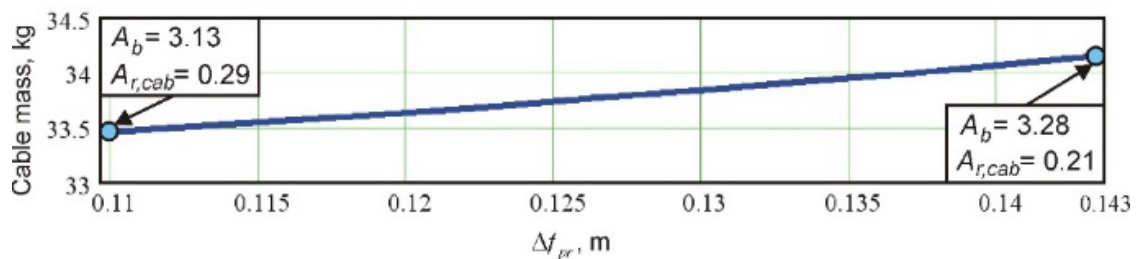**(cross section areas of the chords are indicated in cm^2).**

Considering the girder made of two channel bars, the stress-strength ratios (11, 12) are shown in Fig. 12 for the two load cases: uniform and non-uniform impacts on the roof (Fig. 5). The figure shows, that the half-span load results in higher stress level in the girder, than the full uniform load.
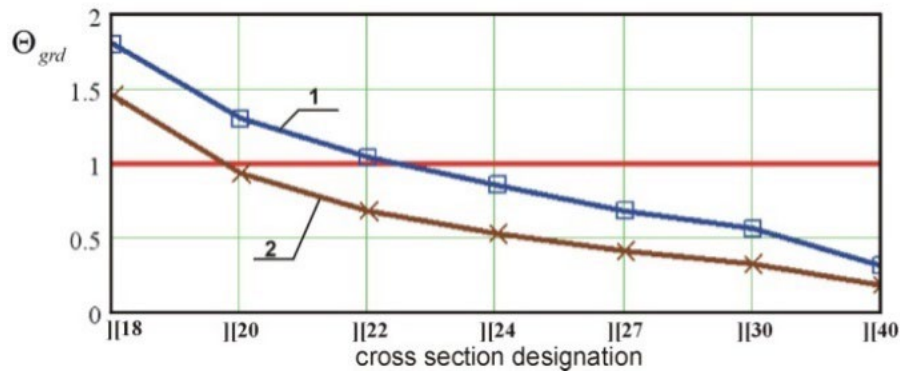
Figure 12. Girder's stress-strength ratios, Θ_{grd}: 1 – partial uniform load Q_{prt} with the half-span load Q_{hlf}; 2 – the full uniform load Q_{tot}.

The graph of structural deformation at the quarter of the span $\omega_{h,1/4}$ brought about by the non-uniform load is shown in Fig. 13. The $\omega_{h,1/4}$-value is derived from the expression (54c). It is the difference between the roof cambering at the pre-stressing phase and the overall displacement of the cable truss under the load: $\omega_{h,1/4} = 0.75 \cdot \Delta f_{pr} - \Delta f_{1/4}$. Figs. 12 and 13 show, that the channel bars [27 meet all the conditions implied by the ultimate and serviceability limit states.
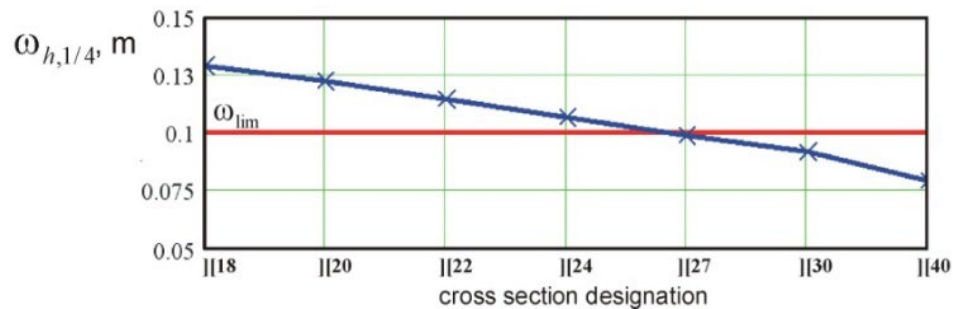
Figure 13. Structural deformation at the quarter of the span induced by the non-uniform load (shown in Fig. 5).

The parameter ξ_{Qh} of splitting the non-uniform load between the cable truss and the girder (33) is shown in Fig. 14. The graph is a hyperbolic-shaped curve, which tends to the asymptote with the increasing of the girder's stiffness.
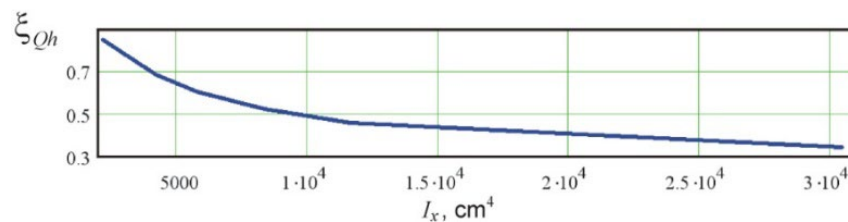
Figure 14. Dependence of the parameter of splitting the load ξ_{Qh} (33) on the moment of inertia of the girder's cross section I_x.

The graph of $h(\xi_{Qh})$-ratio (54b) for the girder's cross section chosen (two channel bars [27) is shown in Fig. 15.
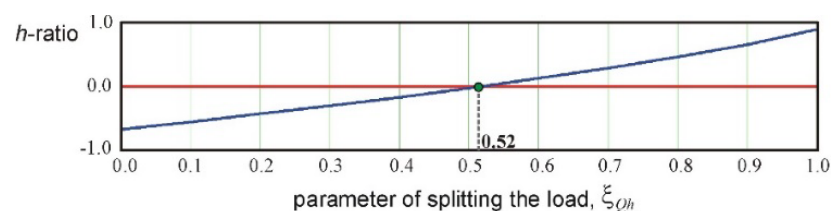
Figure 15. The graph of h-ratio (54b).

The figure shows, that the dependence $h\left(\xi_{Qh}\right)$ is close to the linear one in the allowable range $\xi_{Qh} \in \left(0...1\right]$. Thus, the secant method provides the solution for the equation (54a) in a few iterations. The solution is denoted in the figure by the green point.

3.7. Verification of the results

3.7.1. Comparison with numerical results by the specialized software package

The fragment of the roof, considered in clause 3.6, is numerically simulated using the specialized software package for nonlinear structural analysis EASY.2020 [46] (license no. 15129). The structural model of the roof's fragment is shown in Fig. 16.

Figure 16. Structural model of the roof's fragment: 1 – cable truss; 2 – flexible membrane; 3 – stiffening girder; 4 – ties for simulating the loose connection (design clearance).

The bearer and restraining chords of the roof are adopted of 24.1 mm and 6.1 mm steel cables, respectively [48]. Corresponding c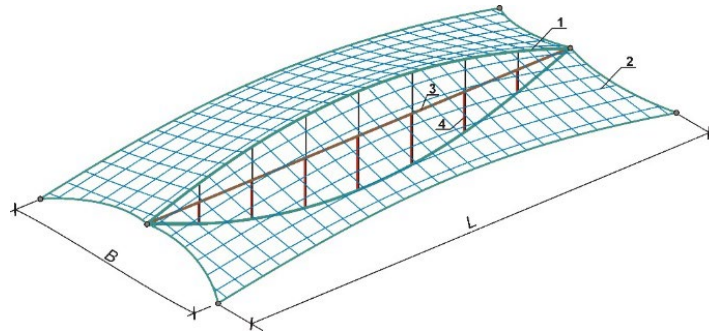ross section areas of the cables are the following: A_b = 3.38 cm² and $A_{r,cab}$ = 0.22 cm². They are taken close to the right bound indicated in Fig. 11. Thus, the cambering of the roof is the following: Δf_{pr} = 0.143 m. The tensioning of the bearer chord during the pre-stressing is obtained from (7) given the geometric length $L_{g,b}$ and the initial chord's length $L_{c0,b}$ (47): ΔL_p = 0.093 m. The stiffening girder is adopted of two steel channel bars [27. The geometrical properties of the overall cross section are the following: A_{grd} = 7.04·10⁻³ m², W_{grd} = 6.16·10⁻⁴ m³ and I_{grd} = 8.32·10⁻⁵ m⁴.

The girder and the roof's framework are not directly connected, unless the supporting points. They are also linked together by vertical ties made of steel cables (elements 4 in Fig. 16). In order to simulate the loose connection, the ties are initially slackened by the design clearance values: $\Delta_{1/2}$ = 0.098 m and $\Delta_{1/4}$ = 0.074 m (50, 52).

Comparison of the main structural parameters, obtained by the proposed expressions, and the results of the numerical analysis by the specialized software package EASY.2020 is given in Table 1.

Table 1. Comparison with the numerical results by the software package EASY.2020.

Designation	Unit	Value		Deviation, ξ, %	Remark
		by the present work	numerically simulated by the EASY-software		
Δf_{pr}	m	0.143	0.139	2.8	(43b)
ω_{ld}	m	0.100	0.101	1.0	must be equal to $\omega_{\lim} = 0.1\,\text{m}$
$\omega_{h,1/4}$	m	0.104	0.098	5.9	(53)
P_{pr}	kN/m	2.16	2.07	4.2	(49)
$N^{pr}{}_{grd}$	kN	52.9	48.3	9.1	(51a)
$N^{ld}{}_{grd}$	kN	236.6	234.9	0.7	(51b)

The table shows good agreement of the results. The peak discrepancy (9.1 %) is at the stage of the pre-stressing, when the axial force in the girder is substantially smaller, than under the external load.

3.7.2. Comparison with the results by the other authors

In order to verify the proposed results the following comparison is implemented. All notations are adopted according to the present paper, except the axial forces in the chords and the horizontal components of the forces, which are denoted by the indexes '*b*' and '*t*' meaning bottom (restraining) and top (bearer) chords.

Consider a symmetric cable truss with the bearer chord arranged above the restraining one [50]. The span of the truss, L, is 60 m. Eight span-to-sag ratios of the chords of the truss are considered: $L/f_{pr,b} = L/f_{pr,r} = \{7.5, 10.0, 12.5, 15.0, 17.5, 20.0, 22.5, 25.0\}$. The initial horizontal components of pretension of the chords are the following: $H_{0,b} = H_{0,t} = 600$ kN. The modulus of elasticity of the cables is $E_{cab} = 1.5 \cdot 10^8$ kN/m². Cross section areas of the chords are the following: $A_b = 2.0 \cdot 10^{-3}$ m² and $A_r = 1.3 \cdot 10^{-3}$ m². Uniformly distributed load is considered throughout the entire span $Q_{tot} = 10.0$ kN/m.

Considering the given rises of the chords f_{pr} and the chords' pretensions H_0, the initial lengths of the chords $L_{c,0}$ are obtained by the Hook's law given the chord's stiffnesses. Then, the chord's relative elongations ε_{pr} are calculated by (5) and the link load P_{pr} is obtained by (48a, 48b). Both the expressions (48), written for different chords, give exactly same result (the discrepancy is less than 10^{-11} %) meaning correctness of the link load calculation for the given cable truss. The link loads, P_{pr}, must, however be compared with the $P_{pr,bound}$-values, which ensure that the full uniform load Q_{tot} is completely taken by the cable truss.

Finding $P_{pr,bound}$-values is performed by (49) given the mid-span vertical deflections of the truss ω_{ld}. The deflections are obtained by nonlinear Finite Element Method. They are taken from the graph (Fig. 10 in [50]): $\omega_{ld} = \{0.110, 0.178, 0.260, 0.353, 0.453, 0.557, 0.655, 0.755\}$ m. Because the deflections ω_{ld} have been obtained regardless the strength properties of the chords, the limiting deformation $\varepsilon_{cab,2}$ in (49) is substituted by the actual deformation of the bearer cable $\varepsilon_{ld,b}$ (5) given ω_{ld}.

Comparison of P_{pr}-values and $P_{pr,bound}$-values, which are derived from different conditions implied on the cable truss, are shown in Figs. 17 and 18. The discrepancy between the link loads is obtained as follows:

$$\rho = 200 \cdot \frac{\left|V_0 - V_{ref}\right|}{V_0 + V_{ref}} \%, \tag{57}$$

where V_0 and V_{ref} are the values to be compared.
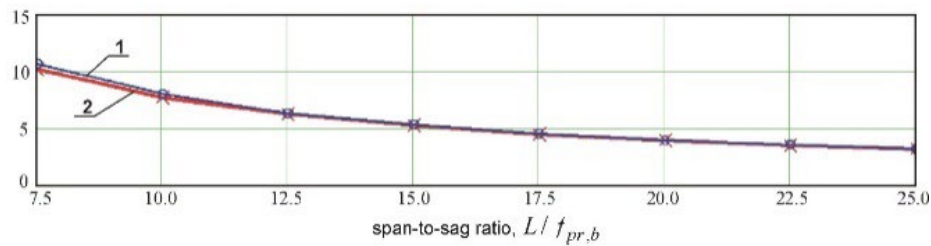

Figure 17. Link loads between the chords, kN/m: 1 – P_{pr}-values (48) given the stiffnesses of the chords; 2 – $P_{pr,bound}$-values (49) given the deflections under the load [50].
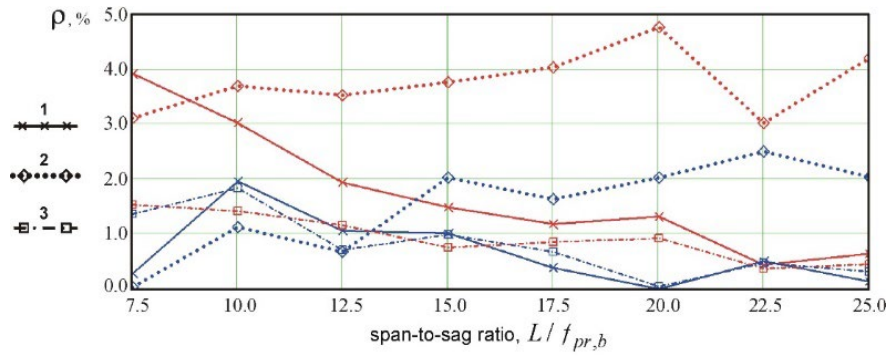
Figure 18. Percentage discrepancies ρ: 1 – discrepancies between the link loads $P_{pr,bound}$ and P_{pr}; 2 – discrepancies between the axial forces in the bottom chord; 3 – discrepancies between the axial forces in the top chord; red color is for the symmetric cable truss, while blue color is for non-symmetric one.

Fig. 18 shows that the discrepancies between the link loads do not exceed 4 % meaning that the cable truss is in equilibrium given the chord's stiffnesses, the external load and the corresponding deflections.

Considering the shallow shape of the chords, the horizontal components of the cable forces, H_b and H_t, are compared with the axial forces in the chords:

$$N_b = EA_r \cdot \varepsilon_{ld,r}; \tag{58a}$$

$$N_t = EA_b \cdot \varepsilon_{ld,b}, \tag{58b}$$

where N_b and N_t are the forces in the bottom and the top chords of the truss; ε_{ld} are the relative elongations of the chords given the deflection of the truss under load ω_{lim} (5).

The horizontal components of the cable force are taken from the graphs (Figs. 8 and 9 in [50]). The comparison of the forces is shown in Figs. 18 and 19.
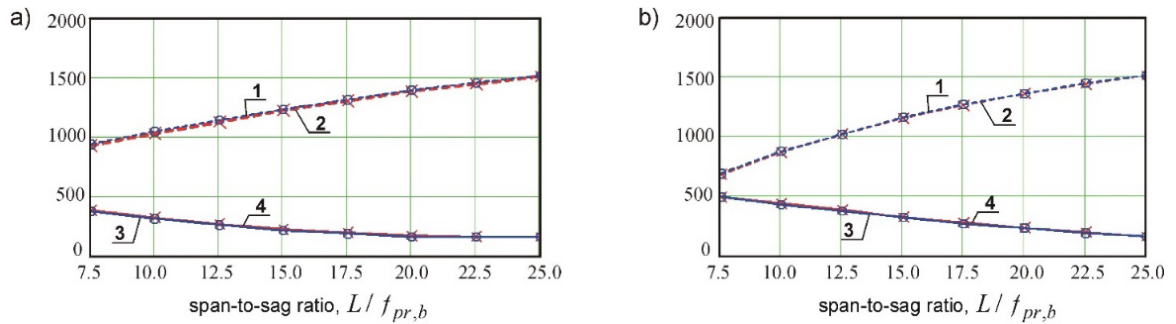
Figure 19. Axial forces and horizontal components of the forces, kN: a, b – symmetric and non-symmetric cable trusses, respectively; 1, 2 – N_t and H_t in the top chord; 3, 4 – N_b and H_b in the bottom chord.

Non-symmetric cable truss of the 60 meters span is also considered. Different span-to-sag ratios are adopted for the bearer chord $\left(L/f_{pr,b}\right)_j$, $j = [1...8]$, while for the restraining chord the constant ratio is taken: $L/f_{pr,r}$ = 25 [50]. The initial horizontal component of pretension of the restraining chord is $H_{0,b}$ = 600 kN, while for the bearer chord it is calculated by the following expression: $H_{0,t} = H_{0,b} \cdot f_{pr,r}/f_{pr,b}$. Mid-span vertical deflections of the truss are taken from the graph (Fig. 13 in [50]): ω_{lim} = {0.162, 0.255, 0.342, 0.444, 0.531, 0.612, 0.689, 0.751} m.

Comparison of P_{pr} and $P_{pr,bound}$ -values (48, 49) given the deflection ω_{lim} is shown in Fig. 18. Comparison of the forces taken from the graphs (Figs. 11 and 12 in [50]) is shown in Figs. 18 and 19.

Figs. 18 and 19 show good agreement with the results [50] under uniformly distributed load acting on the entire span of the truss.

Influence of the load acting on a half of the span is also considered in [50]: Q_L = 8.91 kN/m and Q_R = 0.0. The span of the truss, L, is 60 m. The rises of the chords are the following: $f_{pr,b}$ = $f_{pr,r}$ = 4.02 m. The initial horizontal components of pretension of the chords are the following: $H_{0,b}$ = $H_{0,t}$ = 588.603 kN. The modulus of elasticity of the cables is E_{cab} = 1.48135·10⁸ kN/m². Cross section areas of the chords are the following: A_b = 2.0·10⁻³ m² and A_r = 1.3·10⁻³ m².

The initial rise of the bearer chord is obtained by (39) given the pretension and the stiffness properties: $f_{0,b}$ = 3.66 m. Thus, the deflection of the truss at the stage of the pre-stressing is the following (1a): $\Delta f_{pr} = f_{0,b} - f_{pr,b}$ = −36 m.

The overall displacements of the truss under the loads Q_L and Q_R are obtained by minimizing (36): Δf = −0.5 m and $\Delta f_{1/4}$ = −0.72 m. Thus, the displacements of the truss at the center and at the quarter points of the span are the following: $\omega = \Delta f_{pr} - \Delta f$ = 0.14 m and $\omega_{1/4} = 0.75 \cdot \Delta f_{pr} - \Delta f_{1/4}$ = = 0.45 m. Considering the graph (Fig. 7 in [50]) the corresponding displacements are 0.146 m and 0.459 m. The discrepancies (57) are the following: 4.2 % and 2.0 %.

The comparison implemented in the present clause shows good agreement with the results by the other authors obtained numerically and by using the Finite Element Method.

4. Conclusions

1. The cable roof stiffened with a girder and enveloped with a flexible membrane is considered.

2. The polymer membrane is included into the structural model of the roof by using membrane-simulating element. The numerical technique for estimating the effective stiffness and the allowable relative deformation of the element is proposed.

3. The design clearances are proposed for the structural enhancement. The clearances, being the means of the passive structural adaptation, allow exempting the stiffening girder from uniformly distributed external loads, which are fully sustained by the cable truss. The girder, in turn, mitigates kinematic displacements brought about by non-uniform impacts. The calculating technique for splitting the non-uniform load between the cable truss and the girder is proposed.

4. The computational approach for structural analysis of the roof is proposed. The approach is based on the limit states analysis, which is mandatory for the design practice in Russian Federation.

5. Estimation of the allowable deformations of the roof at the pre-stressing and operational phases is proposed. The expressions for the axial stiffnesses of the cable chords, the design clearances and the link load between the chords at the pre-stressing stage are proposed under the conditions of reaching the allowable deformation and full use of the strength properties.

6. The work contributes to the development of hybrid building constructions, which consist of high-strength flexible cables, polymer membranes and rigid elements made of ordinary structural steel. It facilitates the practical realization of the hybrid roofs by providing the initial data for the conceptual design stage. The results of the present work allow to validate structural models and to verify the results obtained by numerical methods of structural analysis.

References

1. Bridgens, B.N., Gosling, P.D., Birchall, M.J.S. Tensile fabric structures: concepts, practice and developments. The Structural Engineer. 2004. 82 (14). Pp. 21–27.
2. Barozzi, M., Viscuso, S., Zanelli, A. Design novel covering system for archaeological areas. Proceedings of VII International Conference on textile composites and inflatable structures. Structural membranes 2015. 2015. 105–114.
3. Goppert, K. High tension tensile architecture. New stadium projects. Proceedings of VI International Conference on textile composites and inflatable structures. Structural membranes 2013. 2013. Pp. 21–26.
4. Llorens, J.I. Structural membranes for urban spaces. Proceedings of VII International Conference on textile composites and inflatable structures. Structural membranes 2015. 2015. Pp. 133–144.
5. Llorens, J., Zanelli, A. Structural membranes for refurbishment of the architectural heritage. Procedia Engineering. 2016. 155. Pp. 18–27. DOI: 10.1016/j.proeng.2016.08.003

6. Viscuso, S., Dragoljevic, M., Monticelli, C., Zanelli, A. Finite-element analysis and design optioneering of an emergency tent structure. Proceedings of the TensiNet Symposium. Softening the Habitats. 2019. Pp. 208–219.

7. Fangueiro, R., Rana, S. Towards high performance and multi-functional structural membranes using advanced fibrous and textile materials. Proceedings of VII International Conference on textile composites and inflatable structures. Structural membranes 2015. 2015. Pp. 296–305.

8. Wagner, R. Bauen mit Seilen und Membranen. Beuth Verlag GmbH. Berlin, Germany, 2016. 517 p.

9. Mushchanov, V., Rudneva, I., Priadko, Yu. Intense-deformed condition of suspended system of bending-rigid fibers at the account of pliability of supports. Metal Constructions. 2012. 18 (1). Pp. 5–16.

10. Arellano, H., Gomez, R., Tolentino, D. Parametric analysis of multi-span cable-stayed bridges under alternate loads. The Baltic Journal of Road and Bridge Engineering. 2019. 14 (4). Pp. 543–567. DOI: 10.7250/bjrbe.2019-14.457

11. Al-Rousan, R. The impact of cable spacing on the behavior of cable-stayed bridges. Magazine of Civil Engineering. 2019. 91 (7). Pp. 49–59. DOI: 10.18720/MCE.91.5

12. Mushchanov, V., Protopopov, I., Korsun, O., Garifullin, M. Definition of the rational geometry of the cable-beam cover over stadium tribunes. Procedia Engineering. 2015. 117. Pp. 1001–1012. DOI: 10.1016/j.proeng.2015.08.209

13. Yegorov, V.V., Aleksashkin, Ye.N. Predvaritelno-napryazhennaya shprengelnaya ferma [Pre-stressed strutted truss]. Patent RF no. 2169243, 1999.

14. Voyevodin, A.A. Predvaritelno-napryazhennyye sistemy elementov konstruktsiy [Pre-stressed systems of structural elements]. Moskva: Stroyizdat, 1989. 304 str.

15. Liew, J.Y.R., Punniyakotty, N.M., Shanmugam, N.E. Limit-state analysis and design of cable-tensioned structures. International Journal of Space Structures. 2001. 16 (2). Pp. 95–110. DOI: 10.1260/0266351011495205

16. Llorens, J. Detailing masts. Proceedings of the IASS Annual Symposium. Structural membranes 2019. 2019. Pp. 359–366.

17. Goremikins, V., Rocens, K., Serdjuks, D. Cable truss analyses for prestressed suspension bridge. Proceedings of VIII International DAAAM Baltic Conference. Industrial Engineering. 2012. Pp. 45–50.

18. Goremikins, V., Rocens, K., Serdjuks, D. Decreasing of displacements of prestressed cable truss. International Journal of Civil and Environmental Engineering. 2012. 6 (3). Pp. 228–236.

19. Goremikins, V., Rocens, K., Serdjuks, D. Cable truss analyses for suspension bridge. Proceedings of 11 International Scientific Conference. Engineering for Rural Development. 2012. Pp. 228–233.

20. Habraken, A.P.H.W., Sleddens, W., Teuffel, P. Adaptable lightweight structures to minimize material use. Proceedings of VI International Conference on textile composites and inflatable structures. Structural membranes 2013. 2013. Pp. 71–82.

21. Alekseytsev, A.V., Gaile, L., Drukis, P. Optimization of steel beam structures for frame buildings subject to their safety requirements. Magazine of Civil Engineering. 2019. 91 (7). Pp. 3–15. DOI: 10.18720/MCE.91.1

22. Serpik, I.N., Alekseytsev, A.V. Protivoavariynaya stalnaya balochnaya konstruktsiya [Emergency steel beam structure]. Patent RF no. 2556761, 2014.

23. Mikhailov, V.V., Chesnokov A.V., Dolmatov I.V. Pre-stressed cable truss with stiffening girder and design clearance: development and analysis. Proceedings of the TensiNet Symposium. Softening the Habitats. 2019. Pp. 58–70.

24. Freire, A.M.S., Negrao, J.H.O., Lopes, A.V. Geometrical nonlinearities on the static analysis of highly flexible steel cable-stayed bridges. Computers and Structures. 2006. 84 (31–32). Pp. 2128–2140. DOI: 10.1016/j.compstruc.2006.08.047

25. Greco, L., Impollonia, N., Cuomo, M. A procedure for the static analysis of cable structures following elastic catenary theory. International Journal of Solids and Structures. 2014. 51. Pp. 1521–1533. DOI: 10.1016/j.ijsolstr.2014.01.001

26. Coarita, E., Flores, L. Nonlinear analysis of structures cable - truss. International Journal of Engineering and Technology. 2015. 7 (3). Pp. 160–169. DOI: 10.7763/IJET.2015.V7.786

27. Nuhoglu, A. Nonlinear analysis of cable systems with point based iterative procedure. Scientific Research and Essays. 2011. 6 (6). Pp. 1186–1199.

28. Xu, J., Zhang, Y., Yu, Q., Zhang, L. Analysis and design of fabric membrane structures: a systematic review on material and structural performance. Thin-Walled Structures. 2022. 170. Pp. 1–17. DOI: 10.1016/j.tws.2021.108619

29. Nunes, E., Sousa, J.B.M, Baier, B., Freitas, A.M.S. Membrane roof for an amphitheater in Brazil: searching for the optimal design. International Journal of Space Structures. 2015. 30 (3-4). Pp. 261–271. DOI: 10.1260/0266-3511.30.3-4.261

30. Strobel, D., Singer, P., Holl, J. Analytical formfinding. International Journal of Space Structures. 2016. 31 (1). Pp. 52–61. DOI: 10.1177/0266351116642076

31. Tran, H.C., Lee, J. Advanced form-finding for cable-strut structures. International Journal of Solids and Structures. 2010. 47 (14–15). Pp. 1785–1794. DOI: 10.1016/j.ijsolstr.2010.03.008

32. Lang, R., Nemec, I. Form-finding of shell and membrane structures. Proceedings of VIII International Conference on textile composites and inflatable structures. Structural membranes 2017. 2017. Pp. 303–310.

33. Llorens, J.I. Appropriate design of structural membranes. Proceedings of X International Conference on textile composites and inflatable structures. Structural membranes 2021. 2021. DOI: 10.23967/membranes.2021.008

34. Machacek, J, Jermoljev, D. Steel structures in interaction with non-metallic membranes. Journal of Civil Engineering and Management. 2017. 23 (3). Pp. 368–377. DOI: 10.3846/13923730.2015.1128482

35. Stroebel, D., Holl, J. On the calculation of textile halls. Proceedings of X International Conference on textile composites and inflatable structures. Structural membranes 2021. 2021. DOI: 10.23967/membranes.2021.043

36. Hegyi, D. Numerical stability analysis of arch-supported membrane roofs. Structures. 2021. 29. Pp. 785–795. DOI: 10.1016/j.istruc.2020.11.025

37. Dinh, T.D., Rezaei, A., Linthout, T., Mollaert, M., Van Hemelrijck, D., Van Paepegem, W. A computational compensation method for fabric panels of tensioned membrane structures using a shape optimization method based on gradientless algorithms. International Journal of Solids and Structures. 2017. 112. Pp. 16–24. DOI: 10.1016/j.ijsolstr.2017.02.026

38. Haug, E., De Kermel, P., Gawenat, B., Michalski, A. Industrial design and analysis of structural membranes. International Journal of Space Structures. 2009. 24 (4). Pp. 191–204. DOI: 10.1260/026635109789968227

39. Wagner, R. Simplified design tools for single/double curved membranes and inflated cushions. International Journal of Space Structures. 2008. 23 (4). Pp. 233–241. DOI: 10.1260/026635108786959843

40. Grigorjeva, T., Juozapaitis, A. Revised engineering method for analysis of behavior of suspension bridge with rigid cables and some aspects of numerical modeling. Procedia Engineering. 2013. 57. Pp. 364–371. DOI: 10.1016/j.proeng.2013.04.048

41. Yan, H., Wei-ren, L. Static analysis of cable structure. Applied Mathematics and Mechanics (English Edition). 2006. 27 (10). Pp. 1425–1430. DOI: 10.1007/s10483-006-1015-y

42. Forster, B., Mollaert, M. European design guide for tensile surface structures. TensiNet. Brussel, Belgium, 2004. 354 p.

43. Chesnokov, A.V., Mikhaylov, V.V. Analysis of cable structures by means of trigonometric series. Proceedings of VIII International Conference on textile composites and inflatable structures. Structural membranes 2017. 2017. Pp. 455–466.

44. Bridgens, B., Birchall, M. Form and function: the significance of material properties in the design of tensile fabric structures. Engineering Structures. 2012. 44. Pp. 1–12. DOI: 10.1016/j.engstruct.2012.05.044

45. Gosling, P.D., Bridgens, B.N., Albrecht, A., Alpermann, H., Angeleri, A., Barnes, M., Bartle, N., Canobbio, R., Dieringer, F., Gellin, S., Lewis, W.J., Mageau, N., Mahadevan, R., Marion, J.M., Marsden, P., Milligan, E., Phang, Y.P., Sahlin, K., Stimpfle, B., Suire, O., Uhlemann, J. Analysis and design of membrane structures: results of a round robin exercise. Engineering Structures. 2013. 48. Pp. 313–328. DOI: 10.1016/j.engstruct.2012.10.008

46. Lightweight structure design. Easy. [Online]. URL: https://www.technet-gmbh.com/fileadmin/user_upload/technet/Produktinformationen/Easy/Easy_ProductBrochure.pdf. (date of application: 08.11.2022).

47. Chesnokov, A.V., Mikhailov, V.V., Dolmatov, I.V. The influence of material aging on the structural behavior of a flexible roof with a polymer membrane shell. Computer Methods in Materials Science. 2021. 21 (1). Pp. 13–24. DOI: 10.7494/cmms.2021.1.0748

48. European technical assessment. PFEIFER wire ropes. ETA-11/0160. [Online]. URL: https://www.pfeifer.info/out/assets/PFEIFER_WIRE-ROPES_TECHNICAL-APPROVAL-ETA-11-0160_EN.PDF. (date of application: 08.11.2022).

49. Harris, B. Engineering composite materials. The Institute of Materials. London, 1999. 194 p.

50. Kmet, S., Kokorudova, Z. Nonlinear closed-form computational model of cable trusses. International Journal of Nonlinear Mechanics. 2009. 44 (7). Pp. 735–744. DOI: 10.1016/j.ijnonlinmec.2009.03.004

Information about the authors:

Andrei Chesnokov, *PhD in Technical Sciences*
ORCID: https://orcid.org/0000-0003-3687-0510
E-mail: andreychess742@gmail.com

Vitalii Mikhailov, *Doctor of Technical Sciences*
ORCID: https://orcid.org/0000-0001-8274-9346
E-mail: mmvv46@rambler.ru

Dynamic responses of shallow foundations on saturated soil under impact loadings

Azad Hameed Rasheed[1] ✉ (iD) **, Balqees Abdulwahid Ahmed**[2]

[1] *Directorate of Executing Rivers Dredging Works, Ministry of Water Resources, Baghdad, Iraq*

[2] *Department of Civil Engineering, College of Engineering, University of Baghdad, Baghdad, Iraq*

✉ *azad.hameed@muc.edu.iq*

Abstract. In civil engineering, there are many problems related to the transmission of pressure waves through the soil due to dynamic loads. The objective of this investigation is to research the dynamic soil properties. In industrial applications, these vibrations remain often caused by the impact of weights on the foundation machine. This study investigates how saturated soft clay soil responds to a single impulsive load. Deflectometry via falling weights was conducted to produce single pulse energy by dropping different weights from various elevations. Usually, these dynamic foundations have a greater effect on the surface than various depths of the same foundation. Soil surface responses were studied, then the effects occurring at the depth of the soil surface and causing these responses were studied, which include vertical displacements, velocities, and accelerations. Using the same impact weight (5 kg) at both drop heights (250 mm and 500 mm), the average percentage change in the maximum impact force generated at the contact surface increased by 33 %. This decreased the maximum displacement response of the clay soil model by 25 %, and the maximum displacements increased with increasing operational frequency and dynamic loads.

1. Introduction

Dynamic response is one of the primary parameters used to describe the soil behavior under dynamic loads. The machine foundation's behavior is affected by different factors such as soil properties, the weight of machine and foundations, the magnitude of the unbalanced force of machine, contact zone between foundations and soils, and static soil pressure. For these reasons, the most critical step in the design to get a successful machine foundation can be relied an analyzing technique for dynamic responding and it should not surpass the limit given to a machine designer. Anyway, before starting the acceptable limits of the settlement of the machine foundation, it is very important to explain that the failure of the vibrating foundations is reached when the motion exceeds a limiting value, which is usually expressed as displacement of the foundation at specified frequencies [1].

The mechanics of saturated clay are more complex than those of single-phase materials due to the coupling of the responses of their many constituents. For saturated clay, the soil pores are filled with water, which causes the permeability to be low and transient loading to be fast. To properly measure how earth buildings and foundations behave, this connection should be taken into account [2].

Many researchers have investigated the dynamic response under machinery. Additionally, several researches investigated the vertical vibrating manner for surface footing Soil reaction under impacting forces is determined by dynamical soil characteristics. Estimating the activity soil characteristics by monitoring the reactions to impact loading. In dynamic research, stiffness, damping ratio, and unit weight are considered [3–5].

The impacts of surface depth and loading frequency on the modeling of circular shallow foundations in stiff clay soil are investigated. Additionally, impact loads and excess pore water pressure are measured at the foundation's soil surface. It was shown that maximum displacements rise with operating frequency increases with dynamic load and no measured effects of pore water pressures on the model of stiff clay soil. The seismic response of locations is subjective to the dynamical properties of the surface soil. This response affects the performance of embedded or superimposed structures. Identification and inverse problem solution approaches are required for determining in-situ soil variables and calibrating models of soil dynamical loads. The increased availability of high-quality laboratory and field data has led to an increase in soil investigation system identification research [6].

The impacts of surface depth and loading frequency on the modeling of circular shallow foundations in stiff clay soil are investigated. Additionally, impact loads and excess pore water pressure are measured at the foundation's soil surface. It was shown that maximum displacements rise with operating frequency increases with dynamic load and no measured effects of pore water pressures on the model of stiff clay soil. The seismic response of locations is subjective to the dynamical properties of the surface soil. This response affects the performance of embedded or superimposed structures. Identification and inverse problem solution approaches are required for determining in-situ soil variables and calibrating models of soil dynamical loads. The increased availability of high-quality laboratory and field data has led to an increase in soil investigation system identification research [7].

In [8] several natural and forced vertical vibration models performed on surface and embedding modeling for footings on dry and moist poorly graded sand were investigated. Similar findings were presented in [9], indicating that as the footing base area increases, the natural frequency and amplitude The dynamic behavior of the soil-foundation systems is the most important aspect of a machine's successful functioning. The essential objective of the design of a machine's foundation is to restrict its motion to amplitudes that neither endanger the machine's operation nor disturb surrounding personnel. Hence, the engineering study of the footings' response to the projected dynamical force created by the usage of the equipment is a crucial component of a solid foundation design. In addition, when large movements of an existing footing impede the functioning of supported machinery, an investigation must be done to determine the root causes of the issue. Therefore, in an investigation, soil-structure interaction (SSI) phenomena that are exposed to impact load are studied [10]. Firstly, dynamic soil-structure interaction subject to impact forces is tested using vibrating impacts then were explored by contrasting the soil-structure system with a solid footing condition. After that, a mathematical analysis that passes the SSI tests is given. The nonlinear behavior of soil in the finite element simulation is modeled independently using a boundary surfaces deformation method and a related linear approach. The boundary surface plasticity model's estimation outcomes prove to be more accurate than those of the experiments [11].

Modern industry has brought massive machinery that affects the foundation's performance and the soil below, causing another sort of vibration stress. All machine foundations, regardless of dimension and type, should be considered engineering problems, and their designs should be founded on solid engineering methods [12].

Many researchers look into how machinery moves, for instance, the authors of [13–14] and other researchers looked into how vertical vibrations affect surface footings.

When the applied loads from the structure of testing increase and exceed the cracking load, the damaged supporter of individual groups exhibits a relatively high ratio of stiffness drop [15] as an outcome of a portion of the pre-stressing force, which rises the rate of cracking and displacements. Most studies absorbed the dynamic load caused to earthquakes and offshore waves.

The majority of solutions model the machine's base as a block resting on the surface of an elastic earth. Typically, the actual foundations are inserted, which significantly affects the dynamic behavior of the foundation [16].

The primary aims of this study are to evaluate the soil's response to impact loads. The dampening of waves caused by impact stresses via the soil will be emphasized. A decision was made to experiment on clayey soils to identify how to analyze the performance of these soils below the influence of impact loads with variable applied kinetic energy, taking into account the embedment and distance of the footing as well as the impact force.

2. Methods and Materials

The tests were conducted under the standards for identifying the physical and chemical properties of soil, the specifics of these requirements are detailed in Table 1. A sample of clayey soil was taken from a depth of 1.0 m from the soil subsurface of a brick factory site in Al-Nahrawan city (54 km east of Baghdad) [2].

For soft clay conditions, a compliant consolidation test was performed. Table 2 displays the soft clay consolidation test results, and the testing programs are shown in Table 3.

Table 1. Comparison of displacement value with maximum impact loads from the present study area in Iraq.

No.	Author	Year	Study area	Soil type	Soil depth	Displacement value with maximum impact loads
1	Adnan F. et al..	2016	Karbala city	Dry-dense sand	Embedment depth	40–50%
2	Adnan F. et al.	2016	Karbala city	Dry-medium sand	Embedment depth	35–40%
3	Adnan F. et al.	2016	Karbala city	Dry-loose sand	Embedment depth	25–35%
4	Adnan F. et al.	2016	Karbala city	Saturated sand	At surface depth	30–60%
5	Ahmed B.A. et al.	2022	Al-Nahrawan city	Saturated soft clay	At surface depth	50%
6	Ahmed B.A. et al.	2022	Al-Nahrawan city	Saturated stiff clay	At surface depth	80%
7	Rasheed A.H. et al.	2023	Al-Nahrawan city	Saturated soft clay	At surface depth	50%
8	Rasheed A.H. et al.	2023	Al-Nahrawan city	Saturated stiff clay	At surface depth	80%

Table 2. Physical and chemical properties of soil under using standards.

Property	Value	Standard of the test
Specific Gravity, Gs	2.71	ASTM D854
Gravel (> 4.75 mm) %	0	
Sand (4.75–0.075 mm) %	3	ASTM D422
Silt (0.075–0.005 mm) %	40	
Clay (< 0.005 mm) %	57	
Liquid limit (LL)	39	
Plastic limit (PL)	22	ASTM D4318
Plasticity index	17	
Gypsum content ($CaSO_4 \, 2H_2O$) %	0.23	BS 1377-3
Total dissolved salts (TDS) %	0.39	ASTM D5907
SO_3 content, %	0.19	BS 1377-3
Organic matter (OM) %	0.2	ASTM D2974
pH value	9.18	ASTM D4972
Classification according to USCS	CL	ASTM D2487

Table 3. Consolidation test results for soft clay.

Parameter	Soft clay state
Cu	20–25 kN/m^2
e_o	0.73
γ_{dry}	16.45 kN/m^2
γ_{sat}	19.4 kN/m^2
Compression index, Cc	0.19
Expansion index, Cr	0.11

Eight experiments were performed on soft clay soil with impact loads from various sources and measurement of the energy at the soil's surface using two separate footing dimensions (where B is the diameter of the foundations). Fig. 1 shows the tests. A falling weight deflectometer (FWD) was used to

apply impact loads to a modeling technique with a ground baseplate of two sizes that remained measured as a surface footing on the topsoil underneath the impactor. It also included a steel with walls made of plating 2 mm thick and a base that represented a soil container. The two portions of the steel container have dimensions of 1200 × 1200 × 800 mm. Test runs were conducted before beginning the process of prepping the soil. Fig. 2 shows a relationship between the water content and liquidity index to get the soil's undrained shear strength. Following are the preparation steps for the soil layers in the steel container:
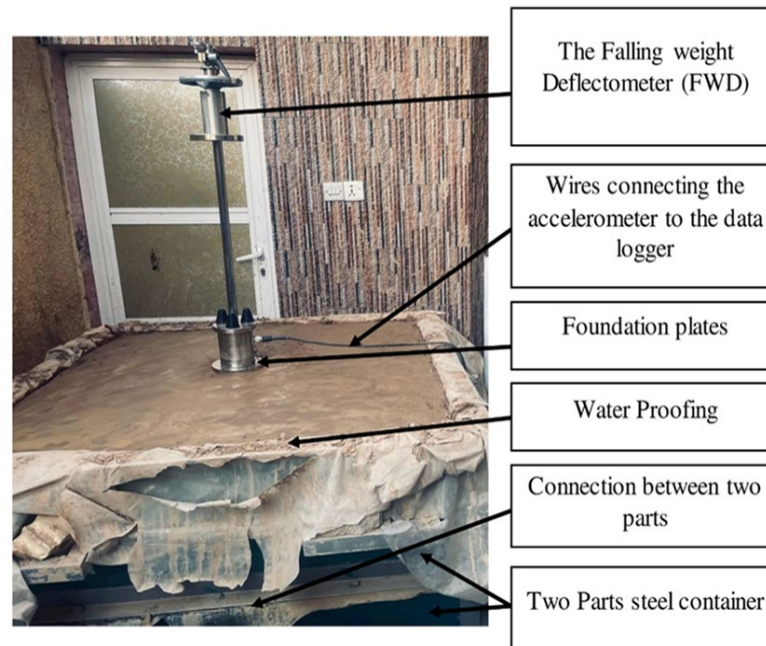
Figure 1. The experimental soil model's setup.
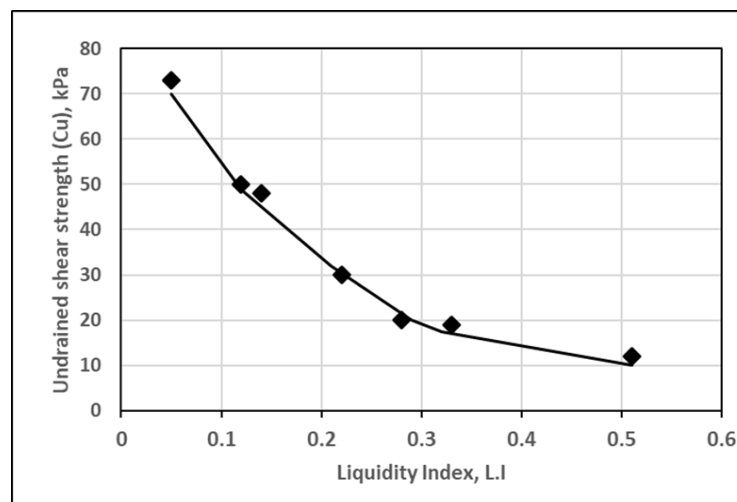
Figure 2. Relations between shear strength and liquidity index.

- A total of 25 kg of dry soil was divided up into groups.
- To achieve an undrained shear strength (Cu) between 20 and 25 kPa, as specified by engineering standards, the soil model was mixed in mixing with sufficient water contents and various proportions. The moisture content value then was chosen from Fig. 3.
- The clay soil was combined with water and placed in parts of the steel container. Each level was then compacted using a specific hardwood tamping hammer measuring 150 × 150 mm. Each layer's outcome was around 50 mm. The operation continued until the clay bed reached its maximum depth.
- After completing the preparations for the clay layers, they were covered with nylon sheets and left for 96 hours to cure.
- Using a portable vane shear apparatus, the undrained shear strength was measured daily to get the closest shear strength value displayed in Fig. 4.

Figure 3. Variation of undrained shear strength vs moisture content.

Figure 4. A portable vane shear device is used to control the undrained shear strength.

2.1. Measuring Instruments

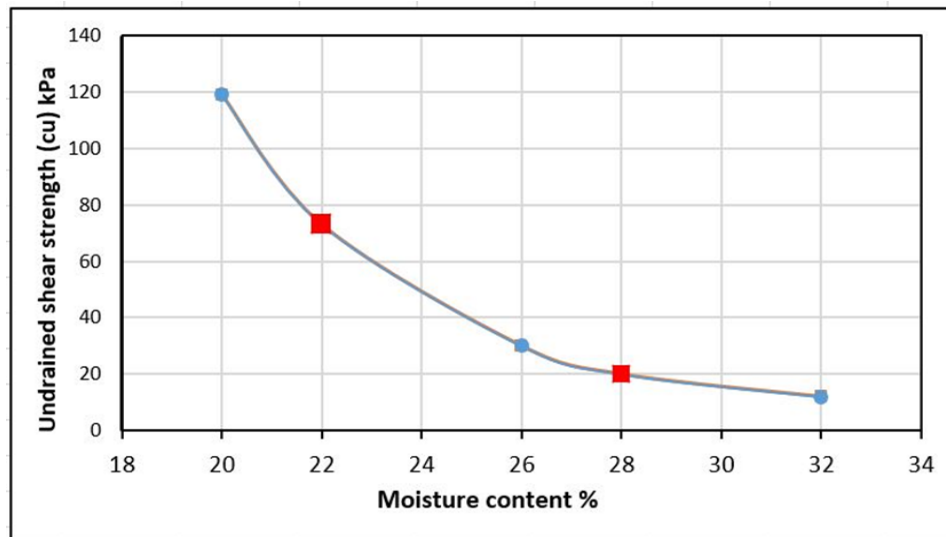The supporting plates were placed directly upon the surface of the ground, and thus the falling weights utilized to transfer the soil model to the vertical impact dynamic loading were of varying weights (5 or 10 kg) and elevations to represent varying values (500 or 250 mm). Two sizes (100 and 150 mm) of foundation contacting plates are utilized to assess the reaction of the soil surface to an impact force. Then, two pore water pressure gauges are placed at a depth of B or 2B, depending on the size of the bearing plates, in the center of the clay layer in the vertical path under the midpoint of the supporting plates. The method of data collection was designed so that all information could be continually evaluated and collected. Using this method, it is possible to measure the transmitted impulse response, the displacement-time history, and the soil surface depths. Using an accelerometer transducer and surface levels for each test, the acceleration-time history was calculated. The fundamental construction of the FWD mechanism consists of a base structure with an integrated accelerometer and indicator unit. The card reader may record and store a wide range of computations. The sensors display the peak load value and the displacement value. Its storage card's data can be delivered directly to a laptop or through the indication. The software comprises a load cell and an accelerometer to measure the impact load and displacements after free-falling the system block of the falling weight deflectometer. The displacement is obtained by integrating the readings in the accelerometer double. The measurement/processing software is essential for a laptop-based system of units. Inside this approach, recorded data from the indicators is transferred directly from the indicators to the laptop. To identify acceleration within the clay.

2.2. Testing Method

The stages describe this test plan:

- Preparing the soft clay layers for a total depth of 800 mm (100 mm per level).
- Putting the accelerometer sensor in the midpoint of the clay soil in a vertical path under the center of the bearing surfaces plate at depths of B or 2B, depending on the size of the bearing surfaces.
- Putting the sensors on the ground horizontally at a depth of 10 mm.
- After putting the base for the model, mount the FWD in the center and ensure that it is perpendicular to the area of the model.
- The file collecting system, as seen in Fig. 5, will record the response to delivering the impacting mass and display the results on a laptop.
- The information of abbreviation for the verified models as well as a specimen of models identification is clarified in Table 4.
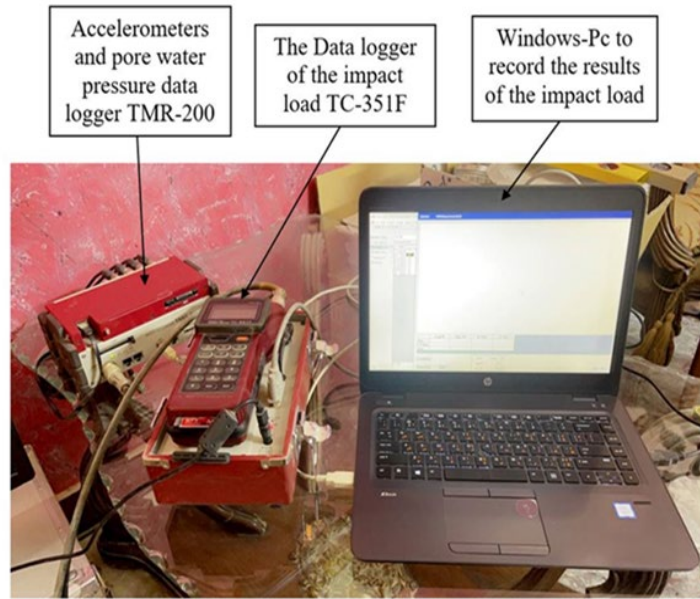

Figure 5. Data acquisition system.

Table 4. Details of the testing program and test designation.

No.	Test designation	Soil state	Soil density	Impact loading state	Size of bearing plate (mm)	The dropping mass (kg)	The height of drop (mm)
1	SsoP100M5H25	Saturated	Soft	At surface	100	5	250
2	SsoP100M5H50	Saturated	Soft	At surface	100	5	500
3	SsoP100M10H25	Saturated	Soft	At surface	100	10	250
4	SsoP100M10H50	Saturated	Soft	At surface	100	10	500
5	SsoP150M5H25	Saturated	Soft	At surface	150	5	250
6	SsoP150M5H50	Saturated	Soft	At surface	150	5	500
7	SsoP150M10H25	Saturated	Soft	At surface	150	10	250
8	SsoP150M10H50	Saturated	Soft	At surface	150	10	500

3. Results and Discussion

Concerning the behavior of soft clay soil, it is essential to note that a range of loading conditions was utilized in impact testing on plates ranging in diameter from 100 to 150 mm, dependent on the supporting plates' location on the soil surface (0B). A weight of 5 or 10 kg was dropped from a height of 500 or 250 mm to produce the impact force. The results of dynamic analysis are shown in Fig. 6–9. The data are shown in sections (a), (b), (c), and (d) of each figure for each reaction, which contains the load history, displacements,

accelerations, and velocity functions of time. All responses are observed directly beneath the surfaces. Variations in vertical displacement (beneath the plates) are depicted in section (c) of each figure.

Figure 6. Dynamic test results for SsoPM5H25 model: (a) and (c) impact force-time history with displacements, (b) acceleration time history, (d) velocity time-history.

Figure 7. Dynamic test results for SsoPM5H50 model: (a) and (c) impact force-time history with displacements, (b) acceleration time history, (d) velocity time-history.

Figure 8. Dynamic test results for SsoPM10H25 model: (a) and (c) impact force-time history with displacements, (b) acceleration time history, (d) velocity time-history.
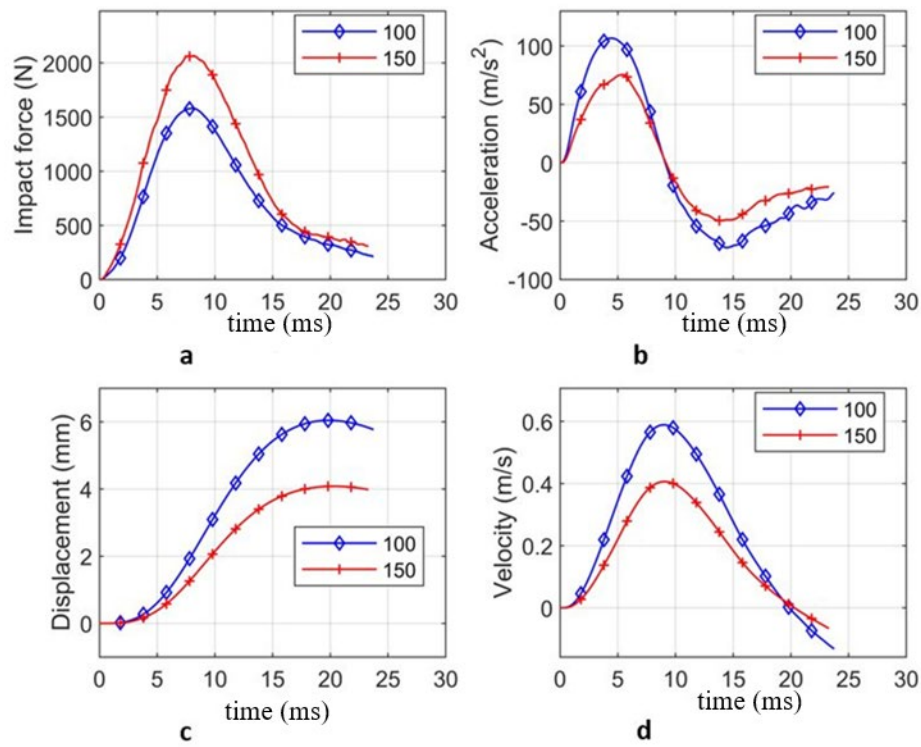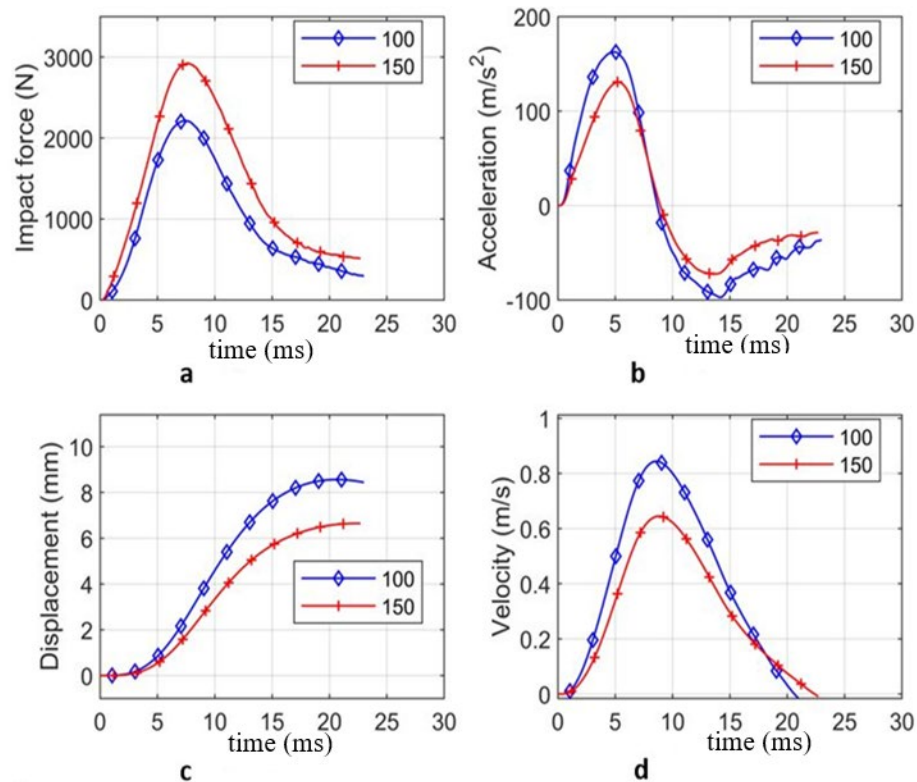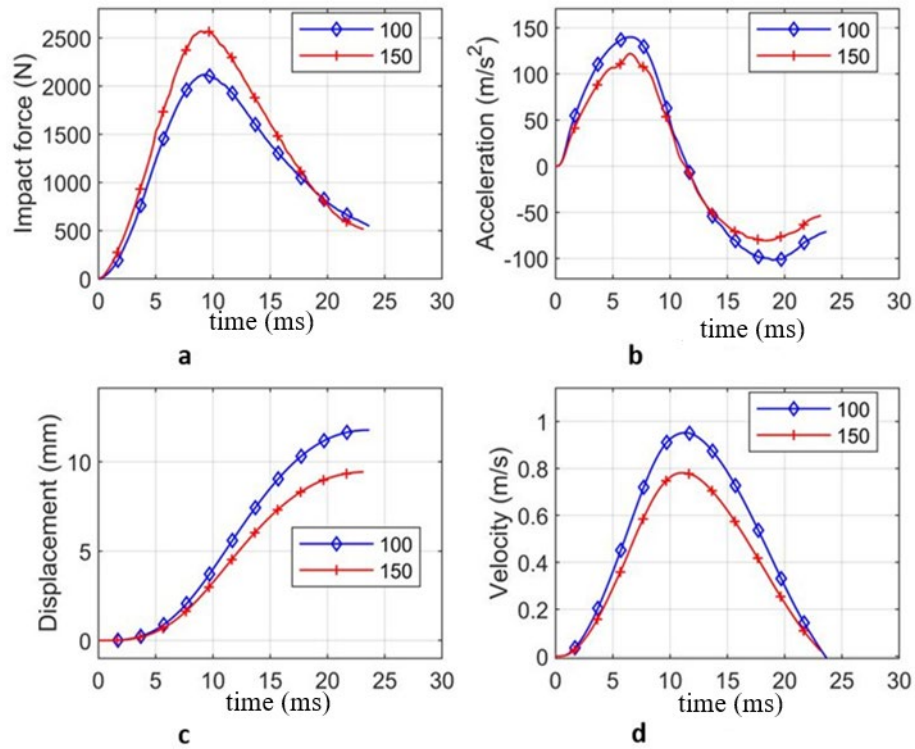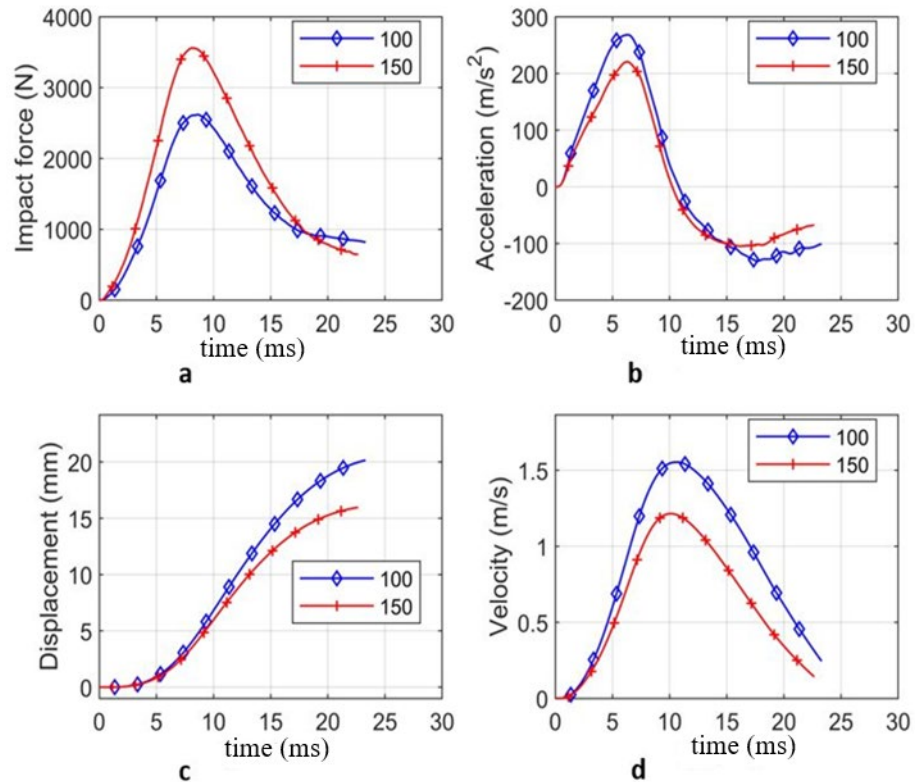

Figure 9. Dynamic test results for SsoPM10H50 model: (a) and (c) impact force-time history with displacements, (b) acceleration time history, (d) velocity time-history.

3.1. *Impacts and Displacements Reactions*

The reaction is related to displacements of the soil surface layer under vertical impacts of energies (measured under the impact plate's middle under surface depth only); these reactions were represented in the bottom section of component (c) of Fig. 6–9. The following are examples of common effects features:

- The highest impacting loading and highest displacements for soft clay occurred only when the impacts plate is placed at the soil surface of the foundations' area (100 mm) and the impactor plate (10 kg) is elevated to a height of 500 mm as seen in Fig. 9.

- It is not possible to predict the highest impact load and highest displacements of soft clay soil according to the modeling data results compared with different soil models. To indicate the excess pore water pressure-time histories gathered by pore water pressure sensors located at levels B and 2B below the middle of the testing bearing surface, two piezometers were placed under the plates to measure the pore water pressure through impact.

The following behavior is shown by a soil-foundations system:

- According to design models, it was observed that the resultant impulse waves have a smaller value in all cases under investigation when the water content of soft clay soil is reduced.

- The maximum displacement responses in the case of the soil model as shown in Fig. 9, have always been found to be greater as the kinetic energy of the dropping hammer increased (mass and level of fall). When either the mass of the hammering or the height of the fall is increased by a factor of doubled (from 5 to 10 kg or from 250 to 500 mm, respectively).

- As a result of a reduction in the water content ratio and a rise in the density of clay particles, as indicated by the soil model, it has been shown that the excess pore water pressure of the soft clay model has measurable complete effect.

- The vertical displacements of the footing block caused by the initial hammer blows were computed using the fatigue damage model proposed in this research and compared with the analytical results [18–21]. It can be shown that the simulation findings for vertical displacement are in good arrangement with the analytical results.

- When comparing the amplitude of displacement for saturated sand with time as a test result for the investigated outcome [22], it can be seen that each test's findings have a different character in the relationship between displacement and time. Concerning the test conditions and reaction of the dynamic behavior of the soil, it seemed that high measurement values at the beginning and end of the test for a low amplitude load. Thus, when a low load amplitude was applied, a large displacement magnitude was detected and remained constant for a lengthy period of testing before the load was released, at which point there was a noticeable decrease in the magnitude of displacement. Therefore, it is clear that the displacement values change over time as the amplitude of the load increases. It follows that a high loading percentage would also have a high displacement and settling value.

- As the soil required time to regain its resistance, the displacement may be higher or lesser than the prior displacement if the loading rate is not uniform [23-25].

Two piezometers were put under experimental bearing plates to monitor the pore water pressure during the impacts. Fig. 10–16 represent the excess pore water pressure-time histories recorded by pore water pressure sensors positioned at levels B and 2B underneath the bearing plate's center. A soil-foundations system displays the following behavior:

- For the soft clay state, based on increasing the water content, it was determined that the resultant impulse waves have a higher peak when increasing the mass energies.

- The peak displacement reactions inside soft clay soil having risen in reactions were seen to be higher when the falling hammer's kinetic energy increased (mass and level of fall). When either the mass of the hammer or the elevation of the fall is doubled (from 5 to 10 kg or from 250 to 500 mm, respectively).

- The vertical displacements for the largest plates (150 mm) are decreasing by 60 % at the depth of the topsoil surface.

- The excess pore water pressure inside the topsoil is shown as a result of three important parameters: impact energy (hammer weight and elevation of drop), size of foundations exposed to the impactor, and soil type. For soft clay soils with constant impact energy, increasing the impact area causes the excess pore water pressure to decrease. In that instance, a 125 % increase in the plate area (from 100 to 150 mm in diameter) causes a 30–40 % drop in the pore water pressure.

Figure 10. Pressure-time history of excess pore water at depth B for the SsoP100M5H25 model.

Figure 11. Pressure-time history of excess pore water at depth B for the SsoP100M5H50 model.

Figure 12. Pressure-time history of excess pore water at depth B for the SsoP100M10H25 model.

Figure 13. Pressure-time history of excess pore water at depth B for the SsoP100M10H50 model.

Figure 14. Pressure-time history of excess pore water at depth B for the SsoP150M5H50 model.
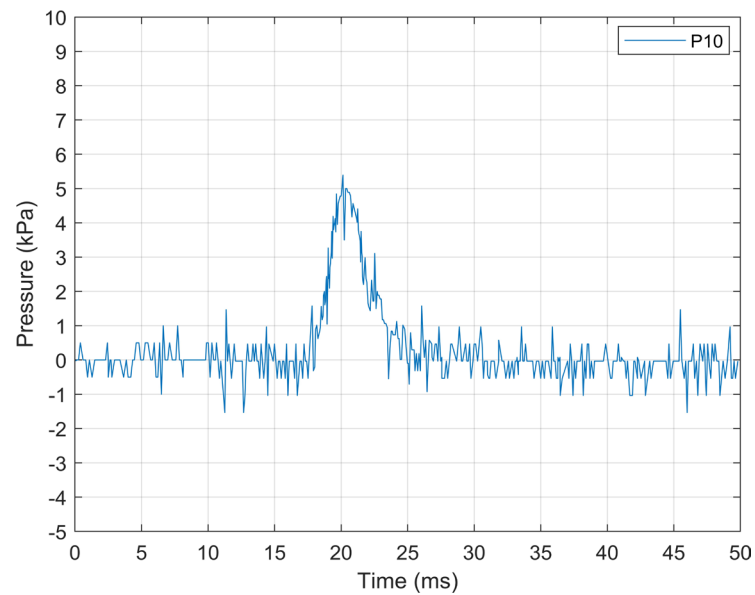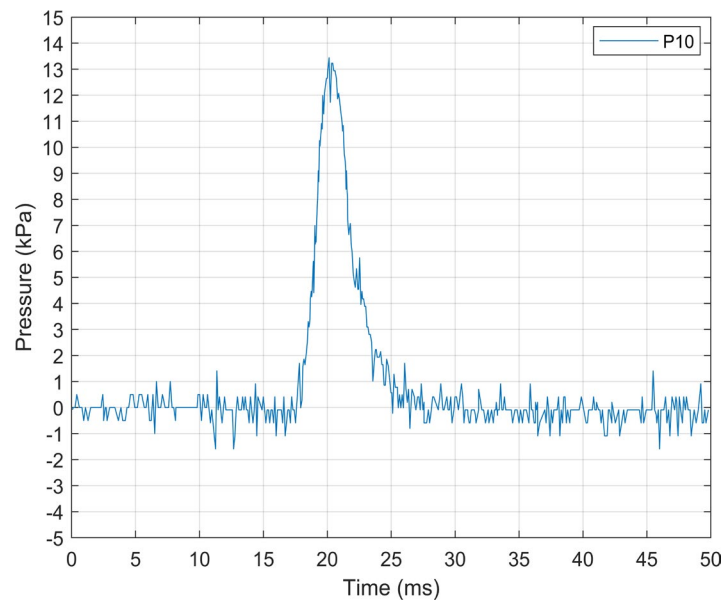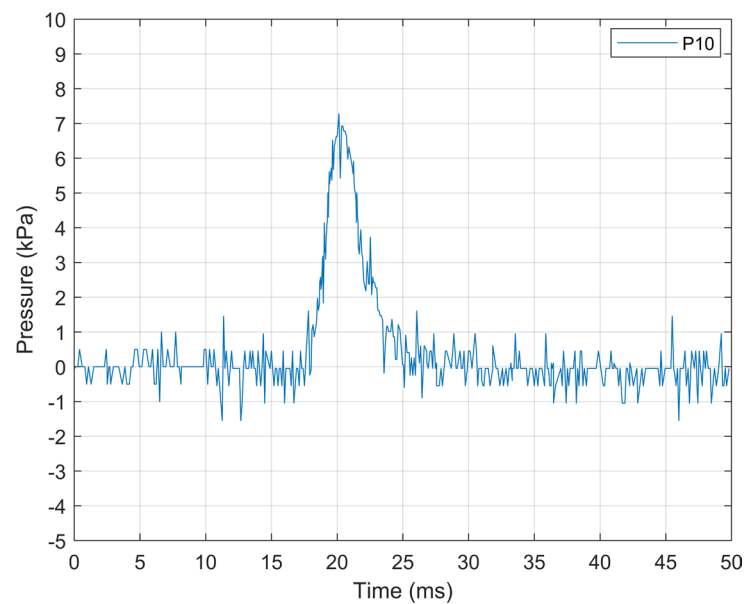

Figure 15. Pressure-time history of excess pore water at depth B for the SsoP150M10H25 model.
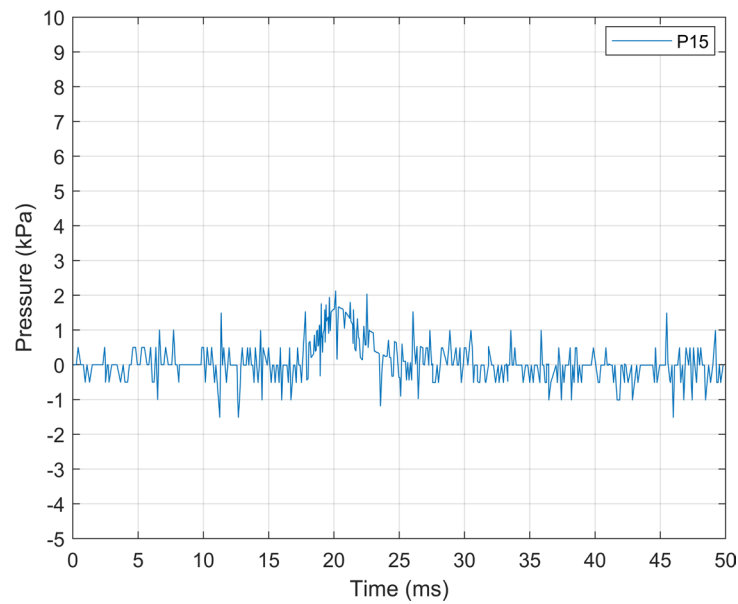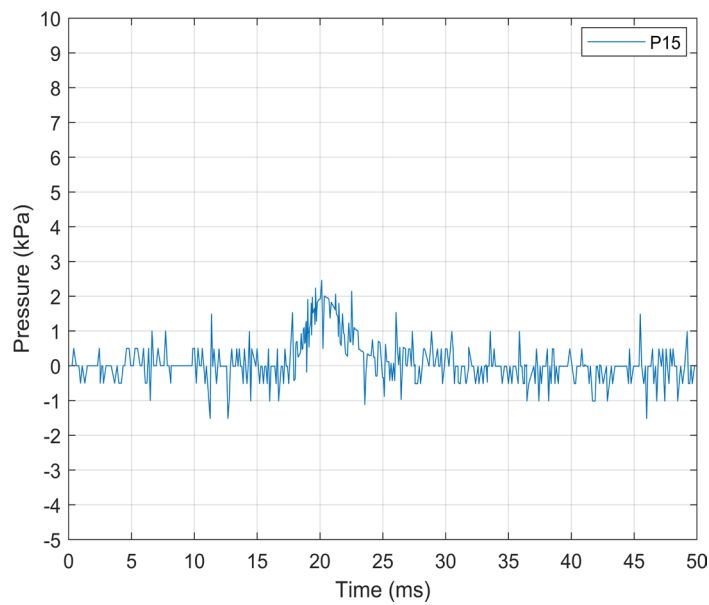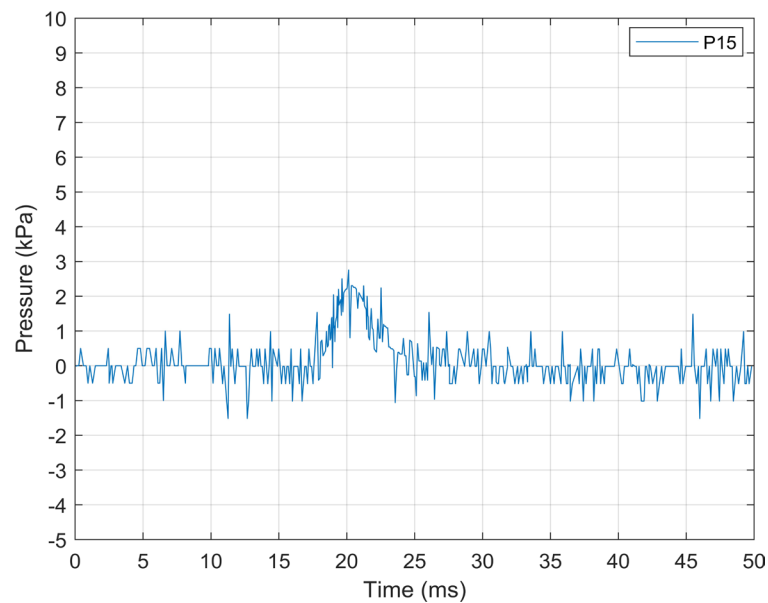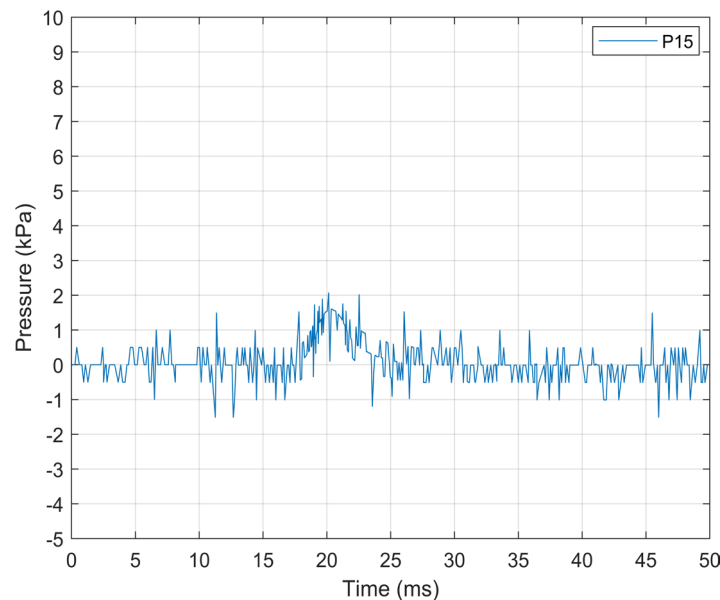
Figure 16. Pressure-time history of excess pore water at depth B for the SsoP150M10H50 model.

4. Conclusions

- The average percentage change in maximum impact forces generated in the contact surface increased by 33 % under the same impact loads (5 Kg) for both dropping heights (250 and 500 mm), which led to a reduction of 25 % in the maximum displacement reaction of the soft clay soil model.

- The amplitude of the force-time history in soft clay is reduced by 40–57 %. This reduction happens since the voids are filled with water, causing fewer contact points between particles.

- The amplitude of the force-time history for soil under impact stress is a single pulse.

- Once the operation frequency increases, the amplitude of displacements on the foundations, total stress, and pore water pressure increased for soft clay shallow foundations at the soil's surface.

- The maximum displacements increased with increasing operational frequency and dynamic loads.

- The dynamic response increases rapidly with the degree of damage, which in turn affects the transmission of damage in the foundation and the soil due to the higher stresses concentrating near the foundation regions. From the computational analysis of the dynamic features of soil damage, it can be observed that as damage rises, the effects of hammer blows on the surface and depth of the soil near the foundation become more important. This enables the development of a method for managing the damage and its progression in a damaged material, as well as the dynamic response of a damaged structure.

Following these conclusions, it is advised that pile foundations in saturated clay soils be used in future works with the same standard specifications. In addition to the possibility of studying the behavior of the plane runways-bearing soil, which is constantly exposed to impact loads at the moment the plane touches the ground.

References

1. Gazetas, G. Analysis of machine foundation vibrations: state of the art. International Journal of Soil Dynamics and Earthquake Engineering. 1983. 2(1). Pp. 2–42. DOI: 10.1016/0261-7277(83)90025-6

2. Abdulrasool, A.S., Fattah, M.Y., Salim, N.M. Experimental investigation for dynamic response of saturated clay under machine foundation. Modern Applications of Geotechnical Engineering and Construction. 2021. Pp. 365–374. DOI: 10.1007/978-981-15-9399-4_30

3. Pandya, S., Sachan, A. Experimental studies on the effect of load repetition on dynamic characteristics of saturated Ahmedabad cohesive soil. International Journal of Civil Engineering. 2019. 17(6). Pp. 781–792. DOI: 10.1007/s40999-019-00392-8

4. Pitilakis, D., Dietz, M., Wood, D.M., Chouteau, D., Modaressi, A. Numerical simulation of dynamic soil-structure interaction in shaking table testing. Soil dynamics and Earthquake Engineering. 2008. 28(6). Pp. 453–467. DOI: 10.1016/j.soildyn.2007.07.011

5. Chehab, A.G., El Naggar, M.H. Response of block foundations to impact loads. Journal of Sound and Vibration. 2004. 276(1-2). Pp. 293–310. DOI: 10.1016/j.jsv.2003.07.028

6. Jayawardana, P., Achuhan, R., De Silva, G.S., Thambiratnam, D.P. Use of in-filled trenches to screen ground vibration due to impact pile driving: experimental and numerical study. Heliyon. 2018. 4(8). e00726. DOI: 10.1016/j.heliyon.2018.e00726

7. Costa, P.A., Calçada, R., Cardoso, A.S. Track–ground vibrations induced by railway traffic: In-situ measurements and validation of a 2.5 D FEM-BEM model. Soil Dynamics and Earthquake Engineering. 2012. 32(1). Pp. 111–128. DOI: 10.1016/j.soildyn.2011.09.002

8. Al-Homoud, A.S., Al-Maaitah, O.N. An experimental investigation of vertical vibration of model footings on sand. Soil Dynamics and Earthquake Engineering. 1996. 15(7). Pp. 431–445. DOI: 10.1016/0267-7261(96)00023-1

9. Liu, S., Li, P., Zhang, W., Lu, Z. Experimental study and numerical simulation on dynamic soil-structure interaction under earthquake excitations. Soil Dynamics and Earthquake Engineering. 2020. 138. 106333. DOI: 10.1016/j.soildyn.2020.106333

10. Luo, C., Yang, X., Zhan, C., Jin, X., Ding, Z. Nonlinear 3D finite element analysis of soil–pile–structure interaction system subjected to horizontal earthquake excitation. Soil Dynamics and Earthquake Engineering. 2016. 84. Pp. 145–156. DOI: 10.1016/j.soildyn.2016.02.005

11. Crockett, J.H., Hammond, R.E. The dynamic principles of machine foundations and ground. Proceedings of the Institution of Mechanical Engineers. 1949. 160(1). Pp. 512–531. DOI: 10.1243/pime_proc_1949_160_048

12. Mohammed, Q.S. Dynamic Behavior of Machine Foundations on layered sandy soil under Seismic Loadings. Journal of Engineering. 2022. 28(8). Pp. 1–20. DOI: 10.31026/j.eng.2022.08.01

13. Al-Azawi, T.K., Al-Azawi, R.K., Al-Jaberi, Z.K. Stiffness and damping properties of embedded machine foundations. Journal of Engineering. 2006. 12(2). DOI: 10.31026/j.eng.2006.02.19

14. Al-Mosawi, M.J., Fattah, M.Y., Al-Ameri, A.F. Effect of saturation of sandy soil on the displacement amplitude of soil foundation system under vibration. Journal of Engineering. 2015. 21(2). Pp. 20–36. DOI: 10.31026/j.eng.2015.02.02

15. Abbas, H.Q., Al-Zuhairi, A.H. Flexural Strengthening of Prestressed Girders with Partially Damaged Strands Using Enhancement of Carbon Fiber Laminates by End Sheet Anchorages. Engineering, Technology & Applied Science Research. 2022. 12(4). Pp. 8884–8890. DOI: 10.48084/etasr.5007

16. Mandal, A., Baidya, D.K., Roy, D. Dynamic response of the foundations resting on a two-layered soil underlain by a rigid layer. Geotechnical and Geological Engineering. 2012. 30(4). Pp. 775–786. DOI: 10.1007/s10706-012-9497-2

17. Xue, X., Ren, T., Zhang, W. Analysis of fatigue damage character of soils under impact load. Journal of Vibration and Control. 2013. 19(11). Pp. 1728–1737. DOI: 10.1177/1077546312450732

18. Gupta, C.P., Visvanathan R. Dynamic behavior of saturated soil under impact loading. Transactions of the ASAE. 1993. 36(4). Pp. 1001–1007. DOI: 10.13031/2013.28427

19. Dobry, R. Dynamic properties and seismic response of soft clay deposits. Proc. of the Int. Symp. on Geotech. Engrg. of Soft Soils. 1987. 2. Pp. 51–86.

20. Chehab, A.G., El Naggar, M.H. Response of block foundations to impact loads. Journal of Sound and Vibration. 2004. 276(1-2). Pp. 293–310. DOI: 10.1016/j.jsv.2003.07.028

21. Karim, H.H., Samueel, Z.W., Hussein, M.A. Investigation of the behavior of shallow machine foundations resting on saturated layered sandy soil subjected to a dynamic load. IOP Conference Series: Materials Science and Engineering. 2020. 888(1). 012055. DOI: 10.1088/1757-899X/888/1/012055

22. Ali, A.F., Fattah, M.Y., Ahmed, B.A. The behavior of the Dry Dense Sand-Foundation System Acted upon by Impact Loads. 2016. 6(4). Pp. 86–103. DOI: 10.5923/j.jce.20160604.02

23. Ahmed, B.A., Rasheed, A.H. Experimental Analysis of the Dynamic Response of Saturated Clayey Soil Under Impact Loading. Engineering, Technology & Applied Science Research. 2022. 12(6). Pp. 9787–9794. DOI: 10.48084/etasr.5388

24. Rasheed, A.H., Ahmed, B.A. Dynamic monitoring of saturated stiff clay soil foundation structure by falling weight deflectometer system under impact loads sensors effect. Measurement: Sensors. 2023. 100673.

25. Karkush, M.O., Kareem, M.A. Behavior of pile foundation subjected to lateral cyclic loading in contaminated soils. Journal of Civil Engineering Research. 2015. 5(6). Pp. 144–150. DOI: 10.5923/j.jce.20150506.03

Information about the authors:

Azad Hameed Rasheed, *PhD*
ORCID: https://orcid.org/0000-0002-6196-1759
E-mail: azad.hameed@muc.edu.iq

Balqees Abdulwahid Ahmed, *PhD*
E-mail: Balqees.a@coeng.uobaghdad.edu.iq

Tuned mass damper for reduction seismic and wind loads

D.E. Bondarev ✉ (iD)

CKTI-Vibroseism Ltd., St Petersburg, Russian Federation

✉ *89523684328@mail.ru*

Abstract. Tuned mass dampers (TMDs) are used mainly for reduction of seismic and wind oscillations in high-rise buildings. It is well known that base isolation is ineffective in tall buildings. In general, TMDs can reduce seismic loads in tall building, but it needs a large mass of TMDs. In addition, TMDs cannot reduce vertical oscillations, which can be very destructive due to P-delta effect. This paper presents an engineering solution for mitigation of structural response caused by seismic excitations. The approach of using the upper part of the building as a TMD can significantly reduce horizontal accelerations and stresses in building elements up to 50 % along the entire height. In addition, the proposed TMD can significantly reduce vertical oscillations in a primary building up to 30 % in comparison with building without TMD. This solution can be used in both existing and new buildings. This solution does not require any additional mass and its transportation to the installation site. An optimization criterion for defining optimal TMD's properties was developed. The criterion is the objective function of maximum difference in accelerations of floors with and without TMD along the entire height. For analytical studies, matrix of stiffness that takes into account bending and sliding motions and dissipation matrix that takes into account damping ratio for soil, TMD constructions and constructions of the building were developed.

1. Introduction

Tuned mass damper (TMD) is a device for reduction of seismic and wind responses of buildings and structures. The first mention of the use of this technology, as far as we know, appeared in 1909 when H. Frahm received a patent for "Device for damping vibrations of bodies" [1]. This device is used in structures to prevent discomfort, damage, or structural failure caused by dynamic excitations. Vibration control of structures can be divided into four groups: active, semi-active, hybrid, and passive systems [2]. It is possible to use several types of vibration control systems in one building [3]. TMD is a passive control device that does not require any external sources of energy. There are many types of TMDs: friction TMD [4], conventional TMD [5], pendulum TMD [6], bidirectional [7], tuned liquid column damper (TLCD) [8], etc. TMDs are widely used in tall structures [9], chimneys [10], long span transmission tower-line systems [11], high-rise buildings [12, 13], flexible bridges [14], etc. Usually, TMDs are installed at the upper floors of high-rise building, under bridge's spans and/or at bridge pylons, etc.

In general, TMD consists of a mass, a spring, and a damper. A two-degree-of-freedom (-DOF) system is shown in Fig. 1 and 2 for seismic and wind excitations respectively.
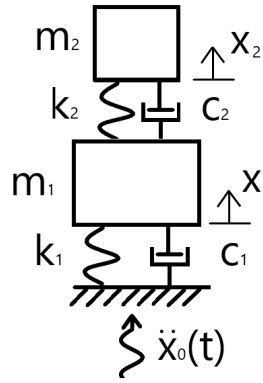
Figure 1. A two-DOF damped system subjected to seismic excitation.

Applying Newton's second law to the main mass m_1 gives:

$$m_1\ddot{x}_1 + c_1\dot{x}_1 + k_1 x_1 + c_2\left(\dot{x}_1 - \dot{x}_2\right) + k_2\left(x_1 - x_2\right) = -m_1\ddot{x}_0. \tag{1}$$

Applying Newton's second law to the mass of a TMD m_2 gives:

$$m_2\ddot{x}_2 + c_2\left(\dot{x}_2 - \dot{x}_1\right) + k_2\left(x_2 - x_1\right) = -m_2\ddot{x}_0. \tag{2}$$

Transforming these equations, we receive a system of differential equations of the second order:

$$\begin{cases} \ddot{x}_1 = -\ddot{x}_0 - \dfrac{k_1}{m_1}x_1 - \gamma^2\mu\omega_1^2\left(x_1 - x_2\right) - 2\xi_2\omega_1\gamma\mu\left(\dot{x}_1 - \dot{x}_2\right) - 2\xi_1\omega_1\dot{x}_1 \\ \ddot{x}_2 = -\ddot{x}_0 - \omega_2^2\left(x_2 - x_1\right) - 2\xi_2\omega_1\gamma\left(\dot{x}_2 - \dot{x}_1\right) \end{cases}, \tag{3}$$

where m_1, k_1, c_1 are the mass, stiffness, and damping of a primary structure; m_2, k_2, c_2 are the mass, stiffness, and damping of a TMD's construction, $\ddot{x}_0$ is time history acceleration of seismic excitation. x_1, x_2, $\dot{x}_1$, $\dot{x}_2$, $\ddot{x}_1$, $\ddot{x}_2$ are displacements, velocities, and accelerations of structure and the TMD; μ represents the ratio of the TMD mass $\left(m_2\right)$ to structural mass $\left(m_1\right)$. ξ_1, ξ_2 are the damping ratios of the structure and the TMD; γ is the ratio of the frequency of the TMD $\left(\omega_2\right)$ to the frequency of the structure $\left(\omega_1\right)$.
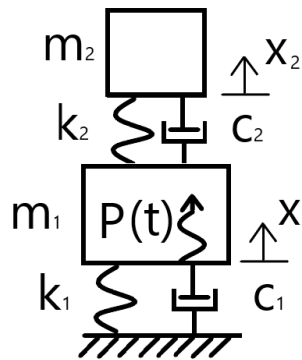
Figure 2. A two-DOF damped system subjected to wind excitation.

For the system subjected to wind excitation where $P(t)$ is a time-dependent external force:

$$\begin{cases} \ddot{x}_1 = \dfrac{P(t)}{m_1} - \dfrac{k_1}{m_1}x_1 - \gamma^2\mu\omega_1^2\left(x_1 - x_2\right) - 2\xi_2\omega_1\gamma\mu\left(\dot{x}_1 - \dot{x}_2\right) - 2\xi_1\omega_1\dot{x}_1 \\ \ddot{x}_2 = -\omega_2^2\left(x_2 - x_1\right) - 2\xi_2\omega_1\gamma\left(\dot{x}_2 - \dot{x}_1\right) \end{cases}. \tag{4}$$

These equations of motion undergoing seismic and wind excitations have an analytical solution if an external force (seismic or wind load) is roughly expressed by harmonic loading. For wind excitation, it is a sinusoidal time-dependent pressure of wind and, in turn, for seismic excitation – a sinusoidal displacement of soil motion [15].

In addition, these equations can be solved by numerical integration method. For instance, it can be solved by Runge–Kutta method where right parts in (3) and (4) are vectors of the first and the second derivatives in an explicit form and, in addition, it is necessary to use a vector of initial conditions, such as velocity and displacement in the beginning of the motion. Using numerical solution of differential equations, it is possible to take into account all frequencies of the external force expressed with accelerograms and wind pressure time histories.

It is well known that there are simple equations to define the optimum damping ratio and frequency (ξ_2, Hz) of a TMD. For minimum structural displacement amplitude, the formulae were given by Den Hartog [16]:

$$f_2 = \frac{f_1}{1+\mu};\tag{5}$$

$$\xi_2 = \sqrt{\frac{3\mu}{8(1+\mu)^3}}.\tag{6}$$

If the acceleration amplitude of the structure is to be minimized:

$$f_2 = \frac{f_1}{\sqrt{1+\mu}};\tag{7}$$

$$\xi_2 = \sqrt{\frac{3\mu}{4(2+\mu)(1+\mu)}}.\tag{8}$$

There are many other criteria of optimization: maximum dynamic stiffness of the main structure [17], maximum effective damping of combined structure [18], minimum travel of damper mass relative to the main structure [18], minimum force in the main structure [19], minimum velocity of the main structure [19] etc. [15, 20, 21].

The equations (3) and (4) are very simply used to demonstrate the basic principles of TMD operation, but they cannot be used in actual engineering practice because real civil engineering structures cannot be considered as single-DOF systems. External excitation does not have the only frequency and structures may undergo nonlinear deformations. In addition, it is necessary to consider the stiffness of soil in equations of motions, if a structure is located at a soft soil.

In general, TMD shall be tuned close to a dominant response frequency of the structure. TMD usually requires an essential mass related to a mass of a primary structure and a large space for its installation at high elevations. Usually ratio μ of a mass of TMD's construction and a mass of a primary construction of building ranges between 0.02 and 0.08 [22] for buildings subjected to seismic excitations and 0.0005 and 0.02 [23] for buildings subjected to wind excitations to achieve demanded TMD efficiency.

TMDs are rather complex and expensive devices that are limited in mass and damping with levels far away from optimal parameters and usually are tuned to only one dominant frequency of the structure providing protection from wind loads only and being ineffective in case of seismic excitation. Inefficiency of the TMD in case of seismic excitation makes researchers find other technological and engineering solutions. It is necessary to search other criterion of optimization for increasing efficiency of the TMD system.

TMD approach described in this paper allows significantly improve TMD efficiency against seismic excitation and create a three-dimensional TMD system with optimal mass, stiffness and damping parameters for structures' protection, while significantly reducing the cost of TMD itself.

2. Methods

2.1. The Motion Equation of a Multi-Degree-Of-Freedom System of Shear-Wall Building with the TMD

The motion equation of a multi-DOF system for the high-rise building subjected to a seismic excitation can be written as follows:

$$[M]\ddot{u} + [C]\dot{u} + [K]u = -[M]\left(\{I_x\}\ddot{x}_0 + \{I_y\}\ddot{y}_0 + \{I_z\}\ddot{z}_0\right), \tag{9}$$

where $[M]$, $[C]$ and $[K]$ represent the mass, damping, and stiffness matrices, respectively. u, $\dot{u}$, $\ddot{u}$ are the relative displacement, velocity, acceleration vectors with respect to the base. $\{I_x\}$, $\{I_y\}$, $\{I_z\}$ are the vectors, which consist of cosines between vector of displacements and vector of excitation. $\ddot{x}_0$, $\ddot{y}_0$, $\ddot{z}_0$ are time history acceleration of a seismic excitation in X, Y, Z directions.

Considering only shear stiffness of the floors and X-direction of seismic excitation, we may use the following equation:

$$[M]\ddot{x} + [C]\dot{x} + [K]x = -[M]\left(\{I_x\}\ddot{x}_0\right). \tag{10}$$

Multi-DOF system with TMD is shown in Fig. 3:

Figure 3. Multi-DOF system of shear-wall building subjected to a seismic excitation in X-direction with TMD located on the top floor.

Stiffness matrix can be written as follows [24]:

$$[K] =$$

$$= \begin{bmatrix}
K_x + K_{1-2} & -K_{1-2} & 0 & \ldots & 0 & K_{1-2}h_1 \\
-K_{1-2} & K_{1-2}+K_{2-3} & -K_{2-3} & 0\ldots & 0 & \left(K_{2-3}h_2 - K_{1-2}h_1\right) \\
0 & -K_{2-3} & \ddots & -K_{n-1-n} & 0\ldots0 & \vdots \\
\vdots & \vdots & -K_{n-1-n} & K_{n-1-n}+K_{TMD} & -K_{TMD} & \left(K_{TMD}h_{TMD}-K_{n-1-n}h_n\right) \\
0 & 0 & 0 & -K_{TMD} & K_{TMD} & -K_{TMD}h_{TMD} \\
K_{1-2}h_1 & \left(K_{2-3}h_2-K_{1-2}h_1\right) & \ldots & \left(K_{TMD}h_{TMD}-K_{n-1-n}h_n\right) & -K_{TMD}h_{TMD} & \sum_{i=1}^{n}\left(K_{i,i+1}h_i^2+K_\varphi\right)
\end{bmatrix} \tag{11}$$

Mass matrix [24]:

$$[M] = \begin{bmatrix}
m_1 & 0 & \ldots & 0 \\
0 & \ddots & 0 & \vdots \\
\vdots & 0 & m_n & 0 \\
0 & \ldots & 0 & I
\end{bmatrix}; \quad I = I_c + \sum_{i=1}^{n} m_i h_i^2, \tag{12}$$

where I_c is a moment of inertia of the construction relative to horizontal axes passing through the center of gravity (CG); h_i is dimension between i-floor and CG; K_x, K_φ are translational and rocking stiffnesses of soil; K_{i-i+1} is shear stiffness of the floor; K_{TMD} is stiffness of the TMD.
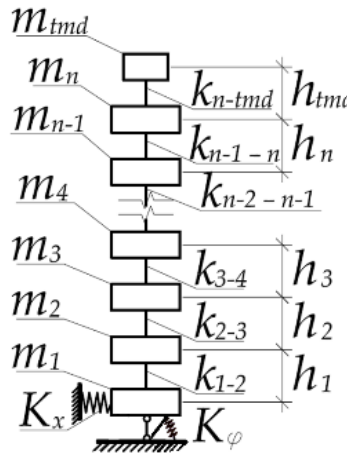
Vector $\{I_x\}$ will be:

$$\{I_x\}^T = \{1 \ldots 1 \, 0\}. \tag{13}$$
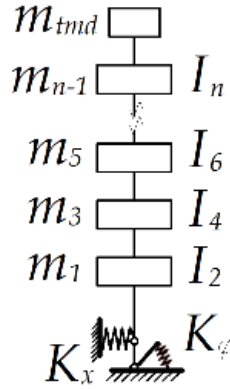
Figure 4. Multi-DOF system of building subjected to a seismic excitation in X-direction with TMD located on the top floor.

Model in Fig. 3 can be used only in case of shear-wall buildings. It is necessary to develop stiffness matrix for considering shear and bending stiffnesses of a building.

2.2.   Multi-DOF System for Building with TMD. Shear and Bending Stiffnesses

In general, to consider shear and bending stiffnesses of floors (Table 1), stiffness matrix can be written as follows (Fig.4):

$$[K] =$$

$$
= \begin{bmatrix}
A\dfrac{12i}{l^2}+\dfrac{12i}{l^2} & \dfrac{6i}{l}-B\dfrac{6i}{l} & -\dfrac{12i}{l^2} & \dfrac{6i}{l} & 0 & 0 & 0 & \cdots & 0 \\[2.5ex]
\dfrac{6i}{l}-B\dfrac{6i}{l} & C4i+4i & -\dfrac{6i}{l} & 2i & 0 & 0 & 0 & \cdots & 0 \\[2.5ex]
-\dfrac{12i}{l^2} & -\dfrac{6i}{l} & \dfrac{12i}{l^2}+\dfrac{12i}{l^2} & 0 & -\dfrac{12i}{l^2} & \dfrac{6i}{l} & 0 & \cdots & 0 \\[2.5ex]
\dfrac{6i}{l} & 2i & 0 & 4i+4i & -\dfrac{6i}{l} & 2i & 0 & \cdots & \vdots \\[2.5ex]
0 & 0 & -\dfrac{12i}{l^2} & -\dfrac{6i}{l} & \dfrac{12i}{l^2}+\dfrac{12i}{l^2} & 0 & \ddots & \dfrac{6i}{l} & 0 \\[2.5ex]
0 & 0 & \dfrac{6i}{l} & 2i & 0 & \ddots & -\dfrac{6i}{l} & 2i & 0 \\[2.5ex]
\vdots & \vdots & 0 & 0 & \ddots & -\dfrac{6i}{l} & \dfrac{12i}{l^2}+K_{TMD} & -\dfrac{6i}{l} & -K_{TMD} \\[2.5ex]
0 & 0 & \vdots & \vdots & \dfrac{6i}{l} & 2i & -\dfrac{6i}{l} & 4i & 0 \\[2.5ex]
0 & 0 & 0 & 0\cdots & 0 & 0 & -K_{TMD} & 0 & K_{TMD}
\end{bmatrix} \tag{14}
$$

where

$$A = \frac{l^2 K_x \left(K_\varphi + i \right)}{l^2 K_x \left(K_\varphi + 4i \right) + 12i \left(K_\varphi + i \right)}; \qquad B = \frac{l^2 K_x \left(K_\varphi + 2i \right)}{l^2 K_x \left(K_\varphi + 4i \right) + 12i \left(K_\varphi + i \right)};$$

$$C = \frac{3i \left(K_\varphi + l^2 K_x \right) + l^2 K_x K_\varphi}{l^2 K_x \left(K_\varphi + 4i \right) + 12i \left(K_\varphi + i \right)}; \quad i = \frac{EI}{l}; \quad l \text{ is the height of the floor; } EI \text{ is bending stiffness of the}$$

floor.

Mass matrix can be written as follows:

$$[M] = \begin{bmatrix} m_1 & 0 & \ldots & \ldots & \ldots & \ldots & \ldots & 0 \\ 0 & I_2 & 0 & \ldots & \ldots & \ldots & \ldots & 0 \\ \vdots & 0 & m_3 & 0 & \ldots & \ldots & \ldots & 0 \\ \vdots & \vdots & 0 & I_4 & 0 & \ldots & \ldots & 0 \\ \vdots & \vdots & \vdots & 0 & \ddots & 0 & \ldots & 0 \\ \vdots & \vdots & \vdots & \vdots & 0 & m_{n-1} & 0 & 0 \\ \vdots & \vdots & \vdots & \vdots & \vdots & 0 & I_n & 0 \\ 0 & 0 & 0 & 0 & 0 & 0 & 0 & m_{TMD} \end{bmatrix}; \quad I_i = \frac{m_i}{12} \left(l^2 + b^2 \right), \qquad (15)$$

where I_i is the moment of inertia of the floor; l is the height of the floor; b is the width of the building.

Vector $\{I_x\}$ will be:

$$\{I_x\}^T = \{1 \ 0 \ 1 \ 0 \ \cdots \ 1 \ 0 \ 1\}. \qquad (16)$$

Table 1. Equations for support reactions for beams supported by springs.

Beam subjected to single displacement	Equations for support reactions
	$M_A = \frac{3i}{l} \left[\frac{K_\varphi}{K_\varphi + 3i} \right]; R = \frac{3i}{l^2} \left[\frac{K_\varphi}{K_\varphi + 3i} \right]$
	$M_A = \frac{6i}{l} \left[\frac{K_\varphi}{K_\varphi + 4i} \right]; M_B = \frac{6i}{l} \left[\frac{K_\varphi + 2i}{K_\varphi + 4i} \right]$ $R = \frac{12i}{l^2} \left[\frac{K_\varphi + i}{K_\varphi + 4i} \right]$
	$M_A = 2i \left[\frac{K_\varphi}{K_\varphi + 4i} \right]; M_B = 4i \left[\frac{K_\varphi + 3i}{K_\varphi + 4i} \right]$ $R = \frac{6i}{l} \left[\frac{K_\varphi + 2i}{K_\varphi + 4i} \right]$
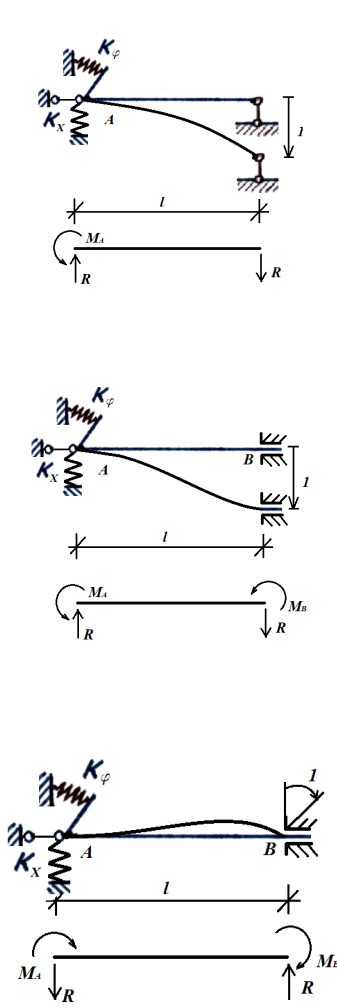
$$M_A = \frac{3i}{l}\left[\frac{lK_xK_\varphi}{lK_xK_\varphi + \frac{3i}{l}K_\varphi + 3liK_x}\right]$$

$$R = \frac{3i}{l^2}\left[\frac{lK_xK_\varphi}{lK_xK_\varphi + \frac{3i}{l}K_\varphi + 3liK_x}\right]$$

$$M_A = \frac{6i}{l}\left[\frac{l^2K_xK_\varphi}{l^2K_x(K_\varphi + 4i) + 12i(K_\varphi + i)}\right]$$

$$M_B = \frac{6i}{l}\left[\frac{l^2K_x(K_\varphi + 2i)}{l^2K_x(K_\varphi + 4i) + 12i(K_\varphi + i)}\right]$$

$$R = \frac{12i}{l^2}\left[\frac{l^2K_x(K_\varphi + i)}{l^2K_x(K_\varphi + 4i) + 12i(K_\varphi + i)}\right]$$

$$M_A = 2i\left[\frac{K_\varphi(l^2K_x - 6i)}{l^2K_x(K_\varphi + 4i) + 12i(K_\varphi + i)}\right]$$

$$M_B = 4i\left[\frac{3i(K_\varphi + l^2K_x) + l^2K_xK_\varphi}{l^2K_x(K_\varphi + 4i) + 12i(K_\varphi + i)}\right]$$

$$R = \frac{6i}{l}\left[\frac{l^2K_x(K_\varphi + 2i)}{l^2K_x(K_\varphi + 4i) + 12i(K_\varphi + i)}\right]$$

To use a superposition of modal responses we must have a diagonal damping matrix. We cannot use Rayleigh damping because our system (Fig. 4) consists of three parts with significantly different levels of damping: soil, TMD, and the rest part of the building. In general, the modal damping ratio for the soil system would be much different from the structure's one, for example 15 to 20 % for the soil conditions compared to 3 to 5 % for the structure [25] and 2 to 15 % for TMD (following (6)). This operation can be used:

$$[C] =$$

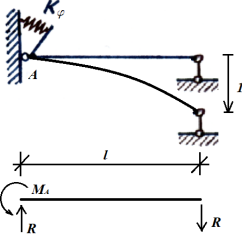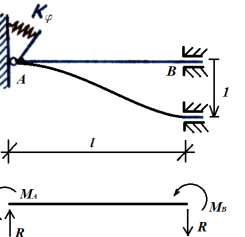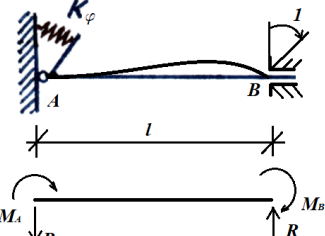$$= \begin{bmatrix} \xi_1\omega_1M_1 & 0 & \dots & \dots & \dots & \dots & \dots & 0 \\ 0 & \xi_2\omega_2M_2 & 0 & \dots & \dots & \dots & \dots & 0 \\ \vdots & 0 & \xi_3\omega_3M_3 & 0 & \dots & \dots & \dots & 0 \\ \vdots & \vdots & 0 & \xi_4\omega_4M_4 & 0 & \dots & \dots & 0 \\ \vdots & \vdots & \vdots & 0 & \ddots & 0 & \dots & 0 \\ \vdots & \vdots & \vdots & \vdots & 0 & \xi_{n-2}\omega_{n-2}M_{n-2} & 0 & 0 \\ \vdots & \vdots & \vdots & \vdots & \vdots & 0 & \xi_{n-1}\omega_{n-1}M_{n-1} & 0 \\ 0 & 0 & 0 & 0 & 0 & 0 & 0 & \xi_n\omega_nM_n \end{bmatrix} \quad (17)$$

where $\xi_1\dots\xi_n$ are damping ratios; $M_1\dots M_n$ are generalized modal masses; $\omega_1\dots\omega_n$ are modal frequencies.

If rocking motion of the building on soil and TMD motion have different modes, it is very simple to use damping ratio for each mode on its own according to the matrix above. Fig. 5 shows mode shapes. In case of using TMD for reduction of wind loads, it is necessary to use TMD tuned to the 1st frequency. In case of using TMD for reduction of seismic loads, it sometimes necessary to use TMD tuned to the 2nd

frequency. It depends on frequency composition of seismic excitation. If high frequencies prevail over low frequencies, it is necessary to tune TMD to the 2nd or (sometimes) to the 3rd eigenfrequency.
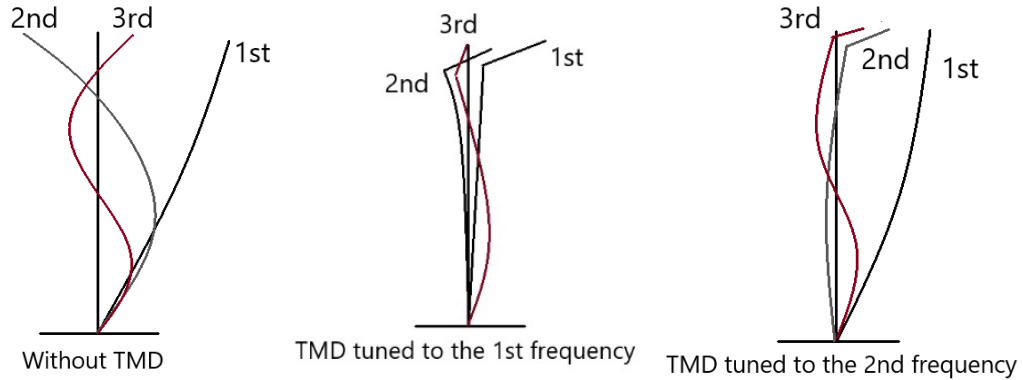
Figure 5. Mode shapes.

2.3.   The Target Building. Optimization Criterion

The target building of this study is a residential high-rise building. It is a 103-m-high reinforced concrete building. Building parameters are: L (length) = 36 m, B (width) = 20 m, N_{floors} (number of floors) = 33 (superstructure) and 2 (substructure), H_{floor} (height of the floor) = 3.1 m, M_{total} (total mass) = 45800 t, $M_{structure}$ (mass of structure) = 36650 t. The typical floor is shown in Fig. 6. Equivalent bending stiffness of a floor is: EI_y = 2123292340 $t \cdot m^2$, EI_x = 2550000000 $t \cdot m^2$, translational and rocking stiffnesses of soil: K_x = 1576390 $\dfrac{t}{m}$, K_φ = 517761250 $\dfrac{t}{m}$, ξ_{soil} = 0.15.
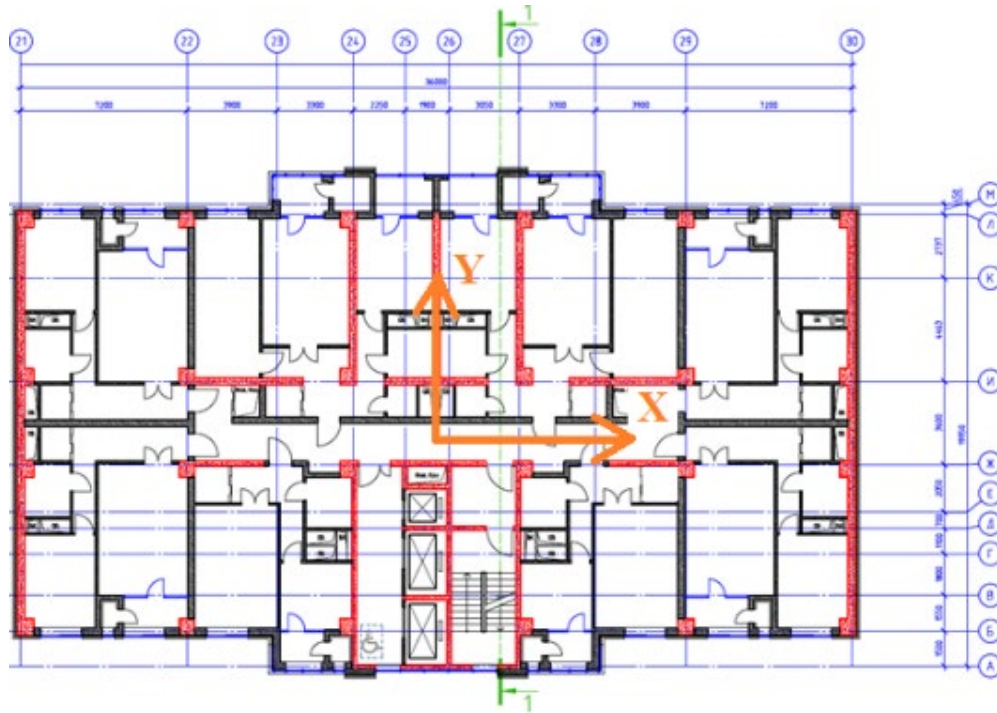
Figure 6. Typical floor plan.

Table 2. Eigenfrequencies of dynamically uncontrolled building without TMD.

Number	Circular frequency, rad/s	Frequency, Hz	Direction	Modal mass, %
1	1.99	0.32	Y	67.46
2	2.04	0.32	X	64.85
3	12.41	1.98	X	21.94
4	12.6	2.01	Y	21.08
5	32.22	5.13	X	9.01
6	33.63	5.35	Y	7.77
7	58.02	9.23	X	3.15
8	61.88	9.85	Y	2.7
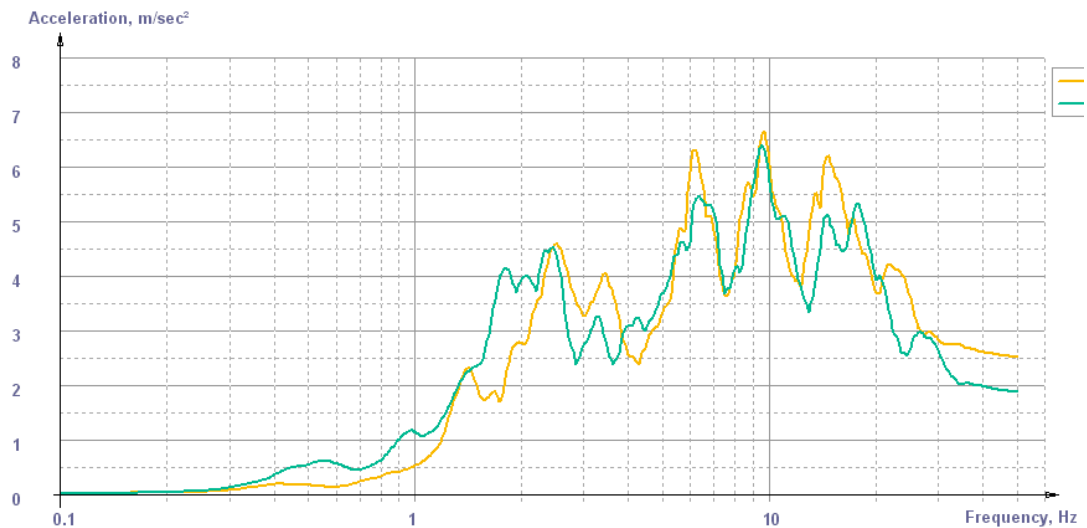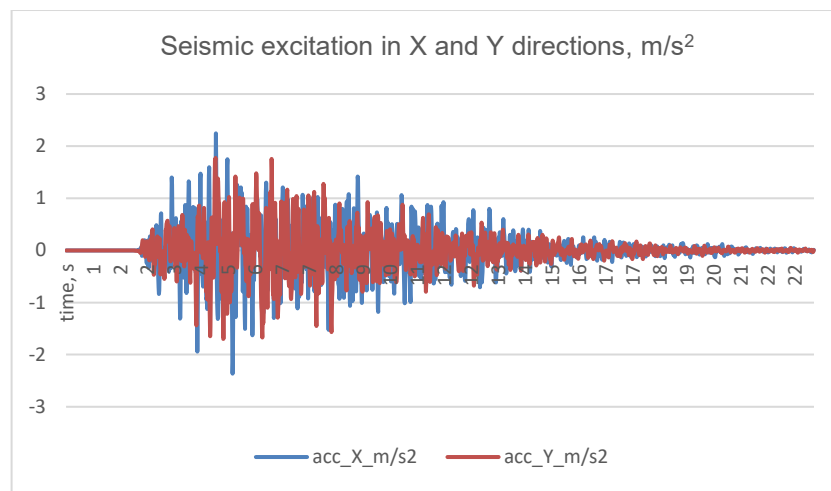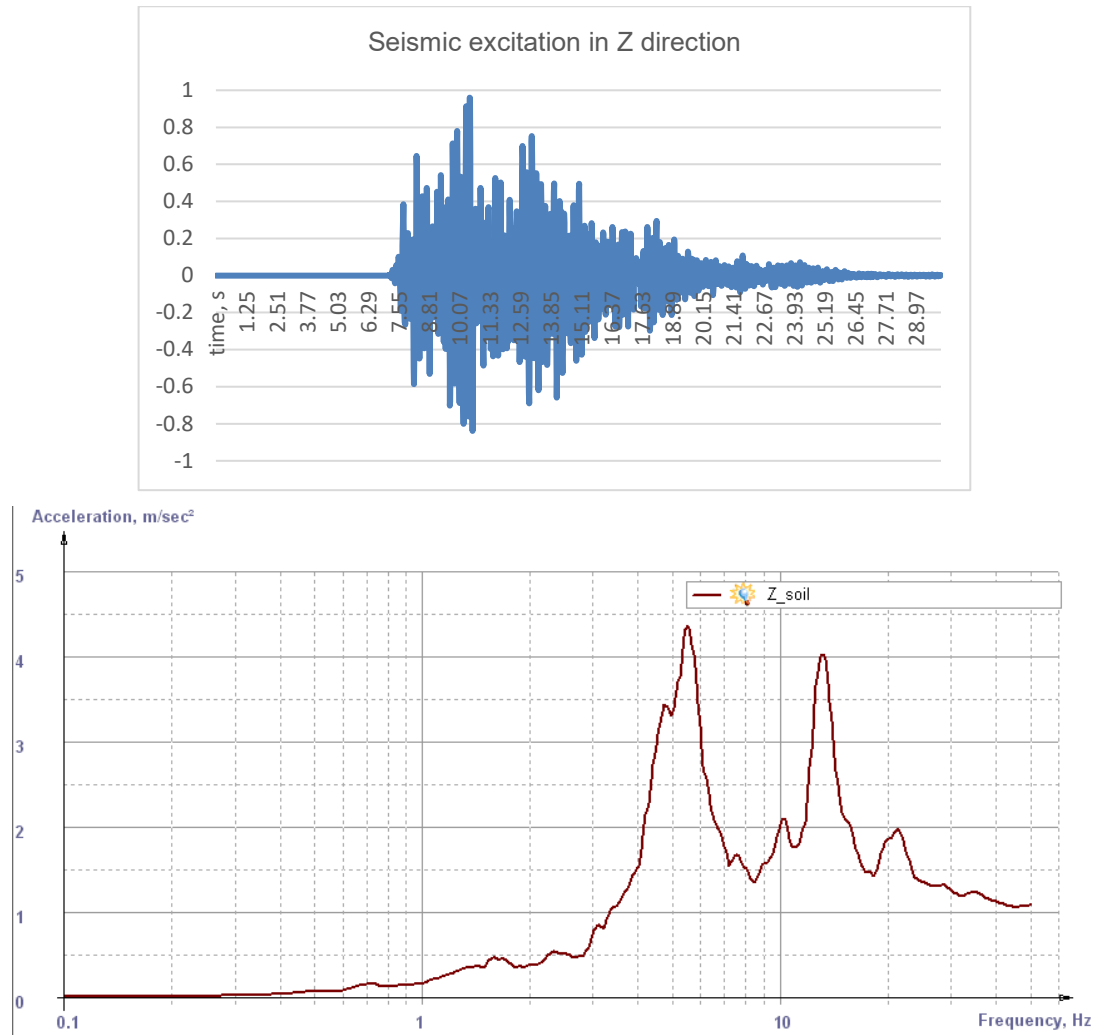
Figure 7. Accelerations on soil in X, Y, Z directions and response spectra (ξ=0.05).

In order to define stiffness, mass and damping ratio of the TMD, it is necessary to carry out optimization analysis. Criterion of optimization:

$$Cr = \max \sum_{i=1}^{n} \left(\max\left|A_i\right| - \max\left|A_i^{TMD}\right| \right), \qquad (18)$$

where n is the number of a floor (substructure); $\max\left|A_i\right|$ are maximum absolute accelerations of the nth floor for the dynamically uncontrolled building (without TMD); $\max\left|A_i^{TMD}\right|$ are maximum absolute accelerations of the nth floor for the dynamically controlled building (with TMD).

3. Results and Discussion

3.1. The Optimum Parameters of the TMD

The optimum parameters were defined by taking damping ratio of the TMD $\xi_{TMD} = 0.1$ (using (8)) for the first iteration of optimization, $M_{TMD} = 1050t$ $M_{TMD} = 1050\,t$ $(\mu = 2.3\%)$ and using the model which is shown in Fig. 4, and consistently varying horizontal stiffness of the TMD. The acceleration along the entire height of the building is shown in Fig. 8, 9. Accelerations of the 13th floor in X and Y direction and response spectra are shown in Fig.10.
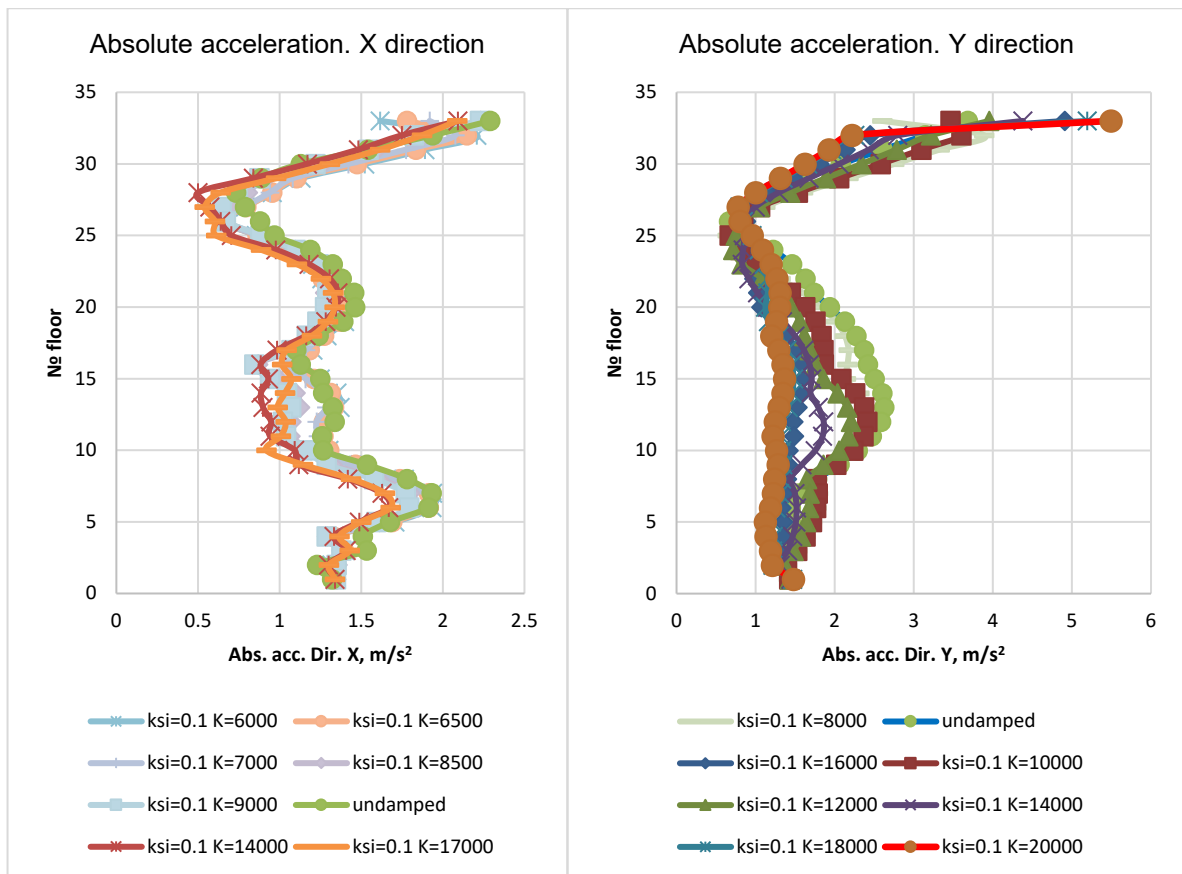
Figure 8. Maximum storey acceleration in X, Y directions.
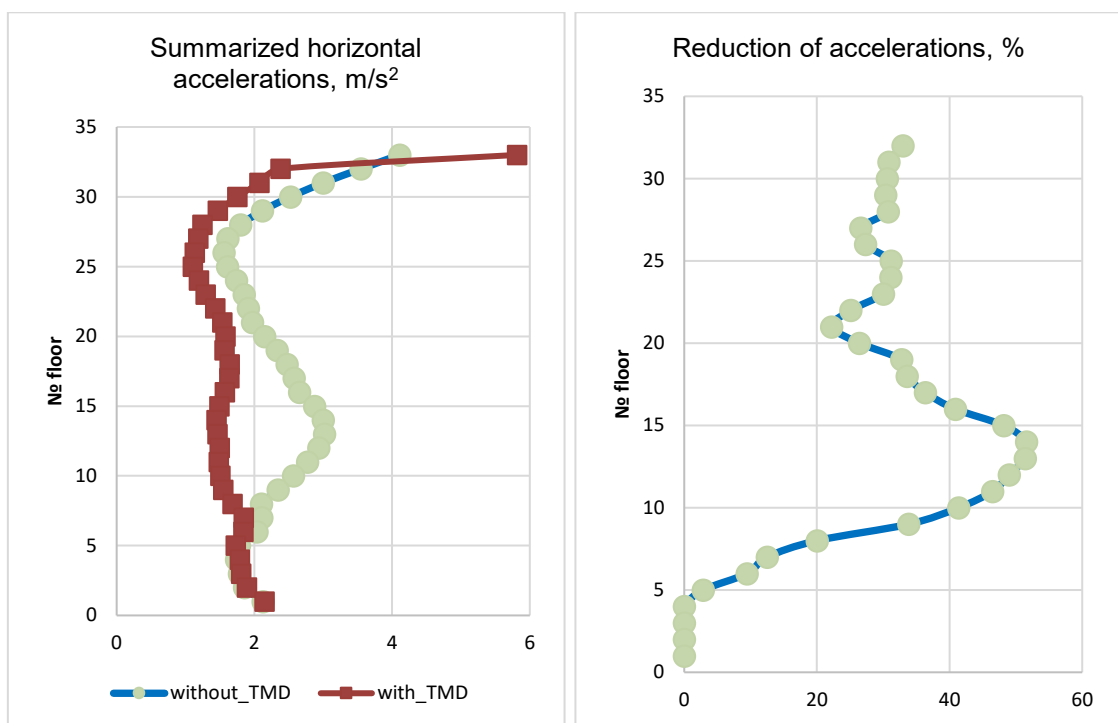
Figure 9. Maximum summarized storey acceleration and the reduction of accelerations.
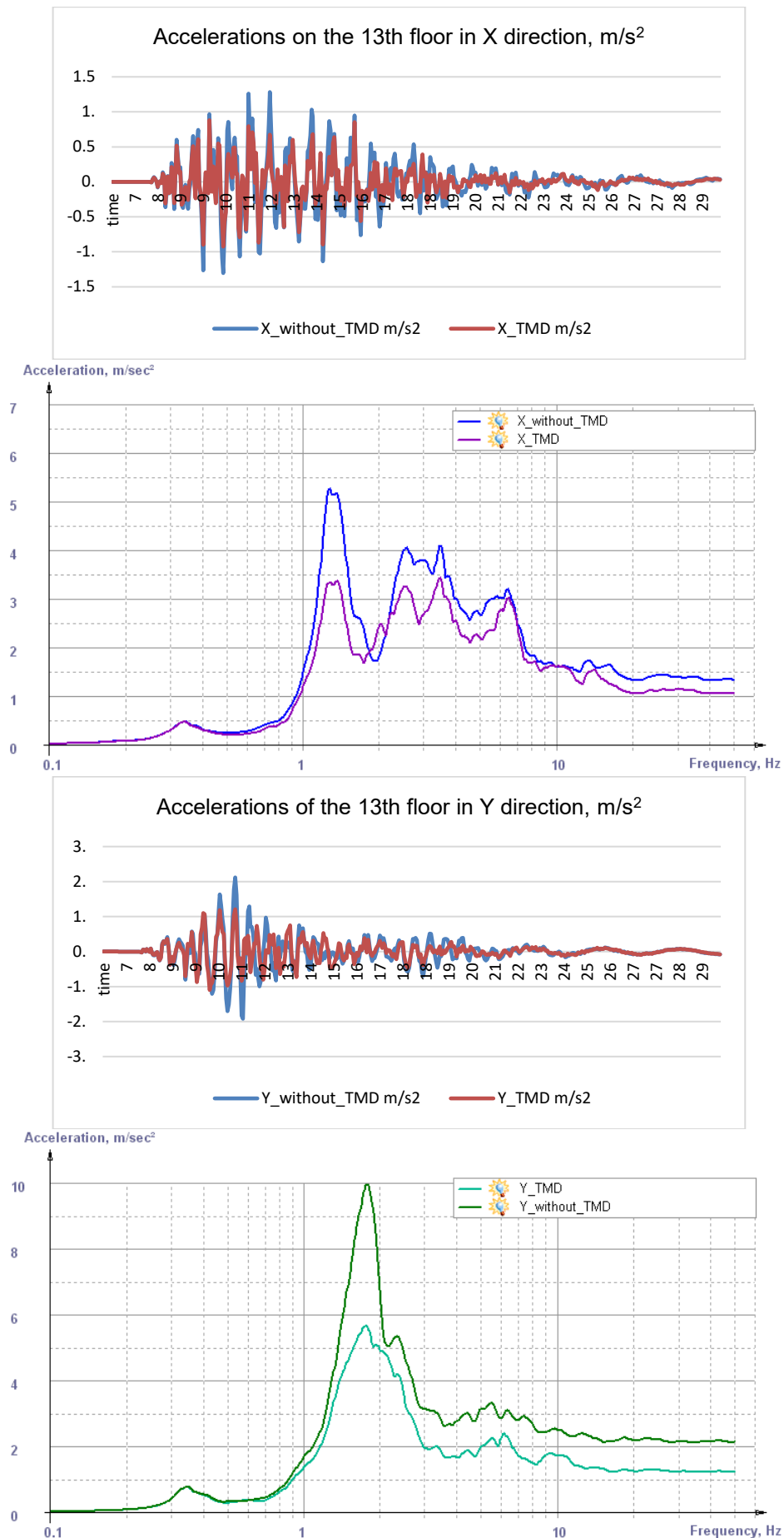
Figure 10. Accelerations of the 13th floor in X and Y direction and response spectra (ξ=0.05).

The optimum parameters for the TMD were installed as follows: $K_x = 12000 \frac{t}{m}$, $K_y = 15000 \frac{t}{m}$, $\xi_{TMD} = 0.1$, $M_{TMD} = 1050\ t$. The TMD with these parameters is tuned close to the 2nd eigenfrequency of the building. During modal analysis in dissipation matrix (16) $\xi_1 = \xi_{soil}$, $\xi_2 = \xi_{TMD}$ were used. Installation of the TMD led to a minor changes in the eigenfrequencies of the dynamically controlled building (Table 3).

Table 3. Eigenfrequencies of the dynamically controlled building

Number	Circular frequency, rad/s	Frequency, Hz	Direction	Modal mass, %
1	1.98	0.32	X	67.46
2	2.03	0.32	Y	64.85
3	10.3	1.64	X	7.54
4	11.1	1.77	Y	10.63
5	13.72	2.18	X	15.22
6	14.41	2.29	Y	11.18
7	33.18	5.28	X	8.73
8	34.69	5.52	Y	7.49

3.2. Configuration of the TMD

Fig. 11 shows the configuration of the TMD developed for the target building. The construction of the TMD consists of the building' technological floor and roof that constitutes TMD's mass supported by BCS (Base Control System) 3D springs and 3D dampers [26, 27] system that provides near-optimum damping ratio $\xi_{TMD} = 0.1$. For the considered building according to the optimization analysis, it is necessary to use 50 spring blocks with vertical stiffness $K_v = 1021 \frac{t}{m}$ and horizontal stiffness $K_h = 298 \frac{t}{m}$ and 25 3D dampers VD 426/219-7 by process conditions[1]. With these near-optimal parameters (mass, stiffness, damping) TMD provides to the building efficient protection from seismic excitation with a quite reasonable relative displacements between TMD and the main structure from 20 to 45 mm only (Fig. 11). Relative displacements between TMD and primary building are shown in Fig. 12.
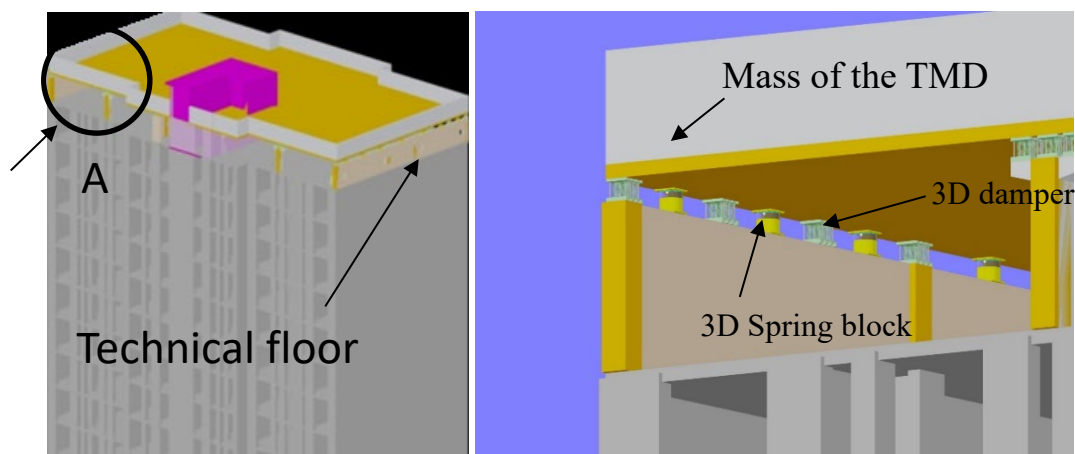
Figure 11. General and detailed view of the building.

---

[1] CKTI-Vibroseism. Viscoelastic dampers VD series. Specifications. TU 4192-001-20503039-01. 1991/2022
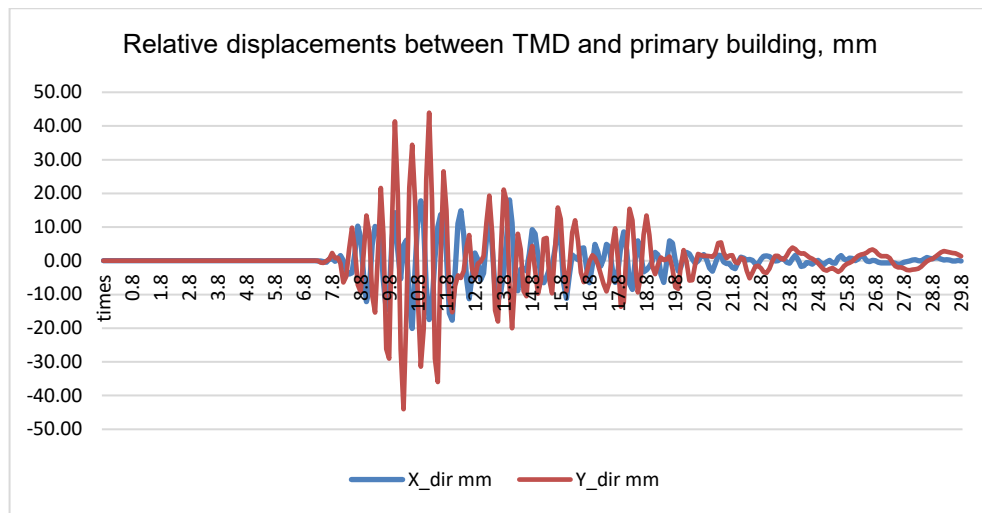
Figure 12. Relative displacements between TMD and primary building.

3.3. Comparison of an Analytical and Finite Element Models. Shear Force and Bending Moment in the Most Loaded Column

Program code of the analytical model mentioned below was written by means of MathCad's software. 3D finite element model (FEM) was used in order to assess stresses in building's elements. 3D building was created by SCad office's software. Fig. 13 demonstrates the 3D FEM of target building. It has 153000 joints and 174400 finite elements. Seismic excitation was presented by kinematic time-dependent displacements of soil. The dissipation matrix for column and beam finite elements is formed by the coefficient of internal inelastic resistance of the material [28]. For beams and columns, damping ratio was used as $\xi_{r.c.}$ = 0.05, for soil – ξ_{soil} = 0.15, and for TMD's constructions – ξ_{TMD} = 0.1.
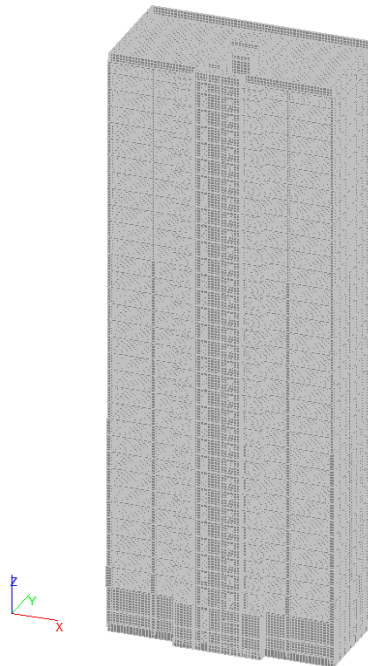
Figure 13. 3D FEM of target building.

The comparison between the analytical and finite element models is shown in Fig. 14 and 15. The displacement of the top floor has a good agreement in terms of maximum and minimum values. The accelerations, in turn, have rather large differences since the analytical model considers non-deformable slabs.
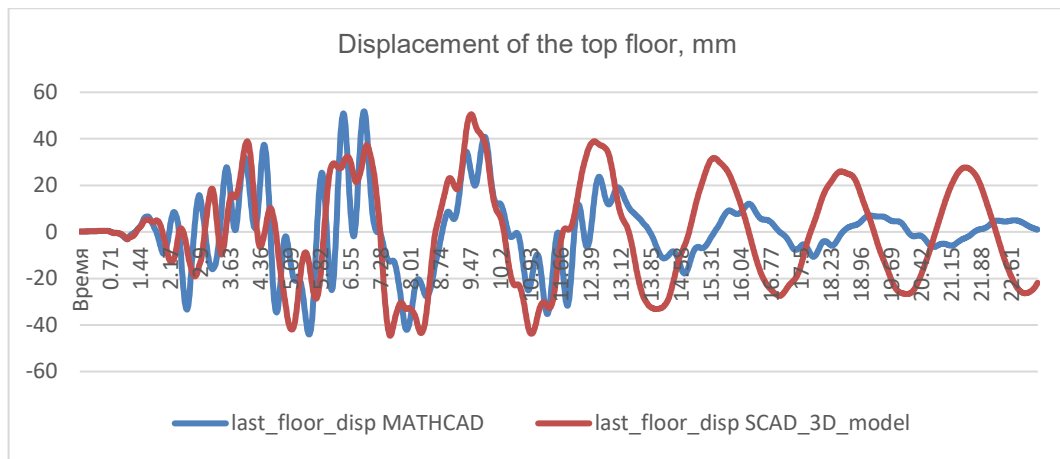
Figure 14. Comparison between two models. Displacement.
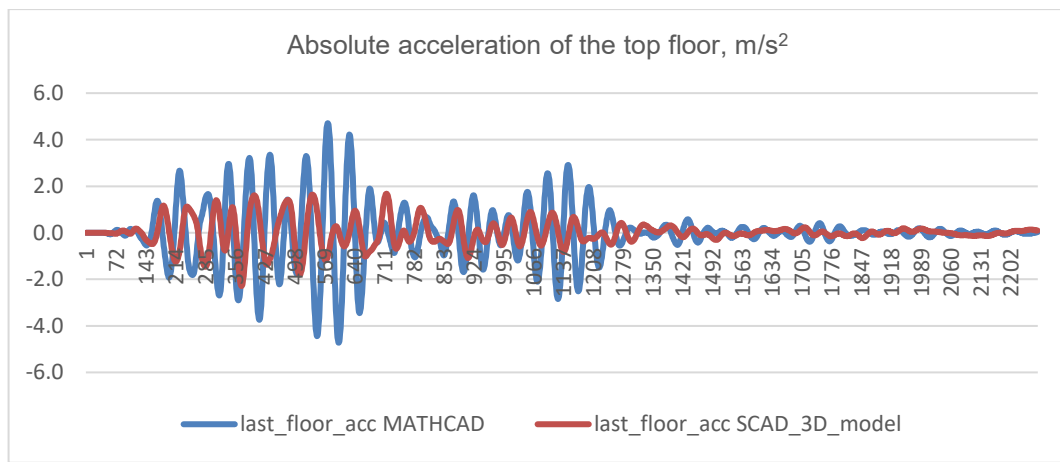
Figure 15. Comparison between two models. Acceleration.

Analytical model allows to define in short time the optimal parameters of TMD's constructions. After this analysis, it is reasonably to use FEM to assess stresses in building's elements. For example, in Fig. 16 and 17 bending model and shear force in the most loaded column are shown. Reduction of the inner forces in column has reached up to 50 %.
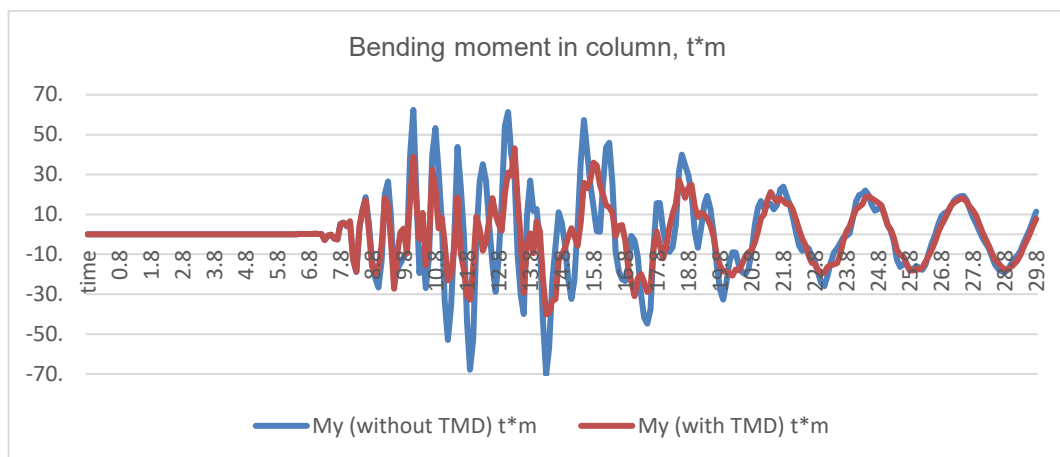
Figure 16. Bending moment in column in target building with and without TMD.

Shear force in column, t
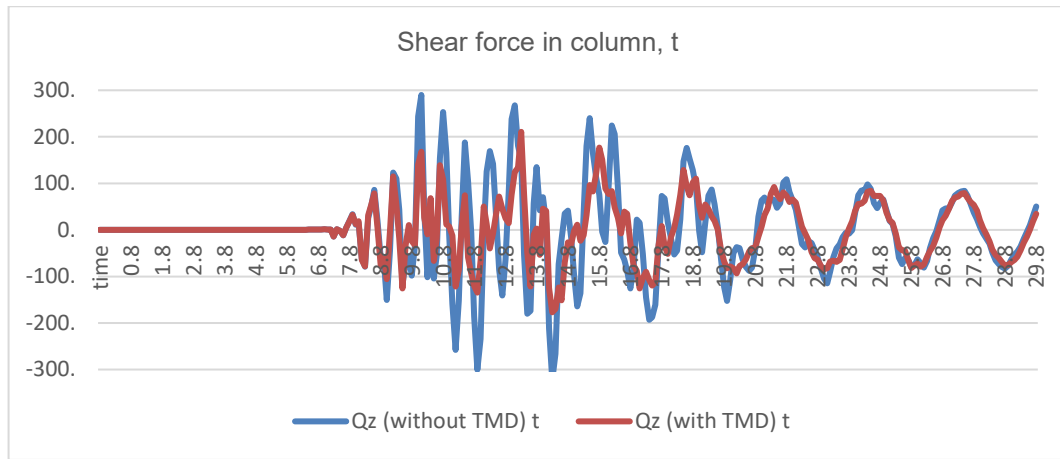
Figure 17. Shear force in column in target building with and without TMD.

3.4.   Reduction of the Vertical Accelerations in Target Building

Due to vertical stiffness of BCS spring blocks and using 3D FEM, it is possible to assess the efficiency of the TMD in Z direction subjected to vertical seismic excitation (Fig. 7). In Fig. 18 and 19 time-history acceleration and response spectra of the point, which is close to shear wall of the building, is shown. The TMD can reduce vertical acceleration up to 30 % in comparison with uncontrolled building. It was achieved principally new effect of efficiency of the TMD in Z direction. This effect has not been mentioned in recent investigations in TMD's field by others researchers [4–6, 12, 20–22].

Absolute acceleration of the top floor in Z-direction, m/s²
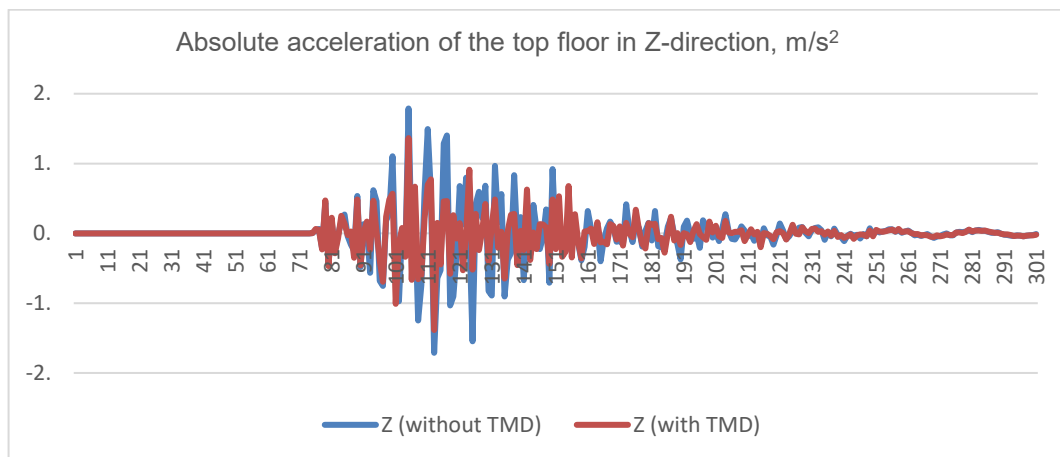
Figure 18. Vertical absolute acceleration of the top floor in target building with and without TMD.
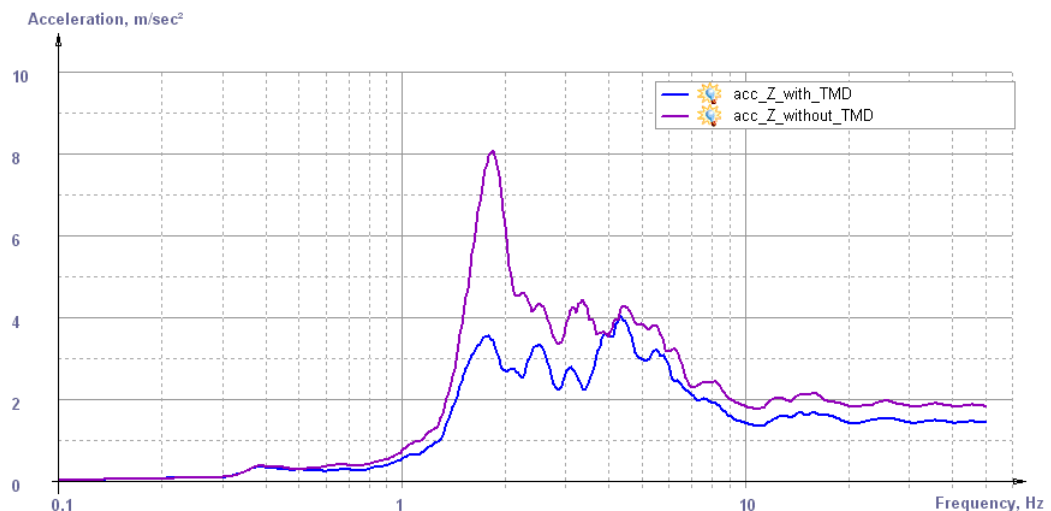
Figure 19. Response spectra (ξ=0.05) of the vertical absolute acceleration of the top floor with and without TMD.

4. Conclusions

The main idea of the proposed TMD is to use the existing upper technological part of the building, located above the residential floors, as a TMD device. This new approach can achieve significant increase in TMD's efficiency by using the optimal mass, stiffness and damping properties of the TMD.

The proposed TMD construction has an optimal mass ratio of about 2 %. It can be installed in existing buildings or in new buildings using the upper technological floor and the roof as the mass of the TMD. This solution does not require transportation of a huge TMD to the installation site on the top floor of the structure. The TMD is a passive seismic and wind control device and does not require any external energy sources or its maintenance. The relative displacements between the TMD and the building are quite acceptable, less than 5 cm, due to the optimal damping of the system.

A stiffness matrix has also been developed. It allows to consider soil stiffness, bending and shifting modes of a building. It is very easy to use the damping ratio in analysis separately for soil and for the TMD in case where the TMD is not tuned to the 1st eigenfrequency of a building.

The approach of using the top of a building as a TMD can significantly reduce response accelerations and stresses in elements of the building along the entire height subjected to seismic and wind loads. It has been shown that the accelerations was reduced by up to 50 % in comparison with a dynamically uncontrolled building.

The developed TMD construction can reduce vertical acceleration and motion in primary building due to the large mass of the roof. It has been shown that the vertical acceleration of the top floor was reduced by up to 30 % in comparison with a dynamically uncontrolled building.

Innovative TMDs were developed to reduce seismic vibrations in high-rise buildings. However, it is also possible to use this construction of TDM for reduction of wind vibrations.

In general, TMD mentioned in this paper is able to reduce rocking and torsional motions caused by earthquake and wind loads and these investigations are ongoing.

References

1. Frahm, H. Device for damping vibrations of bodies. Patent United States no US989958A, 1909.

2. Gutierrez Soto, M., Adeli, H. Tuned Mass Dampers. Archives of Computational Methods in Engineering. 2013. 20(4). Pp. 419–431. DOI: 10.1007/s11831-013-9091-7

3. Stanikzai, M.H., Elias, S., Matsagar, V.A., Jain, A.K. Seismic response control of base-isolated buildings using multiple tuned mass dampers. Structural Design of Tall and Special Buildings. 2019. 28(3). Article no. e1576. DOI: 10.1002/tal.1576

4. Salimi, M., Kamgar, R., Heidarzadeh, H. An evaluation of the advantages of friction TMD over conventional TMD. Innovative Infrastructure Solutions. 2021. 6(2). Article no. 95. DOI: 10.1007/s41062-021-00473-5

5. Anajafi, H., Medina, R.A. Comparison of the seismic performance of a partial mass isolation technique with conventional TMD and base-isolation systems under broad-band and narrow-band excitations. Engineering Structures. 2018. 158. Pp. 110–123. DOI: 10.1016/j.engstruct.2017.12.018

6. de Barros, R.C., Sousa, C.M. Pendulum TMD's in building vibration control. CONTROLO 2016. Lecture Notes in Electrical Engineering. 2017. 402. 559–569. DOI: 10.1007/978-3-319-43671-5_47

7. Farghaly, A.A., Ahmed, M.S. Optimum Design of TMD System for Tall Buildings. International Scholarly Research Notices. 2012. 2012. Article no. 716469. DOI: 10.5402/2012/716469

8. Mondal, J., Nimmala, H., Abdulla S., Tafreshi, R. Tuned liquid damper. Proceedings of the 3rd International Conference on Mechanical Engineering and Mechatronics.2014. Article no. 68.

9. Momtaz, A.A., Abdollahian, M.A., Farshidianfar, A. Study of wind-induced vibrations in tall buildings with tuned mass dampers taking into account vortices effects. International Journal of Advanced Structural Engineering. 2017. 9(4). Pp. 385–395. DOI: 10.1007/s40091-017-0174-9

10. Belver, A.V., Magdaleno, Á., Brownjohn, J.M.W., Lorenzana, A. Performance of a TMD to mitigate wind-induced interference effects between two industrial chimneys. Actuators. 2021. 10(1). Article no. 12. DOI: 10.3390/act10010012

11. Tian, L., Zeng, Y. Parametric Study of Tuned Mass Dampers for Long Span Transmission Tower-Line System under Wind Loads. Shock and Vibration. 2016. 2016(1). Pp. 1–11. DOI: 10.1155/2016/4965056

12. Nakai, T., Kurino, H., Yaguchi, T., Kano, N. Control effect of large tuned mass damper used for seismic retrofitting of existing high-rise building. Japan Architectural Review. 2019. 2(3). Pp. 269–286. DOI: 10.1002/2475-8876.12100

13. Barkhordari, M.S., Tehranizadeh, M. Ranking passive seismic control systems by their effectiveness in reducing responses of high-rise buildings with concrete shear walls using multiple-criteria decision making. International Journal of Engineering. Transactions B: Applications. 2020. 33(8). Pp. 1479–1490. DOI: 10.5829/ije.2020.33.08b.06

14. Li, J., Zhang, H., Chen, S., Zhu, D. Optimization and sensitivity of TMD parameters for mitigating bridge maximum vibration response under moving forces. Structures. 2020. 28. Pp. 512–520. DOI: 10.1016/j.istruc.2020.08.065

15. Christopoulos, C., Filiatrault, A. Principles of Passive Supplemental Damping and Seismic Isolation. Italy: IUSS Press, 2006. 480 p.

16. Den Hartog, J.P. Mechanical vibrations. NY, Toronto, London: McGraw-Hill Book Company, 1934.

17. Falcon, K.C., Stone, B.J., Simcock, W.D., Andrew, C. Optimization of Vibration Absorbers: A Graphical Method for Use on Idealized Systems with Restricted Damping. Journal of Mechanical Engineering Science. 1967. 9(5). Pp. 374–381. DOI: 10.1243/JMES_JOUR_1967_009_058_02

18. Luft, R.W. Optimal Tuned Mass Dampers for Buildings. Journal of the Structural Division. 1979. 105(12). Pp. 2766–2772. DOI: 10.1061/JSDEAG.0005323

19. Warburton, G.B. Optimal Absorber Parameters for Various Combinations of Response and Excitation Parameters. Earthquake Engineering and Structural Dynamics. 1982. 10(3). Pp. 381–401. DOI: 10.1002/eqe.4290100304

20. Liu, Y., Wang, K., Mercan, O., Chen, H., Tan, P. Experimental and numerical studies on the optimal design of tuned mass dampers for vibration control of high-rise structures. Engineering Structures. 2020. 211. Article no. 110486. DOI: 10.1016/j.engstruct.2020.110486

21. Lara-Valencia, L.A., Farbiarz-Farbiarz, Y., Valencia-González, Y. Design of a Tuned Mass Damper Inerter (TMDI) Based on an Exhaustive Search Optimization for Structural Control of Buildings under Seismic Excitations. Shock and Vibration. 2020. 2020(1). Article no. 8875268. DOI: 10.1155/2020/8875268

22. He, H., Wang, W., Xu, H. Multidimensional Seismic Control by Tuned Mass Damper with Poles and Torsional Pendulums. Shock and Vibration. 2017. 2017(1). Article no. 5834760. DOI: 10.1155/2017/5834760

23. Carlot, J. Effects of a Tuned Mass Damper on Wind-Induced Motions in Tall Buildings, thesis (Master of Engineering). Massachusetts Institute of Technology, 2012.

24. Birbraer A.N. Seismic analysis of structures. St. Petersburg: Nauka, 1998. 254 p.

25. Chopra, A.K. Dynamics of Structures. Theory and Applications to Earthquake Engineering. 5th ed. NJ: Prentice Hall, 2012. 944 p.

26. Kostarev, V., Nawrotzki, P., Vasil'ev, P., Vaindrakh, M. Developing and natural scale testing of the 3rd BCS base isolation system. 16th World Conference on Seismic Isolation, Energy Dissipation and Active Vibration Control of Structures. DOI: 10.37153/2686-7974-2019-16-460-472

27. Nawrotzki, P., Kostarev, V., Siepe, D., Barutzki, F., Salcedo, V. 3D seismic isolation systems for the nuclear industry – layout, design & qualification. Transactions, SMiRT-26. Potsdam, 2022.

28. Fialko, S., Karpilovskyi, V. Time history analysis formulation in SCAD FEA software. Journal of Measurements in Engineering. 2018. 6(4). DOI: 10.21595/jme.2018.20408

Information about the Authors:

Dmitrii Bondarev, *PhD in Technical Sciences*
ORCID: https://orcid.org/0000-0002-5364-5473
E-mail: 89523684328@mail.ru

Effect of nanosilica on properties
of porcelanite aggregate concrete

S.I. Ahmed ✉ [1]**, A.M. Hameed** [2]**, A.Sh. Al-Adili** [3]

[1] *Ministry of Science and Technology, Baghdad, Iraq*

[2] *Applied Sciences Department Branch of Materials Sciences, University of Technology, Baghdad, Iraq*

[3] *Civil Engineering Department, University of Technology, Baghdad, Iraq*

✉ *as.18.48@grad.uotechnology.edu.iq*

Abstract. Lightweight concrete has been used in buildings for centuries, due to its longevity and durability. In recent years, new studies have shed light on additives capable of reducing concrete weight while increasing strength. Nanosilica is one of these additives, which regulate the fundamental Calcium Silicate Hydrate CSH process in water. The addition of nanosilica (NS) particles to concrete improves its density and strength. In this work, we started by creating a reference mixture without additives and another mixture containing a different ratio of nanosilica. Porcelanite was used as a lightweight aggregate. First, the porcelanite aggregate was crushed into pieces of different sizes (6 and 9.5 mm). The results of testing under compression showed that mixes containing 1, 1.5, 2 wt. percent of nanosilica gave the best results when compared to a reference mix without nanosilica. Porcelanite rich in SiO_2 and nanosilica were utilized to partially substitute cement. A comparison was made with the reference mix (without nanosilica) to figure out the efficiency of using nanosilica in lightweight porcelanite concrete. The highest average compressive strength at a particle size of porcelanite (6 mm) of 18.1 MPa and 15.3 MPa can be obtained at 28 days using 1.5 and 2 wt. percent of nanosilica, with 40.3 % and 18.6 %, respectively. The addition of 1 wt. percent of NS, on the other hand, has a negative effect on the compressive strength of 6 mm grain size porcelanite by a factor of not more than 2.3 % at 28 days. Flexural strength of 3.04 MPa can be obtained at 28 days using 1.5 wt. percent of NS at a particle size of 6 mm of porcelanite, with percentages of 424.1 %. The flexural strength of porcelanite aggregate concrete increases with a low percentage of various NS. The bulk density decreases when using porcelanite aggregate concrete at 6 mm and 9.5 mm particle sizes with 2 % from nanosilica by 4.84 % and 8.86 %, respectively. field Emission Scanning Electron Microscope FESEM test was carried out to study the structure of the fractured nature of the highest compressive strength samples and reference.

1. Introduction

Lightweight aggregate concrete (LWAC) is not a new concept in the world of concrete; however, it has been used for thousands of years. The durability and longevity of concrete are demonstrated by ancient buildings [1]. LWACs building materials included pumice, scoria, and other naturally occurring volcanic debris [2]. In construction, the weight represents a great issue. Luckily, the LWAC may be produced by utilizing LWA (lightweight aggregates) [3]. Porcelanite lightweight aggregate rocks were discovered to be a locally available material in the production of cost-effective Structural Lightweight Concret (SLWC) [4]. Due

to its low weight and high strength, Lightweight Concrete LWC has recently been the focus of many studies. [5–7]. The equilibrium density of structural lightweight concrete ranges between 1120 and 1920 Kg/m^3.This type of concrete, which is suitable for structural purposes, must have a compressive strength of 17 MPa after a 28-day water cure [8]. Low Strength Concrete LSC is defined as concrete with a compressive strength of less than 17.0 MPa after 28 days; Medium Strength Concrete MSC is defined as concrete with a compressive strength of between 17 and 27 MPa; and High Strength Concrete HSC, which is defined as concrete with a compressive strength of more than 41 MPa [9]. Nanotechnology is a new approach to science that deals with the understanding and control of matter at the nanoscale, or between 1 and 100 nanometers in size [10]. Nanosilica NS is one of the nanomaterials utilized in the formation of building materials, has generated a lot of concern [11]. Adding NS to concrete mixtures has improved the materials properties [12]. NS has a larger surface area due to the small size of its particles, which improves cement hydration and pozzolanic processes, according to recent research   [13]. NS has a high reacting pozzolan that can put away Calcium Hydroxide CH and generate subsidiary Calcium Silicate Hydrate (CSH) [14, 15]. A few studies show that adding nanosilica has a greater effect on primary silicate polymerizing compared to the CSH quantity produced in the end [16]. Microstructural studies indicated that NS considerably impacts the concrete pore properties, resulting in denser and stronger microstructures. [17]. Another process by which NS might affect the characteristics of cement composite is the seeding effect, where hydration products are preferentially exposed to more places for them to precipitate [18, 19].

The application of nanoconcrete is used in civil engineering projects such as highway bridges [20], dams, and structural buildings.

The objective of this study is to investigate their effects on some concrete qualities, such as compressive strength, flexural strength, bulk density, and microstructure analysis by Field Emission Scanning Electron Microscope FESEM, by adding nanosilica to porcelanite aggregate concrete and comparing all properties of porcelanite concrete without nanosilica (reference concrete) with porcelanite concrete with nanosilica. As a lightweight cement substitute, two grain sizes of 6 and 9.5 mm of crushed coarse porcelanite aggregates were used in this work. Nanosilica was added in different percentages (0, 1, 1.5, and 2 wt. percent to the cement content as an aggregate substitute in concrete with a mixing ratio of cement, sand and porcelanite 1:1:1.

2. Materials and Methods

2.1. Materials

table one and table two show the chemical and physical compositions of regular Portland cement Type1 that was utilized, manufactured by al Mass Factory, Iraq. The test results indicate that the adopted cement conformed to ASTM C150-16 [21] and Iraqi Standard Specifications (IQS No.5, 1984) [22].

Table 1. Chemical parameters of regular Portland cement.

Constituent	Lime (CaO)	Silica (SiO$_2$)	Alumina (Al$_2$O$_3$)	Iron Oxide (Fe$_2$O$_3$)	Magnesia (MgO)	Sulfur Trioxide (SO$_3$)
Weights %	61.5	20.8	3.5	3.2	1.7	2.5
ASTM C150-16	–	20 (min)	6 (max)	6 (max)	6 (max)	3 (max)
Limited of IQS No.5 %	–	–	–	–	≤ 5	≤ 2.8

Table 2. Physical parameters of regular portland cement.

Constituent	Specific surface area m^2/kg	The Primary setting time h min	Last setting period h min	Compressive strength (MPa) 3 Days	Compressive strength (MPa) 7 Days
Weights%	350	2 20	8 20	17	24
ASTM C150-16	280 min	00 45	06 25	10 min	17 min
Limited of IQS No 5	–	1 00	10 00	≥ 15	≥ 23

Silicon dioxide (SiO$_2$) nanopowder was also utilized in the current experimentation work, manufactured by skyspring nanomaterials, USA table three shows the properties of the nanomaterial according to data sheet.

Table 3. Nano-silica (SiO₂) Properties.

Product Name	Color	Particle Size (nm)	Surface area (m²/g)	Al₂O₃ (%)	Fe₂O₃ (%)	CaO (%)	MgO (%)
Silica Powder Nano Grade	White	20	160	0.002	0.001	0.002	0.001

In this study, porcelanite was used as a coarse aggregate, it is locally available, and exits in nature as a lightweight and white in color stone. The Ministry of Industry and Minerals State Corporation of Geological Sciences Survey and Mining received porcelanite in huge lumps. Porcelanite stones avail in Wadi Mallusa (Rutba) at a location called El-Anbar Provinces Western Desert, Iraq; it is done according to ASTM, C330-05. [23]. See table four.

Table 4. Properties of lightweight porcelanite aggregate.

Product Name	Color	Water absorption %	Saturation %	Thermal conductivities W/m. K	apparent density Kg/m³	density Kg/m³
Lightweight Porcelanite aggregate	Off white	39	3.5	0.2 -1.0	1600 -1900	1447

EUCOBET SUPER VZ is a superplasticizer with a stunting influence that is made from synthetic materials, manufactured by Swiss Chem., Egypt, table five depicts its proprieties according data sheet.

Table 5. Properties of Superplasticizer according to data sheet.

Product Name	Color	Specific gravity	Chloride content	Air entraining	Compatibility with cement	Shelf life
EZ	Brown	1.1	Nil	Does not entrain air	All type of Portland cement	Up to 2 years

In this work, the cementations mix included NS with a purity of 99.5 percent and a bulk density of 0.08 to 0.10 g/cm³. A commercially available colloidal silica suspension nanosilica NS was used to make the concrete, table three shows nanosilica's characteristics.

3. Methods

3.1. Dispersing nanomaterial in water

Nanosilica must be dispersed in water before adding it into the concrete mix. The ultrasonic method was to disperse the nanomaterial in water [24]. Before starting dispersal, using gloves and face mask. That the handling of nanomaterials is a dangerous process. First, the nanomaterial required for each sample batch of the design mixture was weighed and placed into a beaker. A quantity of water was poured and mixed. Ultrasound for this purpose is placed at a frequency of 100 Hz. Note that mixing the dispersed nanomaterial into the concrete mixture was done within 5 minutes to keep it constant.

3.2. Samples' preparation

table six shows the mixture design employed in the current experimentation, it is done in the concrete laboratory in Technology university as well as the amount of utilized design material. The difference between each batchs mix compositions is the percentage of nanosilica used and the grain size of porcelanite.

Measuring all essential components was done in accordance with the mix design percentage before the concrete mixing commenced. After wetting the concrete mixer, it was added the entire dry mix components, such as porcelanite, sand, and cement. After that, in the mixer, 10 percent of the needed water was provided and thoroughly blended. The left water was then added, preceded by the nanomaterial that had been disseminated. The materials were combined until the mortar and concrete became homogeneous.

For eight of the concrete mixtures containing (48 samples), the concrete got poured and put flat into lubricated cubic molds with dimensions of 100 mm *100 mm * 100 mm . It is done according to BS 1881-116 1983 [25], and prism molds with dimensions 280 mm * 75 mm *75 mm, it is carried out in accordance with BS 1881-101 1983 [26]. Were used to cast three specimens A, B and C at each batch, out of a total 24 cubic samples and 24 prism samples.

For compaction, three layers of concrete were placed in each mold, and a vibrator was used for around 3–4 minutes to equally disperse the concrete. Finally, a trowel was used to smooth out the molds.

For each mixture, three samples are poured and the average is taken for the calculations. All cast specimens were covered for at least 24 hours to avoid any early loss of moisture via evaporation under room conditions, then they were demolded. One got demolded, the mortar specimens were promptly labeled and deposited in the curing tank for a 28-day curing phase. In lab settings, the water in the cure tank was left at room temperature.

Table 6. The Proposed mix of specimen.

Mix type	Cement (kg/m^3)	Sand (kg/m^3)	Porcelanite (kg/m^3)	Water/ cement ratio	Nanosilica (kg/m^3)	Superplastsizer (wt. %)
A1 Ref.	570	570	570	0.35	0	0.4
A2	564.3	570	570	0.38	5.7	0.4
A3	561.45	570	570	0.38	8.55	0.4
A4	558.6	570	570	0.38	11.4	0.4
A5 Ref.	650	650	650	0.35	0	0.4
A6	643.5	650	650	0.38	6.5	0.4
A7	640.25	650	650	0.38	9.75	0.4
A8	637	650	650	0.38	13	0.4

4. Results and Discussion

The property of nano porcelanite concrete is poured into molds to make three cubes and three prism for each batch.

4.1. Compressive strength test

A compressive strength test was employed in the current study, before starting with this testing, each sample was air cured for a period of 21 days to remove extra moisture. The specimen was carefully positioned in the center of the test appliance, in the opposite direction of loading. After that, the compressive strength test appliance was calibrated according to the manufacturers requirements. Until the cube was crushed, the loading ratio got set to 10 KN/s. Fig. 1 and 2 showes the compressive strength with various failure patterns.

At particle size six mm of porcelanite aggregate (PA) all compressive strengths of batch A2, A3 and A4 were greater than the reference A1, but at particle size 9.5 mm of PA the compressive strength little increases than the reference at batches A6 and A7 but at batch A8 decreases than the reference, the efficiency of the nanosilica increases with strength at particle size 6 mm of PA.

fig. 1 and fig. 2 / table six are comparisons of strength of porcelanite aggregate with different nanosilica and different particle size of porcelanite, show that batch A3 is high strength than other batch.
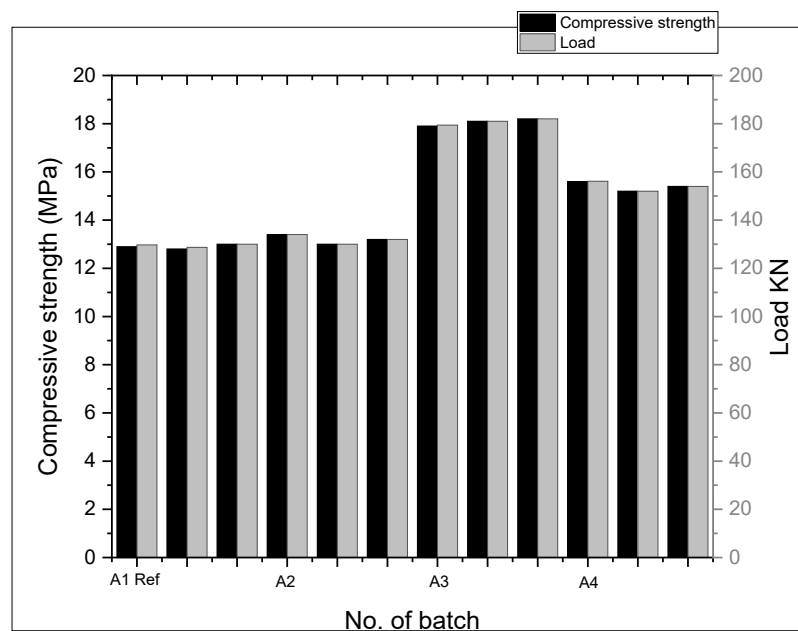
Figure 1. Compressive strength of porcelanite aggregate concrete at coarse porcelanite 6 mm with different ratio of nanosilica.
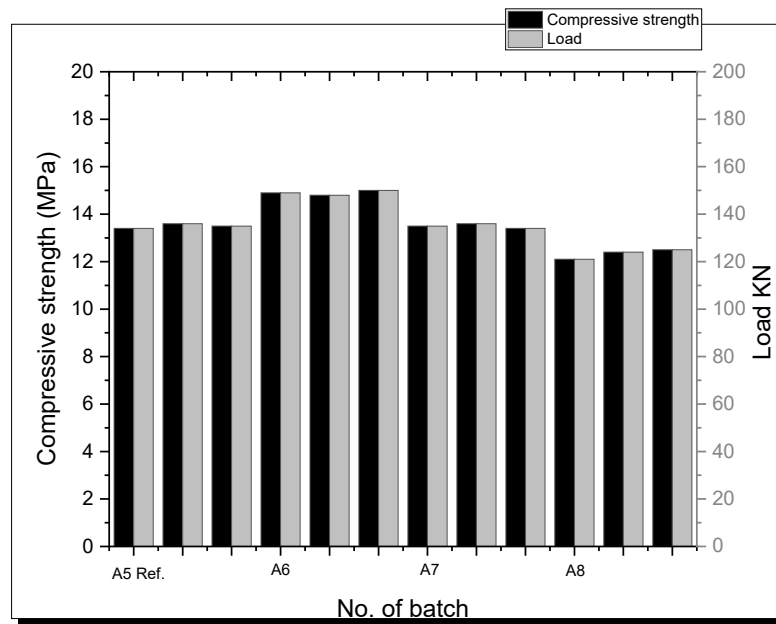
**Figure 2. Compressive strength of porcelanite aggregate concrete
at coarse porcelanite 9.5 mm with different ratio of nanosilica.**

4.2.   Flexural strength

The flexural strength at the 28th day is shown in fig. 3 and fig. 4 / table six. The inclusion of nanosilica boosts it to new heights. The nanoparticles efficiency in enhancing flexural strength increases the following order: A2, A3, A4, A6, A7, and A8, respectively.

The strength of concrete without nanosilica is lower compared to that of concrete with different nano ratios.
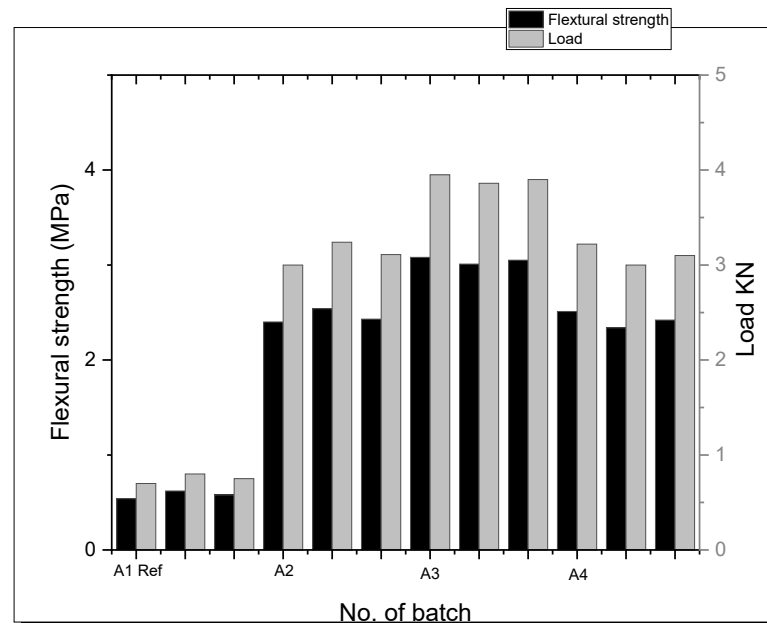
**Figure 3. Flexural strength of porcelanite aggregate concrete
at 6 mm coarse aggregate with different ratio of nanosilica.**

Compressive strength, flexural strength, and density are the most acceptable terms to use when describing concrete strength. The concrete strength in relation to the mortar composition can be used to describe the overall picture of its quality. Adding nanosilica to lightweight aggregate can improve its compressive strength, which can help in the construction industry by casting any thinner section or longer span.
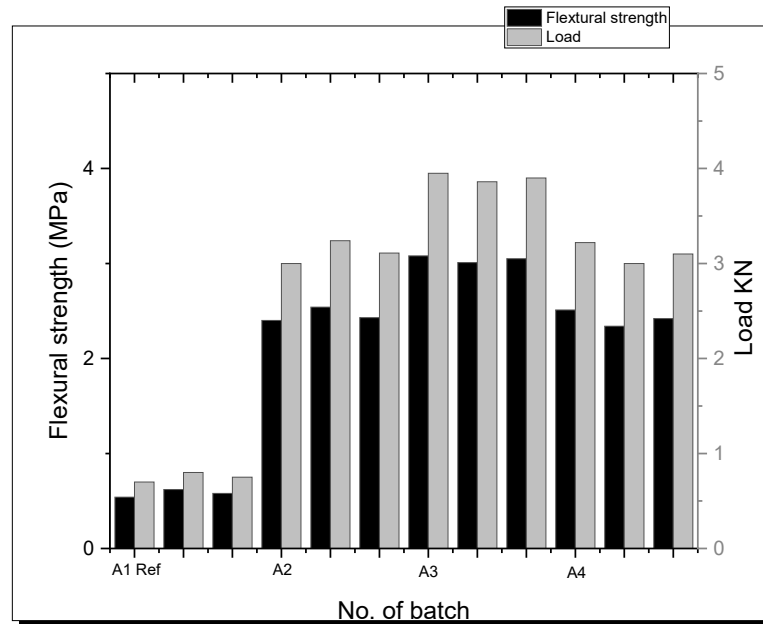
**Figure 4. Flexural strength of porcelanite aggregate concrete
at 9.5 mm coarse aggregate with different ratio of nanosilica.**

4.3. Fresh and bulk density

Fig. 5 and fig. 6 / table six display the fresh and bulk density results batch according to ASTM C642-97 [27]. The variables' weight, density, and the compressive strength need to be considered. Loads at specimens failure and densities from the same batch show significant variation. As illustrated the dispersing techniques of nanomaterial as well as the casting procedure are identical. Because the whole batch was blended together, any weight discrepancy caused by nanoparticles or nanomaterial dispersing is not apparent. Consequently, the weight discrepancies could be explained by the fact that the amount of mortar used in the two molds differs. As a result, the total amount of content may differ. As a result, each specimen weight may differ; this can be attributed to human errors, which is unavoidable. Nonetheless, the demolded cubes showed no signs of wear.
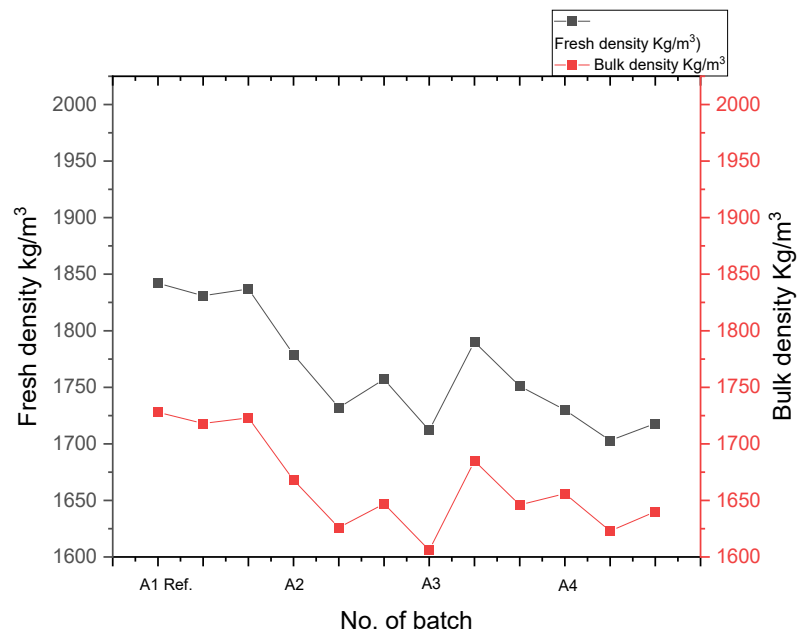
**Figure 5. Fresh and bulk density of porcelanite aggregate concrete
at 6 mm coarse aggregate with different ratio of nanosilica.**

Considering this, there was no deformation in the demolded cubes; the distribution of the mortar was also uniform and smooth. In batches A2, A3, and A6, compacting and distributing the mortar become more difficult because of the hydrophobic qualities of NS. However, with a lot of vibrating and compacting, the distributing was even.

The nanosilica enhancing the densities are lightest than the reference in all batches A2, A3, A4, A6, A7 and A8.
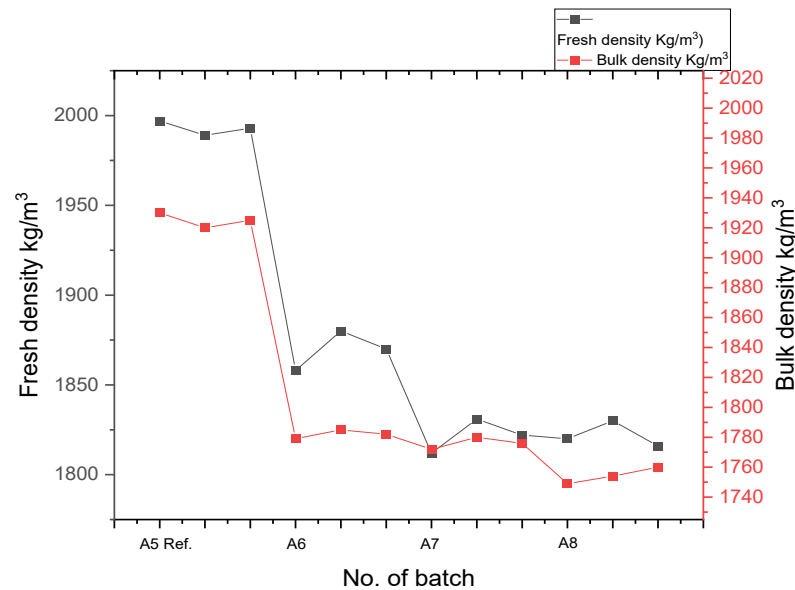
**Figure 6. Fresh and bulk density of porcelanite aggregate concrete
at 9.5 mm coarse aggregate with different ratio of nanosilica.**

4.4. FESEM analysis

After 28 days of water curing and dry the samples, FESEM imaging was performed on the fractured faces of the reference batch and maximum compressive strength batch, as well as the minimum compressive strength batch without nanosilica.

fig. 7 show FESEM micrographs of the reference batch A1 of the material at magnifications ranging from figure 7-A equal 4000X and figure7- B to 15000X.

The three phases of concrete are cementitous paste, aggregates, and the interfacial transition zone (ITZ). Lesser anhydrate cement, lesser CSH, larger calcium hydroxide crystals, more ettringite content, and increased porosity (lower density) characterize the ITZ.

**Figure 7. A, B Field emission scanning electron of reference batch
at particle size of porcelanite 6mm without nanosilica at different magnification.**

Because it strongly depends upon materials porosity, penetrability, and pore size distributing, the pore structure of cementitious materials is well recognized as an important feature because it impacts

parameters like strength and permanency [28, 29]. The micro-structure of the reference batch that has the largest density is extremely compact. It has lesser voids as well as porosity features similar to the needle-like C-S-H crystals. The reference batch has no high compressive strength because the produced voids did not regularly exist and the porosity features did not evenly spread throughout the mix [30, 31].

Three dissimilar areas of the FESEM imaging of the mixture design are shown in fig. 8, it can be noticed that the best compressive strength was achieved at magnifications ranging between 7000 and 13000. Nanosilica fill the openings among aggregates, NS takes the shape of conglomerated clumps, as seen in the figures above. These strengthen the bond strength by filling up any void or space amid the aggregates. Accordingly, this mixture, in comparison to the reference mixture, achieves high compressive strengths while having a lower density.

Figure 8. A, B Field emission scanning electron microscope of best batch of compressive at particle size of porcelanite 6mm with 1.5wt. % nanosilica at different magnification.

Fig. 9 depict reference specimen at grain size of porcelanite 9.5 mm intensification between 8000 and 15000 correspondingly. The specimen is without nanosilica but contains more cracks and voids.

1 wt. % of nanosilica was added to mix A6; this percentage represents the lowest quantity of nanosilica. As it can be seen in fig. 10, C-S-H paste and C-S-H crystal forming are relatively low in FESEM images. C-S-H is formed when cement reacts with water, but because to the high quantity of nanosilica in the cement, the unrestricted water content in the cement could be decreased, leading to less C-S-H creation as well as a porous matrix. This also reveals the samples microstructure, which shows a highly insecurely packed cement matrix, which reduces density and increases compressive strength. fig. 10 shows that the interacting has a crucial function of enhancing the compressive strength of lightweight concrete.
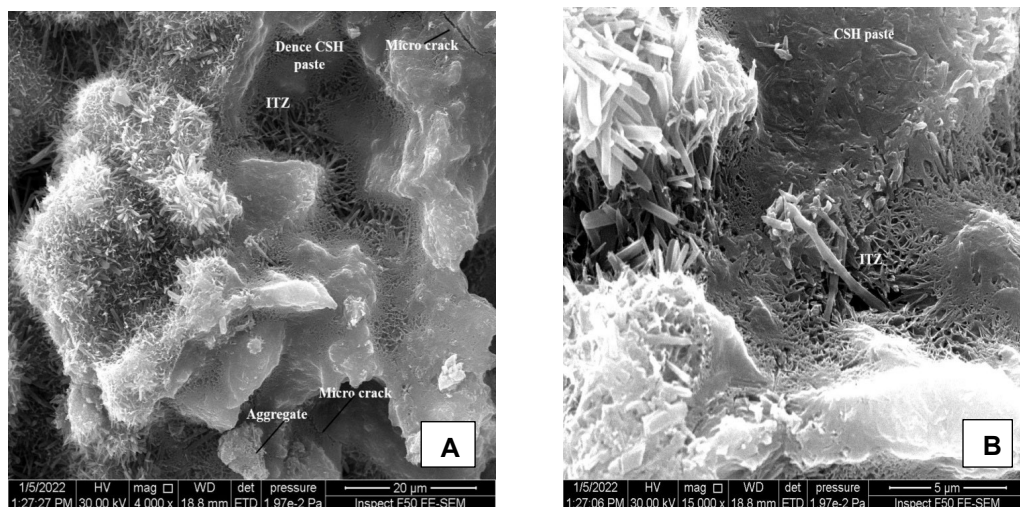

Figure 9. A, B Field emission scanning electron microscope of control batch at particle size of porcelanite 9.5 mm without nanosilica at different magnification.
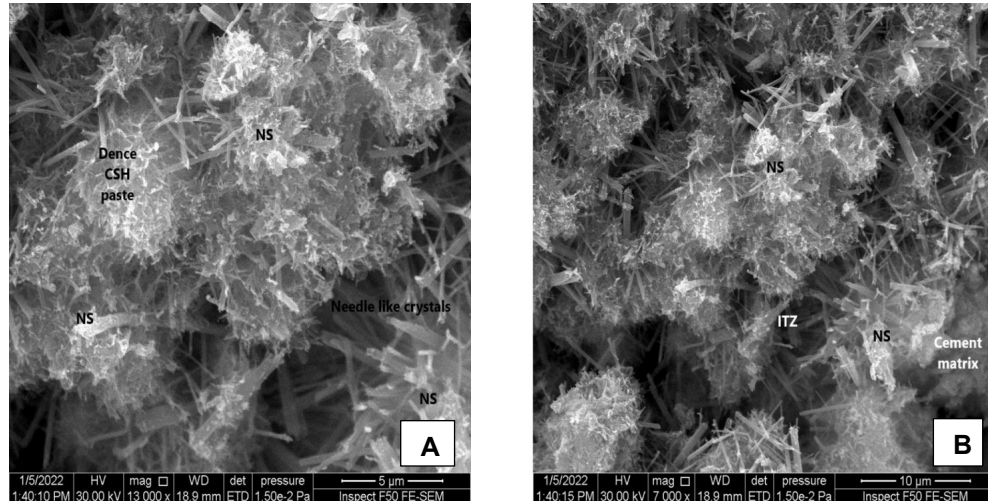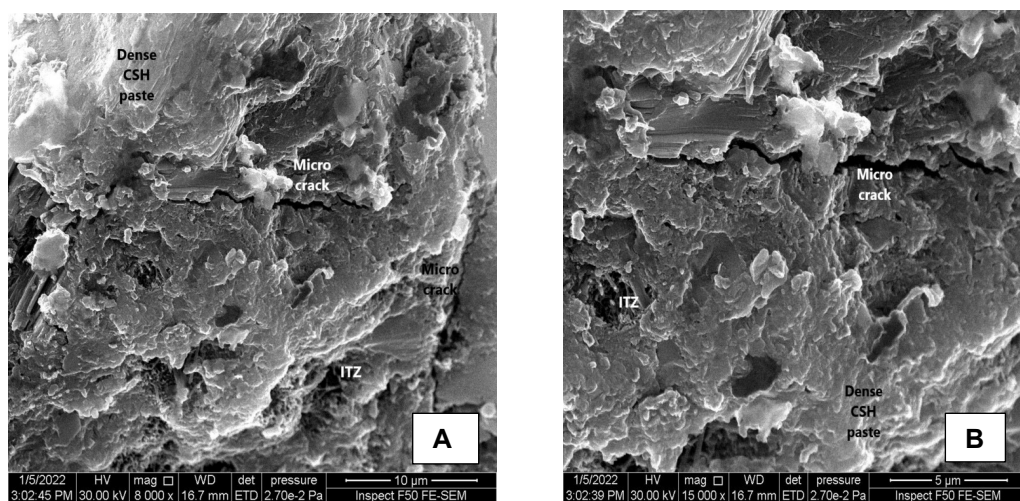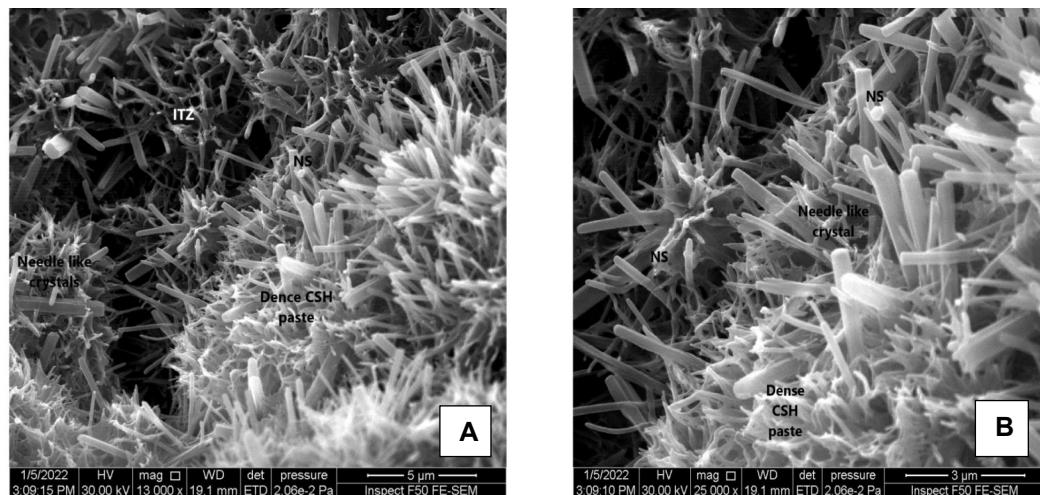
Figure 10. A, B Field emission scanning electron of best batch of compressive strength at particle size of porcelanite 9.5 mm with 1wt. % nanosilica at different magnification.

5. Conclusions

Some conclusions were established based on the investigation of the nanosilica influence upon the compressive strength of lightweight concrete as follow:

1. All specimens classified lightweight concrete LWC.

2. Most of the specimens of nanomaterial reinforced lightweight concrete show an increasing in compressive strength.

3. The density of the concrete is lightest when adding nanoparticles to the mixture. So, it can be considered as Structural Lightweight Aggregate Concrete SLWAC .

4. The costs of nanomaterial reinforced concrete could be reduced to a minimal increase when mass-produced in huge quantities, after reaching industrialized grade NS.

5. After 28 days of curing, the lightweight concrete without nanomaterial for such mixture design had an average compressive strength of 12.9 MPa.

6. Batches A3 and A6 have strong compressive strengths of 18.1 MPa and 14.9 MPa, with 40.3 percent and 10.3 percent increase over the control mixture, respectively.

7. The optimum combination consists of 1.5 wt. percent NS with a grain size of porcelanite six mm, batch, it is consider Medium Strength Concrete MSC.

8. Flexural strength high increased at all ratio of nanosilica and at any particle size, the optimum of flexural percentage increase 424.1 %.

9. FESEM micrographs provided information about pore distribution and voids of the prepared porcelanite concrete. In addition, it is uniform adhesion resulting stronger and lighter.

References

1. Mohammad, A., Sarsam, K., Al-Bayati, N. Shear strength enhancement of lightweight aggregate reinforced concrete deep beams by using CFRP strips MATEC. Web of Conferences. EDP Science. 2018. 162(3). 04011. DOI: 10.1051/matecconf/201816204011

2. Chandra, S., Berntsson, L. Historical Background of Lightweight Aggregate Concrete lightweight aggregate concrete. 2002. 82. Pp. 5–19. DOI: 10.1016/B978-081551486-2.50004-3

3. Piyaphanuwat, R., Asavapisit, S. Utilization Ceramic Wastes from Porcelain Ceramic Industry in Lightweight Aggregate Concrete. 2017, 8(5). Pp. 342–346. DOI: 10.18178/ijesd.2017.8.5.975

4. Al-Jabboory, W.M. Mining Geology of the Porcelanite Deposits in Wadi AL-Jandali-Western Desert. Iraq. MSc Thesis University of Baghdad, 1999.

5. Mansor, A.A., Mohammed, A.S., Salman, W.D. Effect of longitudinal steel reinforcement ratio on deflection and ductility in reinforced concrete beams. IOP Conference Series: Materials Science and Engineering. 2020. 888(1). 012008. DOI: 10.1088/1757-899X/888/1/012008

6. Bremner, T.W. Lightweight concrete Developments in the Formulation and Reinforcement of Concrete. Elsevier Ltd, 2008. Pp. 167–186.

7. Hashim Abbas, Z., Harith, I., Dhahir, M.K. Utilization of Dates Palm Kernel in High Performance Concrete. Journal of Building Engineering. 2018. 20. DOI: 10.1016/j.jobe.2018.07.015

8. C330/C330M-14 A. Standard Specification For Lightweight Aggregates For Structural Concrete. 2014. 4.

9. Poster, D.L., Small, J.A., Postek, M.T. Material Standards for Environmental Health and Safety for Engineered Nanoscale Materials. 2007.

10. Nilson, A.H., Martinez, S. Mechanical properties of high-strength lightweight concrete. Journal proceedings. 1986. Pp. 606–613.

11. Varghese, L., Rao, V.V.L.K., Parameswaran, L. Nanosilica-added concrete: strength and its correlation with time-dependent properties. Proceedings of the Institution of Civil Engineers - Construction Materials. 2017. Pp. 1–10. DOI: 10.1680/jcoma.17.00031

12. Jo, B.W., Kim, C.H., Tae, G.-h., Park, J.-B. Characteristics of cement mortar with nano-SiO2 particles. Construction and Building Materials. 2007. 21(6). Pp. 1351–1355. DOI: 10.1016/j.conbuildmat.2005.12.020

13. Belkowitz, J., Armentrout, D.L. The investigation of nano silica in the cement hydration process. ACI Spec Publ. 2009. Pp. 87–100.

14. Haruehansapong, S., Pulngern, T., Chucheepsakul, S. Effect of the particle size of nanosilica on the compressive strength and the optimum replacement content of cement mortar containing nano-SiO2. 2014. Construction and Building Materials. 50. Pp. 471–477. DOI: 10.1016/j.conbuildmat.2013.10.002

15. Hou, P., Kawashima, S., Kong, D., Corr, D.J., Qian, J., Shah, S.P. Modification effects of colloidal nanoSiO2 on cement hydration and its gel property. Composites Part B: Engineering. 2013. 45(1). Pp. 440–448. DOI: 10.1016/j.compositesb.2012.05.056

16. Björnström, J., Martinelli, A., Matic, A., Börjesson, L., Panas, I. Accelerating effects of colloidal nano-silica for beneficial calcium-silicate-hydrate formation in cement. Chemical Physical Letters. 2004. 392(3). Pp. 242–248. DOI: 10.1016/j.cplett.2004.05.071

17. Sikora, P., Rucinska, T., Stephan, D., Chung, S.Y., Abd Elrahman, M. Evaluating the effects of nanosilica on the material properties of lightweight and ultra-lightweight concrete using image-based approaches. Construction and Building Material. 2020. 264. 120241. DOI: 10.1016/j.conbuildmat.2020.120241

18. Mendoza, O., Sierra, G., Tobón, J.I. Effect of the reagglomeration process of multi-walled carbon nanotubes dispersions on the early activity of nanosilica in cement composites. Construction and Building Material. 2014. 54. Pp. 550–557. DOI: 10.1016/j.conbuildmat.2013.12.084

19. Yakovlev, G.I., Skripkiunas, G., Polianskich, I.S., Lahayne, O., Eberhardsteiner, J., Urkhanova, L.A., et al. Modification of Cement Matrix Using Carbon Nanotube Dispersions and Nanosilica. Procedia Engineering. 2017. 172. Pp. 1261–1269. DOI: 10.1016/J.PROENG.2017.02.148

20. Lam, L.H., Duy, L.D., Huu, P.D. Application of Nano-Silica in Concrete Bridges in Vietnam for Sustainable Development BT. Advances and Challenges in Structural Engineering. GeoMEast 2018. Sustainable Civil Infrastructures. Springer, Cham. 2019. Pp. 23–31. DOI: 10.1007/978-3-030-01932-7_3

21. ASTM A. C150/C150M-16e1: Standard Specification for Portland Cement. 2016.

22. Specification IS. No. 5/1984 Portland Cement. (COSQC) Baghdad; 1984.

23. ASTM C. 330-05. Standard specification for lightweight aggregates for structural concrete. 2006.

24. Wang, H., Hu, Y., Ning, F., Cong, W. Ultrasonic vibration-assisted laser engineered net shaping of Inconel 718 parts: Effects of ultrasonic frequency on microstructural and mechanical properties. Journal of Material Processing Technology. 2020. 276. 116395. DOI: 10.1016/j.jmatprotec.2019.116395

25. BS 1881-116 Testing concrete. Part 116: method for determination of compressive strength of concrete cubes. British.1983 36.

26. BS 1881-101 Testing concrete. Part 101: Method of sampling fresh concrete on site. British Standard Institution. 1983.

27. ASTM C. 642 06: Standard test method for density Absorption, and Voids in Hardened Concrete. 1997.

28. Marchand, J., Hornain, H., Diamond, S., Pigeon, M., Guiraud, H. The microstructure of dry concrete products. Journal of Cement Concrete Research. 1996. 26(3). Pp. 427–438.

29. Santos, A.G., Rincón, J.M., Romero, M., Talero, R. Characterization of a polypropylene fibered cement composite using ESEM, FESEM and mechanical testing. Journal of Construction and Building Material. 2005. 19(5). Pp. 396–403. DOI: 10.1016/j.conbuildmat.2004.07.023

30. Adak, D., Sarkar, M., Mandal, S. Structural performance of nano-silica modified fly-ash based geopolymer concrete. Journal of Construction and Building Material. 2017. 135. Pp. 430–439. DOI: 10.1016/j.conbuildmat.2016.12.111

31. Shi, X., Fay, L., Peterson, M.M., Berry, M., Mooney, M. A FESEM/EDX investigation into how continuous deicer exposure affects the chemistry of Portland cement concrete. Journal of Construction and Building Material. 2011. 25(2). Pp. 957–966. DOI: 10.1016/j.conbuildmat.2010.06.086

Information about authors:

Sahar I. Ahmed,
E-mail: as.18.48@grad.uotechnology.edu.iq

Awham M. Hameed,
E-mail: awham.m.hameed@uotechnology.edu.iq

Aqeel Sh. Al-Adili,
E-mail: Aqeeladili@hotmail.com

Research article

Assessment of two nearby interfering strip footings of different embedment depths in saturated cohesive soils

M.A. Ayasrah [1] ✉ (iD) **, M.Y. Fattah** [2]

[1]*Department of Civil Engineering, Faculty of Engineering, Al Al-Bayt University, Mafraq 25113, Jordan*

[2]*Civil Engineering Department, University of Technology, Baghdad, Iraq*

✉ momen_992@yahoo.com

Abstract. There are instances where foundations are closely spaced, such as around railroad sleepers and foundations close to property lines. In such circumstances, the stress isobars of the separate footings may interact and combine to generate an overlapping stress isobar that affects a wider zone of the foundation soil and alters the individual foundations behavior, which would be different from that of the isolated footings. As a result, an examination of such issues should be conducted by taking into account all the variables that realistically affect the interference behavior of such closely spaced footings. This paper has been conducted to understand the behaviour of closely placed strip footings of different depths embedded in saturated cohesive soils under various factors such as the groundwater table, soil undrained shear strength, footing depth, and the spacing between footings using a three-dimensional finite element model (Midas GTS-NX). The evaluated ultimate bearing capacity (UBC) and settlements are represented in terms of non-dimensional efficiency factors for UBC: ξ_L/ξ_R (Left/Right). It was concluded that when the spacing between footings is increased from S/B = 1 to 2, there would be an increase in the UBC of both footings when D_{fr}/D_{fl} increases, then the bearing capacity decreases when S/B is increased to 4. For footings of different embedment depths, when the ground water table is deep (at 4 m depth), the values of UBC ratio ξ_R increase with S/B while ξ_L decreases. This is because of various embedment between the two adjacent footings. In all cases, when the ground water table is at the ground surface, lower values in ξ_L are at Cu = 60 kPa, while the higher values in ξ_R are found at this strength.

1. Introduction

One significant design factor to take into account is the settlement of foundations under working load situations. Designed effectively foundations cause the soil to develop stress-strain conditions that are neither linearly elastic nor perfectly plastic [1]. Settlements usually prioritize footing construction over bearing capacity when working with soft clay and sand. Therefore, for the construction of shallow foundations, settlement calculations are crucial. The impact of nearby footings is usually disregarded while assessing isolated footing capacity when taking permissible settlement requirements into account. In this regard, numerous studies using both experimental and numerical methods have been performed to determine the interference impact of two nearby shallow foundations [2].

According to Kumar and Ghosh (2007) [3], an upper bound limit analysis was used to ascertain the ultimate bearing capacity (UBC) of two closely spaced strip footings installed on a cohesionless medium that were loaded simultaneously to failure at the same magnitude of the failure load. Each footing edge was

assumed to have a logarithmic spiral radial shear zone made up of many triangular rigid blocks. The ultimate bearing capacity was discovered to correspond to a specific essential spacing between the two footings. For spacing greater than the critical, it was discovered that the bearing capacity decreased continuously as the distance increased. The obtained results indicate a reasonable degree of agreement with the available experimental and theoretical data.

In the article [4], an attempt has been made to simulate the settling behavior of two strip footings situated near each other on a layered soil deposit, featuring a strong upper layer and a weaker lower layer. The governing differential equations were derived using the theory of elasticity and then solved using the finite difference analysis. Many parameters have been investigated on the settlement behavior of closely spaced footings, such as the footing load, clear distance between the footings, and the elastic moduli and thickness of the two layers. The results of the theoretical investigation show that the settlement of closely spaced footings is larger than that of a single isolated footing and that the settlement decreases as the spacing between the footings increases.

The interaction of two closely spaced rigid strip footings resting on a homogeneous soil bed was examined in [2] using finite element analysis (FEA) in order to find their UBC and settlement behavior subjected to inclined loading. The foundation soil was modeled as elastoplastic material obeying the Mohr-Coulomb failure criterion. Numerous parametric studies were performed by varying the angle of inclination of load and clear spacing between the footings. The findings showed that both bearing capacity and settlement of interacting footings compared to that of an isolated footing increased with decrease in spacing, whereas the effect on the UBC for footings was not significant.

On the other hand, the performance of two closely spaced strip footings resting on the surface of the semi-infinite clay soil medium was examined [4]. Two-dimensional plane strain FEA was used to observe the effect of interference on characteristic behavior such as bearing pressure, tilt, and settlement. A parametric study has been conducted by altering the clear spacing and depth of the footings and examining the impact of these changes on the load-settlement characteristic, bearing pressure, and settlement variation with clear spacing. The study concluded that the interference impacted the isolated footing's performance. In contrast, the study observed an increase in settlement compared to the isolated footing, and a decrease in bearing pressure as the clear spacing between the footings decreased.

Parametric studies were done in [6] for two foundations by varying the spacing between the foundations and the footing width. In the first instance, both footings were simultaneously loaded up to failure. In the second instance, an already existing footing was loaded with half of the estimated failure load of single independent strip footing and second adjacent footing was loaded up to failure. The interference effect was observed to be particularly significant in terms of the settlement and tilt. In addition, it was observed that the presence of shear keys has a significant effect on interference between footings when compared to not having them, particularly in reducing foundation tilt.

However, the impact of the embedment on the interaction of closely spaced footings is seldom highlighted. In order to better understand the effect of footing depth on the interference effect, two adjacent interfering strip footings at different depths in saturated cohesive soils were studied.

In this study, two strip footings are considered to investigate the effect of their interference on the bearing capacity of saturated cohesive soils. The strip footings have 0.3 m of thickness (H) and 2.0 m of width (B), as shown in Fig. 1. In addition, the depth of footings (D_f), the spacing between footings (S), the undrained shear strength of the clay (C_u), and the groundwater table level (GWT) are changed. As a result, FEA is applied to each case. Table 1 lists the parametric studies considered in this analysis.
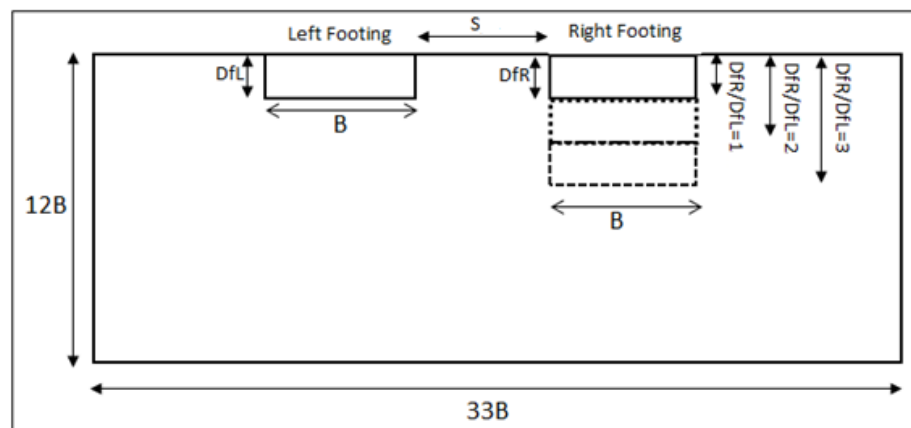
Figure 1. Schematic representation of nearby footings.

Table1. Soil properties, footings, and parametric studies.

Parameters	γ, kN/m³	Cu, kN/m²	E, kN/m²	υ
		40	40000	
Clay	18	60	60000	0.3
		100	100000	
Footings	24		25x10⁶	0.2
Range of varying parameters				
S/B	0.5	1	2	4
GWT	0	2	4	
Cu	40	60	100	
Special Case: Footings of different depths				
Depth of left footing, Dfl		1 m	1 m	1 m
Depth of right footing, Dfr		1 m	2 m	3 m
Dfr/Dfl		1	2	3

2. Methods

2.1. Finite Element Method

In this study, the behavior of closely spaced strip footings embedded in saturated cohesive soils is examined numerically using a finite element analysis (Midas GTS-NX). The model size was 33B x 12B in both horizontal and vertical directions, with B representing the width of the strip footings. These dimensions were sufficient to reduce boundary effects in numerical modeling, as increasing mesh size did not affect the study results. Furthermore, the mesh simulation was conducted using a reasonably fine mesh close to the strip footings and a coarser mesh further away from these zones. The boundary condition assumed that the bottom surface was hinged to prevent both horizontal and vertical movement and that a roller had been applied to the right and left sides of the soil to permit only vertical movement [7-10]. Fig. 2 displays the geometrical boundaries and plane strain mesh. It is important to note that the load on each footing is applied with uniform pressure. The mesh of this model has 6591 components and 6706 nodes. Due to the auto mesh generating method used by the Midas GTS-NX program, it should be noted that the numbers of elements and nodes in each model differ slightly.
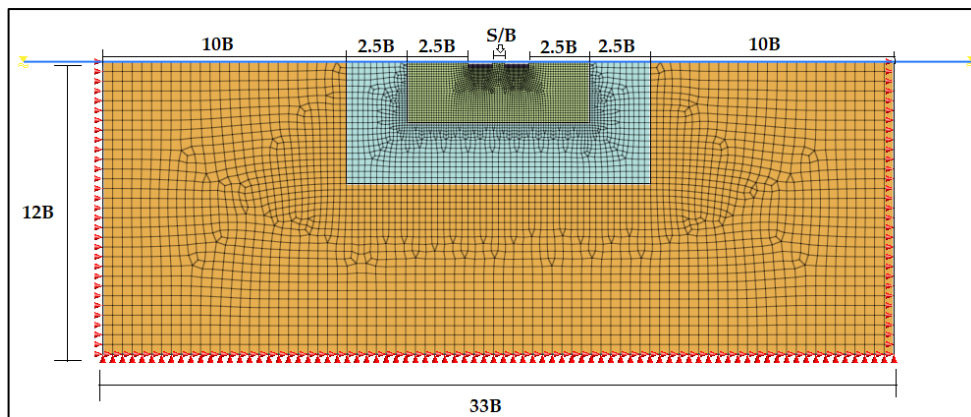
Figure 2. Finite element mesh of the problem and boundary conditions.

The soil was simulated using the Mohr-Coulomb constitutive model because of its simplicity and correctness [11]. This model is widely used in the FEA of geotechnical engineering, including the undrained bearing capacity problems [12–22]. In addition, a linear elastic model was used to simulate the footings. Table 1 presents the required soil and footing parameters.

In the current study, all the models are simulated using Midas GTS-NX utilizing the undrained parameters. Consequently, the dilation angle (ψ) and friction angle (φ) are equal to zero under undrained conditions. Moreover, the undrained modulus of clays (E_u) is estimated using the following equation, which is suggested by [23]:

$$E = (100 - 1000) Cu. \tag{1}$$

Fundamental to note that the undrained Poisson's ratio for soil undrained is used with 0.495 rather than 0.50 to evade any numerical issues. In addition, the drainage parameter is selected with the third option: Undrained (Effective stiffness/Undrained strength) in Midas GTS-NX. Furthermore, the lateral earth pressure coefficient at rest (k_0) has been computed as 1.00, using the following equation:

$$k_0 = \frac{v}{(1-v)},$$ (2)

where v is undrained Poisson's ratio.

2.2.   Construction Stages

The two-dimensional model was constructed using the same soil characteristics and footing elements stated in Table 1. The stages are summed up as follows:

1. Initial Stage (I.S): this stage starts with applying the gravity load to create the initial soil stress prior to the installation of strip footings. Also, the boundary conditions were activated in this stage.

2. Stage 1 (S1): Both footings are installed. Moreover, the displacements were reset to zero at this stage to begin calculating the bearing capacity resulting from the applied loads alone.

3. Stage 2 (S2): the loads were applied using Forty incremental loading steps to simulate the load-settlement behavior.

2.3.   Definition of Bearing Capacity Ratio (ξ)

The evaluated UBC (q_u) and settlements are represented in terms of non-dimensional efficiency factors for UBC: ξ_L / ξ_R (Left/Right).

$$\xi_L / \xi_R = \frac{q_u \; of \; left/right \; footing \; in \; presence \; of \; right/left \; footing}{q_u \; of \; identical \; isolated \; footing}.$$ (3)

3.   Results and Discussions

Fig. 3 shows the load-settlement curves for the two nearby footings in clayey soil with Cu = 40 kPa of different embedment depths and water table level. The values of bearing capacity of all the cases analyzed in this study are summarized in Table 2.

a)
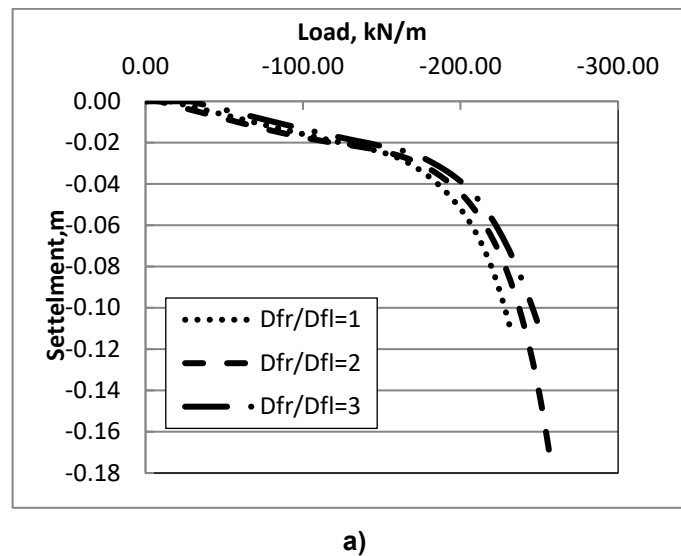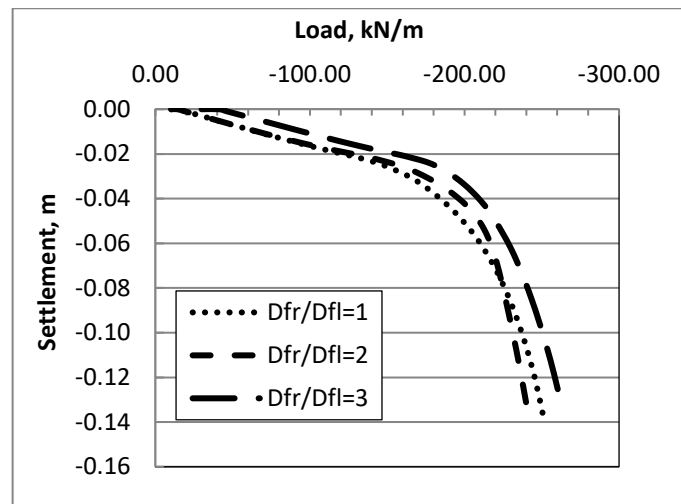
b)
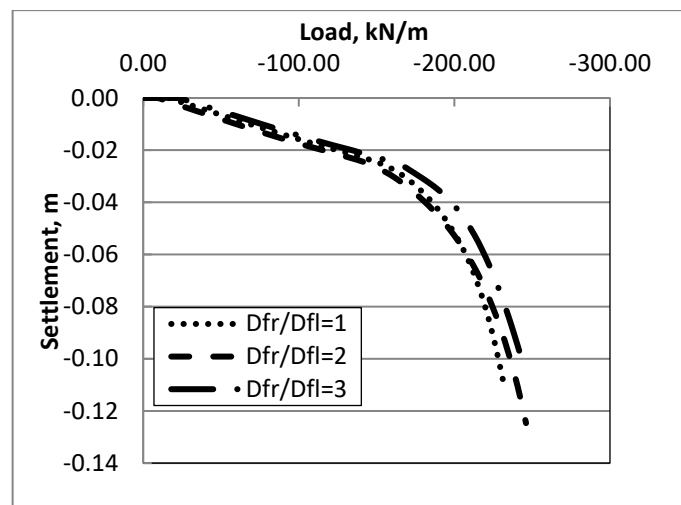
c)

Figure 3. Load settlement curve on soil with Cu = 40 kPa for left and right footing with S/B=0.5 and a) GWT= 0, b) GWT = 2 m and c) GWT = 4 m.

Table 2. Ultimate bearing capacity of footings based on the load settlement curves.

Cu, kPa	GWT m	S/B	D_{fr}/D_{fl}	q_u kPa	Cu kPa	GWT m	S/B	D_{fr}/D_{fl}	q_u kPa	Cu kPa	GWT m	S/B	D_{fr}/D_{fl}	q_u kPa
			1	280				1	350				1	588
		1	2	285			1	2	365			1	2	594
			3	290				3	375				3	600
			1	250				1	340				1	580
	0	2	2	260		0	2	2	350		0	2	2	587
			3	275				3	365				3	596
			1	245				1	338				1	575
40		4	2	250	60		4	2	347	100		4	2	582
			3	265				3	355				3	588
			1	290				1	375				1	592
		1	2	294			1	2	383			1	2	597
	2		3	300		2		3	390		2		3	605
			1	255				1	365				1	585
		2	2	265			2	2	374			2	2	592
			3	278				3	380				3	598

C_u, kPa	GWT m	S/B	D_{fr}/D_{fl}	q_u kPa	C_u kPa	GWT m	S/B	D_{fr}/D_{fl}	q_u kPa	C_u kPa	GWT m	S/B	D_{fr}/D_{fl}	q_u kPa
			1	253				1	360				1	580
	4	4	2	260		4	4	2	367		4	4	2	585
			3	269				3	375				3	592
			1	295				1	390				1	595
		1	2	300			1	2	395			1	2	600
			3	305				3	403				3	607
			1	275				1	383				1	590
4	2	2	2	280		4	2	2	390		4	2	2	594
			3	287				3	397				3	601
			1	265				1	378				1	585
		4	2	270			4	2	384			4	2	593
			3	280				3	390				3	597

It is noticed that the bearing capacity values increase with the increase of the undrained shear strength, depth of footing, and water table depth.

When the spacing between footings is increased from S/B = 1 to 2, there would be an increase in UBC of both footings when Dfr/Dfl increases. In addition, the bearing capacity decreases when S/B is increased to 4. This can be illustrated as follows. When S/B = 1, there must be some interlocking between the failure slip surfaces of the nearby footings, which decreases the ultimate bearing capacity, such interlocking is overcome when S/B becomes 2. As the spacing ratio increases to S/B = 4, the footings act separately and the effect of confinement vanishes.

According to test results obtained by [24, 25], the presence of a bounding wall has a significant impact on bearing capacity, improving it by varying percentages depending on the wall's depth and distance from the edge of the footing. This improvement is caused by an increase in soil confinement beneath the footing.

3.1. Footings of Different Depths

Fig. 4–7 present the variation of bearing capacity ratio for the left and right footings with Cu for different spacing between footings and water table level. Table 3 summarizes the values of ξ_L and ξ_R for different S/B values when Cu = 40 kPa. Table 4 present the values for footings with Cu = 60 and 100 kPa. In all cases, when the ground water table is at the ground surface, lower values in ξ_L are at Cu = 60 kPa, while the higher values in ξ_R are found at this strength.

Table 3. Variation of ξ_L and ξ_R with S/B for D_{fr}/D_{fl}, Cu = 40 kPa.

GWT (m)	S/B	D_{fr}/D_{fl}	ξ_L	ξ_R
		1	1.00	1.01
	1	2	1.02	1.08
		3	1.05	1.12
		1	0.98	0.99
0	2	2	1.00	1.02
		3	1.04	1.06
		1	0.96	0.97
	4	2	0.98	1.00
		3	1.02	1.04
		1	0.99	1.00
	1	2	1.03	1.05
2		3	1.05	1.08
	2	1	0.98	1.00
		2	1.02	1.04

GWT (m)	S/B	D_{fr}/D_{fl}	ξ_L	ξ_R
		3	1.04	1.06
		1	0.98	0.97
	4	2	1.01	1.02
		3	1.02	1.05
		1	0.99	1.00
	1	2	1.03	1.05
		3	1.05	1.08
		1	0.98	1.00
4	2	2	1.02	1.04
		3	1.04	1.06
		1	0.98	0.97
	4	2	1.01	1.02
		3	1.02	1.05

Table 4. Extent of variation of ξ_L and ξ_R with S/B for D_{fr}/D_{fl}, Cu = 60 and 100 kPa.

Cu (kPa)	GWT (m)	S/B	D_{fr}/D_{fl}	ξ_L	ξ_R	Cu (kPa)	GWT	S/B	D_{fr}/D_{fl}	ξ_L	ξ_R
		1	1	0.97	0.98			1	1	1.03	1.04
			2	1.00	1.01				2	1.05	1.06
			3	1.01	1.06				3	1.06	1.07
		2	1	0.96	0.97			2	1	1.03	1.04
	0		2	0.99	1.00		0		2	1.04	1.05
			3	1.00	1.04				3	1.05	1.06
		4	1	0.95	0.96			4	1	1.02	1.03
			2	0.97	0.98				2	1.03	1.04
			3	0.99	1.03				3	1.04	1.05
		1	1	0.96	0.97			1	1	1.02	1.03
			2	0.99	1.00				2	1.03	1.05
			3	1.01	1.03				3	1.04	1.06
60	2	2	1	0.95	0.96	100	2	2	1	1.01	1.02
			2	0.97	0.99				2	1.02	1.04
			3	1.00	1.01				3	1.03	1.06
		4	1	0.94	0.95			4	1	1.00	1.02
			2	0.96	0.98				2	1.01	1.04
			3	0.97	1.00				3	1.02	1.05
		1	1	0.95	0.96			1	1	1.02	1.03
			2	0.99	1.01				2	1.03	1.04
			3	1.01	1.02				3	1.04	1.05
		2	1	0.94	0.95			2	1	1.01	1.02
	4		2	0.97	0.98		4		2	1.02	1.03
			3	0.99	1.00				3	1.03	1.04
		4	1	0.93	0.94			4	1	1.00	1.01
			2	0.96	0.97				2	1.01	1.02
			3	0.98	0.99				3	1.02	1.04
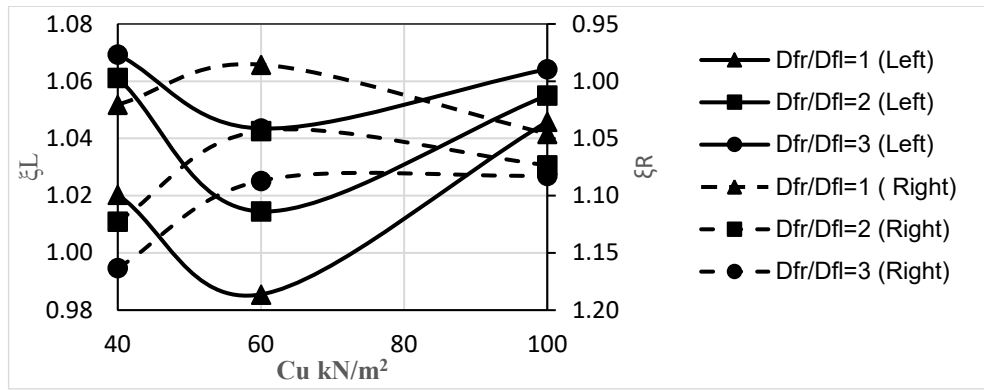
a)
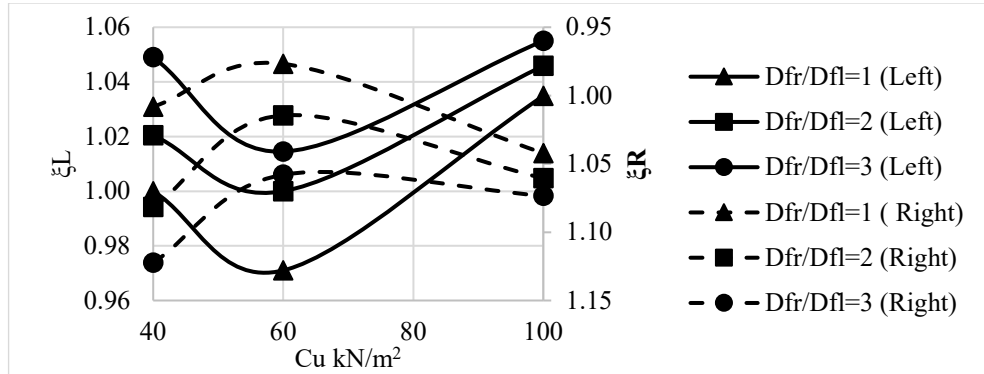
b)
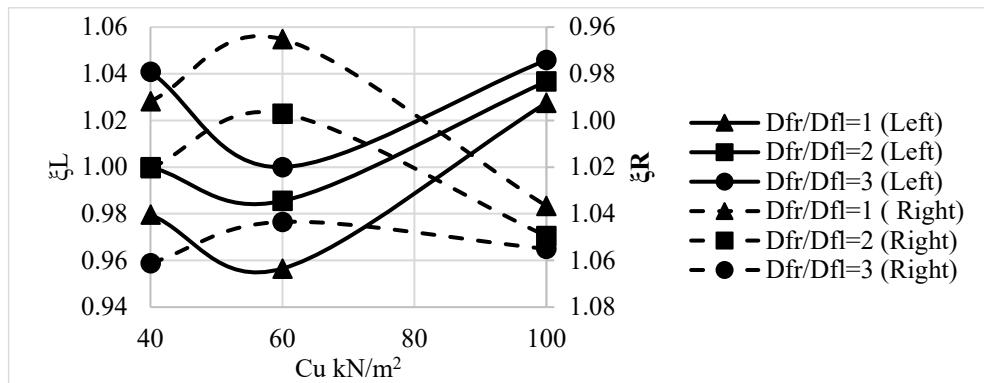
c)
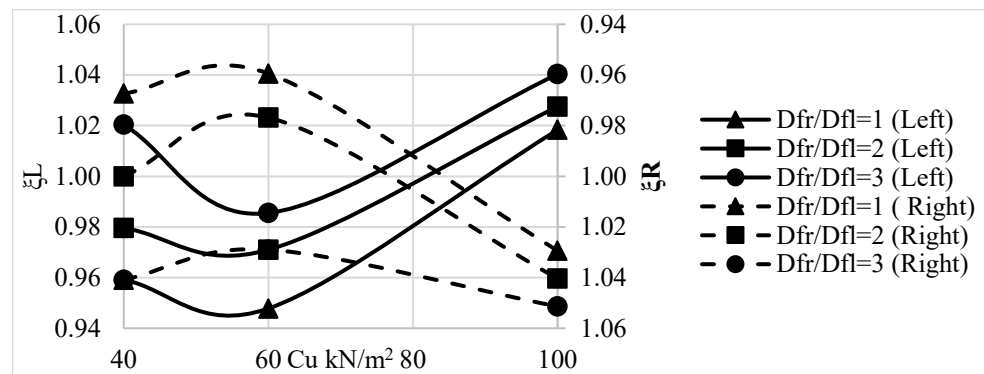
d)

Figure 4. Variation of ξ_L ξ_R with Cu for different D_{fr}/D_{fl} (left and right footing) and GWT = 0 for a) S/B = 0.25, b) S/B = 1, c) S/B = 2 and d) S/B = 4.
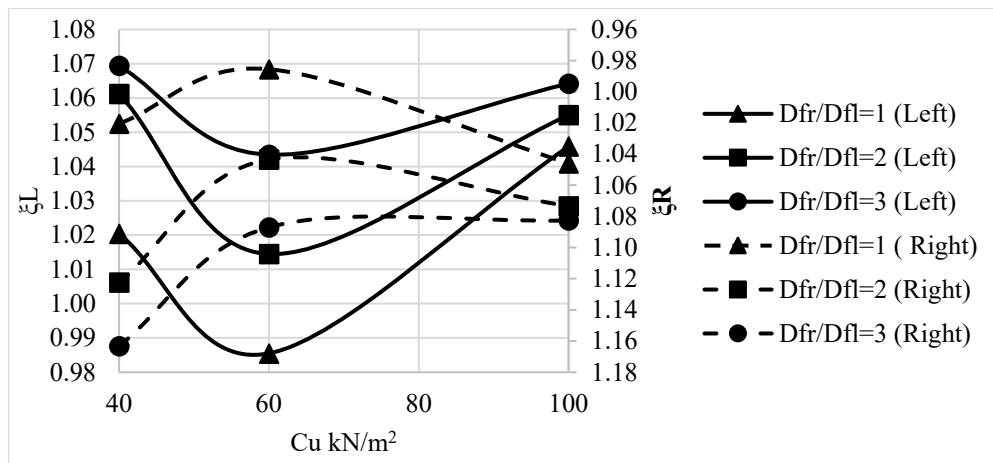
a)
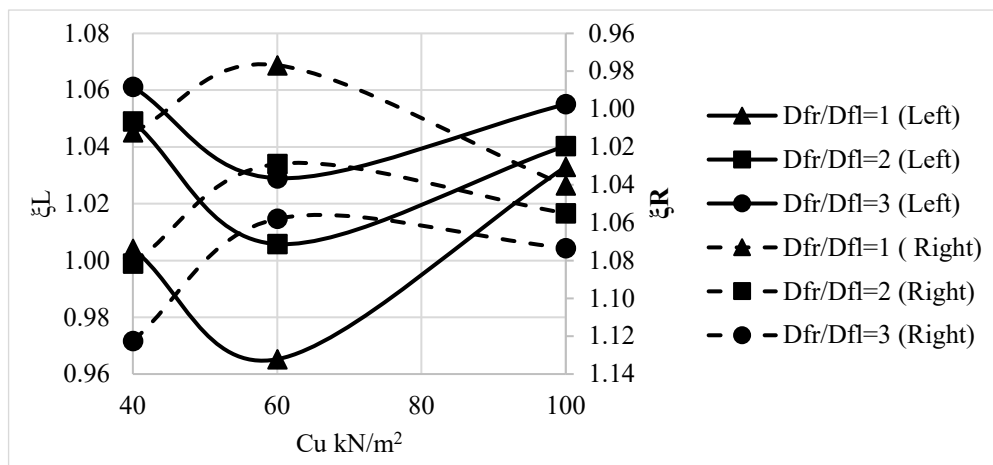
b)
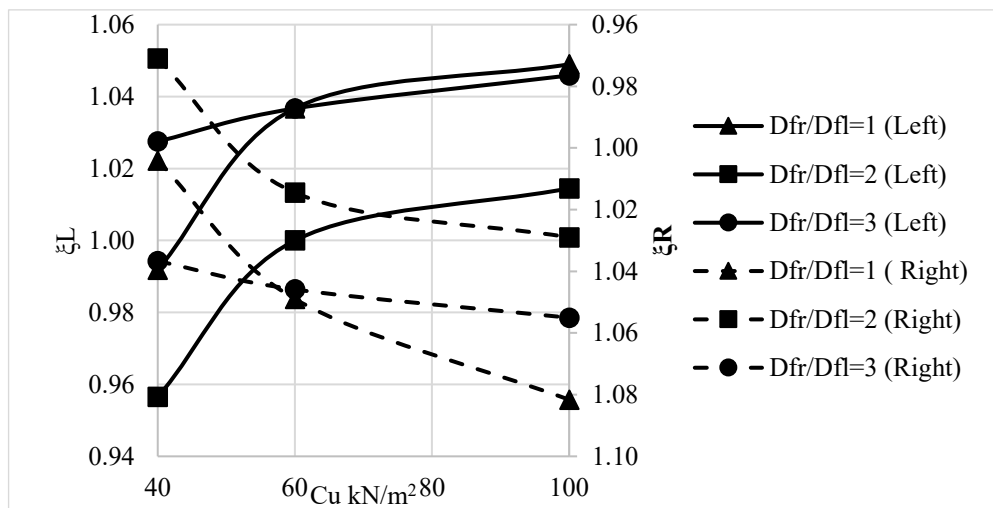
c)

Figure 5. Variation of ξ_L, ξ_R with Cu for different D_{fr}/D_{fl} (left and right footing) and S/B = 0.5 for a) GWT = 0, b) GWT = 2 m, and c) GWT = 4 m.
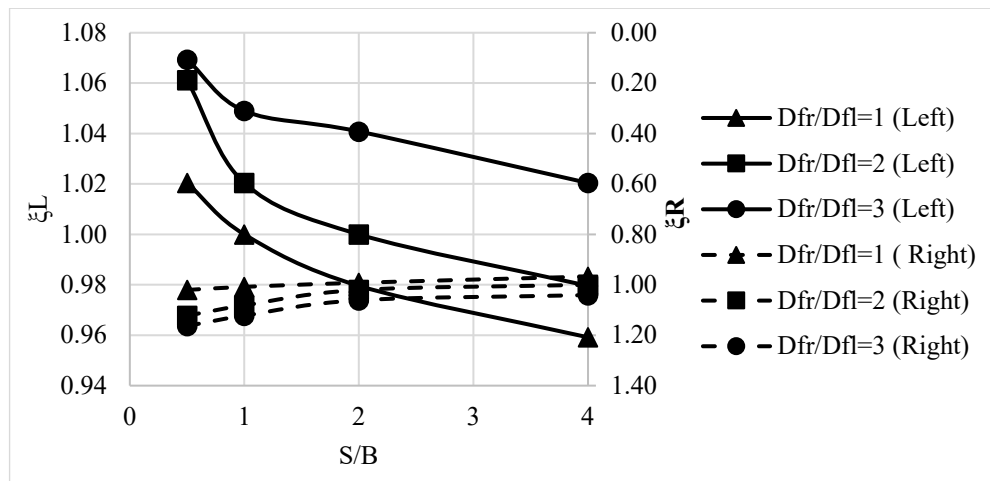
a)
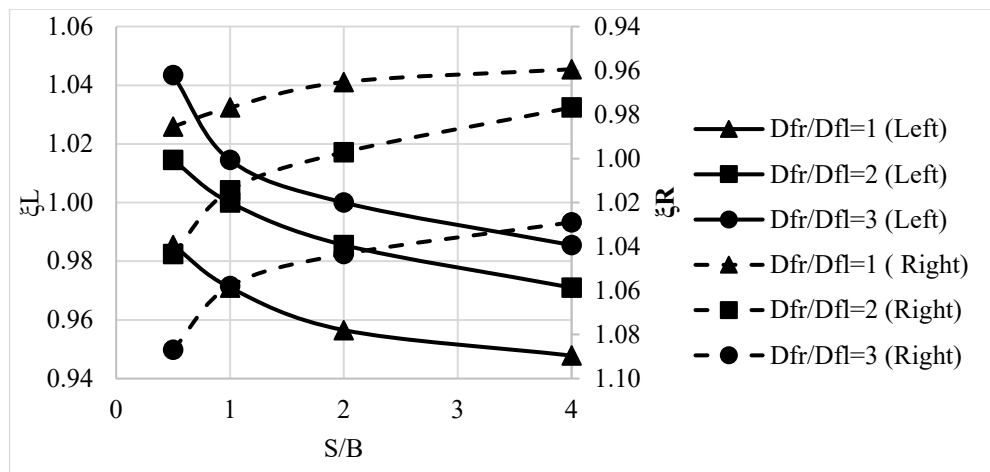
b)
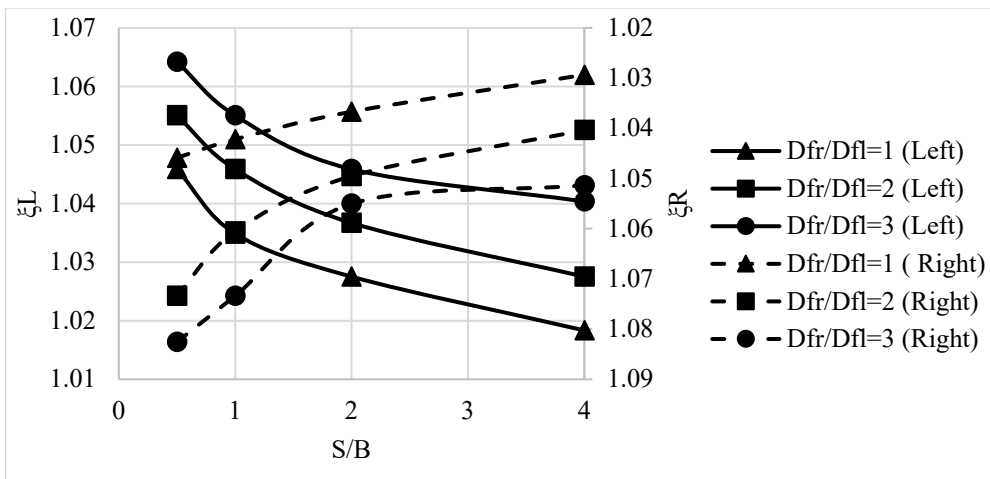
c)

Figure 6. Variation of ξ_L, ξ_R with S/B for different D_{fr}/D_{fl} (left and right footing) and $GWT = 0$ for a) $Cu = 40$, b) $Cu = 60$, and c) $Cu = 100$.
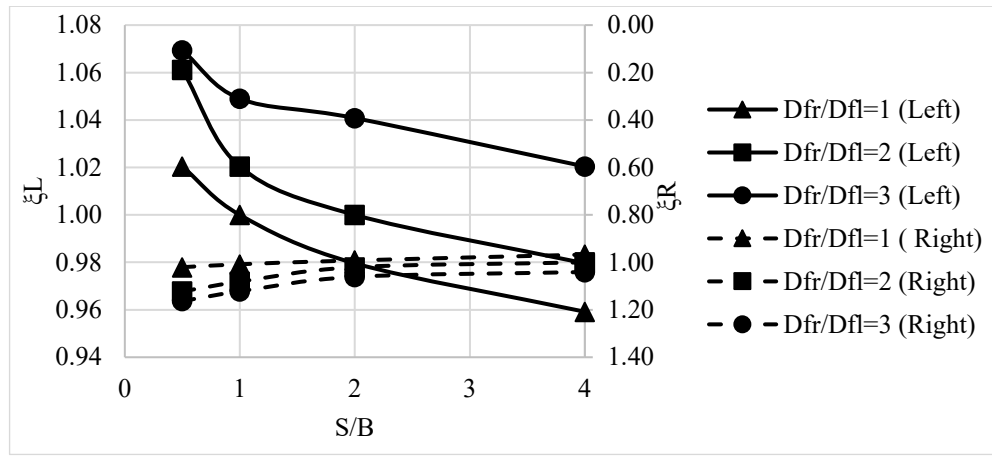
a)
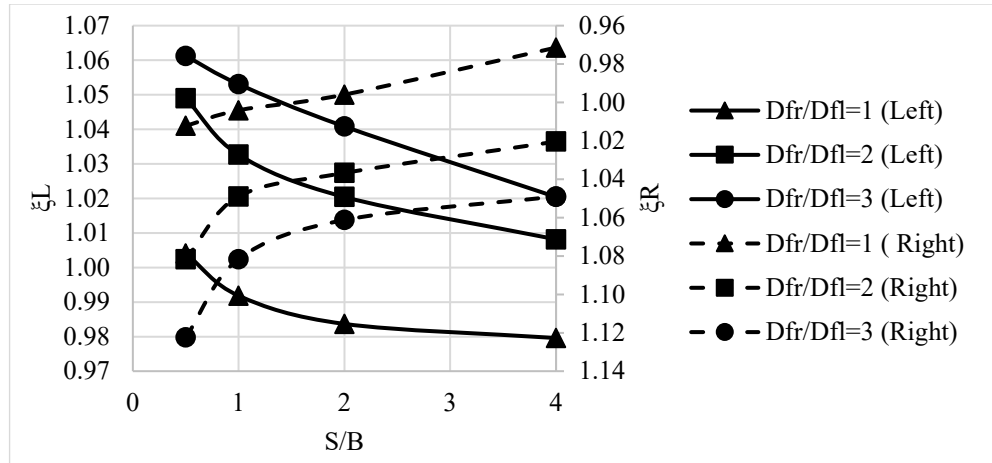
b)
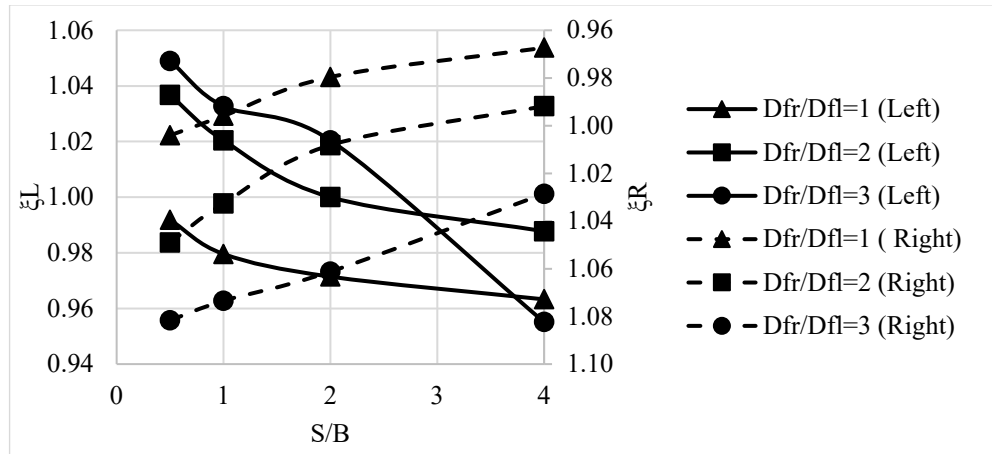
c)

Figure 7. Variation of ξ_L, ξ_R with S/B for different D_{fr}/D_{fl} (left and right footing) and Cu = 40 for a) GWT = 0, b) GWT = 2, and c) GWT = 4 m.

When the ground water table is deeper (at 4 m depth), the values of ξ_R increase with S/B while the values of ξ_L decrease. This is caused by the embedment of right footing. Fig. 8 displays clearly the extension of failure zones below footings when the depth of nearby footings changes from D_{fr}/D_{fl} = 1 to 2 and 3.

a)

b)

c)
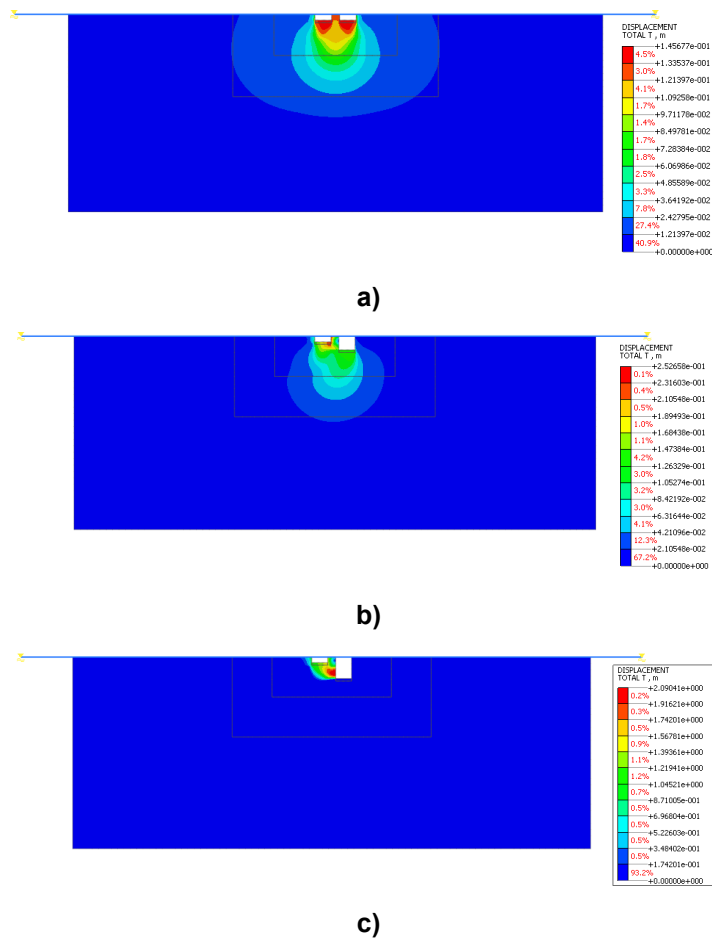
Figure 8. Total-displacement contour plots for footings of different depths when Cu = 40 kPa, GWT = 0, and S/B = 0.5 for a) D_{fr}/D_{fl} = 1, b) D_{fr}/D_{fl} = 2, and c) D_{fr}/D_{fl} = 3.

4. Conclusions

This paper examined the impact of two adjacent interfering strip footings embedded in saturated cohesive soils. For this purpose, the finite element program Midas GTS-NX has been adopted. The following major conclusions can be drawn from the results:

1. The soil cohesion and the footing depth ratio have a notable influence on the interference of closely spaced footings.

2. When the spacing between footings is increased from S/B = 1 to 2, there would be an increase in the ultimate bearing capacity of both footings when D_{fr}/D_{fl} increases, then the bearing capacity decreases when S/B is increased to 4.

3. For footings of different embedment depths, when the ground water table is deep (at 4 m depth), the values of ξ_R increase with S/B, while the values of ξ_L decrease. This is caused by the embedment of right footing.

4. In all cases, when the ground water table is at the ground surface, lower values in ξ_L are at Cu = 60 kPa, while the higher values in ξ_R are found at this strength.

References

1. Lee, J., Salgado, R. Estimation of footing settlement in sand. The International Journal Geomechanics. 2002; 2(1):1-28. DOI: 10.1061/(asce)1532-3641(2002)2:1(1).

2. Nainegali, L.S., Ghosh, P., Basudhar, P.K. Interaction of nearby strip footings under inclined loading. Proceedings of the 18th International Conference on Soil Mechanics and Geotechnical Engineering. Paris, 2013. Pp. 3459–3462.

3. Kumar, J., Ghosh, P. Upper bound limit analysis for finding interference effect of two nearby strip footings on sand. Geotechnical and Geological Engineering. 2007. 25. Pp. 499–507. DOI: 10.1007/s10706-007-9124-9

4. Ghosh, P., Sharma, A. Interference effect of two nearby strip footings on layered soil: theory of elasticity approach. Acta Geotechnica. 2010. 5. Pp. 189–198. DOI: 10.1007/s11440-010-0123-2

5. Nainegali, L., Ekbote, A.G. Interference of two nearby footings resting on clay medium. Geotechnical Applications: Lecture Notes in Civil Engineering. 2019. 13. Pp. 59–67. DOI: 10.1007/978-981-13-0368-5_7

6. Anaswara, S., Shivashankar, R. A numerical study on interference effects of closely spaced strip footings on cohesionless soils. Recent Trends in Civil Engineering. 2021. 105. Pp. 231–237. DOI: 10.1007/978-981-15-8293-6_20

7. Ayasrah, M., Fattah, M.Y. Finite Element Analysis of Two Nearby Interfering Strip Footings Embedded in Saturated Cohesive Soils. Civil Engineering Journal. 2023. 9(3). Pp. 752–769. DOI: 10.28991/CEJ-2023-09-03-017

8. Azzam, W. R., Basha, A. M. Utilization of micro-piles for improving the sub-grade under the existing strip foundation: experimental and numerical study. Innovative Infrastructure Solutions. 2018. 3, 1-11. DOI: 10.1007/s41062-018-0149-0

9. Chavda, J. T., Dodagoudar, G. R. Finite element evaluation of ultimate capacity of strip footing: assessment using various constitutive models and sensitivity analysis. Innovative Infrastructure Solutions. 2018. 3, 1-10. DOI: 10.1007/s41062-017-0121-4

10. Ekbote, A. G., Nainegali, L. Interference of two closely spaced footings embedded in unreinforced and reinforced soil medium: a finite element approach using ABAQUS. Arabian Journal of Geosciences. 2019. 12, 1-21. DOI: 10.1007/s12517-019-4868-0

11. Chen, W.F., Saleeb, A.F. Constitutive Equations for Engineering Materials. Amsterdam: Elsevier, 1982.

12. Wang, G., Sitar, N. Numerical analysis of piles in elasto-plastic soils under axial loading. 17th ASCE Engineering Mechanics Conference. Newark, DE, 2004.

13. Merifield, R.S., Nguyen, V.Q. Two- and three-dimensional bearing-capacity solutions for footings on two-layered clays. Geomechanics and Geoengineering: An International Journal. 2006. 1(2). Pp. 151–162. DOI: 10.1080/17486020600632637

14. Seol, H., Jeong, S., Kim, Y. Load transfer analysis of rock-socketed drilled shafts by coupled soil resistance. Computers and Geotechnics. 2009. 36(3). Pp. 446–453. DOI: 10.1016/j.compgeo.2008.08.012

15. Nguyen, V.Q., Merifield, R.S. Undrained bearing capacity of surface footings near slopes. Australian Geomechanics. 2011. 46(1). Pp. 77–94.

16. Lee, J.K., Jeong, S., Shang, J.Q. Undrained bearing capacity of ring foundations on two-layered clays. Ocean engineering. 2016. 119. Pp. 47–57. DOI: 10.1016/j.oceaneng.2016.04.019

17. Ouahab, M.Y., Mabrouki, A., Frank, R., Mellas, M., Benmeddour, D. Undrained bearing capacity of strip footings under inclined load on non-homogeneous clay underlain by a rough rigid base. Geotechnical and Geological Engineering. 2020. 38. Pp. 1733–1745. DOI: 10.1007/s10706-019-01127-1

18. Zhu, M., Michalowski, R.L. Shape factors for limit loads on square and rectangular footings. Journal of Geotechnical and Geoenvironmental Engineering. 2005. 131(2). Pp. 223–231. DOI: 10.1061/(ASCE)1090-0241(2005)131:2(223)

19. Zhang, Q., Wu, S., Wu, L., Liu, Z. Theoretical analysis of bearing capacity of shallowly embeded rectangular footing of marine structures. Journal of Ocean University of China. 2019. 18. Pp. 123–132. DOI: 10.1007/s11802-019-3792-y

20. Li, J.-P., Chen, L.-Y., Liang, F.-Y. Effects of footing shape on bearing capacity of rectangular footings. Contemporary Topics in Ground Modification, Problem Soils, and Geo-Support. 2009. Pp. 481–487. DOI: 10.1061/41023(337)61

21. Pusadkar, S.S., Ninghot, K.R. Interference of square footing on layered soil subjected to vertical load. SSRG International Journal of Civil Engineering (SSRG–IJCE). 2016. 3(6). Pp. 8–12. DOI: 10.14445/23488352/IJCE-V3I6P102

22. Yin, J.-H., Wang, Y.-J., Selvadurai, A.P.S. Influence of nonassociativity on the bearing capacity of a strip footing. Journal of Geotechnical and Geoenvironmental Engineering. 2001. 127(11). Pp. 985–989. DOI: 10.1061/(ASCE)1090-0241(2001)127:11(985)

23. Ameratunga, J., Sivakuga, N., Das, B.M. Correlations of soil and rock properties in geotechnical engineering. New Delhi: Springer, 2016. DOI: 10.1007/978-81-322-2629-1

24. Fattah, M.Y., Shlash, K.T., Mohammed, H.A. Bearing capacity of rectangular footing on sandy soil bounded by a wall. Arabian Journal for Science and Engineering. 2014. 39. Pp. 7621–7633. DOI: 10.1007/s13369-014-1353-7

25. Fattah, M.Y., Shlash, K.T., Mohammed, H.A. Experimental study on the behavior of strip footing on sandy soil bounded by a wall. Arabian Journal of Geosciences. 2015. 8. Pp. 4779–4790. DOI: 10.1007/s12517-014-1564-y

Information about the author:

Mo'men A. Ayasrah, PhD
ORCID: https://orcid.org/0000-0003-3997-8009
E-mail: momen_992@yahoo.com

Mohammed Y. Fattah, PhD

E-mail: myf_1968@yahoo.com

Ultrasonic characterization of damage induced by temperature variations in concrete medium treated with nanosilica

S.H. Fartosy ✉ iD *, L.M. Abd, M. Kohees, Z.A. Hacheem*

Mustansiriyah University, Baghdad, Iraq

✉ *dr.sabah77@uomustansiriyah.edu.iq*

Abstract. Concrete is widely used as construction material in civil infrastructures. Generally, this type of material can deteriorate due to several reasons, such as temperature variations. It is essential to monitor the changes inside the concrete medium using a suitable technique. In this study, six concrete specimens (three prisms and three cylinders) with different nanosilica contents were made and tested using the ultrasonic pulse velocity (UPV) method. These specimens were evaluated under the effect of daily freeze-thaw (F-T) cycle (71 cycles) under controlled laboratory conditions. A new evaluation approach based on selected frequency bands is proposed to analyze the signal spectra to monitor the damage development inside the concrete medium under temperature variations and compared with other conventional procedures. The results obtained show that the proposed approach could capture the damage progress better than other procedures used to evaluate damage propagation in concrete medium. It is shown that the band with high frequencies (42–65 kHz) is more robust to capture damage in all concrete specimens tested in this study in comparison with the UPV methods. In conclusion, the findings of this study indicate that the proposed new approach can be applied to monitor damage propagation in concrete medium under laboratory and field conditions.

1. Introduction

Non-destructive testing (NDT) methods are widely used to characterize and assess the internal condition of concrete structures, such as deep foundations, bridges, buildings, pavements, dams, and others [1, 2]. In many situations, the consequences of deterioration can include excessive repair, shortened service life, and collapse of the structure. It is essential to assess the condition of concrete members during construction and throughout their service life. NDT methods are generally used for quality control of structure members, for condition assessment of existing structures, for rehabilitation and maintenance, and for quality control of repairs. Ultrasonic pulse velocity (UPV) method is one of these NDT methods that are used widely to assess the condition of cement-based elements, both in laboratory and field conditions.

Recently, the method has been used in various fields, such as chemistry, medicine, biology, engineering, and physics [3–5]. Ultrasound is used in civil engineering for material characterization by NDT. In concrete, the ultrasonic velocity is less sensitive than the wave attenuation [6–14]. Therefore, wave

attenuation may be considered as a key parameter that is required for material characterization. The importance of this parameter is due to the fact that any reduction in the wave attenuation (wave amplitude) indicates a loss of strength or degradation of the material's internal conditions [15, 16]. However, the use of wave attenuation has some limitations due to the difficulty of making reliable measurements at the testing site.

In cold climate areas, the freeze-thaw (F-T) cycle is considered to be the main parameter that causes deterioration in concrete structures [17]. P.J. Nixon [18] stated that V.M. Malhotra is a pioneer in using the UPV method (1976) to evaluate the F-T resistance of concrete containing recycled aggregates. The reduction in UPV was reported after certain F-T cycles, some of which were as high as 4 % after more than 600 cycles. Other researchers also used UPV as NDT procedure in F-T inspection [19, 20]. Other studies have discovered a few drawbacks of UPV under temperature variation [21, 22]. A. Erdélyi et al. [23] found that UPV measurements of heated dried specimens were significantly decreased after F-T cycles, but not on saturated specimens with NaCl. On the other hand, S.F. Selleck et al. [21] explained that the UPV sensitivity to detect changes of microcracking in concrete was not visible.

The literature review presented above highlighted the use of UPV as a suitable tool to assess the concrete conditions under temperature variation. However, the use of UPV alone cannot provide a reliable assessment to evaluate the crack propagation inside concrete medium due to the effect of temperature variations (F-T cycles). Using the wave attenuation under control conditions along with UPV can be considered as a reliable inspection technique to investigate the damages induced inside concrete medium subjected to F-T cycles. Based on that, a new approach is proposed in this study to assess the concrete conditions of specimens treated with nanosilica under F-T cycles.

The objective of this study is to investigate the ability of proposed new approach defining two frequency bands (low and high frequencies) to monitor the influence of temperature variations (F-T cycles) on the integrity of concrete specimens (prisms and cylinders) under controlled testing conditions. UPV and other conventional procedures are used for comparison with the proposed new procedure. Mixing concrete with nanosilica has received more attention due of its ability to enhance the main characteristics of concrete mixtures including compressive strength, durability, and decrease the effect of the F-T cycles [24, 25]. Therefore, the concrete specimens were mixed with different amounts of a nanosilica (0 %, 1 %, 3 %) to investigate the changes in P-wave characteristics that may occur under F-T cycles using UPV and two conventional procedures for comparison with the proposed new technique. The investigation includes proposing a damage index called damage reference (DR) based on wave velocity and signal amplitude to monitor internal damage in the concrete medium during different time periods. The results of the study show that suitability of the proposed new approach to identify the induced damage is better than the traditional measurements of UPV and other conventional procedures.

2. Materials and Methods

2.1. Concrete Specimens

Six concrete specimens (three prisms and three cylinders) with different nanosilica content were manufactured for this research. Cylinder and prism specimens contained three different percentages of nanosilica: one without nanosilica, one specimen with 1 % of nanosilica, and the last one with 3 % of nanosilica. Table 1 shows the properties of the concrete used in manufacturing the concrete specimens.

Table 1. Parameters of the concrete mixture.

Parameter name	Range value
Slump rate	75.0–100.0 mm
Air content percentage	5.0–8.0 %
Water/cement ratio	0.390
Concrete class	C-20
Nominal aggregate size	20.0 mm
Specified compressive strength (28 days)	32.50 MPa

Each concrete specimen (prism and cylinder) was subjected to 71 days of F-T cycles using a special machine with the ability to control the temperature to mimic F-T conditions. Each accelerated F-T cycle represented a full day (24 hours) and was accompanied by a gradual temperature change set to a gradual increase from –25.0 to +25.0 °C with ±2.0 °C.

2.2. Instrumentation Setup

2.2.1. UPV setup

The UPV measurement equipment consisted of four components: 1) pair transducers; 2) a function-generator; 3) oscilloscope; and 4) laptop computer used as a data acquisition system (DAS) (Fig. 1a). A pair of 54 kHz transducers with a diameter of 50 mm was used for measurements, one transducer for transmitting the pulse, and the other for capturing the ultrasonic waves. To obtain consistent results, two 3D-printed transducer holders with elastic cords to control the pressure on both transducers were fabricated (Fig. 1b).

The function generator was used to generate square wave frequency of 60 kHz and amplitude 10.0 vpp. to excite each specimen. Coupling grease was used between specimens' surfaces and the transducers to minimize signal loss due to air voids. The input-output signal data were acquired using a laptop computer with Keysight-BenchVue® software, which was later used to calculate the UPVs and compute the areas below average spectra of signals.

a)   b)
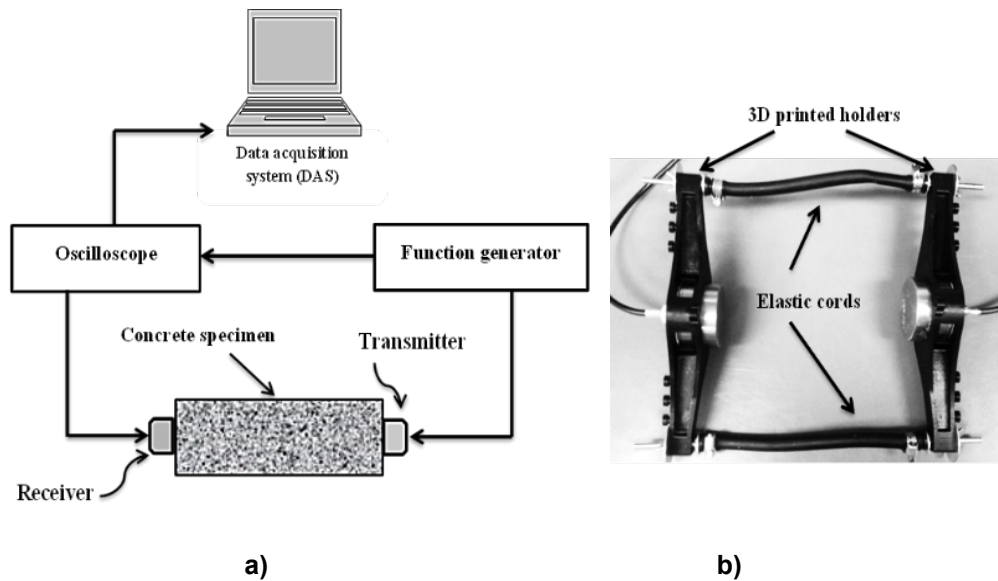
Figure 1. UPV testing configuration: a) testing setup, b) 3D-printed transducer holders.

2.2.2. Damage assessment

For the concrete cylinder specimens, the UPV testing was performed at defined periods of time (before the first F-T cycle, after two days, 15 days and each 7 days until 71 days were reached). To ensure the consistency of the results, each specimen was tested three times. As for the concrete prisms, they were tested to determine whether the UPV results reflect the change in the internal condition of the concrete in two axes (longitudinal and transverse) after 71 F-T cycles. In the transverse direction, four equally spaced points (edge and midpoints) were selected for ultrasonic testing. For that purpose, the average ultrasonic pulse velocities for each point from the three prism sets were determined before and after the F-T cycle tests following the same procedure used for testing the cylinder specimens. In addition, three procedures were used to evaluate the damage based on the signal energy, two of which were conventional and used by other researchers [1, 3, 9] and the last one is proposed in this research project. The first and second procedures take into account the damage inside the specimen based on the signal energy in the time and frequency domains, respectively, using index called the damage reference (DR), which can be estimated using the following equation:

$$DR = \frac{S_o - S_d}{S_o}(\%),\qquad(1)$$

where S_o is the energy of signal in the time or frequency domain for intact specimen (no damage); S_d is the energy of signal in the time or frequency domain for specimen with damage. The larger the DR mains, the more damage exists inside the concrete specimen, and vice versa.

The third procedure is new and proposed in current research based on the definition of two frequency bands in the spectrum of each signal. Low frequency band (LFB ≈ 15–35 kHz) and high frequency band (HFB ≈ 42–65 kHz), which are shown more changes than other band frequencies. In addition, this

procedure uses the DR by calculating the area under each band to evaluate the damage inside concrete specimen induced by temperature variations. All the results obtained by the traditional methods and the proposed method are compared to investigate the feasibility of the proposed third method for assessing the damage in concrete specimens under temperature variations.

3. Results and Discussion

3.1. Freeze-Thaw Effect on Concrete Prisms

3.1.1. Damage assessment using UPV

Fig. 2 shows the average P-wave velocities calculated from the longitudinal configuration test data compared to the F-T cycles for the three concrete prisms. The figure shows that in all cases (with and without nanosilica), the P-wave velocity of the specimens does not show any significant trend throughout the test period, which can be attributed to the selection procedure of the arrival time based on the UPV device readings.

In the initial periods (from 0 to 7 days), the velocity of the specimen with nanosilica shows a clear decrease and then increases to a value exceeding that of the specimen without nanosilica after 71 days. The difference between the calculated wave velocities of the specimens with and without nanosilica was obtained after two days, and it has a value of 2.6 %. A similar trend of the UPV results was obtained when testing the concrete prism in the transverse direction.
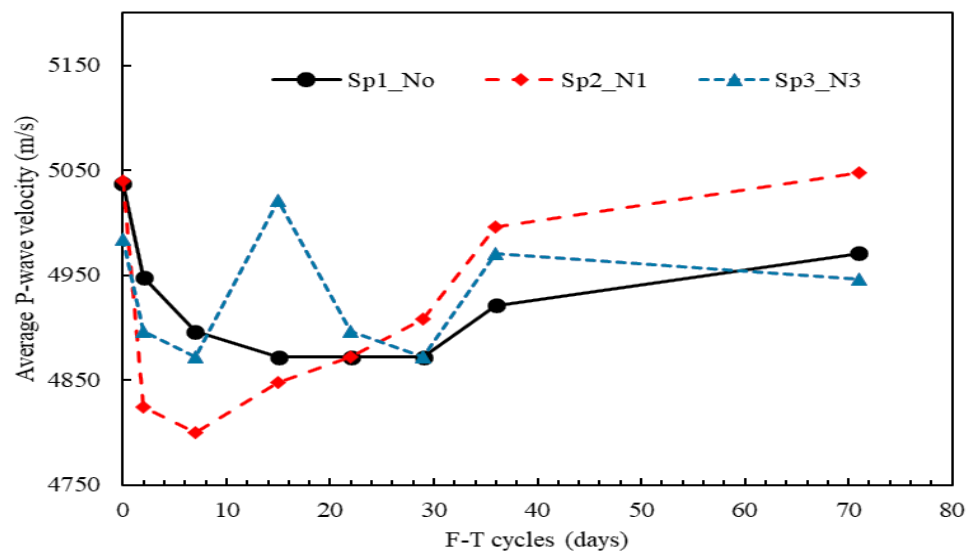
Figure 2. Average P-wave velocities of all prism specimens compared to the F-T cycles.

3.1.2. Damage assessment using signal information

Fig. 3 shows the time signals acquisition for two prisms, a prism with an intact case and a prism with 3 % nanosilica, tested before and after 71 days of F-T cycling. The time signals for the intact case show a significant decrease in the maximum amplitude (~ 28 %), while for the prism mixed with 3 % nanosilica the decrease is smaller than for the intact case (~ 19 %), which can be attributed to the effect of nanosilica that reduced the impact of temperature variations.

Moreover, the frequency spectra of the time signals obtained in Fig. 3 are shown in Fig. 4 with two identified frequency bands that are proposed as the third method for assessing the damage induced by temperature variations. In this figure, both spectra reveal a small difference in the peak frequencies, but the signal energy is significantly reduced for the intact case, while a smaller reduction is observed in the prism with 3 % of nanosilica. Similar results are obtained for the prism with 1 % of nanosilica.

Fig. 5 shows the comparison between the DR values for concrete prisms treated with 0 % and 3 % of nanosilica obtained by three procedures, the first and second depending on the peak amplitude of the signals over time and the total area under the frequency spectra. While the third procedure is proposed in this research and depends on areas under defined frequency bands that are most influenced by damage induced by temperature variations. Although the two conventional methods used to calculate DR for both cases are able to identify the damage progress better than the UPV method, the latter method, which depends on defined bands, shows better results. In particular, the higher frequency band is more robust than low frequency band in capturing the damage progress induced by F-T cycles.

Furthermore, the results in Fig. 5b show the ability of the added nanosilica to reduce the impact of F-T cycles on the internal condition of the prism. The analysis of the signals captured during the pulse velocity test provides an extra source of information that can assist in the examination of the condition of concrete members. This example shows that the proposed procedure was able to identify the damage to a greater extent than other conventional methods currently used in characterization of concrete medium.

On the other hand, the average time signals measured at four different points along the intact prism concrete and the prism treated with 3 % nanosilica before and after 71 F-T cycles are shown in Fig. 6.
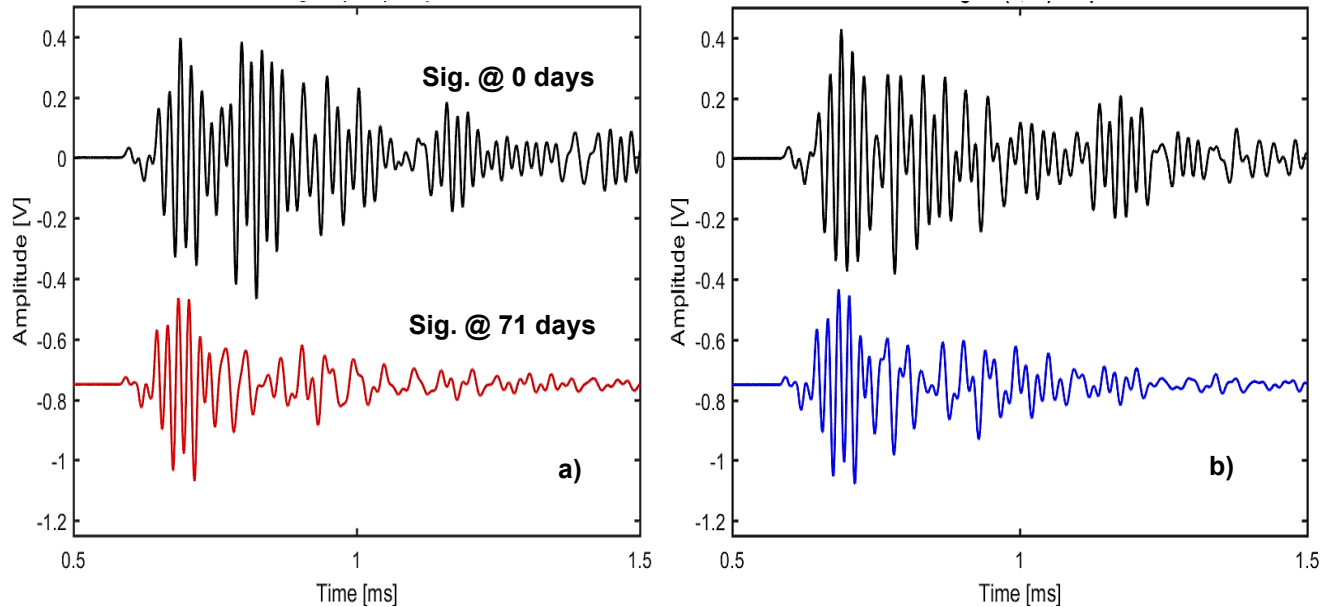
**Figure 3. Typical time signals of the intact prism and the prism
with 3 % nanosilica tested in the longitudinal direction at 0 and 71 days of F-T cycling:
a) intact prism (0 %), b) prism with 3 % of nanosilica.**

**Figure 4. Typical spectra of the intact prism and the prism with 3 % of nanosilica signals
at 0 and 71 days of F-T cycling: a) intact prism (0 %), b) prism with 3 % of nanosilica.**

The figure also reveals that the time signals for the intact case show a clear decrease in the maximum amplitude (~ 23 %), while for the prism mixed with 3 % of nanosilica the decrease is smaller than that of the intact case (~ 14 %), which can be related to the addition of nanosilica that reduced the impact of F-T cycles. In addition, the frequency spectra of the time signals obtained in Fig. 6 are shown in Fig. 7 with two identified frequency bands that are proposed as the third method for assessing the damage induced by temperature variations.

In this figure, both spectra reveal a small difference in peak frequencies, but the signal energy is significantly reduced for the intact case, while in the prism treated with 3 % of nanosilica a smaller decrease is observed. Similar results are obtained for the prism with 1 % of nanosilica.
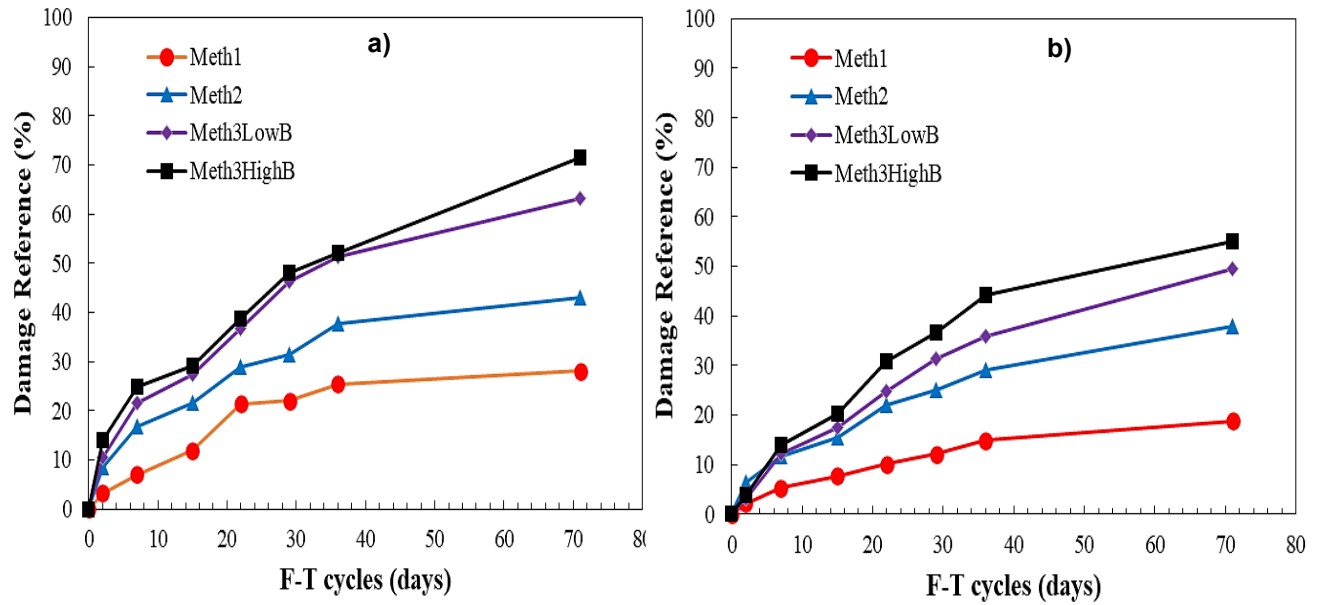
**Figure 5. Comparison between DRs of the intact prism and the prism with 3 %
of nanosilica signals under 71 days of F-T cycling: a) intact prism (0 %), b) prism with 3 %
of nanosilica. Meth1 represents the 1ˢᵗ procedure based on the peak amplitude, Meth2 represents
the 2ⁿᵈ procedure based on the total area under spectrum, Meth3LowB and Meth3HighB represent
areas under low and high band spectra, respectively.**
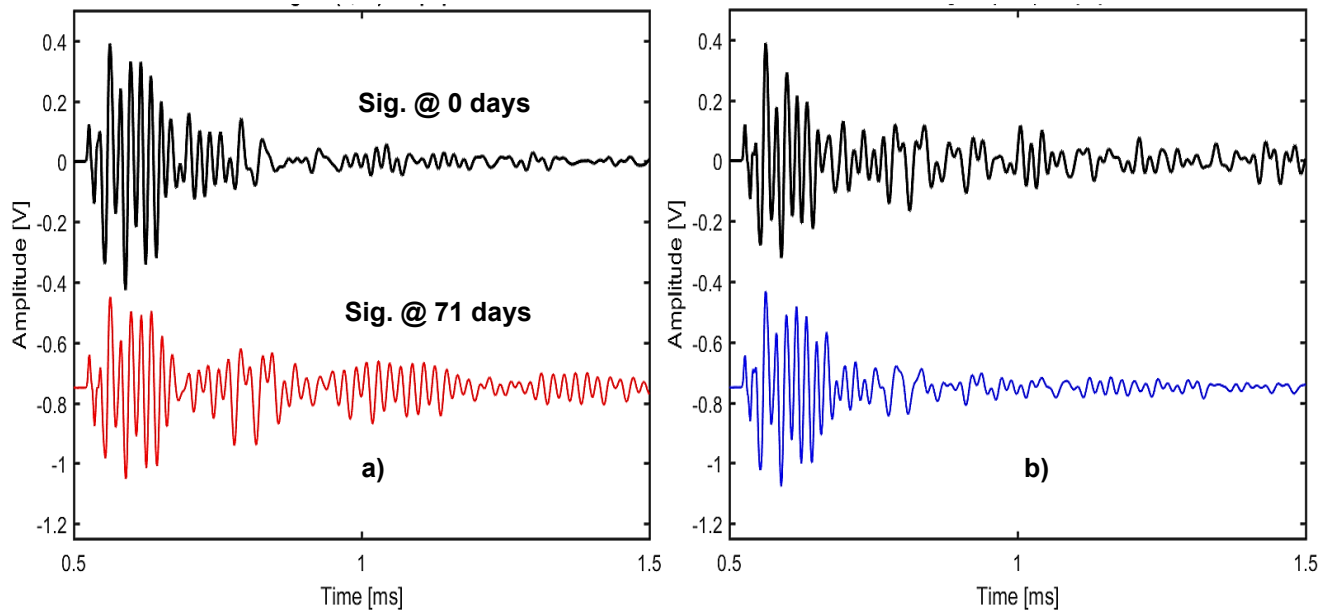
**Figure 6. Average time signals of the intact prism and the prism
with 3 % nanosilica tested in the transverse direction at 0 and 71 days of F-T cycling:
a) intact prism (0 %), b) prism with 3 % of nanosilica.**

Fig. 8 shows the DR values for concrete prisms with 0 % and 3 % of nanosilica, which are calculated using three procedures similar to the analysis of the testing result in the longitudinal direction. Although the two conventional methods used to calculate the DR for both cases are able to identify the damage progress better than the UPV method, the latter method, which depends on defined bands, shows better results. In particular, the higher frequency band is more robust than low frequency band in capturing the damage progress induced by F-T cycles.
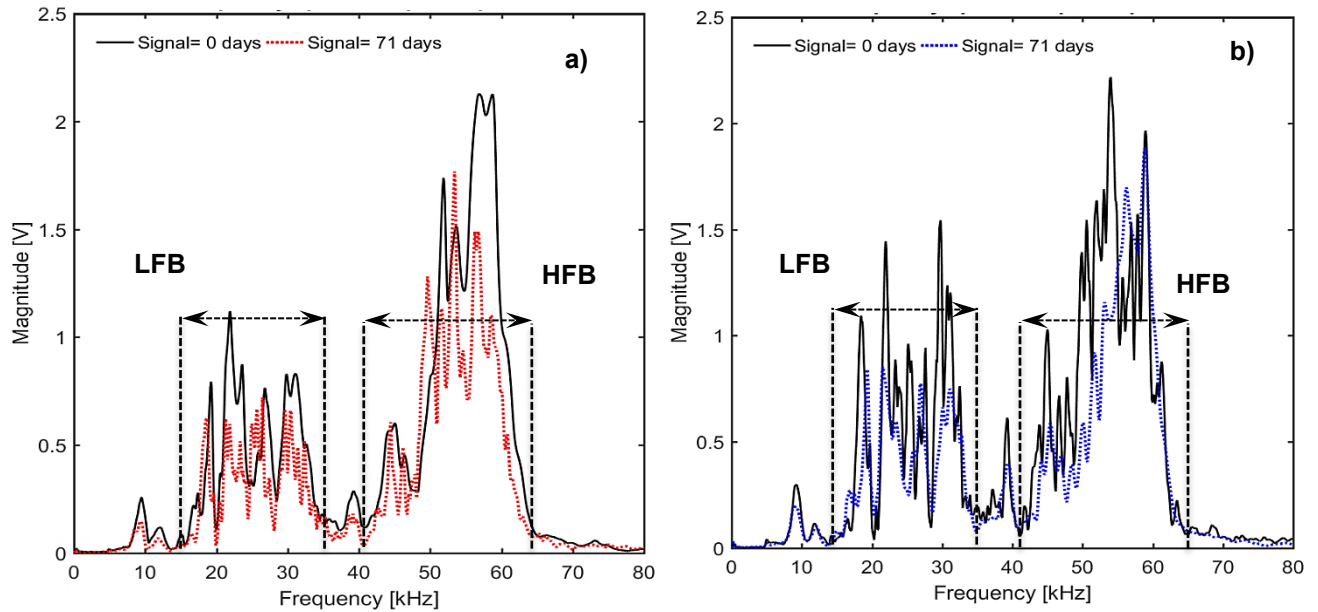
**Figure 7. Typical spectra of the intact prism and the prism
with 3 % of nanosilica signals tested in the transverse direction at 0 and 71 days of F-T cycling:
a) intact prism (0 %), b) prism with 3 % of nanosilica.**
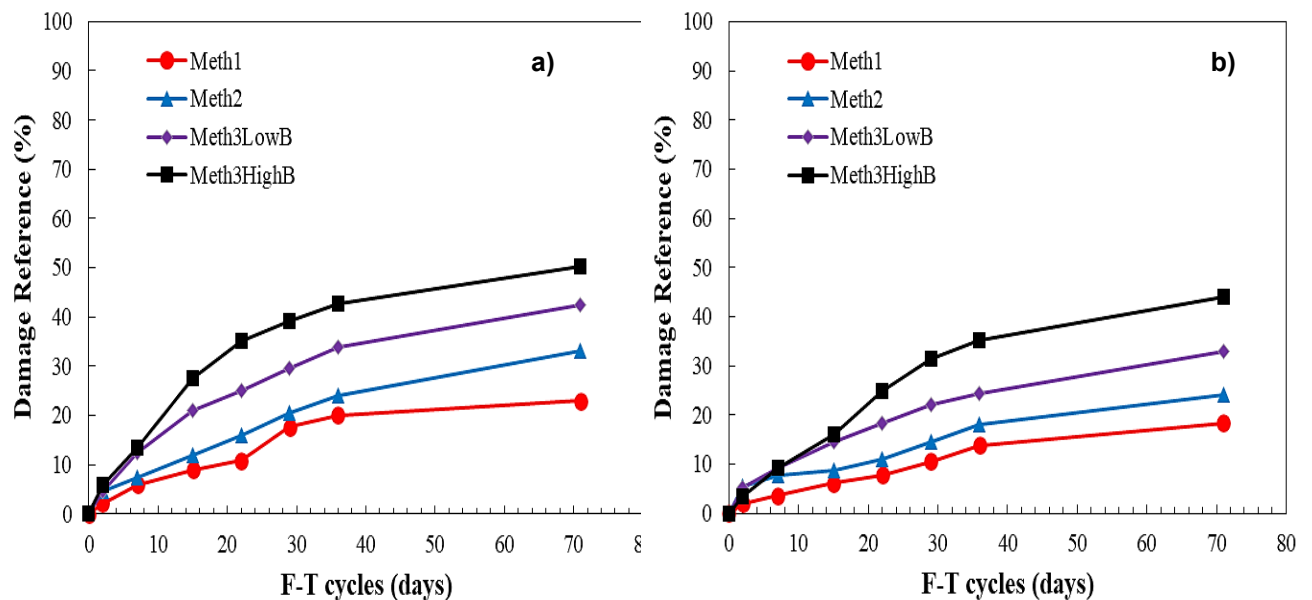
**Figure 8. Comparison between DRs of the intact prism and the prism with 3 %
of nanosilica signals tested in transverse direction after 71 days of F-T cycling:
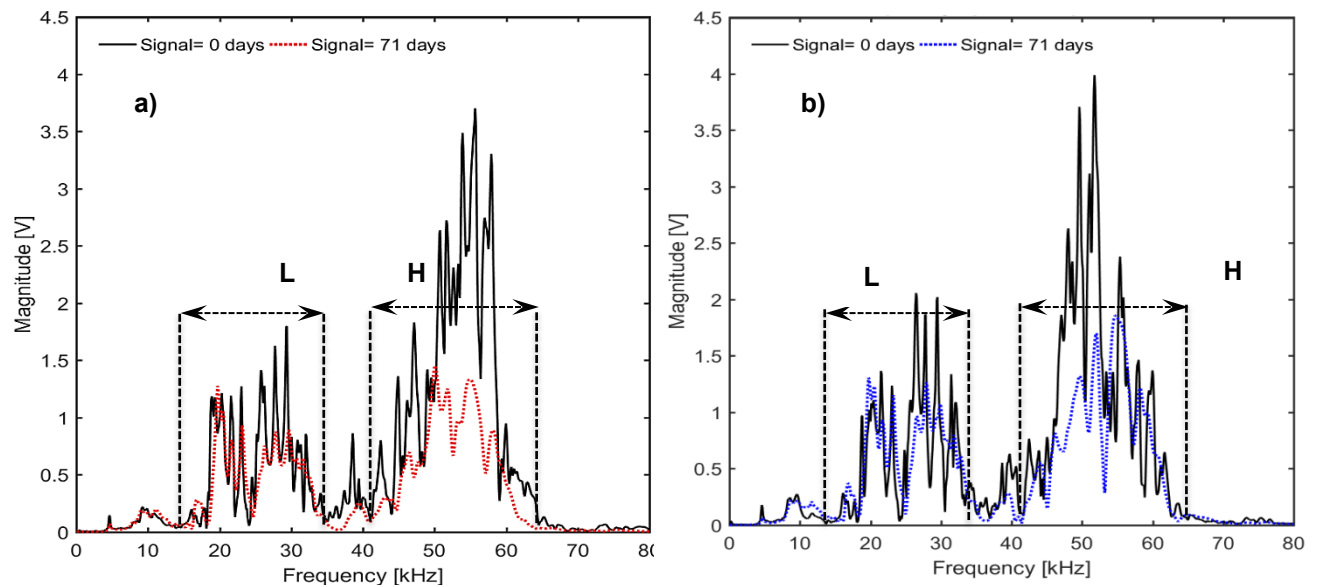a) intact prism (0 %), b) prism with 3 % of nanosilica. Meth1 represents the 1ˢᵗ procedure
based on the peak amplitude, Meth2 represents the 2ⁿᵈ procedure
based on the total area under spectrum, Meth3LowB and Meth3HighB represent areas
under low and high band spectra, respectively.**

3.2. Freeze-Thaw effect on Cylinder Specimens

3.2.1. Damage assessment using UPV

Fig. 9 shows the average wave velocities plotted against the test periods for three specimens (0 %, 1 %, and 3 % of nanosilica). The average velocity of the specimen with 3 % of nanosilica showed a decreasing trend until it reached a steady-state level after 7 days. In contrast, the intact specimen (0 %) reveals an initial decrease in average velocity and after 7 days increases until it reaches a maximum value after

71 days. On the other hand, the UPV results did not show any consistent trend, which can be used to identify the damage induced by F-T cycles.
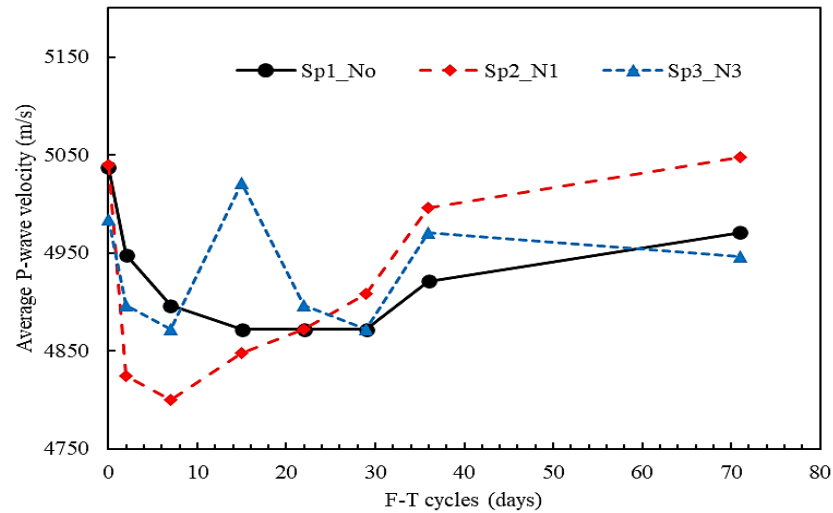
**Figure 9. Typical average P-wave velocities of all cylinder concrete specimens
(intact and with 1 % and 3 % of nanosilica).**

3.2.2. Damage assessment using signal information

The time signals acquisition for two-cylinder specimens with the intact case and specimen with 3 % of nanosilica tested before and after 71 days of F-T cycling are shown in Fig. 10. The figure shows that the time signals for the intact case show a significant decrease in a maximum amplitude (~ 30 %), while for the cylinder mixed with 3 % of nanosilica, the decrease is smaller than that of the intact case (~ 12 %), which can be due to the effect of nanosilica that reduced the impact of F-T cycles.
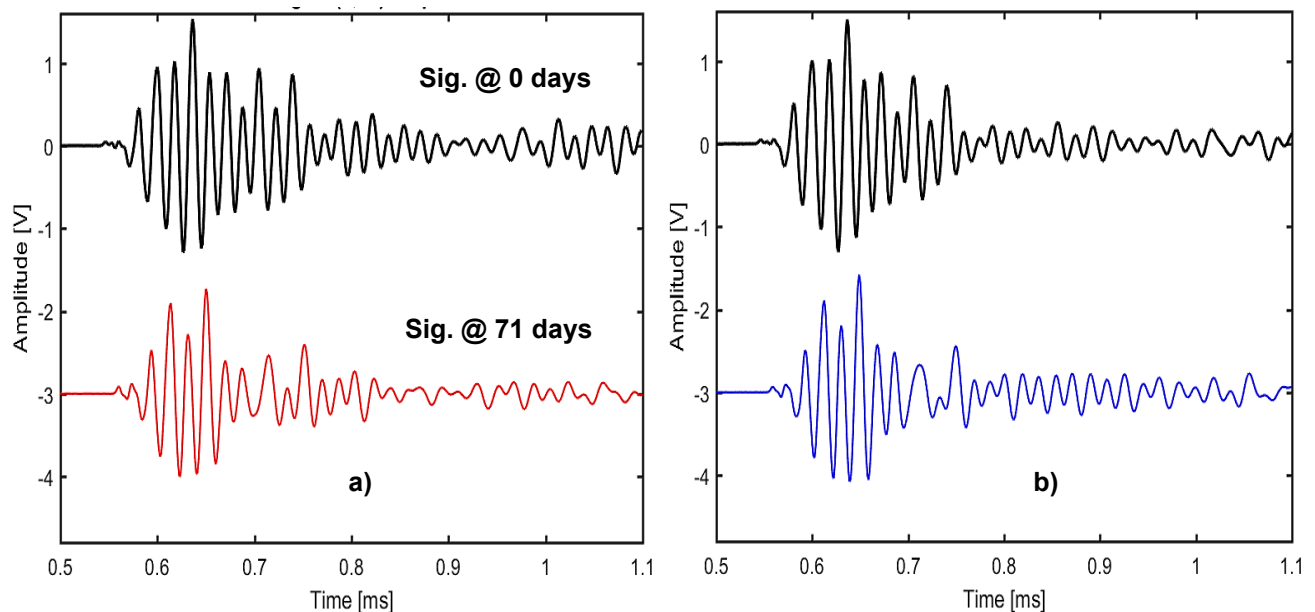
Figure 10. Average time signals of the intact concrete cylinders without and with 3 % of nanosilica tested at 0 and 71 days of F-T cycling: a) intact cylinder (0 %), b) cylinder with 3 % of nanosilica.

Furthermore, the frequency spectra of the time signals obtained in Fig. 10 are shown in Fig. 11 with two identified frequency bands that are proposed as the third method for assessing the damage induced by temperature variations. In this figure, both spectra appear to have a little change in the peak frequencies, but the signal energy is significantly reduced for the intact case, while in the cylinder with 3 % of nanosilica shows smaller decrease. Similar results are obtained for the cylinder with 1 % of nanosilica.
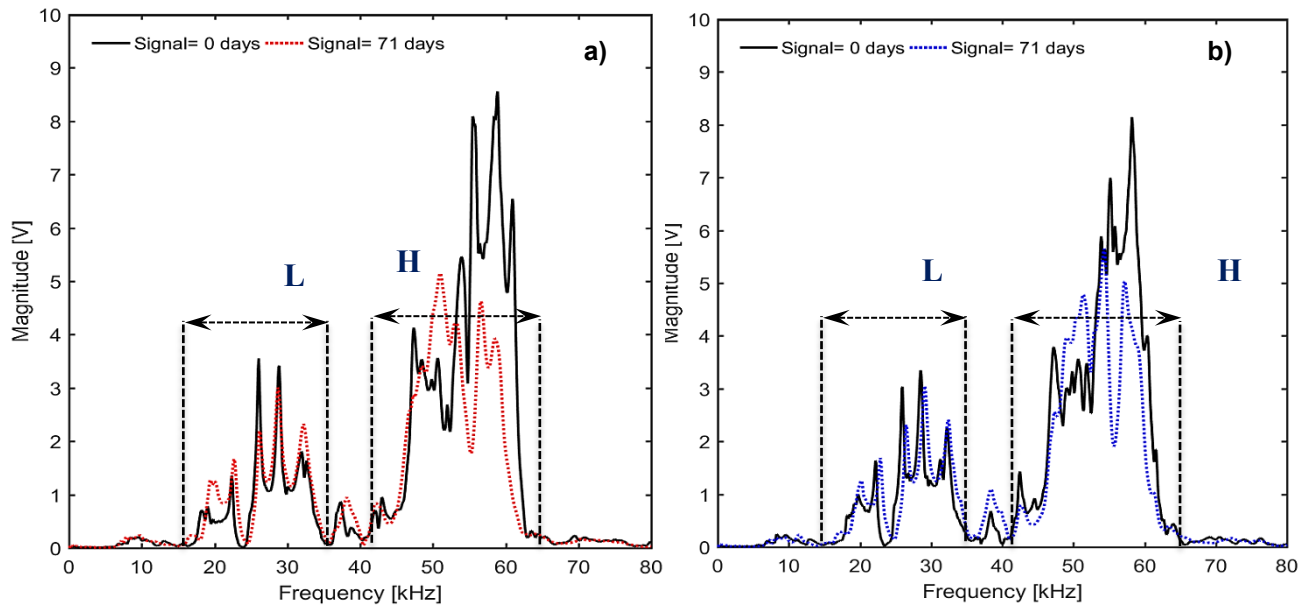
Figure 11. Typical spectra of the intact cylinders without and with 3 % of nanosilica signals at 0 and 71 days of F-T cycling: a) intact cylinder (0 %), b) cylinder with 3 % of nanosilica.

Fig. 12 shows the comparison between the DR values for concrete cylinders treated with 0 % and 3 % of nanosilica, which are calculated using three approaches, the first and second depending on the peak amplitude of the signals over time and the total area under the frequency spectra. While the third procedure is proposed in this research and depends on areas under defined frequency bands that are most influenced by damage induced by temperature variations. In addition, the two conventional methods used to calculate DR for both cases are able to identify the damage progress better than the UPV method, the latter procedure, which depends on defined bands, shows better results. In particular, the higher frequency band is more robust than low frequency band in capturing the damage progress induced by F-T cycles.

In addition to that, the observations in Fig. 12b confirm the ability of the added nanosilica to reduce the impact of F-T cycles on the internal condition of the cylinder, as was noticed with the prism specimens.
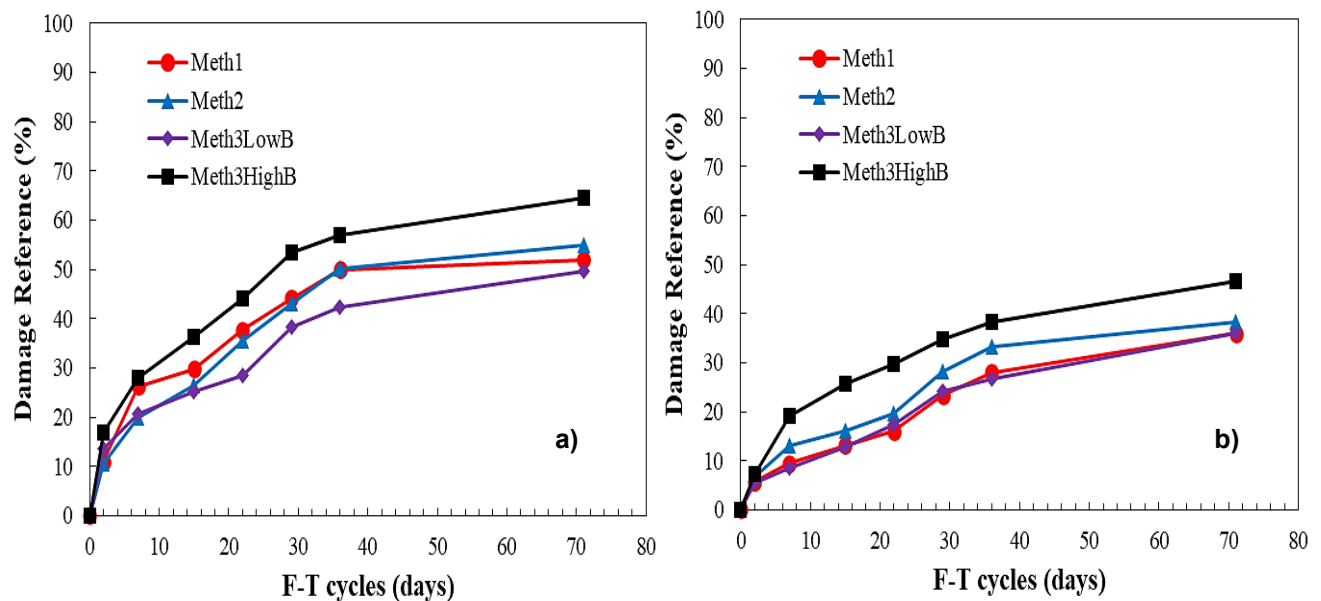
Figure 12. Comparison between DRs of the intact cylinders without and with 3 % of nanosilica signals tested after 71 days of F-T cycling: a) intact cylinder (0 %), b) cylinder with 3 % of nanosilica. Meth1 represents the 1st procedure based on the peak amplitude, Meth2 represents the 2nd procedure based on the total area under spectrum, Meth3LowB and Meth3HighB represent areas under low and high band spectra, respectively.

4. Conclusions

Different approaches based on the UPV testing including the proposed new approach are used to assess its potential to capture damage progress in two groups of concrete specimens (prism and cylinder) under the impact of 71 F-T cycles, each cycle lasting 24 hours. The UPV testing of all concrete specimens is conducted under controlled conditions to ensure the stability of the signals. The proposed technique depends on defining two frequency bands: low (15–35 kHz) and high (42–65 kHz) – on each signal spectrum obtained from testing of the concrete specimen. In addition, the DR is proposed to monitor the damage propagation inside concrete medium and to compare the conventional procedures with the proposed new technique. The following conclusions are drawn from the conducted study:

1. It was found that there is no significant variation was observed in the wave velocities measured by the conventional procedure during the study (less than 3 % changes) for all the specimens.

2. The results obtained from the time and frequency domains indicate a significant change in the specimens' condition under the impact of the F-T cycles.

3. The proposed new procedure with high frequency band was found to be more robust than other conventional procedures in assessing the damage induced in concrete specimens.

4. At the end of testing period, the DR values calculated based on three procedures for all tested prisms with nanosilica (0 % and 3 %) were in the range of 20–63 % and 14–55 %, respectively. While for the tested cylinders, the DR were 50–62 % for the intact case and 34–45 % for the case with 3 % of nanosilica. The lower values of DR are related to the 1st procedure, and the higher ones – to the 3rd procedure with high frequency band.

5. The results obtained in this research work indicated that a single pulse velocity measurement may not be sufficient to capture internal change in concrete medium.

6. Based on the results obtained in this study, exploring the suitability use of the proposed new procedure (HFB 42–65 kHz) to overcome the low sensitivity of the UPV measurements is a good choice for monitoring the integrity of concrete medium under temperature variations.

References

1. Bungey, J.H., Grantham, M.G. Testing of concrete in structures. 4th ed. CRC Press. London, 2006. 352 p. DOI: 10.1201/9781482264685

2. Carino, N.J., Chang, K.C.E. Nondestructive Testing of Concrete: History and Challenges. SP-144: Concrete Technology: Past, Present, and Future. American Concrete Institute. Farmington Hills, 1993.

3. Malhotra, V.M., Carino, N.J. Handbook on nondestructive testing of concrete. 2nd ed. CRC Press. Boca Raton, 2004. 384 p. DOI: 10.1201/9781420040050

4. Popovics, S. Effects of uneven moisture distribution on the strength of and wave velocity in concrete. Ultrasonics. 2005. 43(6). Pp. 429–434. DOI: 10.1016/j.ultras.2004.09.007

5. Krautkrämer, J., Krautkrämer, H. Ultrasonic Testing of Materials. 2nd ed. Springer. Berlin, Heidelberg, 2013. 373 p. DOI: 10.1007/978-3-662-02296-2

6. Ribeiro Filho, S.L.M., Thomas, C., Durão, L.M.P., Christoforo, A.L., Bowen, C., Scarpa, F., Panzera, T.H. Ultrasonic pulse velocity and physical properties of hybrid composites: A statistical approach. 2023. Hybrid Advances. 2. Article no. 100024. DOI: 10.1016/j.hybadv.2023.100024

7. Chai, H.K., Momoki, S., Kobayashi, Y., Aggelis, D.G., Shiotani, T. Tomographic reconstruction for concrete using attenuation of ultrasound. NDT & E International. 2011. 44(2). Pp. 206–215. DOI: 10.1016/j.ndteint.2010.11.003

8. Yim, H.J., Kwak, H.-G., Kim, J.H. Wave attenuation measurement technique for nondestructive evaluation of concrete. Nondestructive Testing and Evaluation. 2012. 27(1). Pp. 81–94. DOI: 10.1080/10589759.2011.606319

9. Fartosy, S., Gomez-Rodriguez, D., Cascante, G., Basu, D., Dusseault, M.B. Effects of a Fracture on Ultrasonic Wave Velocity and Attenuation in a Homogeneous Medium. Geotechnical Testing Journal. 2020. 43(2). Pp. 394–413. DOI: 10.1520/GTJ20180200

10. Fartosy, S., Abdalqadir, N.A., Al-Mussawy, H.A., Jafar, N.Q., Ghosh, S. A Combined Ultrasonic Procedure to Evaluate Damage in Concrete Beams Subjected to Static Load. Journal of Engineering and Sustainable Development. 2024. 28(2). Pp. 213–221. DOI: 10.21272/jeasd.28.2.5

11. Ramaniraka, M., Rakotonarivo, S., Payan, C., Garnier, V. Effect of Interfacial Transition Zone on diffuse ultrasound in thermally damaged concrete. Cement and Concrete Research. 2022. 152. Article no. 106680. DOI: 10.1016/j.cemconres.2021.106680

12. Komloš, K., Popovics, S., Nürnbergerová, T., Babál, B., Popovics, J.S. Ultrasonic pulse velocity test of concrete properties as specified in various standards. Cement and Concrete Composites. 1996. 18(5). Pp. 357–364. DOI: 10.1016/0958-9465(96)00026-1

13. Helal, J., Sofi, M., Mendis, P.A. Non-Destructive Testing of Concrete: A Review of Methods. Electronic Journal of Structural Engineering. 2015. 14(1). Pp. 97–105. DOI: 10.56748/ejse.141931

14. Drabkin S., Kim D. Failure monitoring of concrete specimen using frequency characteristics of ultrasonic waves. American Concrete Institute. Farmington Hills, 1994. 143(1). Pp. 257–274.

15. Ensminger, D., Bond, L.J. Ultrasonics: Fundamentals, Technologies, and Applications. 4th ed. CRC Press. Boca Raton, 2011. 904 p. DOI: 10.1201/9780429286964

16. Fartosy, S.H., Waleed, J.F., Abd, H.Z., Al, M.A.S.T. Evaluation bearing capacity of ring footings on reinforced loose sand. Journal of Applied Engineering Science. 2023. 21(1). Pp. 29–35. DOI: 10.5937/jaes0-37350

17. Shang, H.-S., Cao, W.-Q., Wang, B. Effect of Fast Freeze-Thaw Cycles on Mechanical Properties of Ordinary-Air-Entrained Concrete. The Scientific World Journal. 2014. Article no. 923032. DOI: 10.1155/2014/923032

18. Nixon, P.J. Recycled concrete as an aggregate for concrete – a review. Material and Structures. 1978. 11(5). Pp. 371–378. DOI: 10.1007/BF02473878

19. Richardson, A., Coventry, K., Dave, U., Pienaar, J. Freeze/Thaw Performance of Concrete Using Granulated Rubber Crumb. Journal of Green Building. 2011. 6(1). Pp. 83–92. DOI: 10.3992/jgb.6.1.83

20. Van Wesenbeeck, B.K., Wolters, G., Antolínez, J.A.A., Kalloe, S.A., Hofland, B., de Boer, W.P., Çete, C., Bouma, T.J. Wave attenuation through forests under extreme conditions. Scientific Reports. 2022. 12(1). Article no. 1884. DOI: 10.1038/s41598-022-05753-3

21. Selleck, S.F., Landis, E.N., Peterson, M.L., Shah, S.P., Achenbach, J.D. Ultrasonic investigation of concrete with distributed damage. ACI Materials Journal. 1998. 95(1). Pp. 27–36.

22. Molero, M., Aparicio, S., Al-Assadi, G., Casati, M.J., Hernández, M.G., Anaya, J.J. Evaluation of freeze–thaw damage in concrete by ultrasonic imaging. NDT & E International. 2012. 52. Pp. 86–94. DOI: 10.1016/j.ndteint.2012.05.004

23. Erdélyi, A., Csányi, E., Kopecskó, K., Borosnyói, A., Fenyvesi, O. Deterioration of steel fibre reinforced concrete by freeze-thaw and de-icing salts. Concrete Structures. 2008. 9. Pp. 33–44.

24. Pandiaraj, K.P., Sankararajan, V. Effect of nano silica on the properties of concrete and mortar – A state of art. International Review of Applied Sciences and Engineering. 2021. 13(1). Pp. 70–79. DOI: 10.1556/1848.2021.00309

25. Chekravarty, D.S.V.S.M.R.K., Mallika, A., Sravana, P., Rao, S. Effect of using nano silica on mechanical properties of normal strength concrete. Materials Today: Proceedings. 2022. 51(8). 2573–2578. DOI: 10.1016/j.matpr.2021.12.409

Information about the authors:

Sabah Hassan Fartosy, *PhD*
ORCID: https://orcid.org/0000-0001-5831-297X
E-mail: dr.sabah77@uomustansiriyah.edu.iq

Lubna Mohammed Abd
E-mail: lubna.m8877@uomustansiriyah.edu.iq

Mithaq Kohees, *PhD*
E-mail: mithaq.kohees@gmail.com

Zuhair Abd Hacheem, *PhD*
E-mail: zuhairabd@uomustansiriyah.edu.iq

Magazine of Civil Engineering

journal homepage: http://engstroy.spbstu.ru/

Research article

Concrete beams reinforced with longitudinal and transverse GFRP bars

S.A. Mohammed✉ *, A.I. Said*

The University of Baghdad, Baghdad, Iraq

✉ *shaysh96@outlook.com*

Abstract. This research investigated experimentally and numerically the general behavior of six concrete beams reinforced with longitudinal and transverse bars made of Glass Fiber Reinforced Polymer (GFRP) or steel. Six beams were divided into three groups with different variables. The first group consisted of two beams reinforced with GFRP bars in main direction and with steel stirrups. The variable of this group was the spacing between the stirrups. The second group consisted of two beams also reinforced with GFRP bars in the longitudinal direction and with stirrups in the transverse direction. The variable of this group was the same – spacing between the stirrups. As for the third group, it consisted of two beams reinforced with GFRP bars in the longitudinal direction and without stirrups in the transverse direction. The variable of this group was the main reinforcement ratio. The results showed that the beams reinforced with GFRP bars improved their behavior, bending strength and the deflection with different ratios, but had somewhat limited shear resistance when using GFRP stirrups. All the tested beams exhibited linear elastic behavior until failure, with GFRP being more brittle compared to that of ductile steel. The numerical simulation of six beams using ABAQUS software showed good agreement with the experimental data obtained in the laboratory.

1. Introduction

Concrete and steel are foundational materials in construction, renowned for their strength and durability. However, given the widespread use of these materials, the search for superior alternatives has become essential. Fiber Reinforced Polymer (FRP), particularly Glass Fiber Reinforced Polymer (GFRP), has emerged as a promising substitute due to its advantageous properties over steel. GFRP is lightweight, possesses higher tensile strength than steel, and is resistant to magnetic fields, making it especially suitable for civil engineering applications [1–4]. Bank, L.C. [5] discussed FRP's potential to extend the lifespan of structures in harsh environments, while Saraswathy, T. et al. [6] investigated the flexural behavior of reinforced concrete beams using GFRP bars. Their study explored parameters, such as failure mode, crack pattern, load carrying capacity, load deflection behavior, and ductility in GFRP-reinforced concrete beams. GFRP materials offer advantages, such as corrosion resistance and a high strength-to-weight ratio, making them suitable for reinforced concrete applications where conventional steel reinforcement faces serviceability issues. Ahmed, A. et al. [7] further validated the superior performance and cost-effectiveness of GFRP-reinforced concrete beams. GFRP addresses critical challenges, such as steel corrosion, which compromises structural integrity and increases maintenance costs. Its corrosion resistance, lightweight nature, and electromagnetic neutrality make GFRP ideal for applications in marine infrastructure, MRI centers, and electrical substations [8]. Despite these advantages, the long-term performance of GFRP-reinforced structures requires further study. According to the ACI 440.IR-15 guidelines [9], GFRP-reinforced concrete beams should be over-reinforced to fail by concrete crushing rather than bar rupture. The flexural

behavior of these beams is less ductile due to the linear elastic and brittle nature of GFRP bars until failure. The aim of this study is to evaluate the structural performance of concrete beams reinforced with GFRP bars, focusing on their flexural behavior, shear resistance, and the effects of varying stirrup configurations. Specifically, the study investigates how increasing the number of GFRP stirrups impacts load-bearing capacity and deflection, and compares the performance of GFRP to steel reinforcement. Through this research, the study seeks to contribute to the development of optimized design practices for integrating GFRP in construction.

2. Methods

2.1. Specifications of the Beams under Test

The experimental program consisted of testing six beams under four-point loading. The beams were divided into three groups with different variables, such as the main reinforcement ratio, the distances between the stirrups, as well as the stirrup type used to reinforce the beams (steel or GFRP). All beams had the same dimensions of 2700 mm in length, 180 mm in width, and 260 mm in depth, with the clear span of 2500 mm. The first group included two beams reinforced with GFRP bars in the main direction and steel stirrups in the transverse direction, labeled B.S1 and B.S3. The second group included two beams reinforced with GFRP bars in the longitudinal direction with GFRP stirrups in the transverse direction, labeled B.G1 and B.G3. The third group included two beams reinforced with GFRP bars in the main direction without stirrups, labeled G1 and G3. Fig. 1 and Table 1 show the details of all the tested beam specimens.
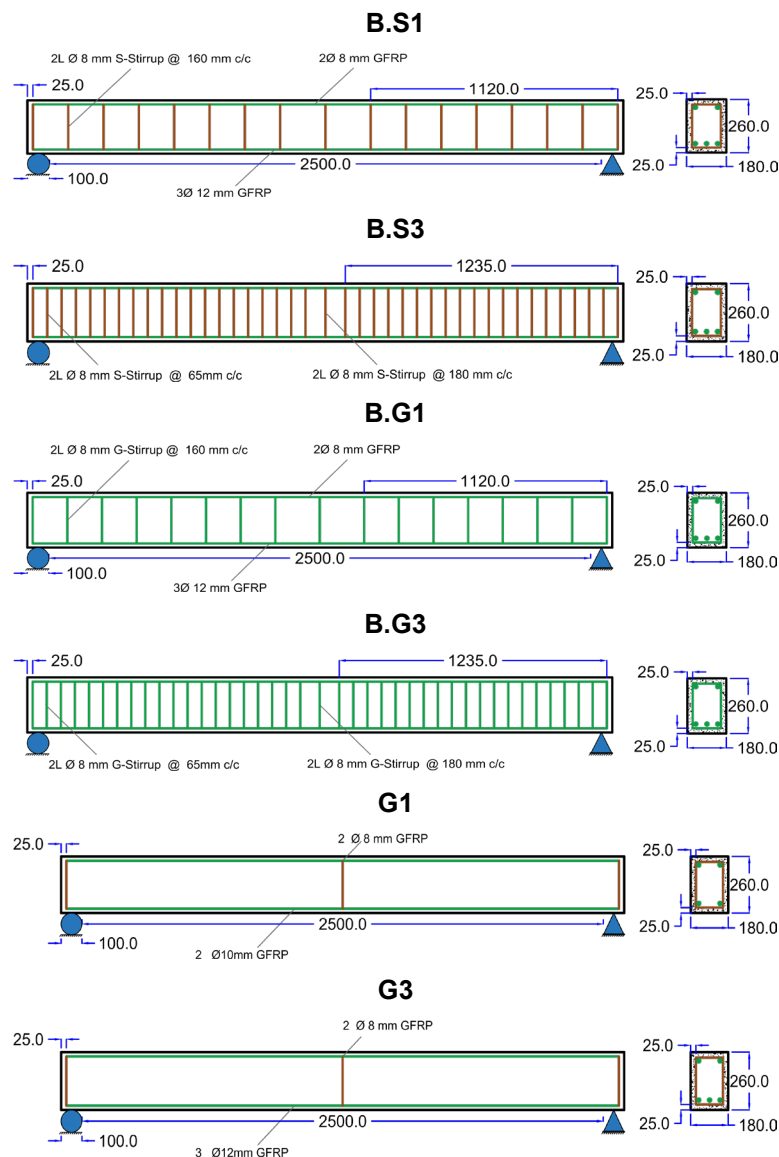
Figure 1. Details of all tested beams.

Table 1. Details of reinforcement of the beams.

Groups	Sample	Spacing	Type of stirrups	Bar top	Bar bottom
Group 1	B.S1	160 mm	Steel – Ø 8 mm	2 Ø 8 mm	3 Ø 12 mm
	B.S3	65 mm	Steel – Ø 8 mm	2 Ø 8 mm	3 Ø 12 mm
Group 2	B.G1	160 mm	GFRP – Ø 8 mm	2 Ø 8 mm	3 Ø 12 mm
	B.G3	65 mm	GFRP – Ø 8 mm	2 Ø 8 mm	3 Ø 12 mm
Group 3	G1	N/A	N/A	2 Ø 8 mm	2 Ø 10 mm
	G3	N/A	N/A	2 Ø 8 mm	3 Ø 12 mm

*N/A: not applicate

2.2. Material Properties

2.2.1. Concrete mix design

The concrete mix was designed according to ACI 211.1-22 guidelines [10] to achieve a compressive strength of 40 MPa. This concrete mix consisted of sand, gravel, cement, water, and some chemical additives to increase workability without affecting the strength of the hardened concrete. Table 2 shows the concrete mix proportions for one cubic meter of this material.

Table 2. Proportions of the concrete mix components.

Cement, kg/m^3	Gravel, kg/m^3	Sand, kg/m^3	Water, $liter/m^3$	Silica, kg/m^3
475	1030	640	170	20

2.2.2. GFRP bars

The longitudinal reinforcement consisted of GFRP bars of 8, 10, and 12 mm diameters. The stirrups are closed loops made of GFRP with 8 mm diameter. Several tensile tests were carried out on GFRP bars as shown in Fig. 2, for different diameter, and the results showed high tensile strength. The tensile tests were carried out in accordance with the ISO10406-1 specifications [11]. According to ISO requirements, a number of steel tubes of different diameters and fixed lengths, as shown in Fig. 2, were manufactured. GFRP bars were inserted into these tubes using epoxy adhesive from Sika Company (Sika AnchorFix®-3030), as shown in Fig. 2, because, due to their high tensile strength, the GFRP bars may fall out of the tensioning machine during testing. The manufacturer's manual reported a modulus of elasticity of 70000 MPa for all GFRP bars. Table 3 shows the results of the tensile tests on GFRP bars. The Laboratories of the Consulting Office at the College of Engineering, University of Baghdad, conducted all the tensile test.

Figure 2. Details of tensile strength test.

Table 3. Results of the tensile strength test of GFRP bar.

Type of bar	Ultimate tensile strength, MPa	Yield strength, MPa
GFRP	1350	N/A

*N/A: not applicate

2.3. Testing Procedure

The laboratory setup for the test consisted of a frame with supports spaced according to the design specifications. The specimen geometry specifications were 2700 mm long, 2500 mm span between the supports, and the width of support is 100 mm. Welded supports held up the specimens. Rubber pads and spirit level were used to level and stabilize these specimens. The concrete beam model was painted with a light white color to enhance the visibility of cracks during the test. After that, strain gauges were installed in bending and shear areas as well as an LVDT. After that, the specimen was lifted and placed on the frame, and the hydraulic jack and the load cell were installed on the I-section. The measuring devices were connected to the computer and data logger. A simple preliminary test was performed to verify the readings

of the strain gauges and the LVDT. The specimen was tested by applying an incremental load of 250 kg per stage until the hydraulic jack failed. The concrete beam was monitored during the test to determine the cracks formation from an incremental load. The cracks were marked with black lines along with the corresponding load values. All test results were recorded by the data logger in the form of tables, containing hundreds of thousands of data until the ultimate failure of concrete beams. Fig. 3 shows the details of the test setup components.
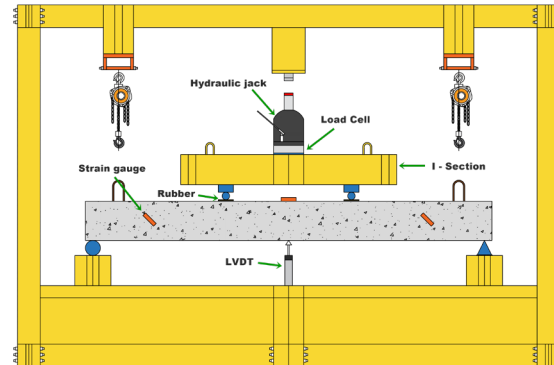
Figure 3. Details of the test setup components.

2.4. Finite Element Simulation

To gain a better understanding of the behavior of GFRP and obtain reliable scientific results, the beams were modeled using ABAQUS and a variety of theories to simulate four-point bending. The models of the materials used were determined by their properties and the adopted theories that were divided into two parts. The first part involved the representation of concrete using the concrete damaged plasticity model, similar to the smeared cracking model but more accurate. The second part involved the representation of steel using the classical theory of metal plasticity. This concept is based on the well-known von Mises yield criterion [12]. The beam components included GFRP, steel, stirrups, as well as a set of bearing plates. These components were assigned the material properties defined in the property field where the elastic behavior of concrete and the plastic behavior of concrete damage were specified. After that, elasticity and plasticity for GFRP and steel were defined, and the modulus of elasticity and Poisson's ratio were also defined for concrete. The bearing plates were assumed to be made of elastic steel. In next phase of the modeling process, the beam components were assembled, and the static loads applied to the beams were defined. The nature of the bond between GFRP and concrete was assumed to be ideal, and the interaction between all beam sections was described. After that, the loads and constraints for roller and hinge supports were also defined. There were some attempts to find the optimal mesh size and shape during the meshing phase, with generally good results.

2.4.1. Bar properties

Due to their high tensile strength and low elastic modulus, GFRP bars exhibit brittle behavior and unexpected failure, but the modulus of elasticity in steel is higher. The manufacturer characteristics of GFRP and steel bars are shown in Table 4.

Table 4. The manufacturer characteristics of GFRP and steel bars.

Type of Bar	Tensile strength f_y	Rupture strain ε	Modulus of elasticity E
GFRP	1350 MPa	0.0192	70000 MPa
Steel	510 MPa	0.0025	200000 MPa

2.4.2. ABAQUS parameters

The finite element theories rely on parameters that reflect the general properties of concrete in its common state. These parameters were determined by extensive research and investigations on concrete behavior [13]. Concrete damage plasticity data used in models are shown in Table 5.

Table 5. Concrete damage plasticity.

Parameters	ψ	ε	fb0/fc0	K	μ
Values	45	0.1	1.17	0.668	0.0001

3. Results and Discussion

The result of testing the six concrete beams showed good resistance to bending loads. As well, the deflection has decreased. The resistance of GFRP to shear forces was somewhat limited. The failure patterns and the number of cracks were affected by changing the spacing between the stirrups, in addition to that the type of the stirrups also had a significant impact on the stiffness of the beams, as the ability of the beam to carrying loads increased significantly with the increase in the number of stirrups, in addition to significantly reducing the spacing between the stirrups also contributed to changing the pattern failure. In terms of the longitudinal reinforcement, the deflection decreased as the proportion of the longitudinal reinforcement increased due to the effect of dowel action, and the resistance of beams to shear forces increased as the proportion of the main reinforcement improved [14].

3.1. Cracks Patterns and Fracture Mode

The first group of beams consisted of two beams that were reinforced with GFRP in the longitudinal direction as a main reinforcement in the same ratio for all beams ($1.5\,\rho_b$) and with steel stirrups in the transverse direction with different spacing (160 and 65 mm), which is the main variable for this group. In beam B.S1, the first crack appeared vertically (at an angle of 90°) in the tension area at a load of 15 kN between the two loading points in the mid-span, which is about 10.35 % of the ultimate load capacity. The cracks began to spread to the right and left in equal measure in the bending moment area until the model failed suddenly at a load of 145 kN. The sudden failure was caused by the concrete collapsing before the GFRP bars ruptured in the tension zone, which is known as compressive failure.

In B.S3 beam, the first cracks were also vertical and occurred in the tension zone at a load of 15 kN as well, 8.9 % of the ultimate load capacity. In this model, the spacing between stirrups was decreased by 59.3 % from that of the B.S1 beam. The increase in the stirrups by narrowing the spacing between them led to an increase in bearing capacity of beam by 16.5 % compared to the B.S1. The beam failed suddenly at a load of 168 kN. Concrete collapsing followed by the GFRP bars rupture directly in the compression zone. This beam was stiffer because the distance between the steel stirrups was reduced by a larger percentage than in the beam B.S1. Hence, higher bearing capacity in addition to smaller crack width and fewer cracks. Fig. 4 shows the crack pattern of the tested beams of the first group.

Figure 4. Crack pattern of the beams B.S1 and B.S3.

The second group also included two beams that have been over-reinforced to resist tensile forces with GFRP stirrups to resist shear forces. These beams were reinforced with GFRP bars in the longitudinal direction as the main reinforcement. The primary variable in this group was spacing (160 and 65 mm) between the GFRP stirrups, and the main reinforcement was a constant ratio ($1.5\,\rho_b$) in all beams. Due to the use of stirrups made entirely of GFRP, the pattern of cracks and failures in this group differed from that of the first group. The first crack in the beam B.G1 appeared in the tension region between two loading points at a load of 15 kN, 12.8 % of the ultimate load capacity. The cracks continued to increase in width and length in the bending moment area and started to spread diagonally at a distance (d) from the support face at a 45° oblique angle in the shear zones. These cracks persisted in the shear zone until the beam suddenly failed at a load of 117 kN, at which point the concrete in this zone collapsed and the GFRP stirrups ruptured, followed by splitting in the concrete cover. When compared to B.S1, this beam showed that the stirrups made of GFRP are generally weak in compression and have low elastic modulus compared to stirrups made of steel. This caused the failure pattern for B.S1 to change from compression failure to shear failure in B.G1. Because the GFRP stirrups weakly confine the concrete to the beam compared to steel stirrups, splitting in the concrete was also present in this beam.

The failure pattern of B.G3 beam differed from that of the previous beam. In the compression zone close to the loading zone, where this model failed due to sudden collapsing of the concrete, a condition

known as compression failure at a load of 142 kN occurred. The first vertical crack appeared at a load of 17.5 kN, 12.3 % of the ultimate load capacity, in the tension zone. The cracks spread between the two loading points in the bending moment area until the model failed due to compression. Due to excessive and further confinement of the beam, the failure pattern changed from shear to compression, and the distance between the stirrups became 59.3 % smaller than in the model B.G1. Thus, the addition of more stirrups along the beam increased its capacity to resist shear forces and changed its failure pattern.

The probability of large diagonal cracks in the shear zones or splits in the concrete cover, as occurred with previous beams of the same group, was significantly reduced as a result of the increase in the number of stirrups and the bonding strength between GFRP bars and the concrete. By reducing the beam size, the number of cracks and their width were significantly reduced. Fig. 5 shows the crack pattern of beams of the second group.

Figure 5. Crack pattern of the beams B.G1 and B.G3.

In the third group of beams, shear is the main cause of failure. In the model G1, the first crack appeared at a load of 10 kN, which is about 11 % of the ultimate load capacity, between the two loading points in the mid-span. Directly below the two loading points, cracks continued to develop and grew in length and width. At a load of 35 kN, the cracks began to tilt slightly and spread clearly in an oblique pattern beyond the two loading points on the right and left. When the load was 91 kN and the angle was 45 degrees, shear failure suddenly occurred. The cracks continued to branch in the shear zones and spread diagonally. Horizontal sliding and slight splitting of the concrete cover along the beam illustrates the pattern of failure in this beam. The longitudinal reinforcement with GFRP bars, which was used to resist shear forces, caused splitting in the concrete cover.

In beam G3, the first crack appeared at a load of 7.5 kN, which is about 6.3 % of the ultimate load capacity. First crack appeared vertically between the two loading points. Cracks began to spread in the bending moment area and increased in length and perpendicularity at a load of 20 kN. At a load of 35 kN, cracks began to increase below the loading points on the left and right and spread slightly obliquely. At a load of 70 kN, cracks began to spread in the shear zones. Then, the crack widths began to increase gradually in the shear zones near the supports as the applied load increased, and this was followed by a horizontal crack in the concrete cover beneath the bottom of the beam. This beam exhibited the effect of dowel action, wherein the longitudinal GFRP bars resisted a portion of the shear forces in the beam via dowel action, which had a greater effect than in beam G1. By increasing the ratio of longitudinal GFRP bar reinforcement by 200 % compared to beam G1, the resistance of the beam to shear forces increased by about 29.6 %. The failure pattern consisted of cracking of the concrete cover, an increase in diagonal cracks on both sides of the beam, and a sudden shear failure at a load of 118 kN. Fig. 6 shows the crack pattern of beams of the third group.

Figure 6. Crack pattern of the beams G1 and G3.

3.2.   Load–Deflection

The four-point bending test of the concrete beams involved measuring the load and the midspan displacements at each loading stage. The resulting load–displacement curves revealed a distinct behavior for the beams reinforced with GFRP bars compared to those with all-steel bars. The GFRP-reinforced beams exhibited larger deflections than the steel reinforced beams, regardless of the orientation of the GFRP bars. This can be attributed to the lower elastic modulus of the GFRP bars relative to the steel bars. The service load deflections were also higher for the GFRP-reinforced beams than for the steel-reinforced beams. Thus, GFRP-reinforced concrete beams should be designed with serviceability criteria (deflection and cracks) in mind due to its low modulus of elasticity [15–19]. The type of stirrups, whether GFRP or steel, had barely noticeable impact on the load–displacement curves.

The first group's main variable was steel stirrup spacing. The maximum service load for this group was 60 % of B.S3 beam. Load–deflection curves showed that increasing the number of steel stirrups by gradually reducing their spacing did not affect deflection much as shown in Fig. 7. At service load, B.S1 beam deflection was 15 % lower than that of B.S3. Despite the densification of the steel stirrups, the longitudinal reinforcement ratio with GFRP bars in three beams remained constant, limiting beam deflection. As can be seen from the curves, increasing the number of steel stirrups in the beams increased their load-bearing capacity. The beams failed linear elastic and brittle.
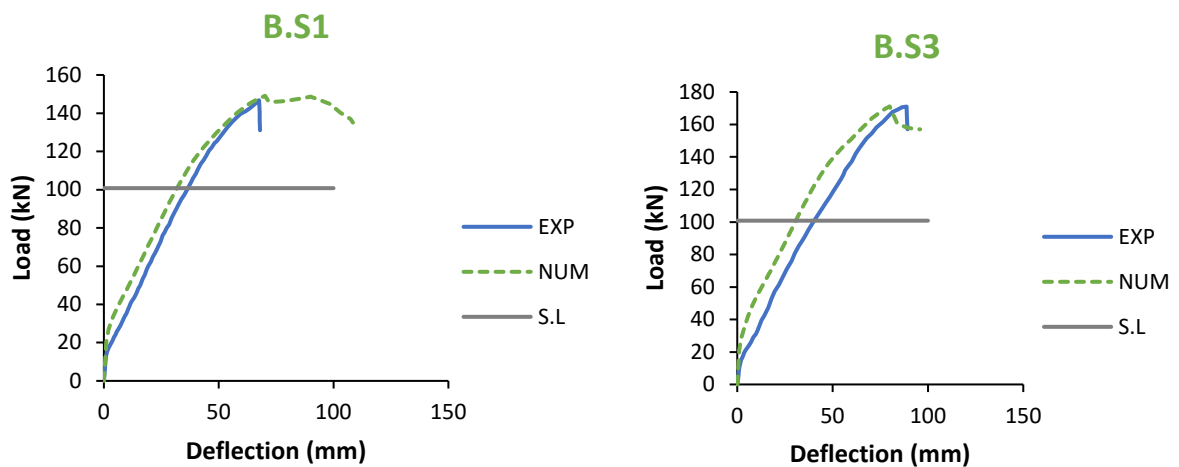
Figure 7. Load–deflection curves for B.S1 and B.S3 beams.

The maximum service load for the second group was the same – 60 % of B.G3 beam. As shown in Fig. 8, increasing the number of GFRP stirrups in concrete beams only slightly affected deflection. Reducing the spacing between them resulting in beam B.G3 deflecting 9.4 % less than B.G1 beam at service load. The deflection was not affected by the spacing between stirrups, but it did affect the pattern of failure in the beams and their capacity to support loads. The curves below show that the beams exhibit linear elastic behavior until failure. In contrast to ductile steel, the beams failed brittle and linearly.
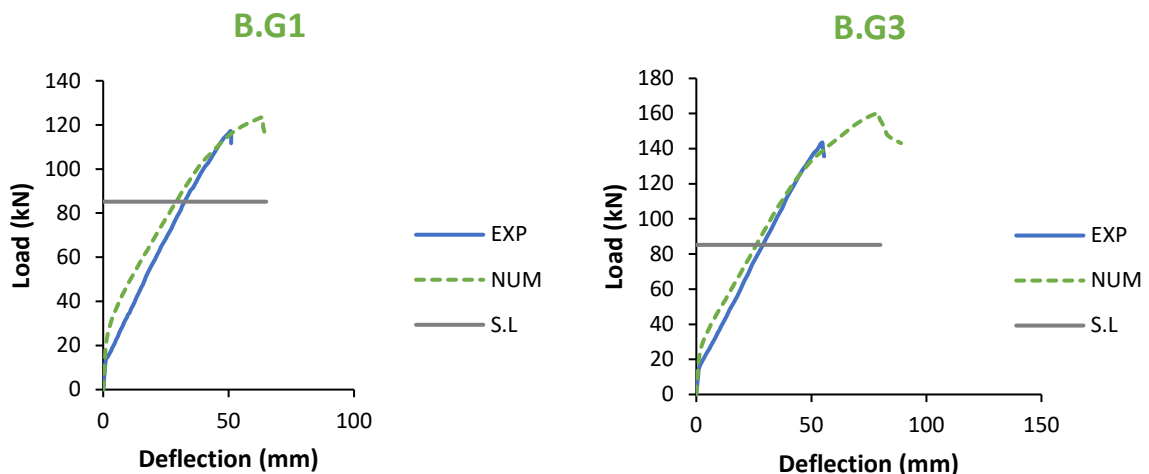
Figure 8. Validation of load–displacement for (B.G1 & B.G3) beams.

The service load ratio in the third group was approximately 60 % of the ultimate load for G3. According to the load–deflection results shown in Fig. 9, increasing the longitudinal reinforcement ratio has contributed to a significant reduction in deflection in G3 beam at service load compared to that of model G1. The curves below show that the deflection in the G3 model is 52 % less than that of model G1 as a result of the increase in the main reinforcement ratio. Increasing the main reinforcement ratio increased the ultimate load bearing capacity of the beams. The behavior of the beams reinforced with GFRP bars under the influence of loads was linear elastic until failure, indicating that the beam exhibited brittle behavior, in contrast to behavior of beams reinforced with steel bars, which was more ductile.
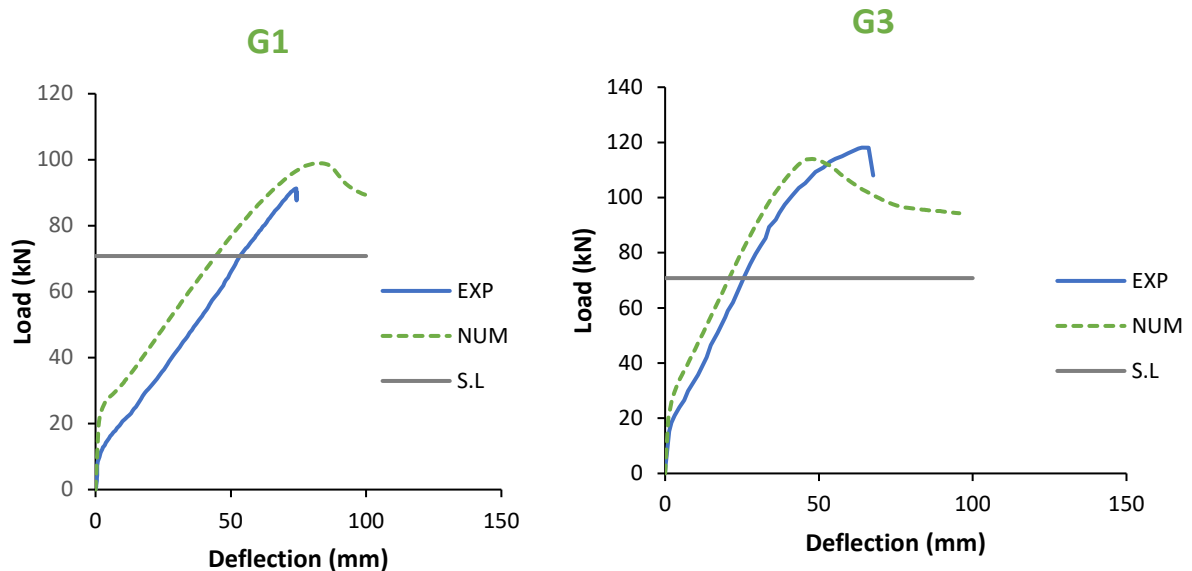
Figure 9. Validation of load–displacement for (G1 & G3) beams.

3.3. Numerical Results

The numerical values showed high consistency and accuracy with the experimental data regarding beam load-bearing capacity and ultimate deflection. The numerical validation revealed that the load–deflection curves had a similar trend to the experimental results. Moreover, the failure mode was also consistent between the experimental and numerical aspects. The results showed that the finite element method (FEM) was more rigid than the experiment test data [20]. The ultimate loads obtained from the experimental test were lower than the final loads obtained from the finite element analysis (FEA), which were significantly higher. These differences were within an acceptable range, and as a result, the FEM could be used for further studies by changing the parameters in question. The agreement between experimental and numerical results in load–deflection was good as shown in the previous curves. The results of the numerous analyses in the ABAQUS program were based on a number of theories and attempts to achieve this accuracy and agreement between the results for the experimental and numerical sides. Since the GFRP had lower compressive strength than the tensile strength, each element in the concrete beams was modeled according to its properties and in a way that is closer to the experimental side. It is worth noting that the GFRP stirrups were modeled in a solid form in order to take the changes in three directions, not only in compression and tension, and for the results to be as realistic as possible [21–25]. Fig. 10 shows the crack pattern of all tested beams using ABAQUS software.
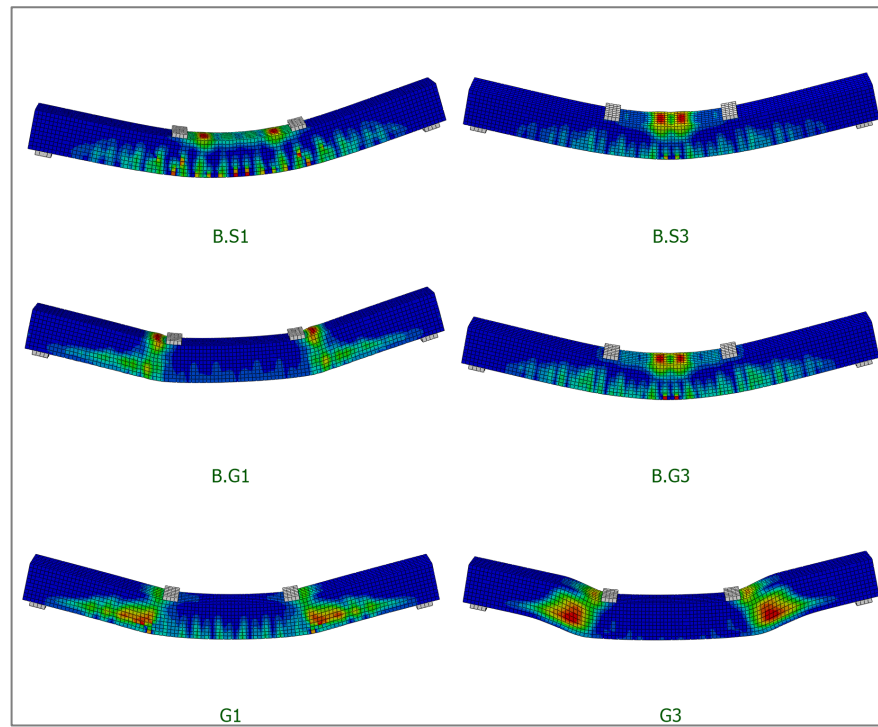
Figure 10. Crack pattern of all tested beams modeled using ABAQUS software.

4. Conclusions

- The results showed that the beams reinforced with GFRP bars exhibited linear elastic and brittle behavior until failure, whereas the beams reinforced with steel bars displayed ductile behavior with. This was attributed to the low modulus of elasticity of GFRP bars compared to the high modulus of elasticity of steel bars.

- Increasing the number of steel stirrups by reducing the spacing between them did not significantly affected deflection, but it contributed to increasing the stiffness of the beam as well as increasing the ability of the beam to bear the bending loads by 16.5 %.

- The resistance of the GFRP stirrup to shear forces was limited compared to the steel stirrup, but the increase in the number of stirrups led to making the beam more confined, and thus the failure pattern shifted from shear failure to compression failure.

- Increasing the number of GFRP stirrups increased the beam capacity to bear loads by 21.4 % and reduced the deflection by 9.4 %. However, increasing the number of steel stirrups at beam B.S3 by a large percentage contributed to increasing deflection because the weight of GFRP is lighter than that of steel.

- By adding more GFRP bars to the main reinforcement, the beam was able to resist shear forces by 29.6 % and reduced deflection by 52 % because of the dowel action effect.

References

1. Said, A.M.I., Abbas, O.M. Evaluation of Deflection in High Strength Concrete (HSC) I-Beam Reinforced with Carbon Fiber Reinforced Polymer (CFRP) Bars. The 7th Asia Pacific Young Researchers and Graduates Symposium "Innovations in Materials and Structural Engineering Practices". Kualapor, 2015. Pp. 519–533.

2. Said, A.M.I., Tu'ma, N.H. Numerical Modeling for Flexural Behavior of UHPC Beams Reinforced with Steel and Sand-Coated CFRP Bars. IOP Conference Series: Earth and Environmental Science. 2021. 856(1). Article no. 012003. DOI: 10.1088/1755-1315/856/1/012003

3. Said, A.I., Abbas, O.M. Serviceability behavior of high strength concrete I-beams reinforced with carbon fiber reinforced polymer bars. Journal of Engineering. 2013. 19(11). Pp. 1515–1530. DOI: 10.31026/j.eng.2013.11.01

4. Ali, S.I., Allawi, A.A. Effect of web stiffeners on the flexural behavior of composite GFRP-concrete beam under impact load. Journal of Engineering. 2021. 27(3). Pp. 73–92. DOI: 10.31026/j.eng.2021.03.06

5. Bank, L.C. Composites for Construction: Structural Design with FRP Materials. John Wiley & Sons, 2006. 576 p.

6. Saraswathy, T., K. Dhanalakshmi. Investigation of Flexural Behaviour of RCC Beams using GFRP Bars. International Journal of Scientific & Engineering Research. 2014. 5(1). Pp. 333–338.

7. El-Nemr, A., Ahmed, E.A., El-Safty, A., Benmokrane, B. Evaluation of the flexural strength and serviceability of concrete beams reinforced with different types of GFRP bars. Engineering Structures. 2018. 173. Pp. 606–619. DOI: 10.1016/j.engstruct.2018.06.089

8. Emparanza, A.R., Kampmann, R., De Caso, F., Morales, C., Nanni, A. Durability assessment of GFRP rebars in marine environments. Construction and Building Materials. 2022. 329. Article no. 127028. DOI: 10.1016/j.conbuildmat.2022.127028

9. Guide for the design and construction of structural concrete reinforced with FRP bars. ACI 440.1R-15. American Concrete Institute (ACI), 2015. 88 p.

10. Selecting proportions for normal-density and high density-concrete – guide. ACI PRC-211.1-22. American Concrete Institute (ACI), 2022.

11. Fibre-reinforced polymer (FRP) reinforcement of concrete – Test methods – Part 1: FRP bars and grids. ISO 10406-1:2015. International Organization for Standardization (ISO), 2015. 39 p.

12. Besseling, J.F. A theory of Elastic, Plastic, and Creep Deformations of an Initially Isotropic Material Showing Anisotropic Strain-Hardening, Creep Recovery, and Secondary Creep. Journal of Applied Mechanics. 1958. 25(4). Pp. 529–536. DOI: 10.1115/1.4011867

13. Genikomsou, A.S., Polak, M.A. Finite element analysis of punching shear of concrete slabs using damaged plasticity model in ABAQUS. Engineering Structures. 2015. 98. Pp. 38–48. DOI: 10.1016/j.engstruct.2015.04.016

14. Yost, J.R., Gross, S.P., Dinehart, D.W. Shear Strength of Normal Strength Concrete Beams Reinforced with Deformed GFRP Bars. Journal of Composites for Construction. 2001. 5(4). Pp. 268–275. DOI: 10.1061/(ASCE)1090-0268(2001)5:4(268)

15. Lin, X., Zhang, Y.X. Bond-slip behaviour of FRP-reinforced concrete beams. Construction and Building Materials. 2013. 44. Pp. 110–117. DOI: 10.1016/j.conbuildmat.2013.03.023

16. Murthy, A.R., Pukazhendhi, D.M., Vishnuvardhan, S., Saravanan, M., Gandhi, P. Performance of concrete beams reinforced with GFRP bars under monotonic loading. Structures. 2020. 27. Pp. 1274–1288. DOI: 10.1016/j.istruc.2020.07.020

17. Ibrahim, T.H., Allawi, A.A. The Response of Reinforced Concrete Composite Beams Reinforced with Pultruded GFRP to Repeated Loads. Journal of Engineering. 2023. 29(1). Pp. 158–174. DOI: 10.31026/j.eng.2023.01.10

18. Mohammed, S.A., Said, A.I. Analysis of concrete beams reinforced by GFRP bars with varying parameters. Journal of the Mechanical Behavior of Materials. 2022. 31(1). Pp. 767–774. DOI: 10.1515/jmbm-2022-0068

19. Ali, H.H., Said, A.M.I. Flexural behavior of concrete beams with horizontal and vertical openings reinforced by glass-fiber-reinforced polymer (GFRP) bars. Journal of the Mechanical Behavior of Materials. 2022. 31(1). Pp. 407–415. DOI: 10.1515/jmbm-2022-0045

20. Allawi, A.A., Ali, S.I. Flexural Behavior of Composite GFRP Pultruded I-Section Beams under Static and Impact Loading. Civil Engineering Journal. 2020. 6(11). Pp. 2143–2158. DOI: 10.28991/cej-2020-03091608

21. Raza, A., Khan, Q.Z., Ahmad, A. Numerical Investigation of Load-Carrying Capacity of GFRP-Reinforced Rectangular Concrete Members Using CDP Model in ABAQUS. Advances in Civil Engineering. 2019. 2019(1). Article no. 1745341. DOI: 10.1155/2019/1745341

22. Stoner, J.G. Finite element modelling of GFRP reinforced concrete beams. Computers and Concrete. 2020. 25(4). Pp. 369–382. DOI: 10.12989/cac.2020.25.4.369

23. Metwally, I.M. Three-dimensional nonlinear finite element analysis of concrete deep beam reinforced with GFRP bars. HBRC Journal. 2017. 13(1). Pp. 25–38. DOI: 10.1016/j.hbrcj.2015.02.006

24. Gemi, L., Madenci, E., Özkılıç, Y.O. Experimental, analytical and numerical investigation of pultruded GFRP composite beams infilled with hybrid FRP reinforced concrete. Engineering Structures. 2021. 244. Article no. 112790. DOI: 10.1016/j.engstruct.2021.112790

25. Stoner, J. Finite element modelling of GFRP reinforced concrete beams. MS thesis. University of Waterloo, 2015. DOI: 10.12989/cac.2020.25.4.369

Information about the authors:

Shaysh A. Mohammed,
E-mail: shaysh96@outlook.com

AbdulMuttailb I. Said,
E-mail: dr.abdulmuttalib.i.said@coeng.uobaghdad.edu.iq

Magazine of Civil Engineering

Soil information model
for prediction the soil properties characteristics

A.V. Gruzin ✉ iD

Omsk State Technical University, Omsk, Russian Federation

✉ *polyot-m@mail.ru*

Abstract. The soil properties characteristics are the object of the current study. Determination of the soil properties characteristics is a complex and responsible engineering and geological task. Reliability of engineering construction and its cost depend on the quality of solution of this task. The article presents the results of the study of the possibility of predicting the soil properties characteristics on the example of determining the sand deformation modulus. Based on the analysis of previous studies of correlation between the soil properties characteristics, the list of independent soil properties characteristics was determined: soil genesis, static normal stress, granulometric composition, initial density and humidity of the soil sample. The main disadvantages of existing methods of predicting the soil properties characteristics were identified. The possibility of using artificial neural network for predicting the soil properties characteristics was determined. The soil deformation modulus was selected as a response (dependent variable). The presence of not only numerical but also classification features among the independent characteristics did not allow predicting the soil properties characteristics within the framework of the classical regression model. A soil information model, based on an artificial neural network, was used to solve this problem because not only continuous quantitative but also discrete classification parameters (genesis) can be used among the independent parameters of the soil information model. Laboratory studies of 655 samples of alluvial sand of the Irtysh River floodplain were performed to confirm the possibility of using the soil information model. 5895 data vectors were obtained, including information on independent and response parameters. A detailed study of two granulometric compositions demonstrated limited possibilities for using known statistical methods for determining the soil properties characteristics. In 9 out of 20 cases, the results of the studies did not follow a normal distribution. The use of the soil information model allowed to solve this problem – the absolute percent error in determining the deformation modulus did not exceed 12.55 % (mean – 5.05 %), the coefficient of determination R^2 was at least 0.83 for unloaded sand samples, and at least 0.94 for loaded ones, for all datasets – 0.97. The performed studies confirmed the prospects of using the soil information model for predicting soil properties based on its known characteristics, which reduced the cost of engineering and geological surveys while ensuring the required accuracy of determining the soil characteristics.

1. Introduction

Characteristics of soil properties are used to classify soils, describe their condition and reaction to external influences of various nature. Determination of the characteristics of the physical and mechanical soils properties is a complex engineering task. At the present time both theoretical and practical scientists continue to solve this task, despite the rich scientific and practical experience of engineering and geological surveys, laboratory determination and subsequent statistical processing of the obtained data. The reason for this is not only the variety of characteristics of various soil properties: physical, mechanical, chemical,

etc., used for engineering purposes, but also the soils variability, caused by the stochastic nature of their genesis. Evidently, this diversity of characteristics, combined with soil variability, requires a large number of samples to ensure the required reliability of the results of the characteristics determination. Since after laboratory studies, as a rule, the studied samples have a broken structure and are unsuitable for reuse as samples, the task of determining the required soil characteristics ceases to be only an engineering task. There is an economic aspect – the need to increase research expenses.

To solve the problem, the author proposes a method, which reduces the number of samples needed and the number of studies for determining and predicting the soil properties characteristics. It is based on both correlations between characteristics and modern digital technologies. Thus, the soil properties characteristics are the object of the current study. A new method for predicting the soil properties characteristics is the subject of the study.

1.1. Correlations between the Soil Properties Characteristics

The solution to the problem of reducing the number of definitions of the soil properties characteristics is seen in the search for a correlation between the characteristics of various soil properties. Thus, the correlation between the characteristics of various soil properties will allow predicting the required characteristics based on the characteristics already studied.

In 1925, K. Terzaghi was one of the first to point out the possibility of a correlation between the characteristics of soil properties [1]. He systematically identified the factors "on which the occurrence and course of phenomena depend, with special consideration for the two elements of deformation and time". He established the influence of packing density on the friction coefficient in sand, water content and previous loading history in loams and clays as well. Analyzing the experience accumulated by his predecessors, K. Terzaghi assigned the leading role in the science of soils to the knowledge of the soil physical properties, suggesting "to rely more on the physical properties of the soil". He wrote about "the need to build the structural mechanics of the soil based on the physics of the soil". He stated that "knowledge of the physical properties of the soil gives us the opportunity to establish a causal relationship between physical causes and technical action in soil construction (landslide, sediment, failure of the foundation, etc.) and when we are not able to present this relationship completely in mathematical form".

In 1941, N.N. Maslov formulated the basic law of the relationship between the soil properties and their formation conditions (genesis). This law establishes that rocks that are identical in their composition, genesis, and occurrence conditions and have undergone the same subsequent changes have the same engineering and geological properties [2].

In 1955, A.K. Birulya reported on the influence of the soil granulometric composition (grain-size distribution, GSD), the composition of its colloidal part, density, humidity and temperature on the soil strength [3].

In 1967, G. Müller pointed out the influence of the processes of soil particles weathering and transportation, that is, the conditions of their formation, on their shape, which determines, in turn, the nature of the mutual adhesion of particles in the soil, the mechanism of their contact [4].

In 1971, M.N. Gol'dshtejn noted "the complexity and diversity of natural conditions that determine the soils mechanical properties" [5]. The author reported on the need "for engineering and geological studies to constantly reveal the relationship between the properties of soils and the conditions of their formation and occurrence, and the material accumulated in this way by survey organizations should be systematically generalized by specialists in the field of engineering geology". It was also noted that "the physical and mechanical properties of those sedimentary rocks that are classified as non-rock soils are determined, firstly, by the relative content of particles of various minerals and the size of these particles, and secondly, by the properties of substances that fill the pores of the soil".

In 1975, F.J. Pettijohn reported on the influence of the formation (genesis), sand mineral composition, and the shape of its particles on the classification characteristics of sandy soil [6].

In 1981, L.M. Arya and J.F. Paris presented a model to predict the moisture characteristic of a soil from its particle-size distribution, bulk density, and particle density parameters [7]. Their model predictions for several soil materials show close agreement with the experimental data.

B.J. Cosby et al. reported, "the name used for the soil in the description relates to the principal soil type and, in general, is based on particle size or the presence of organic material. The soil name thus provides valuable qualitative information concerning the physical and mechanical properties of the material" [8].

In 1989, V.A. Korolev established on the basis of thermodynamics the basic laws of changes in the phase composition and phase ratios of dispersed soils, including during compressive compaction of soils, allowing to predict changes in a number of soil properties during these processes [9].

In 1990, E.C. Drumm et al. reported about the need to take into account the influence of the magnitude of cyclic deviator stress to characterize the soil subgrade and related soil-index properties and the moduli obtained from unconfined compression tests, to resilient modulus M_R [10].

In 1994, D. Li and E.T. Selig developed a method that takes into account the influence of soil physical state, moisture content, stress state, and soil type on M_R of compacted fine-grained subgrade soils [11].

C.R.I. Clayton et al. reported on the influence of the soil particles size on its physical and mechanical properties and on the classification of soils based on their quantitative characteristics [12].

In 1996, S.F. Brown having studied pavement failure mechanisms reported about the influence of soil moisture and loading regime on the soil M_R [13].

L.M. Arya et al. used particle-size data and form of soil particle in their investigation to estimate the soil-water characteristic [14].

In 2002, M.D. Fredlund et al. used information on GSD and the volume-mass properties of a soil for developing a procedure for estimating the soil-water characteristic curve [15]. They also reported about potential to use GSD as a basis for estimating soil behavior [16].

In 2004, N. Khoury and M.M. Zaman studied the influence of moisture changes on the M_R of subgrade soils. They reported that M_R-moisture content relationships for clayey soil exhibit a hysteretic behavior due to wetting and drying. A similar behavior was observed for sandy soil. The clayey soil was more susceptible than the sandy soil to moisture variation. They reported that changes in M_R values and suction were influenced by the initial moisture content [17].

P.S.K. Ooi et al. suggested using data on stress state, soil type, soil structure, and the soil physical state to improve the model for predicting the soil M_R [18].

In their studies, X. Yu et al. demonstrated that "the parameters affecting the shear strength therefore depend on the relative density, gradation, particle strength, particle size and shape, and degree of saturation of the specimen" [19].

In their experimental researches, J.H.S. Kung et al. demonstrated that the stress state, moisture content, and soil suction influenced the M_R and the plastic strain [20]. Unsaturated subgrade M_R reduces with increasing deviator stress and decreasing matric suction. The subgrade plastic strain increases as the deviator stress increases and the matric suction decreases.

T. Wichtmann and Th. Triantafyllidis presented "a study of the influence of GSD curve on the small strain shear modulus G_{max} of quartz sand with sub-angular grain shape" [21]. The article reported on the need to take into account the shape of soil particles when modeling the effect of granulometric composition on its characteristics.

H. Nowamooz et al. carried out an experimental study of the repeated load response of a compacted clayey natural sand at different water contents. It has been proven that there is a strong link between the variation of the bearing capacity of low traffic pavement and the water content of the unbound layers [22].

In 2012, A. Ward reported that "particle size is a fundamental property of any sediment, soil or dust deposit. It influences a variety of other soil properties" such as natural isotope abundance, hydraulic properties, transport properties, thermal properties, reactive properties, and electrical properties [23].

N. Khoury et al. conducted several studies to develop relationships between the M_R of subgrade soils and moisture conditions [24]. They reported that the relationships between M_R and the moisture content exhibit a hysteretic behavior similar to the soil-water characteristic curve; specimens subjected to drying exhibited higher M_R values than specimens subjected to wetting. M_R values on the drying-wetting-drying path are different from the corresponding values on the wetting-drying path.

In 2013, T. Enomoto et al. reported about correlation between increasing of soil grain size and uniformity coefficient and G_{vhd} shear modulus by dynamic measurement and G_{vhs} shear modulus converted from E_{vs} quasi-elastic vertical Young's modulus by static measurement [25].

In 2013, A. Shaqlaih et al. reported about modeling of the M_R correlation with routine properties of subgrade soils and state of stress for pavement design application [26].

C.W.W. Ng et al. investigated using a suction-controlled cyclic triaxial apparatus M_R values of a subgrade soil under various stress and suction conditions. They reported that the measured M_R is highly dependent on the stress state [27].

In 2014, Z. Han and S.K. Vanapalli proposed equations for predicting the M_R of granular materials by using soil-water characteristic curve and GSD [28].

In 2014, N. Lu and M. Kaya reported that for soils, in addition to their well-known dependence on stress, elastic moduli (Young's modulus and shear modulus) depend on volumetric water content and/or matric suction, particularly for silty and clayey soils [29].

In 2015, G.G. Boldyrev and M.V. Malyshev noted that the physico-mechanical soils properties are the result of a complex and long-term interaction of physico-chemical conditions of rock formation, conditions of their occurrence, tectonic processes, regional geological processes associated with the action of gravity of water, gases, temperature fluctuations, biological factors. It was noted that the aerometric definitions data can be useful for assessing the physical and mechanical soils properties as well [30]. It was also noted that in the first approximation, to solve the problems of designing foundations, the angle of internal friction of loose soils can be determined from the correlation of data by statistical probing, relative density, and classification indicators. The shape of the particles, especially sandy soils, affects their strength properties. The soils genesis most often determines their basic physical and mechanical properties.

In 2015, V.A. Korolev and S. Chzhan reported the results of their studies of the effect of the granulometric composition of a mixture of various sizes fractions on the indicators of physical and physico-mechanical properties – density, porosity, internal friction angle, etc. As factors of influence, they considered GSD, addition density, mineral composition, humidity [31]. They found that for sandy and coarse-grained soils, the leading factors are GSD, particle shape and density of soil composition.

I. Ishibashi and H. Hazarika reported on the influence of GSD of the soil and its origin on its properties: "since soil is an assemblage of particles, interlocking of those particles and their contact mechanism – in particular, for larger particles – determines many important mechanical properties of soils such as strength, rigidity, permeability, and compaction" [32]. They reported about soil characteristics correlation: from GSD curve, several key parameters can be obtained, such as the effective grain size (D_{10}), the mean grain size (D_{50}), the coefficient of uniformity (C_u), and the coefficient of gradation (C_g). Those parameters will be used in soil classification practices and will be correlated with many engineering properties of soils such as in compaction, permeability, etc.

A.V. Mel'nikov and G.G. Boldyrev proposed to include the consistency index I_L from the cone penetration tests (CPT) data for clay soils as an additional argument in the correlation equations for clay soils and the specific sleeve resistance f_s – for sands to increase the determination accuracy of deformation modulus E [33]. They reported about decreasing the determination accuracy of the E with increasing content of grainy and clayey fractions in soils as well.

In 2016, A.V. Gruzin et al. proposed a method for regulating the deformation properties of an incoherent dispersed soil based on the granulometric composition [34].

M. Goudarzy et al. conducted "a series of resonant column and compression wave velocity tests simultaneously on dense and loose specimens containing 0, 10, 20, 30, 40 and 50 gravimetric percentages of fine particles to measure the small strain moduli (G_{max}, M_{max} and E_{max}) of the mixtures. Mixture samples were prepared by the moist tamping method and subjected to isotropic confining pressure levels of 50, 100, 150 and 200 kPa" [35]. The authors found that "the accuracy of the predicted maximum stiffness depends on the accuracy of the equivalent granular void ratio".

At the same time, T. Enomoto reported after series of drained triaxial compression tests that quasi-elastic vertical Young's moduli, E_{vs}, measured statically, were generally independent of maximum and mean particle diameters and the effects of fines content and particle angularity on the E_{vs} values were not clear [36].

W.-T. Hong et al. reported on the particle size influence on the soil-water characteristic curve during cyclic tests [37].

In his experiments, M.A. Khasawneh showed a slight increase in M_R values with an increase in confining pressure and a noteworthy decrease in M_R accompanied by an increase in deviatoric stress [38]. Also based on the independent samples t-test analysis, it was revealed that soil type and water content caused statistically significant difference in M_R values.

G.I. López researched grain size analysis methods and noted that granulometry is a basic analytical technique. Several sediment, soil, or material properties are directly influenced by the size of its particles as well as their shape (form, roundness, and surface texture of the grains) and fabric (grain-to-grain interrelation and grain orientation), such as texture and appearance, density, porosity, and permeability [39].

I. Dyka et al. presented the results of laboratory tests that verify the correlation between the grain-size characteristics of non-cohesive soils and the value of the dynamic shear modulus [40].

F.F. Badhon and Md.A. Islam reported about studying the gradation effect on shear strength of sand with various water contents [41]. They performed several direct shear tests on reconstituted sand samples having different GSD (well graded (WG), gap graded (GG), and uniform graded (UG)) with varying water content of 15 % and 25 %. They have established that higher shear strength was obtained for GG soil as compared with the WG and UG.

The research of P.H. Thinh et al. was focused on the correlation between compression index C_c and other properties of the marine dark grey lean clay layer. Their research results showed that the correlation between C_c and liquid limit is the tightest [42].

Y. Sun et al. reported about development of the new grading parameter that considered the size distribution of the entire aggregates to capture the grading-dependence of the shear stiffness of heterogeneous granular aggregates [43]. The grading parameter was found by them to increase with decreasing coefficient of uniformity and median particle size where higher shear stiffness was observed. It was also found that the proposed grading parameter exhibited an improved power-law correlation with the material constants from Hardin's stiffness formula compared with the traditional grading parameter, the coefficient of uniformity.

In their monograph, G.G. Boldyrev and I.H. Idrisov reported numerous empirical dependencies that allow determining the elastic shear modulus G_{max} of coarse – grained and sandy soils based on data on the granulometric composition, particle shape, porosity coefficient, and initial stress conditions [44].

Y. Yao et al. used correlations between the physical properties of subgrade soils including the percentage passing through the No. 200 sieve (0.075 mm), plasticity index, liquid limit, dry density, and the regression coefficients of the new model [45].

In 2019, A.V. Gruzin proposed a method for regulating the characteristics of physical and mechanical properties of dispersed unconnected soil by granulometric synthesis [46].

In their research, B. Ghorbani et al. used the accurate determination of M_R of pavement subgrade soils with its dependence on several influential factors, such as soil physical properties, applied stress conditions, and environmental conditions [47].

The report of C. Mendoza et al. presented the compression behavior of Bogotá's diatomaceous soils. The investigations results have found several practical relationships for secondary consolidation, compressibility index, yield point, initial void ratio, and soil structure. These results show the importance of geological history for soil structure and secondary consolidation [48].

D. Watanabe et al. reported about GSD influence on degree of size segregation in granular flow simulations [49]. They confirmed that the inherent degree of the size segregation clearly affects the run-out distance.

The previously reviewed articles analysis shows that the characteristics of the soil physical properties are most often used as independent variables (often called "predictors" or "features"), such as GSD, density, humidity, and genesis (formation). Many authors reported about the need to take into account influence of the soil stress state as well. Numerous authors most often considered as dependent variables ("responses") the characteristics of the soils mechanical properties, namely the resilient modulus M_R and shear modulus G. Evidently, such a choice is due to the practical relevance of these characteristics.

1.2. Methods for Predicting the Soil Properties Characteristics

There are many methods for developing correlation models for predicting the soil properties characteristics: analytical, empirical, statistical, etc. At present time, regression models (RMs) have become widely used. Such models make it possible to locally solve the problems of predicting the required soil characteristics by using independent predictors. The development of scientific basis for processing the results of partial definitions of the characteristics of the object under study is the one reason for the widespread RMs using. The second reason is the practical confirmation of the adequacy of the results of forecasting performed using RMs. According to the Interstate standard GOST 24026-80, regression analysis model is the dependence of the response on quantitative factors and errors of observation of the

response; regression analysis is a statistical method of analyzing and processing experimental data when only quantitative factors affect the response, based on a combination of the apparatus of the least squares method and the technique of statistical hypothesis testing. It is evident that the engineering and geological conditions uniqueness of each new construction site and the stochastic nature of the soils formation each time give rise to the need to develop new adequate RMs. The scientific approach to planning experimental studies of the soils characteristics allows us to comprehensively solve the problems of both the stochastic nature of the soil properties and the need to ensure the required accuracy of determining the desired characteristic. Many articles are devoted to problems related to the experimental studies planning, the RMs development and their practical use for predicting the characteristics of the soils properties.

In his monograph, C.R. Hicks in detail described the basic concepts of experimental design, from the problem formulation to the results interpretation [50]. Author analyzed the advantages and disadvantages of various models and pointed out the need to establish a list of independent variables that can influence the dependent variables. The same principles and approaches are followed by the authors of [51]. The methods presented by them make it possible to develop a RM for a wide range of cases encountered in practice, including those related to the need for optimization. In [8] the authors reported about possibility to construct models that are based on continuous spatial variation in physical soil properties (such as sand or clay content) which provide even better simulations of soil moisture. In [10] the authors described and demonstrated two statistical models for 11 soils from throughout the state of Tennessee. Authors reported both models provide a good characterization of the response for the soils investigated. In [11] the authors proposed to quantify the soil physical state effect by combinations of two equations relating M_R to moisture content. In [21] the authors reported the proposed correlations predict quite well most of the small strain shear modulus G_{max}-values reported in the literature for sands with a sub-angular grain shape. In [26] the authors developed statistical models to correlate M_R with routine properties of subgrade soils and state of stress. In 2014, a series of uniaxial compression tests were conducted on various compacted soils under varying volumetric water content [29]. The authors of this research proposed a simple power law to describe the dependence of Elastic moduli (Young's modulus and shear modulus) on volumetric water content for all types of soils. In [31] the authors have considered questions of modeling of sandy soils with specified physical and physical-mechanical properties using triangular diagrams represented by modified Feret triangles. X. Luo et al. reported in [52] about development and verification moisture-sensitive and stress-dependent mechanistic-empirical models to predict soil M_R. In [42] the authors revised Terzaghi and Peck formula and proposed a new formula most suitable for the correlation between compression index and liquid limit of the soil layer for geotechnical design in Vietnam and Cambodia. In [45] the authors reported about the development of RM to predict M_R based on subgrade soil physical properties. Authors stated that M_R can be predicted much more easily with physical parameters of subgrade soils rather than conducting triaxial tests. In 2019, A.V. Gruzin proposed computer program modeling the properties of a three-component system using the Gibbs method [53]. The program is designed to calculate using one of the four proposed regression equations and visualize the obtained numerical values of the characteristics of the physical and mechanical properties of dispersed noncohesive soil by constructing a 3D-surface as a function of three independent predictors (fractions of dispersed noncohesive soil). The author reported in [54] a percent error of less than 13.6 % for the physical properties characteristics and less than 2.6 % for the mechanical properties characteristics when predicting using the proposed model, based on Gibbs–Roseboom method. In [47] the authors used the accurate determination of M_R of pavement subgrade soils with its dependence on several influential factors, such as soil physical properties, applied stress conditions, and environmental conditions.

The main RM advantage is an ease of understanding and using for predicting an algebraic equation based on basic statistical principles. At the same time there are some disadvantages of RM, such as certain difficulties in working with categorical variables, in correctly describing nonlinear correlations, in decreasing of the RMs reliability with the variables number increasing and some others.

1.3. Predicting Models based on the Artificial Neural Networks

Many modern studies have shown that the use of the artificial neural networks (ANNs) successfully solves such RM problems as working with categorical (classification) variables.

An attempt at a systematic approach to the analysis of the prospects for the use of ANNs in civil engineering is undertaken by I. Flood and N.A. Kartam in [55, 56]. The authors reported neural networks advantage compared to conventional digital computing techniques, and procedural and symbolic processing. They noted that designing a successful approach for applying ANNs to a specific problem requires experience and imagination as well. E. Tutumluer and R.W. Meier attempted to train ANN constitutive model for computing the M_R of gravels as a function of stress state and various material properties [57]. They reported the pitfalls inherent in the indiscriminate application of ANNs to numerical modeling problems. M. Shahin et al. analyzed many reports on the use of ANNs in engineering fields. They

reported that ANNs have been applied successfully for many geotechnical engineering areas, one of is the prediction of soil properties and behavior [58]. In 2004, they investigated four data division methods used for training ANNs. It was reported that the statistical properties of the data in the training, testing, and validation sets need to be taken into account to ensure that optimal model performance is achieved [59]. Y.M.A. Hashash et al. have developed self-learning in engineering simulation analysis framework, which extracts relevant soil behavior using boundary measurements of load and displacement, facilitated by use of ANN constitutive model [60]. M. Zaman et al. developed four different feedforward-type ANN models: linear network, general regression NN, radial basis function network, and multilayer perceptrons network (MLPN) [61]. In each of these models, the input layer consists of seven nodes, one node for each of the independent variables. The output layer consists of only one node – M_R. The MLPN model with two hidden layers was found to be the best model for the present development and evaluation data sets. In 2012, M.D. Nazzal and O. Tatari developed the ANN models resulted in subgrade M_R predictions with significantly higher accuracy than those estimated using RMs with the same input variables [62]. They reported the use of genetic algorithms in developing the ANN models resulted in enhancing their prediction significantly.

S.-H. Kim et al. developed of an ANN model to estimate subgrade M_R [63]. Authors reported the stress state and physical properties on resilient behavior of subgrade soils were successfully correlated with developed ANN model. H. Tao et al. used back propagation (BP) neural networks algorithm to simulate parameter model of soil GSD based on soil particle analysis tests, and used to simulate the function relationship between soil volumetric water content and matrix suction, which were calculated based on Arya–Paris model [64]. Authors reported about applicability and reliability of their proposed method. To achieve the specified accuracy, the authors used two hidden layer nodes of BP neural networks algorithm. S. Saha et al. developed ANN models to predict the coefficients of a stress- and moisture-dependent M_R model for plastic and nonplastic soils [65]. The developed ANN models consist of three layers, seven input variables, ten hidden neurons, and one output variable. Their models are the three-layered ANNs. The authors did not recommend ANNs for use as a prediction tool for the values that are out of the range of training dataset. The authors reported a good prediction accuracy of the developed models results in better estimation of the M_R of base materials – the R^2 value between the measured and predicted validation M_R values was 0.8. In 2022, I.V. Ofrikhter et al. reported on the successful use of ANN in solving the problem of predicting soil properties [66]. As a result of their research, obtained ANN predicts the angle of friction and specific cohesion of clay soil with reasonable accuracy. The authors proposed the topology of the ANN and carried out the comparison of the estimation accuracy with the existing equations.

ANNs using has become a new stage in the development of RMs for predicting the soils properties characteristics. A review of recent publications confirms this fact.

1.4. Soil Information Model

The previously performed studies analysis allows us to conclude about the complexity of the task of the soil physical and mechanical properties characteristics predicting. When predicting responses (dependent variables), there are different approaches in the selection of influence factors (independent variables). Some of authors mention both quantitative and classification factors as well [2, 6, 30]. Evidently, for correct statistical processing of laboratory results, it is necessary to establish type of probability distribution. Statistical processing of laboratory research results, as a rule, includes the search for and exclusion from consideration of the so-called "gross errors". Previously performed studies do not provide an explanation for such a phenomenon as "gross errors" during the research data statistical processing. Obviously, the reason for the presence of so-called "gross errors" is ignoring the influence of certain factors (features) that are not included in the developed RM. The solution of this problem is seen in the development and use of a soil information model based on RM developed using ANNs, since, according to the Interstate standard GOST 24026-80, the classical regression analysis model is the dependence of the response (dependent variables) on continuous quantitative factors (independent variables) and response observation errors (error terms).

Soil information model (SIM) is an object-oriented electronic (virtual) parametric model that digitally represents the characteristics of the soil (or its separated components) in the form of a set of information-rich elements (features, parameters, characteristics – continuous quantitative and discrete classification) for various external conditions.

It should be noted that in addition to solving the problem of predicting the soil properties characteristics, an important advantage of SIM is its open architecture. This makes it possible to develop SIM by adding to it both new research results and new influence factors (independent variables). It is expected that such SIM will allow predicting soil characteristics using fewer soil samples in comparison with existing methods. This means that SIM using will lead to a reduction of material expenses and waste of time when conducting engineering and geological surveys while maintaining the reliability and necessary accuracy of the obtained characteristics.

Thus, the main purpose of the current study is to develop a method for predicting the soil properties characteristics based on the correlation between the various soil properties characteristics – continuous quantitative and discrete classification and on ANN using.

To achieve this goal, the following tasks were solved:

- the list of independent soil properties characteristics was determined, the main disadvantages of existing methods for predicting the soil properties characteristics were identified, the ANN using possibility to predict the soil properties characteristics was determined, based on the analysis of previously performed studies;

- the laboratory studies of soil samples were carried out in order to determine the values of independent characteristics of soil properties and the necessary information database for ANN training and testing was formed;

- SIM, based on a trained ANN, was developed for predicting the soil properties characteristics and the accuracy of predicting the soil properties characteristics on its base was evaluated.

2. Materials and Methods

2.1. Laboratory tests

According to the Russian Code of Practice SP 22.13330.2016, the calculation of the engineering construction foundation for the second group of limit states (by deformation) using the deformation modulus E is always performed, with the exception of three trivial cases. Therefore, E is selected as a response (dependent variable) of the developed SIM. The availability of proven methods and certified laboratory equipment can reduce the risks of methodological and operational errors in determining E.

2.1.1. Experiment design

The minimum number of soil samples (≥ 6) was determined for each combination of the specified independent soil characteristics (variables, factors), according to the Russian Code of Practice SP 22.13330.2016. As independent soil characteristics, the following were selected: soil genesis, static normal stress σ, soil sample granulometric composition, its initial density ρ and moisture w. The test program developed in accordance with the Interstate standard GOST 12248.4-2020 is shown in Fig. 1.
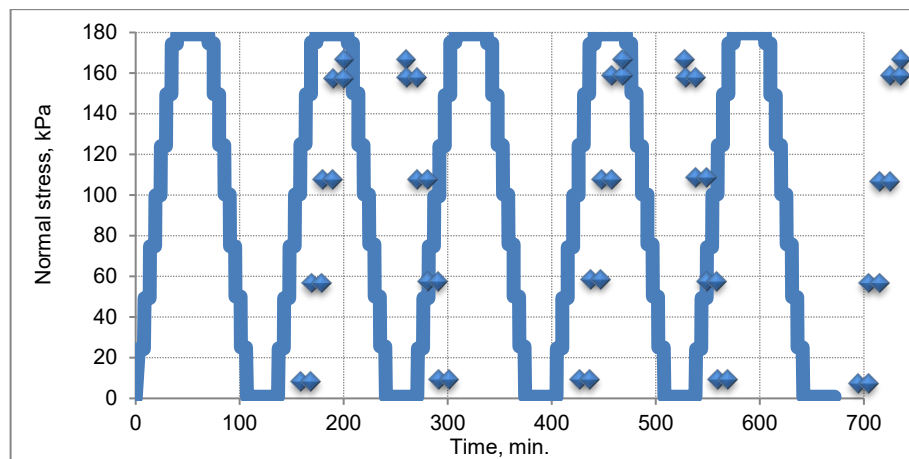
Figure 1. Program of the soil compressibility laboratory tests.

The maximum σ value is determined by the operating conditions for the bases of vertical steel tanks for storing oil and its refined products [67].Compression tests are cyclical in nature and consist of five stages. The number of loading stages shown in Fig. 1 is due to the need to study the effect of the soil initial density ρ on the deformation modulus E.

Statistical processing of the results of laboratory studies for each combination of the specified independent soil characteristics and for each static normal stress σ stage was performed in accordance with the methods presented in [50, 51]. Statistical processing of the results of laboratory soil samples tests included the following main stages: verification of the laboratory data to follow normal distribution, exclusion of "gross errors" of measurement results, determination of the normative soil characteristic value and its root-mean-square deviation (RMSD).

2.1.2. Materials

Sand was chosen as a dispersed incoherent soul because it is necessary to correctly change the soil GSD and to provide the required and controlled values of its independent characteristics for all test samples. Alluvial sand of the Irtysh River floodplain was used for laboratory studies. The initial dry sand was separated by the sieve method into grain size fractions, which were then used to prepare test-samples (Table 1) for laboratory studies in accordance with the research program. The laboratory equipment used for compression tests limited the maximum particle size of the soil test samples. Therefore, fractions with a particle size of more than 10 mm were not used in the studies. The mass fraction of such particles in the original sand was less than 0.2 %.

Table 1. Sand test-samples used in the present study.

Sand sample ID	The soil mass fraction as a function of the sieve mesh size							Number of samples
	5.0 mm	2.0 mm	1.0 mm	0.5 mm	0.25 mm	0.1 mm	Pan	
01							1.0	35
02						1.0		45
03					1.0			30
04				1.0				65
05			1.0					50
06		1.0						35
07	1.0							130
08		0.5	0.5					30
09	0.5		0.5					40
10	0.5	0.5						40
11	0.34	0.33	0.33					105
12	0.2	0.4	0.4					50

Samples dimensions are 25 mm in height and 78 mm in diameter. Fig. 2 illustrates examples of sand test samples with different granulometric composition.

(a) ID 08	(b) ID 09	(c) ID 10

(d) ID 11	(e) ID 12
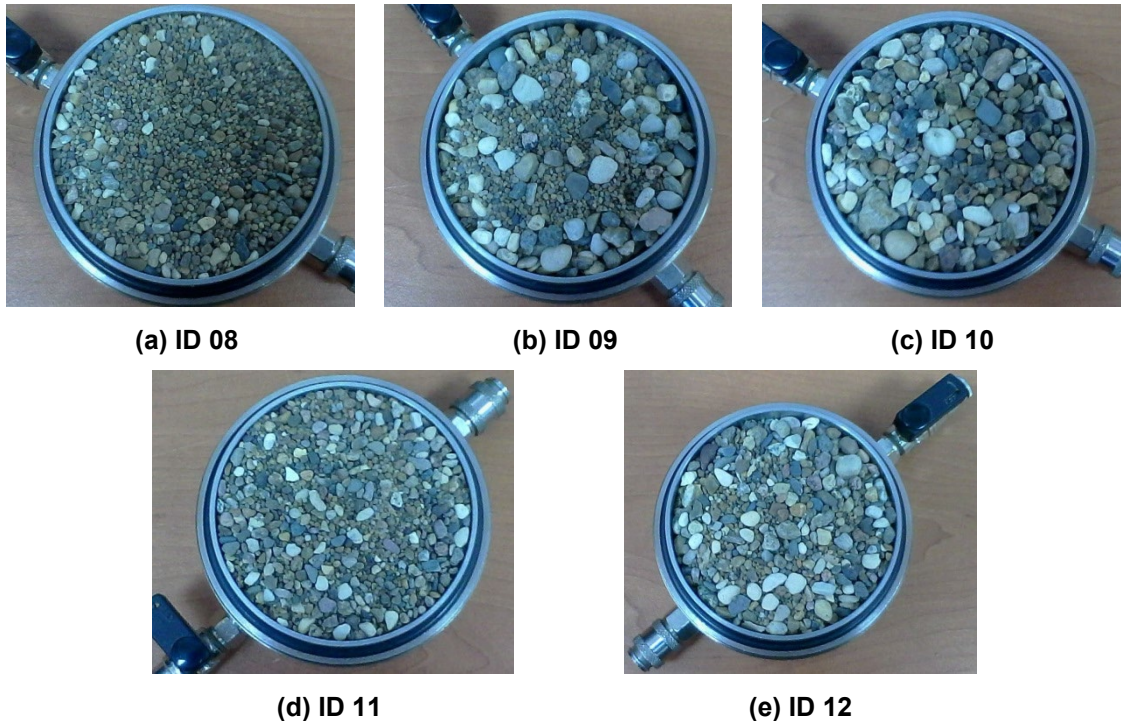
Figure 2. Sand mix test samples.

The different mineralogical composition of the sand test-samples did not allow for the same values of the initial values of its density ρ. Therefore, the actual value of ρ was determined before each test. The results of determining ρ for various stages of cyclical compression tests are shown in Fig. 3 where **ave** is the arithmetic mean, **s** is RMSD, **max** is the maximum value ρ, **min** is the minimum value ρ. The values of the initial density ρ were in the range of 1.30–1.64 g/cm^3 as the measurements showed.
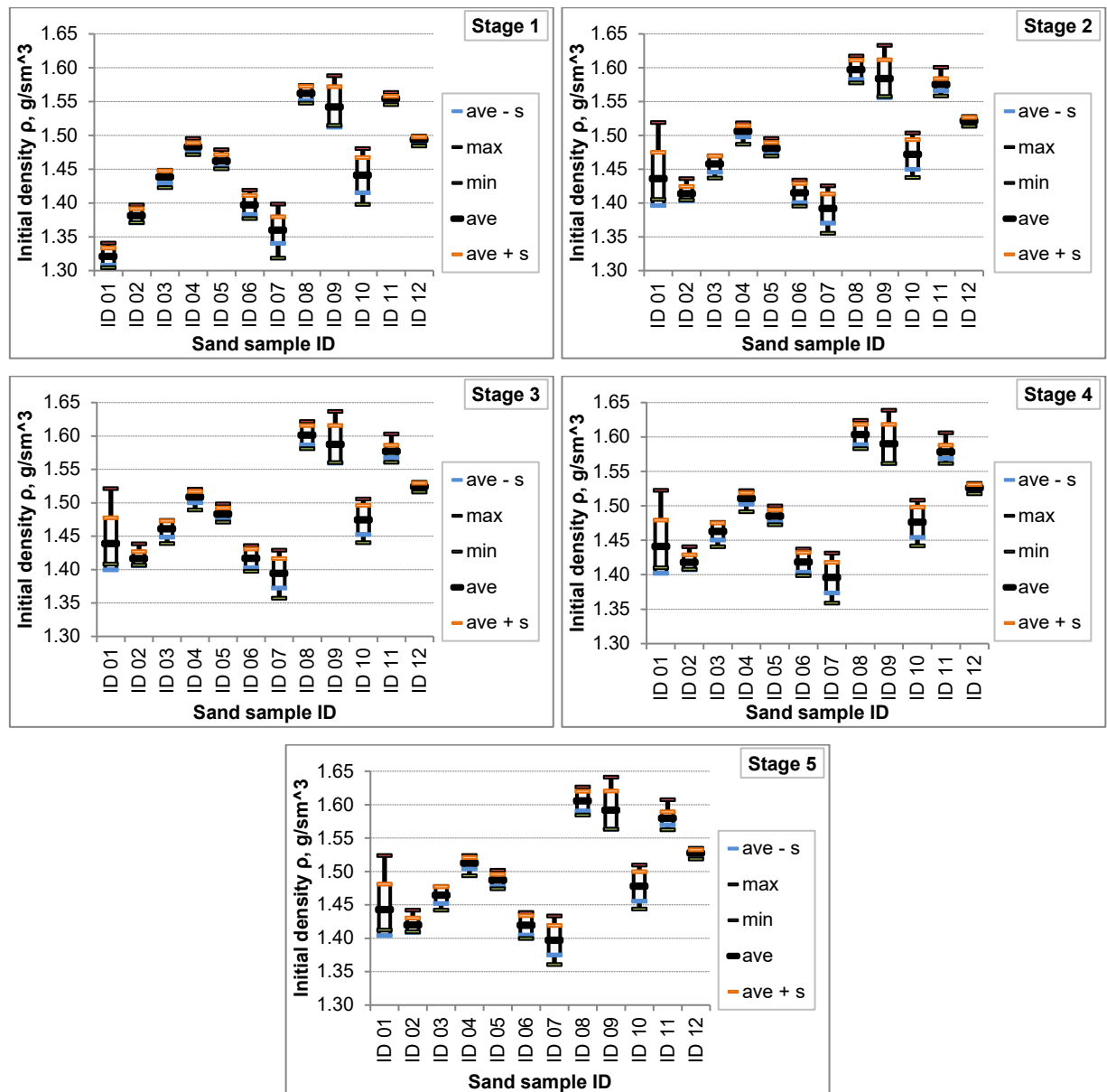
Figure 3. Samples initial density ρ.

In addition, taking into account the complex nature of the sand humidity w influence on its deformation properties [68], it was decided to limit the studies to air-dry sand, the humidity w of which was controlled before laboratory tests and was in the range 0.001÷0.0013.

2.1.3. Laboratory equipment

Fig. 4 illustrates universal automated ASIS test complex for conducting compressibility laboratory tests.

Figure 4. ASIS – equipment for soil compressibility laboratory tests.

The main elements of the ASIS are a loading device (1), a compression oedometer (2), specialized software for computer-based automation of the tests processes (3). The ASIS software regulates the amount and duration of soil sample loading in accordance with the compression test program shown in Fig. 1. The current time, the amount of soil sample loading, and the soil sample deformation are recorded during compressibility laboratory tests.

2.2. Soil Information Model

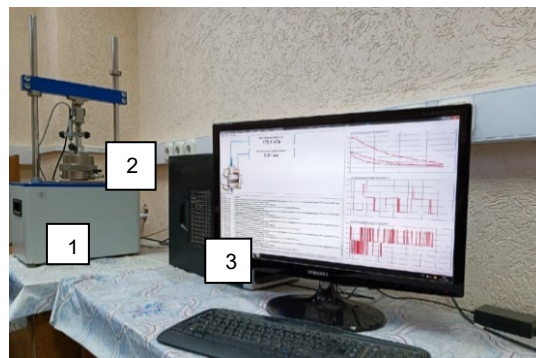As it was noted earlier, the presence of not only numerical but also classification features among the independent variables does not allow predicting the soil properties characteristics within the framework of the classical RM. Sand formation (genesis), for example, is the one of such classification features. It is obvious that further research will also solve this problem since, at a minimum, the classification concept of the soil genesis should include the soil mineralogical composition, the particles shape, that is, characteristics having non-classification quantitative representation. But at this stage of investigations, such detail would obviously significantly complicate the planned research. Thus, since there are classification features among the independent variables, the prediction of the soil properties characteristics can be implemented using SIM based on ANN.

Previous studies review and analysis have shown that ANNs are widely used to solve engineering forecasting problems [55–66]. There are various software approaches for ANN implementation and subsequent modes of its development. The choice was made in favor of the "open source deep learning framework for Python – Keras" due to its simplicity, sufficient number of training materials and accessibility [69, 70]. Work with ANNs starts with its algorithm development. The ANN algorithm used in the research included the following stages of working with the source data: loading and subsequent separation of data into independent variables (features) and response, normalization of the source data, their random permutation and subsequent division into three groups – training, control-verification, and test datasets. The training dataset is needed to train ANN. The control and verification dataset are used for the current control of ANNs training. The test dataset is to evaluate the trained ANN. 655 sand samples were used in the studies, for which 5895 different measurements were performed. In accordance with the recommendations [69], 60 % of the data (3537 measurement results) were used for ANN training, 20 % (1179) – for its current verification, the remaining 20 % (1179) – for evaluation of the trained ANN. The next stage was the ANN model development. A sequential model consisting of 8 layers was used as ANN model: 12 neurons in the input layer, 64 neurons in the hidden layers, and 1 neuron in the output layer. ANN training is an important stage. "Supervised learning" was chosen from the existing methods of ANN training [69]. "Supervised learning" assumes that there is a target vector representing the desired output for each input data vector. Together they are called a training pair. This choice is due to the implementation simplicity and the operational ability to evaluate the results of trained ANNs. The model was trained for about 1200 epochs. As a loss function there was used mean squared error (MSE), widely used in regression analysis, which calculates the square of the difference between the predicted and target values [69]. Program control was carried out to prevent ANN overfitting (overtraining) during the ANN training process. At the final stage, the trained ANN was tested on a test dataset to assess the accuracy of response prediction.

3. Results and Discussion

3.1. Laboratory Studies

During laboratory studies, 655 soil samples were tested. 5895 data vectors were obtained, including independent variables (features) and response. The results of the laboratory studies is presented in Fig. 5.
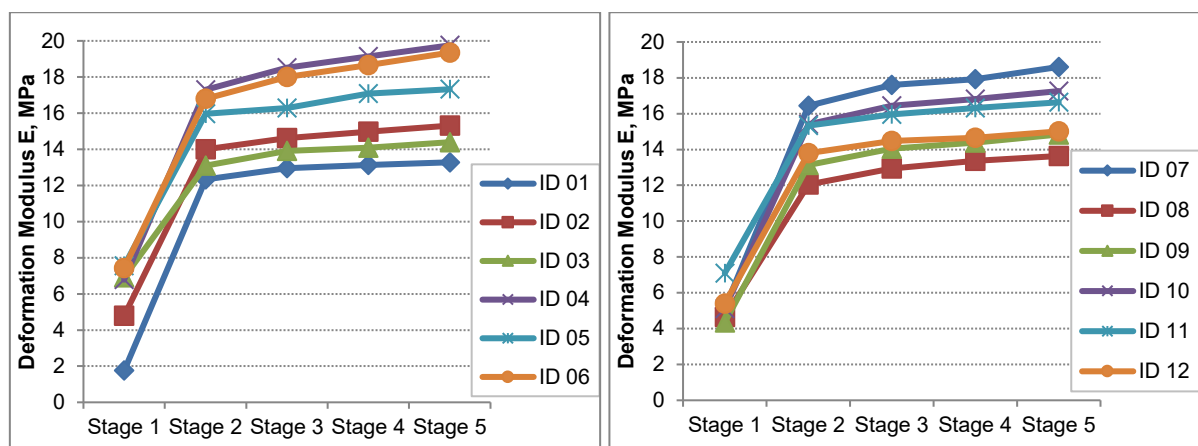

Figure 5. Soil samples deformation modulus E changing during compression tests.

Nonlinear nature of the change of the deformation modulus E of sand samples, depending on the number of stages of their loading, was established during the processing the compression tests results. Minimal changes of the deformation modulus E were observed for the sample ID 03. After the second stage of loading, the deformation modulus E of the sample ID 03 increased by 1.89 times (from 6.92 MPa to 13.10 MPa), after the third – by 1.06 times (from 13.10 MPa to 13.60 MPa), after the fourth – by 1.01 times (from 13.90 MPa to 14.08 MPa), after the fifth – by 1.02 times (from 14.08 MPa to 14.39 MPa). Thus, after five loading stages, the deformation modulus E of the sample ID 03 increased by 2.08 times. The maximum changes in the deformation modulus E were observed for the sample ID 01. After the second stage of loading, the deformation modulus E of the sample ID 01 increased by 7.05 times (from 1.75 MPa to 12.34 MPa), after the third – by 1.05 times (from 12.34 MPa to 12.95 MPa), after the fourth – by 1.01 times (from 12.95 MPa to 13.12 MPa), after the fifth – by 1.01 times (from 13.12 MPa up to 13.28 MPa). Thus, after five loading stages, the deformation modulus E of the sample ID 01 increased by 7.58 times. The performed studies have established the nonlinear nature of the influence of the granulometric composition on the deformation modulus E of sand.

The results of deformation modulus E determining for various stages of cyclic loading are shown in Fig. 6 where **ave** – arithmetic mean, **s** – standard deviation, **max** – maximum value, **min** – minimum value.
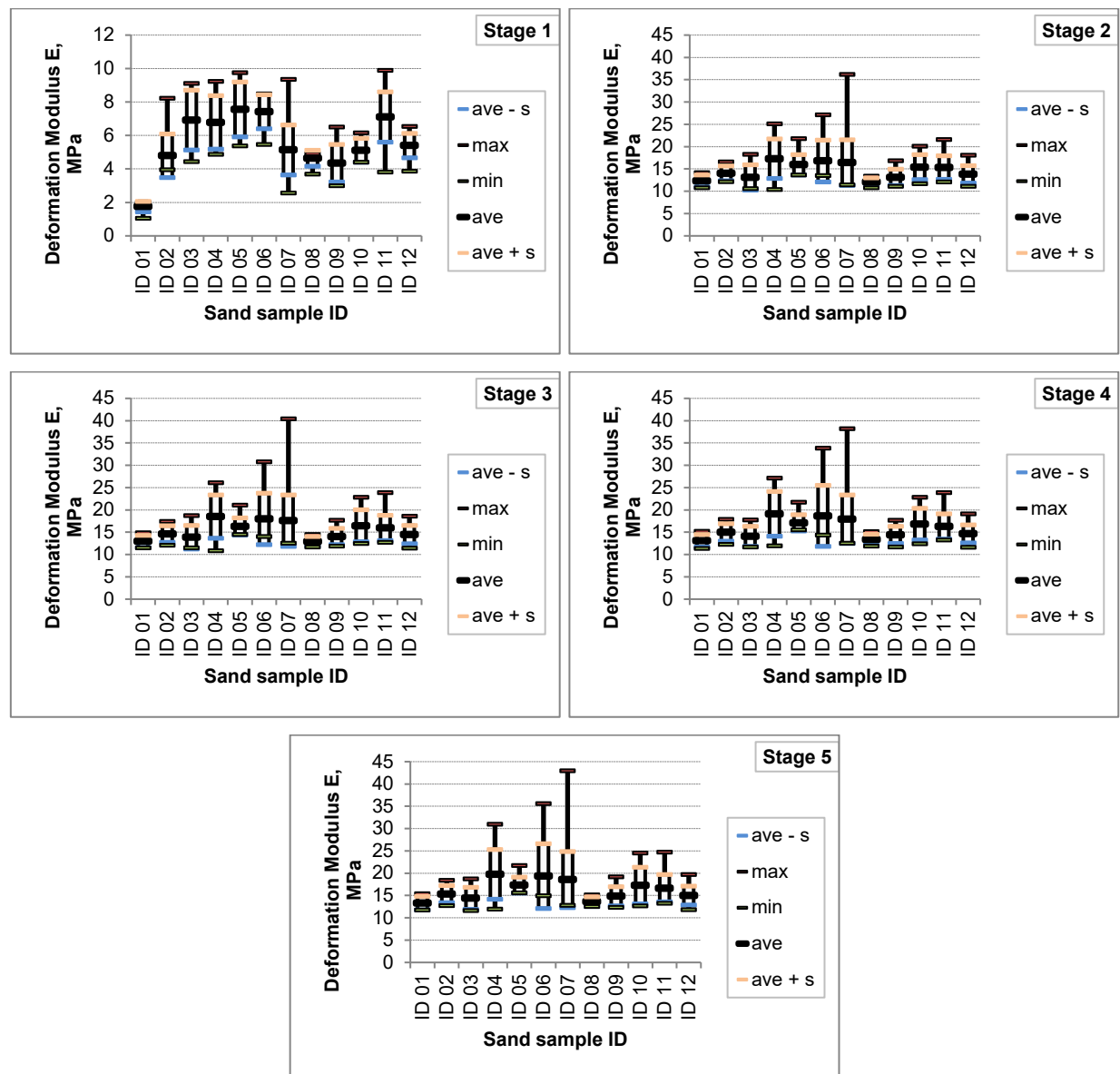

Figure 6. Soil composition influence on deformation modulus E.

As can be seen from the laboratory data, the minimum values of the coefficient of variation (CV) of the deformation modulus E for all loading stages were obtained for the sample ID 08 – from 0.0788 to 0.1025. The maximum CV values were obtained for samples ID 06 and ID 07 – from 0.2899 to 0.3765. At

the same time, the minimum CV values of the initial density ρ were obtained for samples ID 11 and ID 12 – from 0.0023 to 0.0034. The maximum CV values were obtained for samples ID 01 and ID 09 – from 0.0194 to 0.0267 (Fig. 3). Thus, during the conducted studies there was not revealed a significant influence of the precision and repeatability of the determinations of the initial density values on the precision and repeatability of the determinations of the deformation modulus E. It was established that CV of the initial density ρ values is, as a rule, ten times less than the CV of the deformation modulus E. In the studied range of normal stress, there is established the linear nature of the influence of the soil sample initial density ρ on its deformation modulus E.

According to the Interstate standard GOST R 8.736-2011 for samples ID 07 and ID 11, there was verified the hypothesis that the results of independent testing of the initial density ρ and the deformation modulus E follow the normal probability distribution law. Initially, according to the Interstate standard GOST 20522-2012, for the samples ID 07, it was established that for all loading (normal stress) stages, the soil initial density ρ dataset is homogeneous (CV ≤ 0.15). At the same time, the soil deformation modulus E dataset for the first stage of loading is homogeneous (CV ≤ 0.3), for the other remaining loading stages it is inhomogeneous. For sample ID 07, 5 soil samples were excluded from 26 soil samples as having "gross errors". After excluding "gross errors", all the remaining datasets on their soil deformation modulus E and the initial density ρ were homogeneous. Table 2 presents the results of verifying the hypothesis that the results of independent testing of remaining 21 samples follow the normal probability distribution law at a significance level q over 5 %.

Table 2. Sand samples ID 07 and ID 11 testing results.

Sand sample ID	Soil characteristics	Stage	Initial number of samples	Allowed number of samples	Mean	s	Follows the normal distribution
ID 07	Initial density ρ	1	26	26	1.360	0.020	Yes
		2	26	25	1.393	0.022	No
		3	26	25	1.395	0.022	Yes
		4	26	23	1.399	0.022	No
		5	26	24	1.398	0.023	No
	Deformation modulus E	1	26	26	5.138	1.490	No
		2	26	25	15.652	3.199	No
		3	26	25	16.688	3.468	No
		4	26	23	16.319	2.376	No
		5	26	24	17.120	3.048	No
ID 11	Initial density ρ	1	21	21	1.555	0.004	No
		2	21	20	1.574	0.007	Yes
		3	21	19	1.575	0.007	Yes
		4	21	20	1.577	0.008	Yes
		5	21	20	1.578	0.008	Yes
	Deformation modulus E	1	21	21	7.100	1.503	Yes
		2	21	20	15.466	2.654	Yes
		3	21	19	15.675	2.214	Yes
		4	21	20	16.435	2.838	Yes
		5	21	20	16.777	3.058	Yes

The hypothesis that the remaining initial density ρ dataset follows the normal probability distribution law was confirmed only for the first and third normal stress stages. The hypothesis that the remaining deformation modulus E dataset follows the normal probability distribution law was not confirmed for any normal stress stage.

For the samples ID 11, it was established that for all normal stress stages, the soil initial density ρ dataset is homogeneous (CV ≤ 0.15). For all normal stress stages the soil deformation modulus E dataset is homogeneous (CV ≤ 0.3) as well. However, according to the Interstate standard GOST R 8.736-2011, 3 soil samples were excluded from 21 soil samples ID 11 as "gross errors". Table 2 presents the results of verifying the hypothesis that the results of independent testing of remaining 18 samples follow the normal probability distribution law at a significance level q over 5 %. The hypothesis that the remaining initial

density ρ dataset follows the normal probability distribution law was not confirmed only for the first normal stress stage. The hypothesis that the remaining deformation modulus E dataset follows the normal probability distribution law was confirmed for all normal stress stage.

Thus, the obtained research data demonstrate a limited possibility of using methods for processing measurement results based on the hypothesis that the measurement results follow the normal distribution for such characteristics of soil properties as the sand initial density ρ and its deformation modulus E. The impossibility of developing adequate regression models for these characteristics is an important consequence of this conclusion.

3.2.   Prediction based on SIM

The developed SIM on the basis of a trained ANN made it possible accuracy evaluation of the soil deformation modulus E predicting. The remaining 20 % of the dataset (test array) – 1179 laboratory measurement results were used for this purpose. It should be particularly noted that **ALL** (5895, without any exceptions) measurement results of soil samples laboratory tests were used for the training, verification and testing purposes. The results of SIM testing are presented in Fig. 7. The test array contains data of different samples under different normal stress.
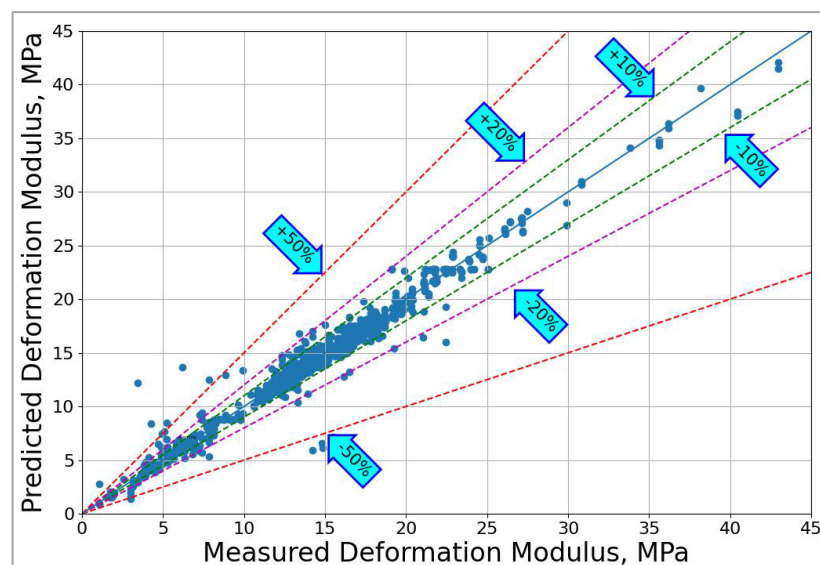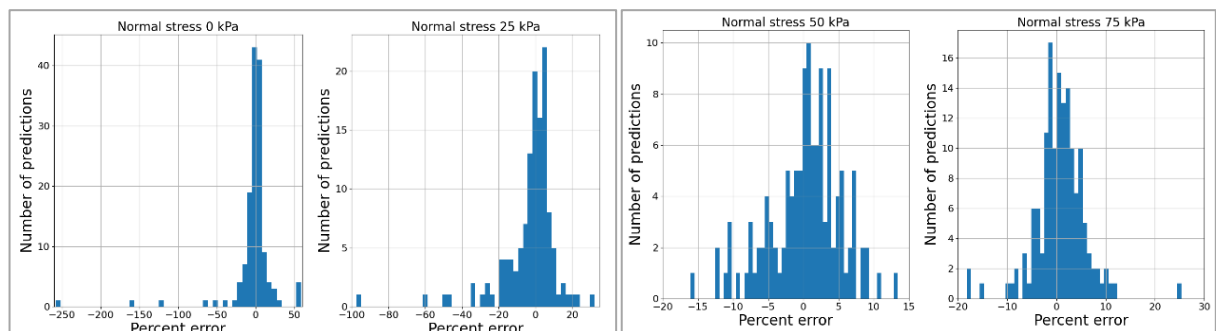

Figure 7. Prediction of the deformation modulus E using SIM.

The percent error (PE) is proposed to use as a characteristic for determination the accuracy predicting. The PE values for various normal stresses, which allow us to estimate the accuracy of deformation modulus E predicting using a SIM, are presented in Fig. 8.
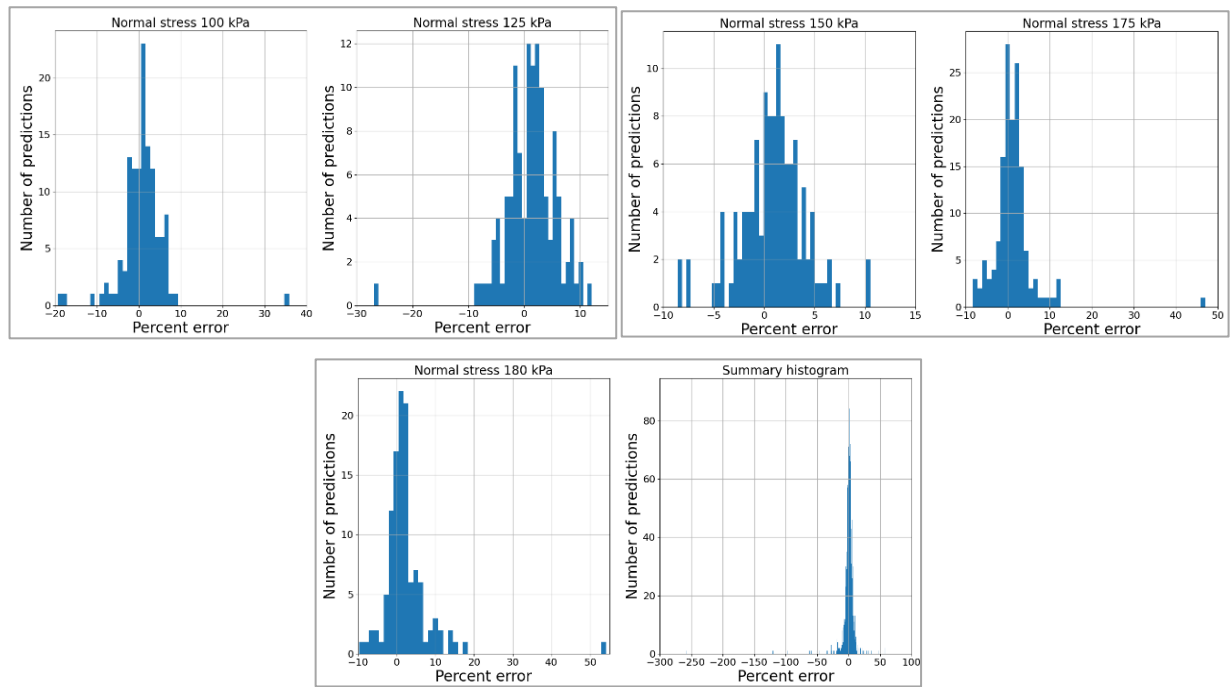
**Figure 8. PE in predicting the deformation modulus E using SIM
for various normal stress conditions of soil samples.**

PE was in the range from –257.81 to 58.66 %, as can be seen from the data presented in Fig. 8. This maximum range (316.47 %) is for unloaded soil samples. For normal stress of 25 kPa, PE range is 129.56 %, for 50 kPa – 29.47 %, for 75 kPa – 43.61 %, for 100 kPa – 55.18 %, for 125 kPa – 39.02 %, for 150 kPa – 19.10 %, for 175 kPa – 55.31 %, for 180 kPa – 63.80 %. Fig. 9 shows the PE values for various normal stress conditions.

Figure 9. Prediction results accuracy.

The maximum absolute PE value (12.55 %) is for unloaded soil samples. The minimum absolute PE value (2.54 %) is for normal stress σ = 150 kPa. Mean absolute percent error (MAPE) is 5.05 %. The results of test array predicting using SIM are presented in Table 3.

Table 3. Results of the test array prediction.

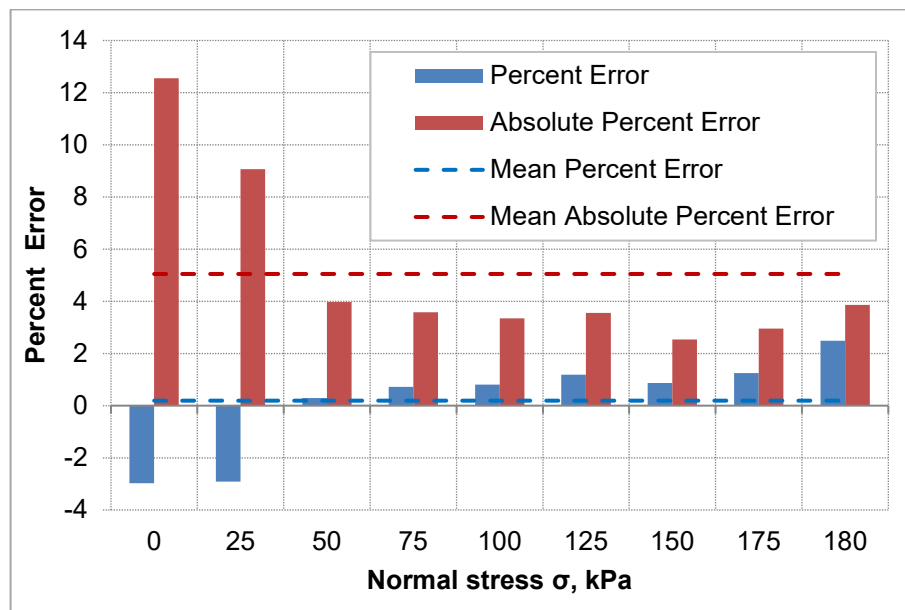| Normal stress σ, kPa	Percent error δ, %				Coefficient of determination R^2
	Min	Max	Mean	Mean absolute	
0	–257.81	58.66	-2.97	12.55	0.8265
25	–97.46	32.10	-2.91	9.06	0.9403
50	–16.06	13.41	0.29	3.97	0.9810
75	–18.21	25.40	0.72	3.59	0.9902
100	–19.32	35.87	0.81	3.35	0.9873
125	–26.93	12.08	1.19	3.56	0.9910
150	–8.57	10.53	0.87	2.54	0.9931
175	–8.34	46.98	1.24	2.96	0.9942
180	–9.71	54.09	2.49	3.86	0.9913
For all dataset	–257.81	58.66	0.19	5.05	0.9684

Analysis of the values in Table 3 shows that the prediction accuracy characteristics (MAPE and coefficient of determination R^2) obtained on base SIM correspond to values of the same characteristics obtained by another researches [65, 66]. In current study the minimum value of coefficient of determination R^2 = 0.8265 is for unloaded soil samples (normal stress σ = 0 kPa), for normal stress σ = 25 kPa – 0.9403, for others – more than 0.98. For all dataset the coefficient of determination R^2 = 0.9684. The reason for the low coefficient of determination values is the greater and stochastic effect of the friction forces between the soil particles on the soil density for small values of normal stress (≤ 25 kPa).

4. Conclusions

The results of the soil properties characteristics prediction using SIM, the independent parameters of which are continuous quantitative and discrete classification features, are presented in the article. The following conclusions are drawn on the basis of laboratory studies outcomes:

1) the possibility of the soil deformation modulus prediction based on its genesis and physical properties characteristics is confirmed;

2) independent variables sufficient set – soil characteristics: genesis, normal stress, granulometric composition, initial density and humidity – has been confirmed to determine soil deformation modulus;

3) the possibility of SIM using based on a trained ANN to predict the soil properties characteristics, including cases when classical regression models using is impossible, has been confirmed;

4) the SIM using experience shows that small amounts of data (less than 10000 measurement results) for training ANN allow us to obtain satisfactory results in the soil properties characteristics predicting;

5) the SIM using allows to abandon the deformation modulus direct studies, and to determine it indirectly using SIM without losing the determination accuracy, minimizing material and time expenses.

References

1. Terzaghi, K. Erdbaummechanik auf Bodenphysikalischer Grundlage [Construction mechanics of soils based on its physical properties]. Leipzig: Franz Deuticke Press, 1925. 399 p.

2. Maslov, N.N. Inzhenernaya geologiya (Osnovy geotekhniki) [Engineering Geology (Fundamentals of geotechnics)]. Leningrad; Moscow: Gosstrojizdat, 1941. 432 p.

3. Birulya, A.K. Dorogi iz mestnyh materialov [Roads made of local materials]. Moscow: Avtotransizdat, 1955. 140 p.

4. Müller, G. Methods in Sedimentary Petrology. New York: Hafner Publishing Co., 1967. 283 p.

5. Gol'dshtejn, M.N. Mekhanicheskie svojstva gruntov [Mechanical properties of soils]. Moscow: Strojizdat, 1971. 368 p.

6. Pettijohn, F.J. Sedimentary Rocks. 3rd Edition, New York: Harper and Row, 1975. 628 p.

7. Arya, L.M., Paris, J.F. A Physicoempirical Model to Predict the Soil Moisture Characteristic from Particle-Size Distribution and Bulk Density Data. Soil Science Society of America Journal. 1981. 45(6). Pp. 1023–1030. DOI: 10.2136/sssaj1981.03615995004500060004x

8. Cosby, B.J., Hornberger, G.M., Clapp, R.B., Ginn T.R. A Statistical Exploration of the Relationships of Soil Moisture Characteristics to the Physical Properties of Soils. Water Resources Research. 1984. 20(6). Pp. 682–690.

9. Korolev, V.A. Termodinamicheskiye zakonomernosti formirovaniya fazovogo sostava nemerzlykh dispersnykh gruntov [Thermodynamic regularities of the formation of the phase composition of unfrozen dispersed soils]. Inzhenernaya geologiya [Engineering geology]. 1989. 3. Pp. 17–32.

10. Drumm, E.C., Boateng-Poku, Y., Pierce, T.J. Estimation of Subgrade Resilient Modulus from Standard Tests. Journal of Geotechnical Engineering. 1990. 116(5). Pp. 774–789. DOI: 10.1061/(ASCE)0733-9410(1990)116:5(774)

11. Li, D., Selig, E.T. Resilient Modulus for Fine-Grained Subgrade Soils. Journal of Geotechnical Engineering. 1994. 120(6).

12. Pp. 939–957. DOI: 10.1061/(ASCE)0733-9410(1994)120:6(939)

13. Clayton, C.R.I., Matthews, M.C., Simons, N.E. Site Investigation. Blackwell Science. Oxford, U.K., 1995. 489 p.

14. Brown, S.F. Soil mechanics in pavement engineering. Géotechnique. 1996. 46(3). Pp. 383–426. DOI: 10.1680/geot.1996.46.3.383

15. Arya, L.M., Leij, F.J., Van Genuchten, M.Th., Shouse, P.J. Scaling Parameter to Predict the Soil Water Characteristic from Particle-Size Distribution Data. Soil Science Society of America Journal. 1999. 63(3). Pp. 510–519. DOI: 10.2136/sssaj1999.03615995006300030013x

16. Fredlund, M.D., Wilson, G.W., Fredlund, D.D. Use of the grain-size distribution for estimation of the soil-water characteristic curve. Canadian Geotechnical Journal. 2002. 39 (5). Pp. 1103–1117. DOI: 10.1139/t02-049

17. Fredlund, M.D., Fredlund, D.D., Wilson, G.W. An equation to represent grain-size distribution: Reply. Canadian Geotechnical Journal. 2002. 39 (6). Pp. 1437–1438. DOI: 10.1139/t02-080

18. Khoury, N., Zaman, M.M. Correlation between Resilient Modulus, Moisture Variation, and Soil Suction for Subgrade Soils. Transportation Research Record Journal of the Transportation Research Board. 2004. 1874(1). Pp. 99–107. DOI: 10.3141/1874-11

19. Ooi, P.S.K., Archilla, A.R., Sandefur, K.G. Resilient Modulus Models for Compacted Cohesive Soils. Transportation Research Record: Journal of the Transportation Research Board. 2004. 1874(1). Pp. 115–124. DOI: 10.3141/1874-13

20. Yu, X., Ji, S., Janoyan, K.D. Direct shear testing of rockfill material in Soil and Rock Behavior and Modeling. Geotechnical Special Publication. American Society of Civil Engineers. 2006. Pp. 149–155.

21. Kung, J.H.S., Lin, H.D., Yang, S.-R., Huang, W.-H. Resilient Modulus and Plastic Strain of Unsaturated Cohesive Subgrade Soils. Fourth International Conference on Unsaturated Soils. 2006. DOI: 10.1061/40802(189)41

22. Wichtmann, T., Triantafyllidis, Th. Influence of the grain size distribution curve of quartz sand on the small strain shear modulus Gmax. Journal of Geotechnical and Geoenvironmental Engineering. 2009. 135(10). Pp. 1404–1418. DOI: 10.1061/(ASCE)GT.1943-5606.0000096

23. Nowamooz, H., Chazallon, C., Arsenie, M.I., Hornych, P., Masrouri, F. Unsaturated resilient behavior of a natural compacted sand. Computers and Geotechnics. 2011. 38(4). Pp. 491–503. DOI: 10.1016/j.compgeo.2011.02.013

24. Ward, A. The Importance of Particle Size Distributions to the Characterization of Soils. Caribbean Institute for Meteorology and Hydrology. October 25, 2012. 43 p.

25. Khoury, N., Brooks, R., Khoury, C.N., Yada, D. Modeling Resilient Modulus Hysteretic Behavior with Moisture Variation. International Journal of Geomechanics. 2012. 12(5). Pp. 519–527. DOI: 10.1061/(ASCE)GM.1943-5622.0000140

26. Enomoto, T., Qureshi, O.H., Sato, T., Koseki, J. Strength and deformation characteristics and small strain properties of undisturbed gravelly soils. Soils and Foundations. 2013. 53(6). Pp. 951–965. DOI: 10.1016/j.sandf.2013.10.004

27. Shaqlaih, A., White, L.W., Zaman, M. Resilient Modulus Modeling with Information Theory Approach. International Journal of Geomechanics. 2013. 13(4). Pp. 384–389. DOI: 10.1061/(ASCE)GM.1943-5622.0000221

28. Ng, C.W.W., Chao, Z., Yuan, Q., Xu, J. Resilient modulus of unsaturated subgrade soil: Experimental and theoretical investigations. Canadian Geotechnical Journal. 2013. 50(2). DOI: 10.1139/cgj-2012-0052

29. Han, Z., Vanapalli, S.K. Prediction of the Variation of the Resilient Modulus with Respect to the Soil Suction for Three Granular Materials Using Three Methods. Conference: Geo-Shanghai 2014. 2014. DOI: 10.1061/9780784413418.041

30. Lu, N., Kaya, M.A. Power Law for Elastic Moduli of Unsaturated Soil. Journal of Geotechnical and Geoenvironmental Engineering. 2014. 140 (1). Pp. 46–56. DOI: 10.1061/(ASCE)GT.1943-5606.0000990

31. Boldyrev, G.G., Malyshev, M.V. Mekhanika gruntov (v voprosakh i otvetakh) [Soil mechanics (in questions and answers)]. Moscow: Prondo, 2015. 426 p.

32. Korolev, V.A., Chzhan, S. Modelirovanie peschanyh gruntov s zadannymi fizicheskimi i fiziko-mekhanicheskimi svojstvami [Modeling of sandy soils with specified physical and physical-mechanical properties]. Inzhenernaya geologiya. 2015. 4.

33. Pp. 6–14.

34. Ishibashi, I., Hazarika, H. Soil Mechanics Fundamentals and Applications. 2nd edn. CRC Press, Taylor & Francis Group. Boca Raton, London, New York, 2015. 432 p. DOI: 10.1201/b18236

35. Mel'nikov, A.V., Boldyrev, G.G. CPT Correlation Equations for the Soil Deformation Modulus. Soil Mechanics and Foundation Engineering. 2015. 52(3). Pp. 115–121. DOI: 10.1007/s11204-015-9316-x

36. Gruzin, A.V., Antropova, L.B., Rusanova, A.D., Katunin, A.V., Gildebrandt, M.I., Sirotin, A.D. Sposob regulirovaniya deformatsionnykh svoystv nesvyaznogo dispersnogo grunta [A method for regulating the deformation properties of an incoherent dispersed soil]. Patent Russia no. 2621799, 2016.

37. Goudarzy, M., König, D., Schanz, T. Small strain stiffness of granular materials containing fines. Soils and Foundations. 2016. 56(5). Pp. 756–764. DOI: 10.1016/j.sandf.2016.08.002

38. Enomoto, T. Effects of grading and particle characteristics on small strain properties of granular materials. Soils and Foundations. 2016. 56(4). Pp. 745–750. DOI: 10.1016/j.sandf.2016.07.014

39. Hong, W.-T., Jung, Y.-S., Kang, S., Lee, J.-S. Estimation of Soil-Water Characteristic Curves in Multiple-Cycles Using Membrane and TDR System. Materials. 2016. 9. Article no. 1019. DOI: 10.3390/ma9121019

40. Khasawneh, M.A. Investigation of Factors Affecting the Behavior of Subgrade Soils Resilient Modulus Using Robust Statistical Methods. International Journal of Pavement Engineering. 2017. 20(3). Pp. 1193–1206. DOI: 10.1080/10298436.2017.1394101

41. López, G.I. Grain Size Analysis. In: Gilbert, A.S. (eds) Encyclopedia of Geoarchaeology. Encyclopedia of Earth Sciences Series. Springer. Dordrecht, 2017. Pp. 341–348. DOI: 10.1007/978-1-4020-4409-0_18

42. Dyka, I., Srokosz, P.E., Bujko, M. Influence of grain size distribution on dynamic shear modulus of sands. Open Engineering. 2017. 7(1). Pp. 317–329. DOI: 10.1515/eng-2017-0036

43. Badhon, F.F., Islam, Md.A. Effect of Gradation on Shear Strength of Sand. Proceedings of the International Conference on Engineering Research, Innovation and Education, 13–15 January 2017, SUST, Sylhet, Bangladesh.

44. Thinh, P.H., Tuan, H.A., Bien, D.C., Ha, N.H. Research on correlation between compression index (Cc) and other properties of soil for geotechnical design in coastal regions of Vietnam and Cambodia. MOJ Civil Engineering. 2017. 2(3). Pp. 97–101. DOI: 10.15406/mojce.2017.02.00034

45. Sun, Y., Shen, Y., Chen, C. A grading parameter for evaluating the grading-dependence of the shear stiffness of granular aggregates. Particuology. 2018. 36. Pp. 193–198. DOI: 10.1016/j.partic.2017.05.006

46. Boldyrev, G.G., Idrisov, I.H. Metody opredeleniya dinamicheskikh svoystv gruntov [Methods for determining the dynamic properties of soils]. Moscow: Prondo, 2018. 488 p.

47. Yao, Y., Zheng, J., Zhang, J., Peng, J., Li, J. Model for Predicting Resilient Modulus of Unsaturated Subgrade Soils in South China. KSCE Journal of Civil Engineering. 2018. 22(6). Pp. 2089–2098. DOI: 10.1007/s12205-018-1703-1

48. Gruzin, A.V. Sposob regulirovaniya kharakteristik fizicheskikh i mekhanicheskikh svoystv dispersnogo nesvyaznogo grunta metodom granulometricheskogo sinteza [A method for regulating the characteristics of physical and mechanical properties of dispersed unconnected soil by granulometric synthesis]. Patent Russia no. 2707112, 2019.

49. Ghorbani, B., Arulrajah, A., Narsilio, G., Horpibulsuk, S., Bo, M.B. Development of genetic-based models for predicting the resilient modulus of cohesive pavement subgrade soils. Soils and Foundations. 2020. 60(2). Pp. 398–412. DOI: 10.1016/j.sandf.2020.02.010

50. Mendoza, C., Caicedo, B., Duque, J. Technical report on the compression, structure, and creep behaviors of lacustrine soil deposits in Bogotá, Colombia. Soils and Foundations. 2022. 62(5). Article no. 101215. DOI: 10.1016/j.sandf.2022.101215

51. Watanabe, D., Moriguchi, S., Terada, K. A numerical study on the effects of particle size distribution on run-out distance of granular flow. Soils and Foundations. 2022. 62(6). Article no. 101242. DOI: 10.1016/j.sandf.2022.101242

52. Hicks, C.R. Fundamental Concepts in the Design of Experiments. Holt, Rinehart and Winston. New York, 1973. 349 p.

53. Adler, Y.P., Markova E.V., Granovskij Y.V. Planirovanie eksperimenta pri poiske optimal'nyh uslovij [Experimental design in the search for optimal conditions]. Moscow: Nauka. 1976. 280 p.

54. Luo, X., Gu, F., Zhang, Y., Lytton, R.L., Zollinger, D.G. Mechanistic-empirical models for better consideration of subgrade and unbound layers influence on pavement performance. Transportation Geotechnics. 2017. 13(1). Pp. 52–68. DOI: 10.1016/j.trgeo.2017.06.002

55. Gruzin, A.V. Modelirovanie svojstv tryohkomponentnoj sistemy po metodu Gibbsa [Modeling the properties of a three-component system using the Gibbs method]. State registration of a computer program no. 2019619804, 2019.

56. Gruzin, A.V. Simulation of "Foundation – A vertical oil storage tank" system by Gibbs-Roseboom method. AIP Conference Proceedings. 2019. 2141. Article no. 030036. DOI: 10.1063/1.5122086

57. Flood, I., Kartam, N.A. Neural Networks in Civil Engineering. I: Principles and Understanding. Journal of Computing in Civil Engineering. 1994. 8(2). Pp. 131–148. DOI: 10.1061/(ASCE)0887-3801(1994)8:2(131)

58. Flood, I., Kartam, N.A. Neural Networks in Civil Engineering. II: Systems and Application. Journal of Computing in Civil Engineering. 1994. 8(2). Pp. 149–162. DOI: 10.1061/(ASCE)0887-3801(1994)8:2(149)

59. Tutumluer, E., Meier, R.W. Attempt at Resilient Modulus Modeling Using Artificial Neural Networks. Transportation Research Record. 1996. 1540(1). Pp. 1–6. DOI: 10.3141/1540-01

60. Shahin, M., Jaksa, M.B., Maier, H.R. Artificial Neural Network Applications in Geotechnical Engineering. Australian Geomechanics Journal. 2001. 36(1). Pp. 49–62.

61. Shahin, M., Jaksa, M.B., Maier, H.R. Data Division for Developing Neural Networks Applied to Geotechnical Engineering. Journal of Computing in Civil Engineering. 2004. 18(2). DOI: 10.1061/(ASCE)0887-3801(2004)18:2(105)

62. Hashash, Y.M.A., Ghaboussi, J., Fu, Q., Marulanda, C. Constitutive Soil Behavior Representation via Artificial Neural Networks: A Shift from Soil Models to Soil Behavior Data. GeoCongress 2006. 2006. DOI: 10.1061/40803(187)126

63. Zaman, M., Solanki, P., Ebrahimi, A., White, L. Neural Network Modeling of Resilient Modulus Using Routine Subgrade Soil Properties. International Journal of Geomechanics. 2010. 10(1). DOI: 10.1061/(ASCE)1532-3641(2010)10:1(1)

64. Nazzal, M.D., Tatari, O. Evaluating the use of neural networks and genetic algorithms for prediction of subgrade resilient modulus. International Journal of Pavement Engineering. 2013. 14(4). Pp. 364–373. DOI: 10.1080/10298436.2012.671944

65. Kim, S.H., Yang, J., Jeong, J.H. Prediction of subgrade resilient modulus using artificial neural network. KSCE Journal of Civil Engineering. 2014. 18. Pp. 1372–1379. DOI: 10.1007/s12205-014-0316-6

66. Tao, H., Chen, C., Jiang, P., Tang, L. Soil Water Characteristic Curves Based on Particle Analysis. Procedia Engineering. 2017. 174. Pp. 1289–1295. DOI: 10.1016/j.proeng.2017.01.273

67. Saha, S., Gu, F., Luo, X., Lytton, R.L. Use of an Artificial Neural Network Approach for the Prediction of Resilient Modulus for Unbound Granular Material. Transportation Research Record. 2018. 2672(52). Pp. 23–33. DOI: 10.1177/0361198118756881

68. Ofrikhter, I.V., Ponomaryov, A.B., Zakharov, A.V., Shenkman, R.I. Estimation of soil properties by an artificial neural network. Magazine of Civil Engineering. 2022. 110(2). Article no. 11011. DOI: 10.34910/MCE.110.11

69. Gruzin, A.V., Grinevich, E.S., Klimanov, D.N. The study of deformation properties of a sand soil – expanded polystyrene granules mixture under cyclic loading conditions. Journal of Physics: Conference Series. 2020. 1441. Article no. 012062. DOI: 10.1088/1742-6596/1441/1/012062

70. Antropova, L.B., Gruzin, A.V., Gildebrandt, M.I., Malaya, L.D., Nikulina, V.B. Study of sandy soil grain-size distribution on its deformation properties. Journal of Physics: Conference Series. 2018. 998. Article no. 012001. DOI: 10.1088/1742-6596/998/1/012001

71. Chollet, F. Deep Learning with Python. 2nd edn. Manning. Shelter Island, NY, 2021. 504 p.

72. Keras Tutorial. Tutorials Point. 2019. V, 93 p. [Online]. System requirements: Adobe Acrobat Reader. URL: https://www.tutorialspoint.com/keras/index.htm (date of application: 13.09.2024).

Information about the authors:

Andrey Gruzin, *PhD in Technical Sciences*
ORCID: https://orcid.org/0000-0003-3479-1907
E-mail: polyot-m@mail.ru

Research article

UDC 69

Buckling of a viscoelastic anisotropic fiber reinforced plate under rapidly increasing shear load

B.Kh. Eshmatov[1], M.M. Mirsaidov[1] (iD) *, R.A. Abdikarimov[2]* (iD) *, N.I. Vatin[3]* ✉ (iD)

[1] *Tashkent Institute of Irrigation and Agricultural Mechanization Engineers (TIIAME), Tashkent, Uzbekistan*

[2] *Tashkent Institute of Architecture and Civil Engineering, Tashkent, Uzbekistan*

[3] *Peter the Great St. Petersburg Polytechnic University, St. Petersburg, Russian Federation*

✉ *vatin@mail.ru*

Abstract. The problem of stability of a viscoelastic anisotropic fiber reinforced plate under the action of a rapidly increasing (dynamic) shear load in a geometrically nonlinear formulation is considered. The mathematical model of the problem is described by a system of nonlinear partial integro-differential equations with singular relaxation kernels. The Bubnov–Galerkin method is used to obtain systems of ordinary nonlinear integro-differential equations. The solution of the system of resolving equations is carried out by a numerical method based on quadrature formulas. To substantiate the accuracy and adequacy of the obtained results, a test problem is solved. A stability criterion for reinforced plates under the action of shear loads is introduced. Depending on various geometric, physical, and mechanical characteristics of the material, the behavior of the reinforced plate is investigated. In particular, it is shown that taking into account the viscoelastic properties of the material leads to a decrease in the critical time, and therefore in the critical force. Depending on various geometric and physical parameters, the difference in critical time values for elastic and viscoelastic plates in some cases is more than 15 %. It is also shown that an increase in the angle of fiber direction in the plates leads to a decrease in the critical time. Among the single-layer reinforced plates, the plate with a fiber direction of 0° is the most resistant to shear loads. An increase in the number of layers in a reinforced plate while maintaining its thickness does not always favorably affect the stability of the plate. In the case of three-layer viscoelastic plates made from KAST-V material with fibers oriented in the direction of 45°/–45°/45°, they are less stable than double-layer plates but more stable than single-layer ones while maintaining equal thicknesses of all three structures.

1. Introduction

The use of composite materials, which exhibit a unique combination of mechanical and operational characteristics, has become indispensable in industry. By ingeniously combining different substances, compositions, and component ratios, these materials yield products with optimal characteristics of their raw

ingredients. Composite materials offer such essential qualities as elasticity, strength, heat resistance, electrical conductivity, etc.

The effectiveness of using composite materials in various structures largely depends on the refinement of mathematical models and calculation methods. Developing calculation methods for structural elements composed of composite materials requires a mathematical problem formulation that reflects the distinctive deformation characteristics of the material, which can substantially impact their load-bearing capacity.

Currently, the volume of scientific research dedicated to the study of structures from composite materials, encompassing various physical and geometric parameters, has a steady upward trend.

A comprehensive review of existing literature on analyzing oscillatory phenomena in fiber reinforced composites is available in [1].

The laminated composite plate dynamic responds, when a mass hits it in the center, and energy transfers from the mass to the plate, were studied in [2]. The plate had initial stress before the impact load. The nonlinear integral equation was used. The key finding was that the higher the initial tension in the plate, the stronger the impact force would be. Additionally, a higher initial tension reduces the amount of energy transferred from the mass to the plate.

The free oscillations and dynamic behavior of polymer composites reinforced with surface-modified basalt fiber were investigated in [3]. Natural frequencies and damping coefficients of layered composites were examined through impact testing and dynamic mechanical analysis.

Meanwhile, [4] studied the effect of stacking and hybridization sequences on the damping properties of epoxy composites made of flax-carbon twill. The dynamic characteristics are examined using the pulse method. For modeling damping, the finite element method is implemented to evaluate the energy dissipation in each layer of carbon-linen laminates.

The paper [5] deals with the free vibration modal analysis of hybrid laminates using a finite element model based on the third order shear deformation theory and the first-order shear deformation theory. A computer code has been developed using MATLAB, 2013. The experimental investigation of the free vibration of hybrid laminates made of carbon and glass fibers is conducted. Numerical results are compared with experimental outcomes, contributing to a holistic understanding.

Further investigations explore the stability of structures made of composite materials. The work [6] investigates the potential for using the produced green composite in load-bearing structures and scrutinize bending properties under axial compression using numerical analysis and ANSYS software.

Additionally, the work [7] examines the stability loss of layered composites when the influence of orthotropic materials is taken into account. This influence justifies the importance of considering orthotropic properties in analyzing the dynamic process.

However, relatively less attention has been dedicated to studying dynamic stability in structures made of composite materials under the influence of shear loads. Most composite materials have pronounced viscoelastic properties. Practical experience in addressing various mechanical problems underscores the significance of incorporating the viscoelastic properties of structural materials. In this regard, the Boltzmann–Volterra integral models are good models that integrate both the relaxation and creep processes.

The developed numerical method based on quadrature formulas was explained in detail in [8]. It facilitates the solution of systems of linear and nonlinear integro-differential equations with different kernels. This method, characterized by its simplicity, convenience, and efficiency in terms of computational time, delivers highly accurate results and accommodates various dynamic viscoelasticity problems. Notably, [9–11] present a series of practical problems solved using the developed method, with the numerical results closely aligned with experimental findings.

The study [12] presents a non-linear dynamic analysis of a cross-ply laminated composite with fiber spacing plates under in-plane loading. The first order shear deformation theory and von Karman nonlinearity are used. Eight-node isoperimetric quadrilateral elements with five degrees of freedom per node are used to maintain geometric nonlinearity. The investigation explores a variety of fiber spacings and orientations to understand their influence on the behavior of samples under this loading condition. The dynamic equilibrium equations are solved using the Newmark integration technique. The nonlinear dynamic analysis examines the effects of changing fiber spacing with various changes in volume percentage and diverse fiber orientations. These variations were found to significantly influence the nonlinear dynamic behavior of the laminated composite plates.

The study [13] investigates the nonlinear bending behavior of laminated composite plates under static and dynamic loads. The plate was reinforced by single-walled carbon nanotubes' fibers and nanoclay particles. The Halpin–Tsai mathematical model, which is based on the self-consistent field method, is applied. This model can be used to predict the modulus of composite materials. The computer program is created to solve this model. The program also considers different support conditions for the plate (clamped or simply supported).

The research [14] investigates how adding fillers can improve the strength and vibration response of laminated composite plates. The laminated composite plates are fabricated by open layup process with epoxy resin, E-glass fiber reinforcement, and fly ash and graphene fillers (up to 5 % total volume). The total fiber and filler content is limited to 60 % by weight. The laminated composite plates are designed with various fly ash-to-graphene ratios. A custom-built vibration testing system is used to measure the free and forced vibrations of simply supported laminated composite plates. These experimental results are compared to mathematical models based on fifth order shear deformation theory and finite element analysis. Finally, the effect of circular holes on the laminated composite plates' vibration characteristics is investigated using simulations. These simulations analyze how hole size and location impact the modal frequencies of the laminated composite plates.

The research [15] investigates the vibration of a curved beam made from layers of composite material reinforced with graphene platelets. The amount of reinforcement varies between layers, creating a specific type of material. The study analyses both vibrations caused by the beam itself (free vibration) and vibrations caused by a moving load (forced vibration). The analysis is validated using existing data and then expanded to explore how different factors influence the vibration. The findings show that the shape of the beam, the amount of graphene reinforcement, and its distribution affect the vibration intensity of the beam in both scenarios. Simply put, a stiffer beam with more graphene reinforcement vibrates less.

The research [16] studies how laminated beams made of composite materials vibrate when they have a separation layer running across their width. The study considers both in-plane and out-of-plane vibrations. The researchers use a computer simulation technique and a special method to account for contact between the separated layers. This research investigates the natural frequencies of a damaged beam and its response to various forces. The analysis includes both constant and moving force applications. The results of the present study are verified by comparing them with those available in the literature. This work provides a complete picture of how these damaged beams vibrate in all directions.

The research [17] focuses on the vibration characteristics of rectangular composite panels used in structures like automobiles. These panels are designed to replace heavier metals for improved efficiency. The study examines how different fiber orientations within the composite panels affect their vibration under external forces. Two methods, analytical and numerical, are used to analyze the vibration behavior. The findings show that the way the fibers are oriented significantly impacts vibration, and this knowledge can be used to design composite structures with better vibration control.

The research [18] focuses on fiber-reinforced polymer composites used in car parts like inlet/exhaust flange gaskets. These composites are desirable due to their strength-to-weight ratio and other properties. However, machining processes like drilling can cause delamination, which can grow and lead to sudden part failure. This study aims to identify such damage beforehand. The research method involves vibration analysis (modal and harmonic) using finite element analysis software. The analysis is performed on a model of a gasket, initially intact and then with deliberate delamination at the drilling location. Different delamination locations and materials are simulated. The results for intact and delaminated plates are compared, including vibration modes, resonance frequencies, and stress distribution.

The study [19] investigates how delamination, a layering separation common in fiber reinforced polymer composites, impacts the vibration and stress behavior of plates with circular holes. It employs a combined approach: the layerwise theory for numerical analysis and the finite element method to simulate delamination effects. The research reveals a significant influence of delamination size on the plate's natural frequency, stress concentration points, and overall impedance.

The research [20] investigates the vibration of composite conical panels made with layers containing different amounts of graphene platelets. The effect of both uniform and non-uniform porosity is also considered. The material properties are estimated using established methods. The analysis uses a specific theory of shells and kinematics to define the energy components. A general method is applied to discretize the energy terms, allowing for various boundary conditions. Standard methods are used to find natural frequencies and track the deflection over time. The results are compared with the available data in the open literature, and new results are presented. The study concludes that both the type of porosity and the graphene platelets distribution significantly affect the frequencies and deflection of the panel.

Despite the abundance of scientific results on structures made of composite materials encompassing diverse physical and geometric parameters, a number of questions remain unanswered. For the first time,

this paper aimed to study the stability of a viscoelastic anisotropic reinforced plate clamped on boundaries constructed from composite material under the influence of rapid, dynamic shear loads.

2. Materials and Methods

The rectangular rigidly pinched fiberglass plate subjected to the dynamic action of shear forces evenly distributed along its edges was considered (Fig. 1). It was assumed that the shear forces increased in proportion to time according to the law

$$P(t) = P_0 \cdot t, \tag{1}$$
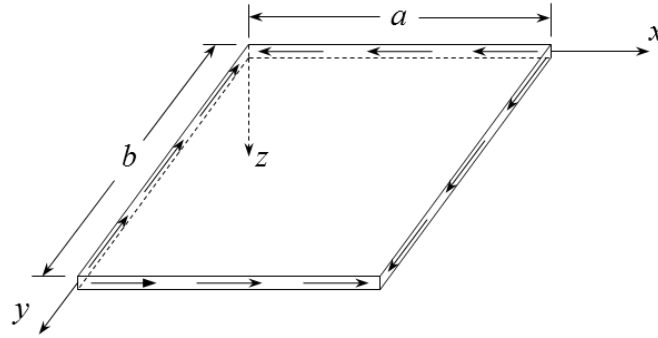
where P_0 is the loading rate.

Figure 1. Rectangular plate under shear load.

The classical Kirchhoff–Love theory was employed to develop a mathematical model for a problem. The resulting stresses and moments were determined in the same manner as described in [21, 22]:

$$
\begin{aligned}
N_x &= A_{11}^* \varepsilon_x + A_{12}^* \varepsilon_y + A_{16}^* \gamma_{xy} + B_{11}^* \chi_x + B_{12}^* \chi_y + B_{16}^* \chi_{xy}, \\
N_y &= A_{12}^* \varepsilon_x + A_{22}^* \varepsilon_y + A_{26}^* \gamma_{xy} + B_{12}^* \chi_x + B_{22}^* \chi_y + B_{26}^* \chi_{xy}, \\
N_{xy} &= A_{16}^* \varepsilon_x + A_{26}^* \varepsilon_y + A_{66}^* \gamma_{xy} + B_{16}^* \chi_x + B_{26}^* \chi_y + B_{66}^* \chi_{xy}, \\
M_x &= B_{11}^* \varepsilon_x + B_{12}^* \varepsilon_y + B_{16}^* \gamma_{xy} + D_{11}^* \chi_x + D_{12}^* \chi_y + D_{16}^* \chi_{xy}, \\
M_y &= B_{12}^* \varepsilon_x + B_{22}^* \varepsilon_y + B_{26}^* \gamma_{xy} + D_{12}^* \chi_x + D_{22}^* \chi_y + D_{26}^* \chi_{xy}, \\
M_{xy} &= B_{16}^* \varepsilon_x + B_{26}^* \varepsilon_y + B_{66}^* \gamma_{xy} + D_{16}^* \chi_x + D_{26}^* \chi_y + D_{66}^* \chi_{xy},
\end{aligned}
\tag{2}
$$

where $A_{ij}^*, B_{ij}^*, D_{ij}^*, i, j = 1, 2, 6$ are operators of the following form:

$$A_{ij}^* \varphi = \sum_{k=1}^{K} \left(\bar{Q}_{ij}^* \varphi \right)_k (z_k - z_{k-1}), \quad B_{ij}^* \varphi = \frac{1}{2} \sum_{k=1}^{K} \left(\bar{Q}_{ij}^* \varphi \right)_k \left(z_k^2 - z_{k-1}^2 \right),$$

$$D_{ij}^* \varphi = \frac{1}{3} \sum_{k=1}^{K} \left(\bar{Q}_{ij}^* \varphi \right)_k \left(z_k^3 - z_{k-1}^3 \right),$$

$$\bar{Q}_{11}^* \varphi = \left[Q_{11} \cos^4 \theta + \frac{1}{2} (Q_{12} + 2Q_{66}) \sin^2 2\theta + Q_{22} \sin^4 \theta \right] \left(1 - \Gamma^* \right) \varphi,$$

$$\bar{Q}_{12}^* \varphi = \left[\frac{1}{4} (Q_{11} + Q_{22} - 4Q_{66}) \sin^2 2\theta + Q_{12} \left(1 - \frac{1}{2} \sin^2 2\theta \right) \right] \left(1 - \Gamma^* \right) \varphi,$$

$$\bar{Q}_{16}^* \varphi = \left[Q_{11} \sin \theta \cos^3 \theta - \frac{1}{4} (Q_{12} + 2Q_{66}) \sin 4\theta - Q_{22} \sin^3 \theta \cos \theta \right] \left(1 - \Gamma^* \right) \varphi,$$

$$\bar{Q}_{22}^*\varphi = \left[Q_{11}\sin^4\theta + \frac{1}{2}(Q_{12}+2Q_{66})\sin^2 2\theta + Q_{22}\cos^4\theta \right](1-\Gamma^*)\varphi,$$

$$\bar{Q}_{26}^*\varphi = \left[Q_{11}\sin^3\theta\cos\theta - \frac{1}{4}(Q_{12}+2Q_{66})\sin 4\theta - Q_{22}\sin\theta\cos^3\theta \right](1-\Gamma^*)\varphi,$$

$$\bar{Q}_{66}^*\varphi = \left[\frac{1}{4}(Q_{11}-2Q_{12}+Q_{22})\sin^2 2\theta + Q_{66}\cos^2 2\theta \right](1-\Gamma^*)\varphi,$$

$$Q_{11}=\frac{E_1}{1-\mu_{12}\mu_{21}}, \quad Q_{22}=\frac{E_2}{1-\mu_{12}\mu_{21}}, \quad Q_{12}=\frac{E_1\mu_{21}}{1-\mu_{12}\mu_{21}}=\frac{E_2\mu_{12}}{1-\mu_{12}\mu_{21}}, \quad Q_{66}=G_{12},$$

$$\Gamma^*\varphi = \int_0^t \Gamma(t-\tau)\varphi(\tau)d\tau$$

Here K is the number of plate layers; E_1, E_2 are the elastic moduli; G_{12} is the shear modulus; μ_{12}, μ_{21} are the Poisson ratios; θ is the angle characterizing the direction of the reinforced fibers relative to the OX axis; Γ^* is the integral operator with the relaxation kernel $\Gamma(t)$.

If the dynamic process is analyzed without considering the propagation of elastic waves, then it becomes possible to discard the inertial terms in the first two equations of the system (3). The relations between the strains in the median surface ε_x, ε_y, γ_{xy}, χ_x, χ_y, χ_{xy} and displacements u, v, w in the x, y, z directions takes into account geometric nonlinearity. In this case, the solution of the resulting system was searched in the form described in the articles [21–23]:

$$\varepsilon_x = \frac{\partial u}{\partial x} + \frac{1}{2}\left(\frac{\partial w}{\partial x}\right)^2, \quad \varepsilon_y = \frac{\partial v}{\partial y} + \frac{1}{2}\left(\frac{\partial w}{\partial y}\right)^2, \quad \gamma_{xy} = \frac{\partial u}{\partial y} + \frac{\partial v}{\partial x} + \frac{\partial w}{\partial x}\frac{\partial w}{\partial y},$$

$$\chi_x = -\frac{\partial^2 w}{\partial x^2}, \quad \chi_y = -\frac{\partial^2 w}{\partial y^2}, \quad \chi_{xy} = -2\frac{\partial^2 w}{\partial x \partial y},$$

(3)

Substituting (1) and (2) into the equations of motion gives the system of nonlinear partial integro-differential equations:

$$\frac{\partial N_x}{\partial x} + \frac{\partial N_{xy}}{\partial y} = \rho\frac{\partial^2 u}{\partial t^2}, \quad \frac{\partial N_{xy}}{\partial x} + \frac{\partial N_y}{\partial y} = \rho\frac{\partial^2 v}{\partial t^2},$$

$$\frac{\partial^2 M_x}{\partial x^2} + \frac{\partial^2 M_y}{\partial y^2} + 2\frac{\partial^2 M_{xy}}{\partial x \partial y} + \frac{\partial}{\partial x}\left(N_x\frac{\partial w}{\partial x} + N_{xy}\frac{\partial w}{\partial y}\right) +$$

(4)

$$+ \frac{\partial}{\partial y}\left(N_{xy}\frac{\partial w}{\partial x} + N_y\frac{\partial w}{\partial y}\right) + q = \rho\frac{\partial^2 w}{\partial t^2}$$

If the dynamic process is considered without the propagation of elastic waves, then it becomes possible to discard the inertial terms in the first two equations of the system (3). In this case, the solution of the resulting system has the form described in the articles [22, 23]:

$$w(x,y,t) = \sum_{m=1}^{M}\sum_{n=1}^{N}\left(\gamma_m\cos\frac{\lambda_m x}{a} - \gamma_m\cosh\frac{\lambda_m x}{a} + \sin\frac{\lambda_m x}{a} - \sinh\frac{\lambda_m x}{a}\right) *$$

$$* \left(\gamma_n\cos\frac{\lambda_n y}{b} - \gamma_n\cosh\frac{\lambda_n y}{b} + \sin\frac{\lambda_n y}{b} - \sinh\frac{\lambda_n y}{b}\right)w_{mn}(t),$$

(5)

where $w_{mn}(t)$, m, $n = 1, 2, 3, \ldots$ are the unknown functions of time; λ_m and λ_n are the roots of the frequency equation:

$$\cos \lambda_m \cosh \lambda_m = 1$$

and

$$\gamma_m = \frac{\cos \lambda_m - \cosh \lambda_m}{\sin \lambda_m + \sinh \lambda_m}.$$

A system of nonlinear ordinary integro-differential equations is obtained by substituting the approximating function (4) into the resulting system of equations and performing the Bubnov–Galerkin method procedure. Further, this system is integrated using the numerical method [8] based on quadrature formulas. A feature of this numerical method in solving systems of nonlinear integro-differential equations is the preliminary transformation of a singular kernel into a regular one.

3. Results and Discussion

To evaluate the accuracy of the chosen method, we solve a system of nonlinear integro-differential equations of the following form:

$$\ddot{u} + \lambda_1^2 u = p_x + \lambda_2 \int_0^t R_1(t-\tau) u(\tau) d\tau + \lambda_3 \int_0^t R_2(t-\tau) v(\tau) d\tau +$$

$$+ \lambda_4 \int_0^t R_3(t-\tau) w(\tau) d\tau + \lambda_5 \int_0^t R_4(t-\tau) w^2(\tau) d\tau,$$

$$\ddot{v} + \varphi_1^2 v = p_y + \varphi_2 \int_0^t R_1(t-\tau) u(\tau) d\tau + \varphi_3 \int_0^t R_2(t-\tau) v(\tau) d\tau +$$

$$+ \varphi_4 \int_0^t R_3(t-\tau) w(\tau) d\tau + \varphi_5 \int_0^t R_4(t-\tau) w^2(\tau) d\tau, \tag{6}$$

$$\ddot{w} + \omega_1^2 w = q + \omega_2 \int_0^t R_1(t-\tau) u(\tau) d\tau + \omega_3 \int_0^t R_2(t-\tau) v(\tau) d\tau +$$

$$+ \omega_4 \int_0^t R_3(t-\tau) w(\tau) d\tau + \omega_5 w(t) \int_0^t R_1(t-\tau) u(\tau) d\tau +$$

$$+ \omega_6 w(t) \int_0^t R_2(t-\tau) v(\tau) d\tau + \omega_7 \int_0^t R_4(t-\tau) w^2(\tau) d\tau$$

with initial conditions $u(0) = 1$, $\dot{u}(0) = -\beta_1$, $v(0) = 1$, $\dot{v}(0) = -\beta_2$, $w(0) = 1$, $\dot{w}(0) = -\beta_3$, where

$$R_1(t) = A_1 e^{-\beta_1 t} t^{\alpha_1 - 1}, \quad R_2(t) = A_2 e^{-\beta_2 t} t^{\alpha_2 - 1}, \quad R_3(t) = A_3 e^{-\beta_3 t} t^{\alpha_3 - 1},$$

$$R_4(t) = A_4 e^{-\beta_4 t} t^{\alpha_4 - 1}, \quad 0 < \alpha_1, \ \alpha_2, \ \alpha_3, \ \alpha_4 < 1;$$

$$p_x = \left(\beta_1^2 + \lambda_1^2 - \frac{\lambda_2 A_1}{\alpha_1} t^{\alpha_1} \right) e^{-\beta_1 t} - \frac{\lambda_3 A_2}{\alpha_2} e^{-\beta_2 t} t^{\alpha_2} -$$

$$- \frac{\lambda_4 A_3}{\alpha_3} e^{-\beta_3 t} t^{\alpha_3} - \frac{\lambda_5 A_4}{\alpha_4} e^{-\beta_4 t} t^{\alpha_4};$$

$$p_y = \left(\beta_2^2 + \varphi_1^2 - \frac{\varphi_3 A_2}{\alpha_2} t^{\alpha_2} \right) e^{-\beta_2 t} - \frac{\varphi_2 A_1}{\alpha_1} e^{-\beta_1 t} t^{\alpha_1} -$$

$$- \frac{\varphi_4 A_3}{\alpha_3} e^{-\beta_3 t} t^{\alpha_3} - \frac{\varphi_5 A_4}{\alpha_4} e^{-\beta_4 t} t^{\alpha_4};$$

$$q = \left(\beta_3^2 + \omega_1^2 - \frac{\omega_4 A_3}{\alpha_3} t^{\alpha_3} \right) e^{-\beta_3 t} - \frac{\omega_2 A_1}{\alpha_1} e^{-\beta_1 t} t^{\alpha_1} - \frac{\omega_3 A_2}{\alpha_2} e^{-\beta_2 t} t^{\alpha_2} -$$

$$- \frac{\omega_5 A_1}{\alpha_1} e^{-(\beta_1+\beta_3)t} t^{\alpha_1} - \frac{\omega_6 A_2}{\alpha_2} e^{-(\beta_2+\beta_3)t} t^{\alpha_2} - \frac{\omega_7 A_4}{\alpha_4} e^{-2\beta_3 t} t^{\alpha_4}.$$

The system of equations (6) has an exact solution: $u = e^{-\beta_1 t}$, $v = e^{-\beta_2 t}$, $w = e^{-\beta_3 t}$, satisfying the initial conditions. Integrating the system of equations (6) twice and taking into account the initial conditions, the approximate values $u_n = u_n(t)$, $v_n = v_n(t)$, $w_n = w_n(t)$ at the nodes $t_n = (n-1)\Delta t$, $n = 1, 2, 3, \ldots$ are found from the relations:

$$u_n = 1 - \beta_1 t_n - e^{-\beta_1 t_n} + \sum_{i=0}^{n-1} B_i (t_n - t_i) \left[p_x(t_i) - \lambda_1^2 u_i + \sum_{k=0}^{i} \left(\frac{\lambda_2 A_1}{\alpha_1} C_{1k} e^{-\beta_1 t_k} u_{i-k} + \right. \right.$$

$$\left. \left. + \frac{\lambda_3 A_2}{\alpha_2} C_{2k} e^{-\beta_2 t_k} v_{i-k} + \frac{\lambda_4 A_3}{\alpha_3} C_{3k} e^{-\beta_3 t_k} w_{i-k} + \frac{\lambda_5 A_4}{\alpha_4} C_{4k} e^{-2\beta_3 t_k} w_{i-k}^2 \right) \right],$$

$$u_n = 1 - \beta_2 t_n - e^{-\beta_2 t_n} + \sum_{i=0}^{n-1} B_i (t_n - t_i) \left[p_y(t_i) - \varphi_1^2 v_i + \sum_{k=0}^{i} \left(\frac{\varphi_2 A_1}{\alpha_1} C_{1k} e^{-\beta_1 t_k} u_{i-k} + \right. \right. \tag{7}$$

$$\left. \left. + \frac{\varphi_3 A_2}{\alpha_2} C_{2k} e^{-\beta_2 t_k} v_{i-k} + \frac{\varphi_4 A_3}{\alpha_3} C_{3k} e^{-\beta_3 t_k} w_{i-k} + \frac{\varphi_5 A_4}{\alpha_4} C_{4k} e^{-2\beta_3 t_k} w_{i-k}^2 \right) \right],$$

$$w_n = 1 - \beta_3 t_n - e^{-\beta_3 t_n} + \sum_{i=0}^{n-1} B_i (t_n - t_i) \left[q(t_i) - \omega_1^2 w_i + \sum_{k=0}^{i} \left(\frac{\omega_2 A_1}{\alpha_1} C_{1k} e^{-\beta_1 t_k} u_{i-k} + \right. \right.$$

$$+ \frac{\omega_3 A_2}{\alpha_2} C_{2k} e^{-\beta_2 t_k} v_{i-k} + \frac{\omega_4 A_3}{\alpha_3} C_{3k} e^{-\beta_3 t_k} w_{i-k} + \frac{\omega_5 A_1}{\alpha_1} w_i C_{1k} e^{-\beta_2 t_k} u_{i-k} +$$

$$\left. \left. + \frac{\omega_6 A_2}{\alpha_2} w_i C_{2k} e^{-\beta_2 t_k} v_{i-k} + \frac{\omega_7 A_4}{\alpha_4} C_{4k} e^{-2\beta_3 t_k} w_{i-k}^2 \right) \right],$$

where $B_i, C_{1k}, C_{2k}, C_{3k}, C_{4k}$ are the coefficients of the quadrature formula;

$$B_0 = h/2, \; B_i = h, \; i = 1, \ldots, n-1;$$

$$C_{l0} = h^{\alpha_l}/2, \; C_{li} = h^{\alpha_l} \left[i^{\alpha_l} - (i-1)^{\alpha_l} \right]/2, \; C_{lk} = h^{\alpha_l} \left[((k+1))^{\alpha_l} - (k-1)^{\alpha_l} \right]/2,$$

$$k = 1, \ldots, n-1, \; l = 1, 2, 3, 4.$$

Table 1 shows the calculation results performed according to (7) in the range from 0 to 0.1 with a step of Δt = 0.0001. The following initial data were used:

$$\lambda_1 = 1.1; \lambda_2 = 1.2; \lambda_3 = 1.3; \lambda_4 = 1.4; \lambda_5 = 1.5;$$
$$\varphi_1 = 1.2; \varphi_2 = 1.3; \varphi_3 = 1.4; \varphi_4 = 1.5; \varphi_5 = 1.6;$$
$$\omega_1 = 1.3; \omega_2 = 1.4; \omega_3 = 1.5; \omega_4 = 1.6; \omega_5 = 1.7; \omega_6 = 1.8; \omega_7 = 1.9;$$
$$A_1 = 0.01; A_2 = 0.02; A_3 = 0.03; A_4 = 0.04;$$
$$\beta_1 = 0.25; \beta_2 = 0.26; \beta_3 = 0.27;$$
$$\alpha_1 = 0.05; \alpha_2 = 0.06; \alpha_3 = 0.07; \alpha_4 = 0.08$$

Table 1 also shows that the error of the described method coincides with the error of the quadrature formulas used, and the error is in the same order of smallness relative to the interpolation step.

Table 1. Comparison of approximate and exact solutions.

t	Solution		$\Delta, \%$
	Exact	*Approximate*	
0.0	1.000000000	1.000000000	-
0.01	0.997303642	0.998929533	0.296
0.02	0.994614554	0.997560123	0.397
0.03	0.991932717	0.995866611	0.462
0.04	0.989258111	0.993831608	0.491
0.05	0.986590716	0.991439562	0.482
0.06	0.983930514	0.988675329	0.433
0.07	0.981277485	0.985522169	0.340
0.08	0.978631609	0.981957961	0.200
0.09	0.975992868	0.977947442	0.004
0.10	0.973361242	0.973403577	0.004

In calculations, KAST-V plastic with the following physical and geometric parameters was chosen as the plate material: E_1 = 25.5 GPa, E_2 = 14.91 GPa, G_{12} = 4.41 GPa, μ_{12} = 0.2, ρ = 1900 kg/m³, $a = b$ = 0.5 m, h = 0.5 sm, θ = 45°, P_0 = 5 MPa/s. The simplest and, at the same time, quite common weakly-singular Koltunov–Rzhanitsyn kernel [24] of the form $\Gamma(t) = Ae^{-\beta t} t^{\alpha-1} \left(0 < \alpha < 1\right)$ is used as the relaxation kernel where A, α, β are the rheological viscosity parameters determined from the experiments [25].

The graphs below correspond to the results obtained for the midpoint of a rigidly pinched plate under the action of a dynamic load that caused the shift. On the presented graphs, m (meter) is taken as the dimension of the deflection, and *s* (second) is taken as the time.

To ensure the necessary accuracy of the results obtained, the convergence of the Bubnov–Galerkin method was investigated (Fig. 2). The results given below were obtained based on monomial and polynomial approximations. It can be seen from the figure that when calculating the deflection, it is sufficient in (4) to hold the first four harmonics $\left(M = N = 2\right)$. The further increase in the number of members does not significantly impact the dynamic process.
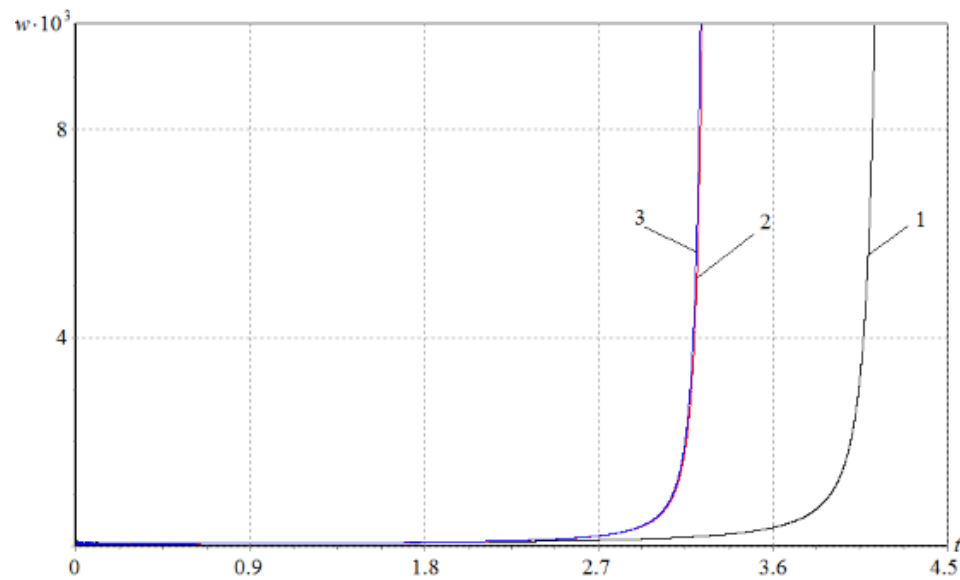
**Figure 2. Convergence of the Bubnov–Galerkin method
(1 – $M = N = 1$; 2 – $M = N = 2$; 3 – $M = N = 3$).**

Fig. 3 illustrate the shape of a deformable rigidly pinched plate under the influence of shear forces. Note that areas with both positive and negative deflections appear on the plate under such loads. It should be noted here that the contact lines of these regions, otherwise called nodal lines or zero deviation lines, do not occur under uniform compressive loads of anisotropic plates. Similar results for elastic static problems were obtained in [22, 23].
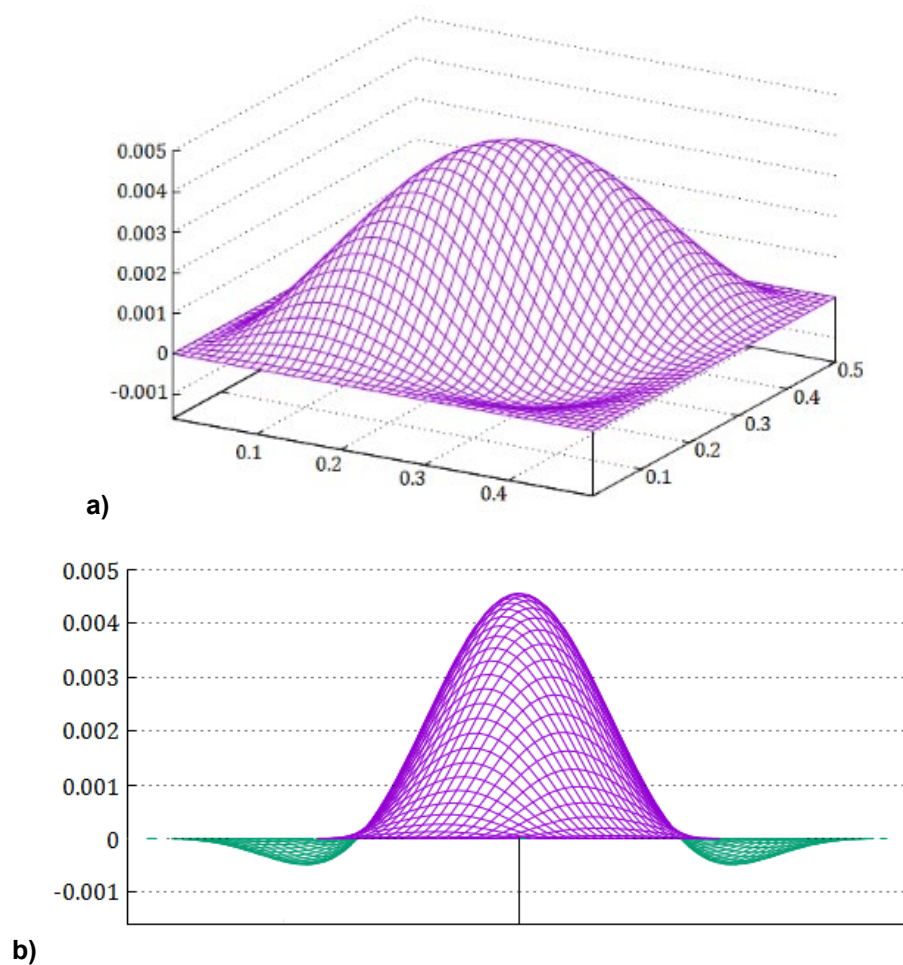

a)

b)

Figure 3. The curved shape of the deformable plate.

The influence of geometric parameters of a rectangular plate on the change of regions with positive and negative deflections is studied (Fig. 4). It is shown that as one of the sides of the plate lengthens, the

area of the region with negative deflections increases. Here λ is the ratio of the sides of the plate. Thus, if λ = 1, then the plate has a square shape.

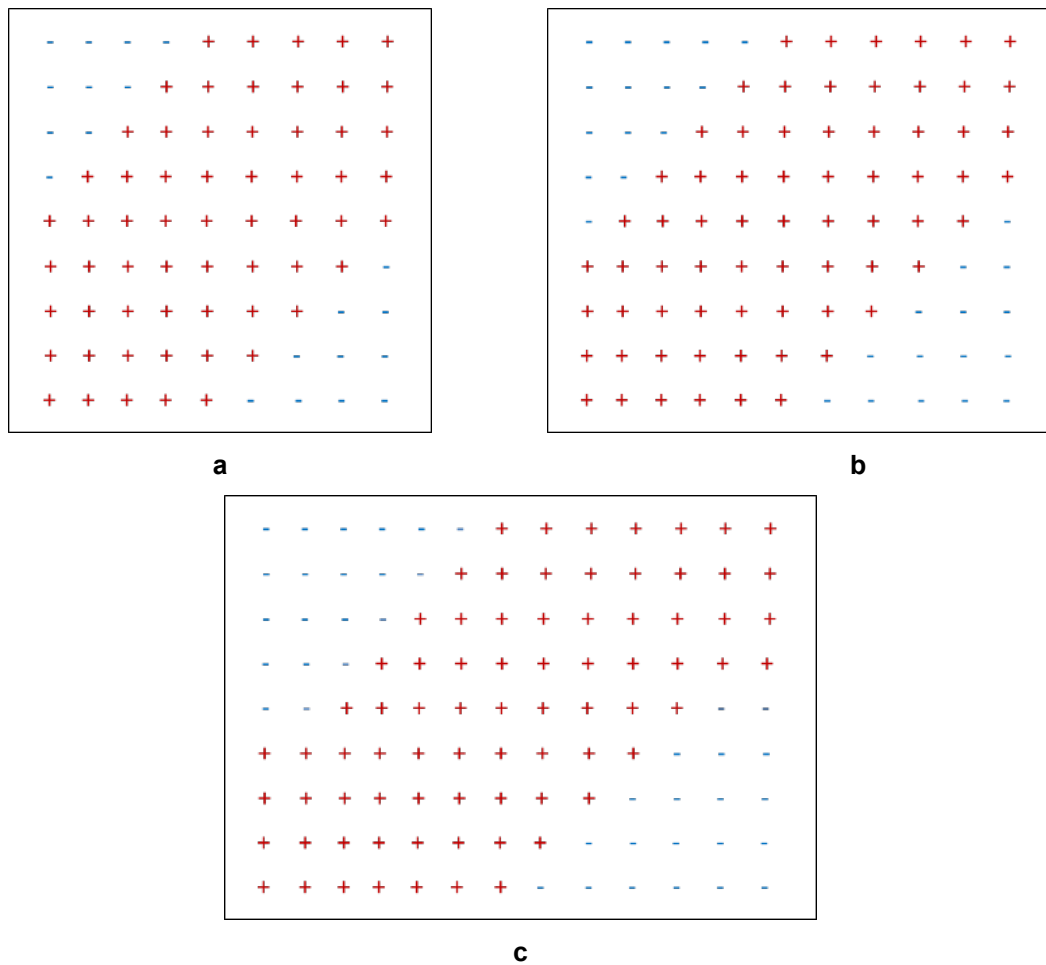a   b

c

Figure 4. Changing the areas of the plate with positive and negative deflections depending on the change in the surface area of the plate: 1 – λ = 1; 2 – λ = 1.2; 3 – λ = 1.4.

In solving problems about the stability of plates under the influence of compressive dynamic loads, as a criterion determining the critical time and critical load, it is conditionally assumed in [26] that the deflection boom should not exceed an amount equal to the thickness of the plate. With such plate deformations, there are no areas with negative deflections.

In our study, we depart from this convention by considering the presence of areas with both positive and negative deflections in the deformable plate. In our calculations, we define the critical dynamic load as the moment when the difference between the deflection values at the highest and lowest points of the plate (referred to as critical points) equals the plate's thickness. It is worth noting that, unlike the uppermost point of the plate (which remains fixed at the intersection of the diagonals, i.e., the midpoint), the location of the lowest point varies with changes in the physical and geometric parameters of the plate.

Fig. 5 and 6 graphically depict the influence of the material's viscoelastic properties on the behavior of the reinforced plate. In these figures, curves 1 and 2 represent results for the viscoelastic problem while curves 3 and 4 pertain to the elastic scenario $\left(A = 0 \right)$. Notably, accounting for the viscoelastic properties of the construction material leads to a reduction in the critical time. The disparity in critical time values between elastic and viscoelastic plates, contingent on alterations in the plate's geometric and physical parameters, can exceed 15 %. Furthermore, we observe that a reinforced plate made of EDF with A = 0.0067 is more resistant to shear forces compared to a reinforced plate made of KAST-V with A = 0.0208. This distinction arises from the fact that the latter exhibits more pronounced viscous properties than the former.
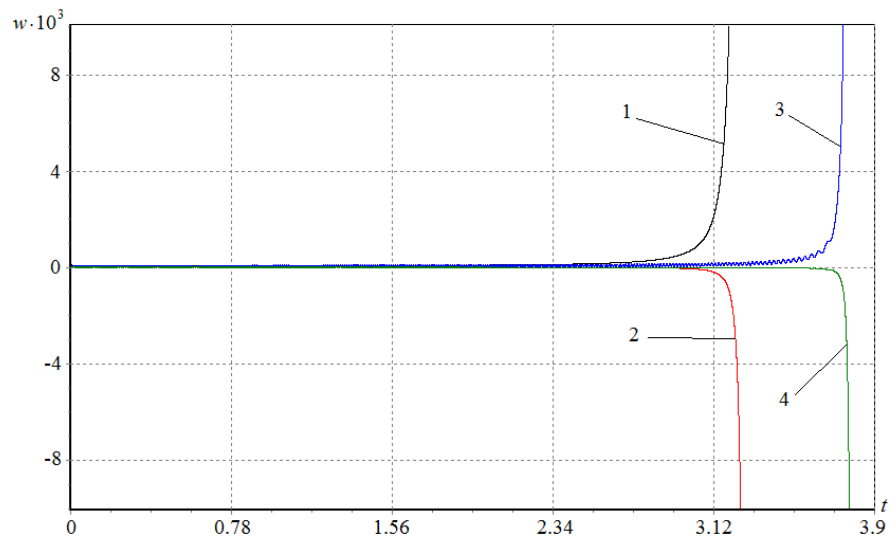
Figure 5. Changing the deflections of the plate from KAST-V at critical points.
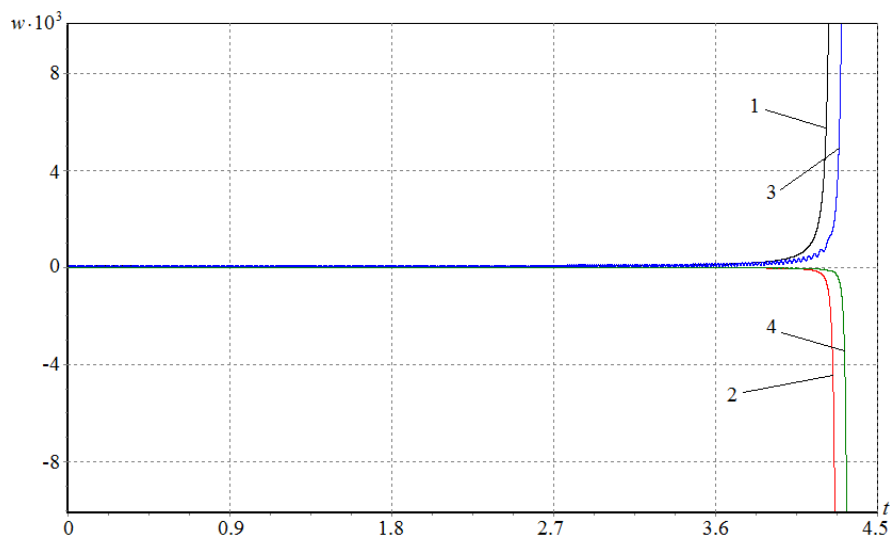

Figure 6. Changing the deflections of the EDF plate at critical points.

An increase in stiffness due to an increase in the thickness of the plate leads to a proportional increase in the critical time value (Fig. 7).
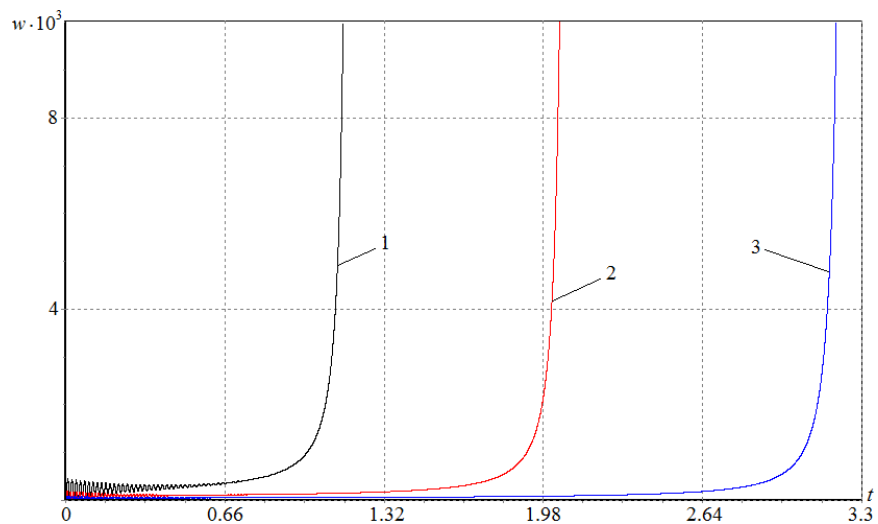

Figure 7. The dependence of the deflection of the reinforced plate on time at different values of its thickness: 1 – h = 0.3 cm; 2 – h = 0.4 cm; 3 – h = 0.5 cm.

Fig. 8 shows similar results for the geometric parameter λ = 1; 1.2; 1.4. As can be seen from the graph, an increase in one of the sides of the plate leads to a shift of the deflection curve to the left (i.e., to a decrease in the critical time).
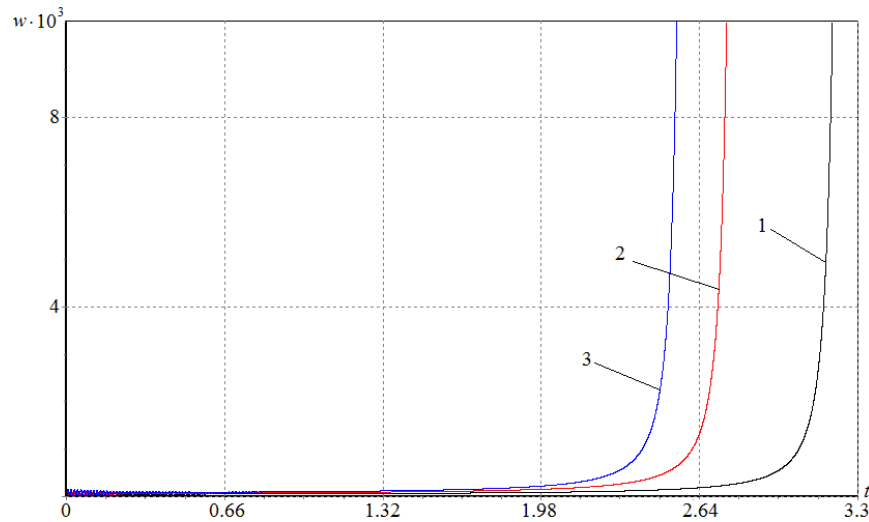

Figure 8. Dependence of the deflection of the reinforced plate on time

at different parameter values $\lambda\left(\lambda = a/b\right)$: **1 –** $\lambda = 1$; **2 –** $\lambda = 1.2$; **3 –** $\lambda = 1.4$.

In Fig. 9, various curves represent cases involving changes in the deflection of the median point of the reinforced rectangular plate at different loading speeds. As expected, higher loading speeds lead to an earlier increase in deflections. These results are similar to the results obtained in the study of the stability of a simply supported plate under the influence of external compressive loads, given in [10].
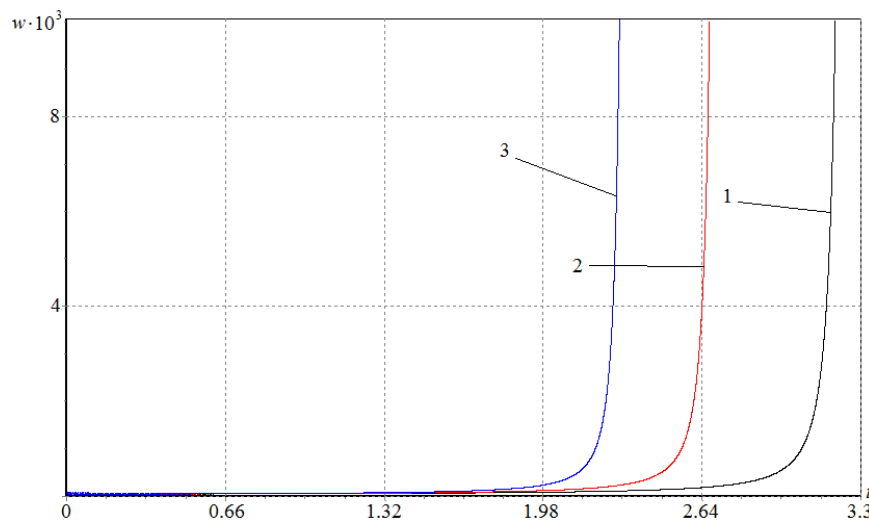

Figure 9. Dependence of the deflection of the reinforced plate on time at different values
of loading speeds: 1 – P_0 **= 5 MPa/s; 2 –** P_0 **= 6 MPa/s; 3 –** P_0 **= 7 MPa/s.**

The presented numerical results in Table 2 offer critical time values for an anisotropic reinforced plate constructed from KAST-V material under the influence of rapidly increasing shear loads. These results have been obtained by considering a wide range of variations in the plate's geometric and physical parameters. It is important to note that the values in the table represent the outcomes for both elastic and viscoelastic problems.

As previously mentioned, accounting for the viscoelastic properties of the construction material significantly impacts the numerical results. This effect becomes especially prominent if an anisotropic plate is subjected to an external static load q in addition to shear loads. It is worth highlighting that for large values of q, the stability of the plate is compromised even at relatively low loading speeds.

Layered composites consisting of alternating reinforcing layers, each with different mechanical properties, have found successful applications in various industries. They have the potential to significantly reduce the weight of structures, increase engine efficiency, and facilitate the creation of innovative, highly efficient, and reliable structures. In light of these achievements, the influence of the number of layers and

the orientation of reinforced fibers inside these layers on the dynamic process under consideration has been studied.

This investigation reveals that two-layer plates exhibit greater shear load resistance than single-layer counterparts. For instance, in a two-layer viscoelastic plate with fibers oriented in directions of 45° and –45°, the critical time is more than 1.2 times longer than that of a single-layer plate with fibers oriented in the direction of 45°. However, it is worth noting that further increasing the number of layers may not always be justifiable. In the case of three-layer viscoelastic plates constructed from CAST-V material with fibers oriented in the direction of 45°/–45°/45°, they are less stable than double-layer plates but more stable than single-layer ones while maintaining equal thicknesses across all three structures.

Table 2. Critical time values at different values of geometric and physical parameters of an anisotropic reinforced plate made of KAST-V.

№	Geometric parameters			Physical parameters		Number of layers	Fiber orientations	Critical time values		
	a, m	b, m	h, sm	q, Pa	P_0, MPa/s			Elastic problem	Viscoelastic problem	Difference (in %)
1	0.5	0.5	0.5	100	5	1	45°	3.7325	3.1629	15.3
2	0.6	0.5	0.5	100	5	1	45°	3.2155	2.7211	15.4
3	0.7	0.5	0.5	100	5	1	45°	2.9677	2.5129	15.3
4	0.5	0.5	0.4	100	5	1	45°	2.3838	2.0194	15.3
5	0.5	0.5	0.3	100	5	1	45°	1.3292	1.1240	15.4
6	0.5	0.5	0.5	200	5	1	45°	3.7136	3.1246	15.9
7	0.5	0.5	0.5	300	5	1	45°	3.7009	3.0946	16.4
8	0.5	0.5	0.5	100	6	1	45°	3.1141	2.6452	15.1
9	0.5	0.5	0.5	100	7	1	45°	2.6711	2.2743	14.9
10	0.5	0.5	0.5	100	5	1	0°	4.2618	3.9568	7.2
11	0.5	0.5	0.5	100	5	1	15°	3.9175	3.4630	11.6
12	0.5	0.5	0.5	100	5	1	30°	3.7667	3.2287	14.3
13	0.5	0.5	0.5	100	5	2	0°/90°	4.2861	3.9712	7.3
14	0.5	0.5	0.5	100	5	2	15°/–15°	4.3527	3.8456	11.7
15	0.5	0.5	0.5	100	5	2	30°/–30°	4.5252	3.8704	14.5
16	0.5	0.5	0.5	100	5	2	45°/–45°	4.6053	3.8919	15.5
17	0.5	0.5	0.5	100	5	3	45°/–45°/45°	3.7993	3.2184	15.3

4. Conclusions

The investigation of the dynamic stability of viscoelastic anisotropic reinforced plates exposed to uniformly distributed shear forces along their edges reveals several significant findings:

1. The importance of accounting for the viscoelastic properties of the construction material is evident. Results highlight that the difference in the critical time between solving elastic and viscoelastic problems for plates constructed from KAST-V, contingent on physical and geometric parameters, can exceed 15 %.

2. In layered structures, the critical time values notably depend on the fibers' orientation in each layer. Among the examined cases, the two-layer plate with fibers oriented in directions 0° and 90° demonstrated the highest resistance to shear loads.

3. Changes in the physical and geometric parameters of the plate substantially affect critical time values. Considering the viscoelastic properties of the structural material demonstrates the change in critical time clearly. The results and conclusions drawn from this study enable accurate predictions of the dynamic behavior of reinforced plates made from composite materials.

References

1. Kalusuraman, G., Kumaran, S.T., Balamurugan, K., Sivashanmugam, N., Sivaprakasam, P., Kurniawan, R., Ezhilmaran, V. Vibration Studies on Fiber Reinforced Composites – a Review. Journal of Natural Fibers. 2023. 20(1). Article no. 2157361. DOI: 10.1080/15440478.2022.2157361

2. Sun, C.T., Chattopadhyay, S. Dynamic response of anisotropic laminated plates under initial stress to impact of a mass. Journal of Applied Mechanics. 1975. 42(3). Pp. 693–698. DOI: 10.1115/1.3423664

3. Amuthakkannan, P., Manikandan, V. Free vibration and dynamic mechanical properties of basalt fiber reinforced polymer composites. Indian Journal of Engineering and Materials Sciences. 2018. 25(3). Pp. 265–270.

4. Assarar, M., Zouari, W., Sabhi, H., Ayad, R., Berthelot, J.M. Evaluation of the damping of hybrid carbon-flax reinforced composites. Composite Structures. 2015. 132. Pp. 148–154. DOI: 10.1016/j.compstruct.2015.05.016

5. Biswas, D., Ray, C. Comparative perspective of various shear deformation theories with experimental verification for modal analysis of hybrid laminates. Journal of Vibration and Control. 2017. 23(8). Pp. 1321–1333. DOI: 10.1177/1077546315592766

6. Gopalan, V., Vardhan, M.S., Thakur, V., Krishnamoorthy, A., Pragasam, V., Degalahal, M.R., Velu, P.S., Raja Annamalai, A., Jen, C.-P. Studies on Numerical Buckling Analysis of Cellulose Microfibrils Reinforced Polymer Composites. Materials. 2023. 16(3). Article no. 894. DOI: 10.3390/ma16030894

7. Niyogi, S.B., Wankhade, R.L., Gajbhiye, P.D. Buckling analysis of laminated composites considering the effect of orthotropic material. Journal of Physics: Conference Series. 2020. 1706(1). Article no. 12188. DOI: 10.1088/1742-6596/1706/1/012188

8. Badalov, F., Eshmatov, Kh., Yusupov, M. On certain methods of solving systems of integrodifferential equations encountered in viscoelasticity problems. Journal of Applied Mathematics and Mechanics. 1987. 51(5). Pp. 683–686. DOI: 10.1016/0021-8928(87)90025-6

9. Khodzhaev, D.A., Abdikarimov, R.A., Mirsaidov, M.M. Dynamics of a physically nonlinear viscoelastic cylindrical shell with a concentrated mass. Magazine of Civil Engineering. 2019. 7(91). Pp. 39–48. DOI: 10.18720/MCE.91.4

10. Eshmatov, B.K., Abdikarimov, R.A., Amabili, M., Vatin, N.I. Nonlinear vibrations and dynamic stability of viscoelastic anisotropic fiber reinforced plates. Magazine of Civil Engineering. 2023. 2(118). Article no. 11811. DOI: 10.34910/MCE.118.11

11. Mirsaidov, M., Abdikarimov, R., Khudainazarov, S., Sabirjanov, T. Damping of high-rise structure vibrations with viscoelastic dynamic dampers. E3S Web of Conferences. 2020. 224. Article no. 02020. DOI: 10.1051/e3sconf/202022402020

12. Mohammed, W.H., Shambina, S., Ammash, H.K. Effect of Fibers Orientation on the Nonlinear Dynamic Performance of Laminated Composite Plate under Different Loading In-plane. Civil Engineering Journal. 2022. 8(12). Pp. 2706–2720. DOI: 10.28991/CEJ-2022-08-12-03

13. Kanu, N.J., Lal, A. Nonlinear static and dynamic performance of CNT reinforced and nanoclay modified laminated nanocomposite plate. AIP Advances. 2022. 12(2). Article no. 025102. DOI: 10.1063/5.0074987

14. Parida, S.P., Jena, P.C. Free and forced vibration analysis of flyash/graphene filled laminated composite plates using higher order shear deformation theory. Proceedings of the Institution of Mechanical Engineers, Part C: Journal of Mechanical Engineering Science. 2022. 236(9). Pp. 4648–4659. DOI: 10.1177/09544062211053181

15. Moghaddasi, M., Kiani, Y. Free and forced vibrations of graphene platelets reinforced composite laminated arches subjected to moving load. Meccanica. 2022. 57(5). Pp. 1105–1124. DOI: 10.1007/s11012-022-01476-x

16. Heshmati, A., Jafari-Talookolaei, R.-A., Valvo, P.S., Saadatmorad, M. Free and forced vibration analysis of laminated composite beams with through-the-width delamination by considering the in-plane and out-of-plane deformations. Mechanics of Advanced Materials and Structures. 2023. 1–20. DOI: 10.1080/15376494.2023.2222399

17. Zhu, C., Li, G., Yang, J. Vibration Analysis of Laminated Composite Panels with Various Fiber Angles. Mechanisms and Machine Science. 2023. 125. Pp. 948–956. DOI: 10.1007/978-3-031-15758-5_98

18. Karthikeyan, M., Jenarthanan, M.P., Rakurty, S.V.S.K., Ganesh, K.R.V.S.S. Vibrational and structural analysis of drilled (delaminated) fibre reinforced polymer composite plates. AIP Conference Proceedings. 2023. 2715(1). Article no. 020020. DOI: 10.1063/5.0154528

19. Moorthy, V., Marappan, K. Free and forced vibration analysis of delaminated FRP composite plate with a circular hole. International Journal of Vehicle Noise and Vibration. 2024. 19(3/4). Pp. 203–211. DOI: 10.1504/IJVNV.2023.136068

20. Mirzaei, M., Rabiei, R. On the free and forced vibrations of porous GPL reinforced composite conical panels using a Legendre-Ritz method. Engineering Analysis with Boundary Elements. 2024. 163. Pp. 378–393. DOI: 10.1016/j.enganabound.2024.03.024

21. Jones, R.M. Mechanics of Composite Materials. Second Edition. Boca Raton: CRC Press, 2018. 519 p.

22. Whitney, J.M. Structural Analysis of Laminated Anisotropic Plates. Lancaster, PA: Technomic Pub. Co, 1987. 342 p. DOI:

23. Ashton, J.E., Whitney, J.M. Theory of Laminated Plates. Stamford, CT: Technomic, 1970. 158 p.

24. Koltunov, M.A. Choice of kernels in solving problems involving creep and relaxation. Polymer Mechanics. 1966. 2(4). Pp. 303–311. DOI: 10.1007/BF00860064

25. Tyuneeva, I.M. Relaxation characteristics of glass-reinforced plastics. Polymer Mechanics. 1970. 6(3). Pp. 492–494. DOI: 10.1007/BF00858221

26. Volmir, A.S. The nonlinear dynamics of plates and shells. Dayton, OH: Foreign Technology Division Wright-Patterson Air Force, 1974. 543 p.

Information about the authors:

Bakhtiyor Eshmatov,
ORCID: https://orcid.org/0000-0003-0198-6679
E-mail: ebkh@mail.ru

Mirziyod Mirsaidov, *Doctor of Technical Sciences*
ORCID: https://orcid.org/0000-0002-8907-7869
E-mail: mirsaidov1948@mail.ru

Rustamkhan Abdikarimov, *Doctor of Physics and Mathematics*
ORCID: https://orcid.org/0000-0001-8114-1187
E-mail: rabdikarimov@mail.ru

Nikolai Vatin, *Doctor of Technical Sciences*
ORCID: https://orcid.org/0000-0002-1196-8004
E-mail: vatin@mail.ru